# Modelling, Distributed Identification and Control of Spatially-Distributed Systems with Application to an Actuated Beam

Vom Promotionsausschuss der
Technischen Universität Hamburg-Harburg
zur Erlangung des akademischen Grades
Doktor-Ingenieurin
genehmigte Dissertation

von

Qin Liu

aus Suining, Sichuan, China

2015

1. Gutachter:
Prof. Dr. Herbert Werner

2. Gutachter:
Prof. Dr.-Ing. Uwe Weltin

Vorsitzende des Promotionsverfahrens:
Prof. Dr. sc. techn. Christian Schuster

Tag der mündlichen Prüfung: 08.06.2015

urn:nbn:de:gbv:830-88213106

TO MY FAMILY

# Contents

# Abstract

This thesis studies the modelling, distributed identification and control of spatially-distributed systems. The development of light-weight piezoelectric materials enables sensing and actuating distributed systems without significantly changing the dynamics of the original system. In this work, a flexible structure – a 4.8 m long aluminium beam equipped with 16 pairs of collocated piezo actuators and sensors – is constructed for experimental study. The piezoelectric finite element method that accounts for both the flexible structure and the distributed piezo pairs is applied to physically model the coupled electric and elastic dynamics. As an alternative to exploring the physical properties of the actuated structure, a local linear parameter-varying (LPV) identification approach is extended from lumped to spatio-temporal systems to identify the frequency response function (FRF) matrix (or the transfer function matrix) by directly modelling its input/output behaviour.

It is well-known that spatially-distributed systems are typically governed by partial differential equations (PDEs). After spatially discretizing the governing PDE, the system can be considered as the interconnection of subsystems, each interacting with its nearest neighbours and equipped with actuating and sensing capabilities. A two-dimensional input/output model, which defines the system dynamics on a single subsystem of small order, is employed as the mathematical model for the distributed identification of both the parameter-invariant and parameter-varying systems, where the dynamics of the parameter-varying systems can be captured by temporal/spatial LPV models.

To apply the well-developed state-space based synthesis conditions, the experimentally identified input/output models are converted into their multidimensional state space representations that lead to an efficient, linear matrix inequality (LMI)-based synthesis of distributed controllers. It is desired that the controller inherits the interconnected structure of the plant. Therefore, a linear time- and space-invariant distributed controller and a temporal/spatial LPV controller are used to control the parameter-invariant and the parameter-varying systems, respectively. To reduce the conservatism caused by the use of constant Lyapunov functions in the LPV controller design, analysis and synthesis conditions using parameter-dependent Lyapunov functions are proposed by extending previous results on lumped systems. The designed controllers are tested experimentally in terms of suppressing the disturbances injected to the actuated beam.

Actuator saturation is usually not taken into account when solving the controller synthesis problem. To overcome the performance degradation caused by the constrained actuator capacity, a distributed anti-windup scheme is proposed. The nonlinear saturation/deadzone operator is characterized in terms of LMIs using integral quadratic constraints (IQCs) with a suitable choice of multiplier. The performance of the distributed anti-windup scheme is compared with that of a decentralized anti-windup scheme.

# Acknowledgement

This thesis is the conclusion of my four years of research work at the Institute of Control Systems (ICS), Hamburg University of Technology (TUHH) from 11.2010 to 10.2014. I would like to thank those people without whose contributions and support this work would not have been possible.

I would like to express my sincere gratitude to my supervisor Prof. Herbert Werner, who gave me the chance to start this journey at the first place and guided me through it with his rich knowledge, vision and patience. Prof. Werner impacted me deeply with his rigorous research attitude and critical thinking, which have helped me to shape my own understanding of conducting research.

I am also grateful to Prof. Uwe Weltin for his willingness to be the second examiner as well as his suggestions which helped to broaden this work, and to Prof. Christian Schuster as the president of the doctoral committee.

I would also like to thank all my colleagues at the ICS for the wonderful teamwork and friendship throughout the years. It was a great experience to work hard together on papers and share the joy after the acceptance. In particular, I am grateful to Annika Eichler, Christian Hoffmann, Antonio Méndez, Dr. Sven Pfeiffer, Simon Wollnack, Fatimah Al-Taie and Dr. Ahsan Ali. The cooperation work and fruitful discussions with them inspired me and improved my work. Many thanks go to my former colleague Mahdi Hashemi, who was also the supervisor of my project work and master thesis. Working together with him reinforced my interest in control engineering. I would also like to thank Herwig Meyer for constructing test-beds for my work and always being helpful when I approached him with various problems, and Klaus Baumgart and Uwe Jahns for their technical support. Our former secretary Mrs. von Dewitz, and current secretaries Bettina Schrieber and Christine Kopf, who have always been great help, are thankfully acknowledged.

In addition to the aforementioned colleagues, I would like to express my gratitude to Dr. Joseph Gross from the Institute for Reliability Engineering, for helping me to learn structural dynamics and answering my questions with enormous patience.

My warmest thanks go to my parents, who have been encouraging me to build and pursue my dreams since I was a kid, even if those dreams take me further and further away from them. It is their unconditional support and love that make everything possible at all. I would like to thank my parents-in-law and brothers-in-law, who care about me like their own daughter / sister. Last and foremost, I would like to thank my beloved husband Sebastian, who is always there for me. His belief in me gave me the strength and courage to accomplish this journey. What this thesis recorded are not only the research results that I have achieved, but also a great time and memory that I will cherish forever.

# Chapter 1

# Introduction

Spatially-distributed systems, a class of *distributed-parameter systems* as opposed to *lumped parameter systems*, arise in various engineering problems. Examples include vehicular platoons [1], modern paper-making machines [2], the distribution of heat or fluid in a given region [3], smart materials and structures [4], etc. Variables in lumped systems are functions of time alone, whereas a common feature of distributed-parameter systems is their underlying independent temporal and spatial dynamics, i.e. all involved signals are functions of time and space. Thus, this class of systems is often addressed in the framework of spatio-temporal systems.

The modelling, analysis and control of one typical spatially-distributed system – flexible structures – have been extensively studied in structural engineering since decades. This thesis addresses these issues in a newly developed framework developing theoretical methods, as well as evaluating them experimentally. This introduction should motivate the problems to be considered in this work. Main contributions and an outline of this thesis are provided at the end of this chapter.

## 1.1 Spatially-Distributed Systems

Flexible structures are spatially-continuous systems whose mass and stiffness are functions of spatial variables. The distributed nature of these systems can be captured using partial differential equations (PDEs). Due to the spatial continuum, this class of systems is often referred to as *infinite-dimensional systems*, indicating the infinite dimension of the state space. The well-developed *semigroup theory* [5] has been widely employed for a precise mathematical treatment of the internal dynamics of an infinite-dimensional system, which is significantly more difficult than the finite-dimensional theory [6].

The active vibration control of flexible structures often involves a large number of spatially-distributed actuators and sensors. Instead of preserving the continuous nature in space, the attachment of actuators and sensors induces a spatial discretization, so that the overall structure can be treated as a physical interaction between spatially-discretized subsystems on one or multidimensional discrete lattices. A one-dimensional flexible structure after the spatial discretization is shown in Fig. 1.1. The dynamics of the spatially-discretized subsystems can be modelled by a finite number of coupled ordinary differential equations (ODEs) [7]. Assumed here are the convergence of finite-dimensional approximation, and sensing and actuating capabilities on each subsystem.

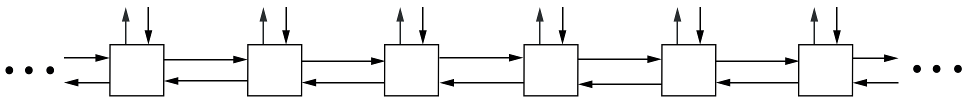

Figure 1.1: Subsystems on one-dimensional lattices after the spatial discretization

The fast development of the microelectromechanical system (MEMS) and light-weight piezoelectric materials makes the manufacturing of large arrays of actuators and sensors feasible and economical. Meanwhile, attaching or embedding microscopic devices on the structural surface enables the spatially-discretized subsystems being equipped with actuating, sensing, and even computing and telecommunication capabilities, without changing its nominal dynamics significantly.

### 1.1.1 Control Architectures

When it comes to the control of these large-scale systems, the choice of the control architecture determines the involved computation effort, as well as the closed-loop performance; it thus plays a crucial role. With each subsystem equipped with collocated or non-collocated actuators and sensors, three prevalent architectures are the *centralized*, the *decentralized*, and the *localized* or so-called *distributed* control schemes, as shown in Fig. 1.2.

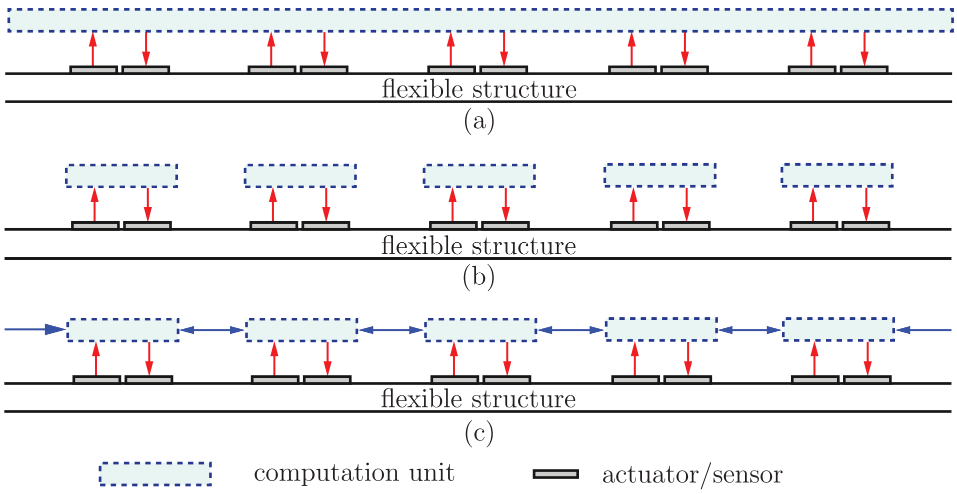


Figure 1.2: Three control architectures for a large-scale system: (a) centralized scheme; (b) decentralized scheme; (c) distributed scheme. Red arrows denote the information flow between actuators/sensors and computation units; blue arrows denote the information flow between computation units.

- Centralized scheme: A centralized control scheme, as shown in Fig. 1.2 (a), treats the distributed system as a lumped system with multiple-input and multiple-output (MIMO). The computation unit – often a central computer – requires the connection with all sensors and actuators. A centralized controller normally possesses a large system order. In many cases it fails to realize an effective control due to a high level of connectivity and computational burden. It is more sensitive to actuator/sensor failures and transmission errors.

- Decentralized scheme: Instead of communicating with a central computer, each subsystem in a decentralized control scheme as shown in Fig. 1.2 (b) is equipped with an independent computation unit executing controller algorithms. It receives the sensing information from its located subsystem, and actuates at the same location. The controller of a decentralized scheme handles the dynamics of a single subsystem of a significantly smaller order compared to that of a centralized system.

- Distributed (localized) scheme: It has been shown in [6], that a spatially-distributed system exhibits some degrees of localization. A distributed control scheme inherits the spatial structure of the plant, where the computation units interact with nearest neighbours as shown in Fig. 1.2 (c). It is different from the decentralized scheme in the sense that the distributed controller exchanges information with the subsystem where it locates, as well as with neighbouring subsystems. In both decentralized and distributed schemes, none of the controller subsystems has the information of the complete system, whereas the communication among subsystems in Fig. 1.2 (c) enables an improved overall performance compared to Fig. 1.2 (b). Thus, the distributed scheme is considered superior to the other two architectures.

### 1.1.2 Construction of a Distributed System

Inspired by the works [6] [8], an actuated flexible structure as shown in Fig. 1.3 has been constructed to study the behaviour of a spatially-distributed system. The flexible structure—an aluminium beam measuring 4.8 m in length, 4 cm in width, and 3 mm in thickness, is equipped with 16 paris of piezoelectric actuators and sensors in collocated pattern. A zoomed-in collocated piezo pair is shown in Fig. 1.4, where the piezo patch on the top functions as actuator, the one at the bottom as sensor.

In order to approximate a free-body suspension condition, where the resonant frequencies of the rigid body modes are at least half of that of the first bending mode [9], 17 soft springs are used to suspend the structure in parallel. A schematic drawing of the test bed is shown in Fig. 1.5.

The attachment of distributed actuators and sensors virtually divides the structure into 16 spatially-interconnected subsystems, each equipped with actuating and sensing capabilities. This thesis is meant to experimentally test the distributed control scheme in Fig. 1.2 (c) due to its superiority. However, constructing 16 physically parallel computation units requires a large amount of expense and effort. Instead, a much cheaper solution as shown in Fig. 1.6 has been employed by using a centralized real-time system to real-

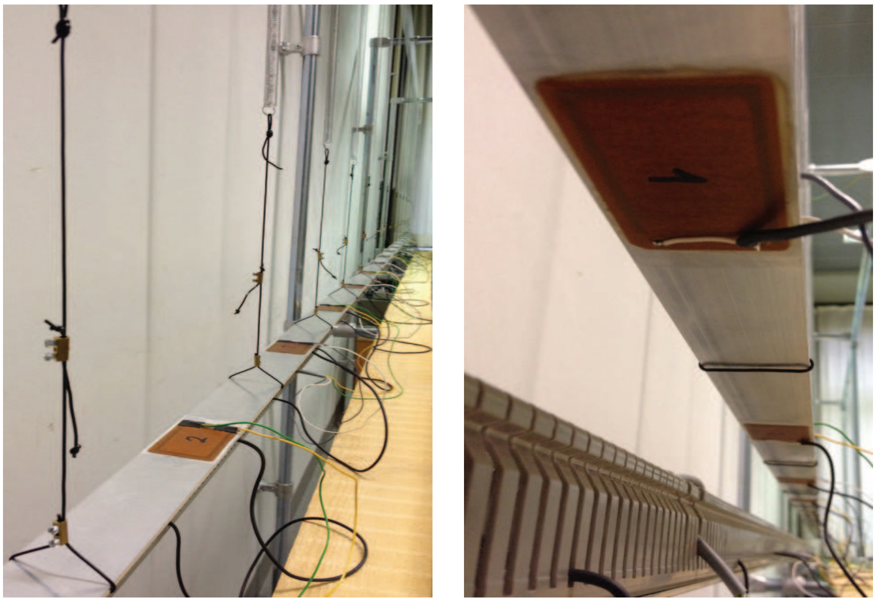

(a) (b)

Figure 1.3: The experimental setup: (a) downward view of 16 actuators; (b) upward view of 16 sensors

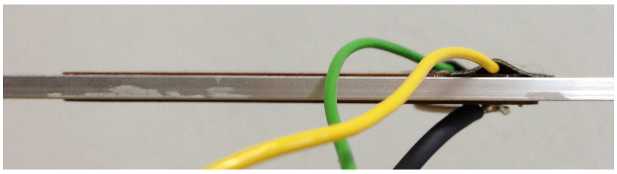

Figure 1.4: One collocated piezo actuator/sensor pair

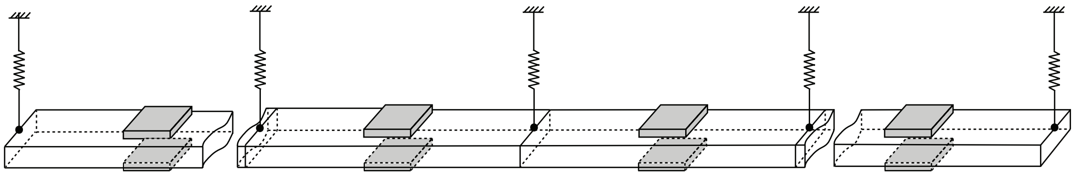

Figure 1.5: A schematic drawing of the experimental setup

ize the computation tasks of 16 parallel units, with the distributed nature of controllers still preserved. The main hardware and software components are listed in Table C.1 (see Appendix C).

### 1.1.3 Linear Parameter-Varying in Distributed Systems

After the spatial discretization, the resulting subsystems may exhibit identical or varying dynamics. Analogous to the definition of linear time-invariant (LTI) systems, let $G$ be

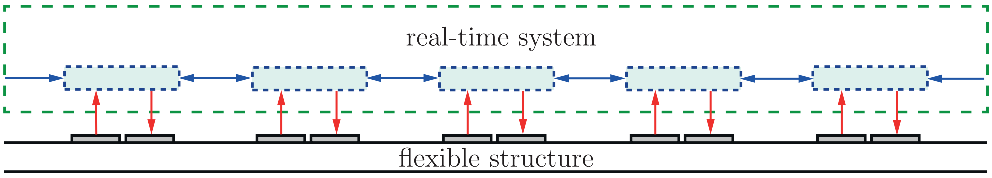


Figure 1.6: Distributed control scheme employed in this work, where the computation is centrally executed via a real-time system.

a two-dimensional operator that maps signal $u(t,s)$ into $y(t,s)$, i.e. $y(t,s) = Gu(t,s)$, where all involved signals are multidimensional with respect to time $t$ and space $s$. A spatially-distributed system is said to be linear time- and space-invariant (LTSI), if the system is linear and invariant under temporal and spatial translations [6] as defined as follows:

- Operator $G$ is linear, if $\forall \alpha, \beta \in \mathbb{R}$

$$G(\alpha u(t,s) + \beta v(t,s)) = \alpha G u(t,s) + \beta G v(t,s). \tag{1.1}$$

- Operator $G$ is time- and space-invariant if $\forall t_0, s_0 \in \mathbb{R}$

$$y(t - t_0, s - s_0) = Gu(t - t_0, s - s_0). \tag{1.2}$$

If condition (1.2) is violated, the distributed system is said to be linear time/space-varying (LTSV).

The framework of linear parameter-varying (LPV) systems was first introduced in [10] to analyse and control nonlinear systems, whose system matrices vary either explicitly with respect to time, or with respect to a temporal-scheduling parameter $\theta$, i.e.

$$\dot{x}(t) = A(\theta(t))x(t) + B(\theta(t))u(t), \tag{1.3}$$
$$y(t) = C(\theta(t))x(t) + D(\theta(t))u(t). \tag{1.4}$$

In general, the scheduling parameters can be exogenous signals, states, inputs or outputs. If the system matrices depend on the scheduling parameters, the LPV state space model (1.3)-(1.4) captures the nonlinear dynamics with a collection of LTI models on the scheduling trajectory.

A heuristic approach to control LPV systems is to design a series of LTI controllers at each frozen point on the scheduling trajectory. The overall control law is realized via controller interpolation. The drawback of such schemes is no guarantee of stability and performance along all possible trajectories. With the extension of $H_\infty$ control theory for LTI systems, the design of gain-scheduling controllers guarantees the stability and certain performance specification along the scheduling trajectories; it has become an active research area in control engineering since 1970s. When the dependence of the plant matrices on scheduling parameters is linear fractional, the LPV model can be written in a linear fractional transformation (LFT) form. Based on the small gain theorem, the existence of a gain-scheduled controller is fully characterized in terms of linear matrix inequalities (LMIs) [11] [12], via searching for Lyapunov functions that establish stability and performance of the closed-loop system. The use of constant Lyapunov functions (CLFs) allows for arbitrarily fast parameter variations, thus resulting conservatism in the case of slowly varying parameters. To reduce the conservatism caused by the use of CLFs, an improvement can be expected by exploiting the concept of parameter-dependent Lyapunov functions (PDLFs), which allows to incorporate the knowledge on the rate of parameter variations in the derivation of analysis and synthesis conditions [13] [14] [15]. A more detailed overview regarding LPV systems and LPV controller design can be found in [16] [17] [18] [19] [20].

Although the LPV framework was first introduced to deal with time-varying systems, it can be extended in a straightforward way to solve analogous problems in distributed systems with varying parameters. If the system matrices can be parametrized as functions of temporal- and/or spatial-scheduling parameters, a temporal/spatial LPV model can be used to capture the structural dynamics over the multidimensional variation range. The controller design techniques developed for temporal LPV models can be extended and applied to LTSV models [21].

## 1.2 Relevant Work in the Field

Theoretical approaches for the modelling, analysis and control of spatially-distributed systems have been developed in numerous works. This section reviews some of them which are relevant to the topics concerned in this thesis, and motivates problems to be addressed.

### 1.2.1 Modelling/Identification

Modelling of continuous structures has been a routine topic of research in structural engineering for decades. The finite element (FE) method [22], as a numerical modelling approach, has been employed extensively in the theoretical analysis of structural behaviour in aeronautics, civil and building structures, biomechanical problems, automotive applications and so on. The standard FE method accounts only for the mechanical energy dissipation, not taking the bonded piezo actuators/sensors – parts of the experimental setup in Section 1.1.2 – into consideration. The piezoelectric effect was first incorporated into the FE modelling in [23] and [24]. The derived piezoelectric FE approach takes care of coupled piezoelectric and elastic effect, and has been widely applied to the modelling of intelligent structures in [25] [26], etc.

Modelling using the FE method helps to understand the physical behaviour of the structure, taking safety and reliability issues into consideration. However, with the increase of structural complexity, the FE modelling can become expensive and involves large computation effort. Meanwhile, the obtained FE model treats the structure as a lumped MIMO system; the resulting large system order makes it unfavourable for further controller design.

In contrast, black-box identification out of experimental measurements does not require a prior knowledge on the principle laws of physics; it thus serves as a fast and efficient solution. It is well-known, that the dynamics of continuous structures are typically governed by PDEs. The temporal and spatial discretization of a governing PDE leads to a two-dimensional input/output model, which could be used as the mathematical model for black-box identification. Based on the least-squares estimation, a black-box identification approach for LTSI systems has been developed in [27]. The identified model defines the dynamics of a single subsystem interacting with its neighbouring subsystems, with the localized nature of the plant preserved. In the presence of temporal/spatial variations, the temporal LPV input/output identification techniques proposed in [28] have been extended in [29] for the identification of temporal/spatial LPV models.

### 1.2.2 Distributed Control

Since last few decades, the design of distributed controllers that preserve the distributed structure of the plant as shown in Fig. 1.7 has received extensive attentions. Several frameworks have been proposed to address this issue from different perspectives [8] [30] [31] [32], etc. Two common features of these approaches are: 1. the overall system is treated as the interconnection of small-order subsystems; 2. the controller inherits the communication topology of the plant.

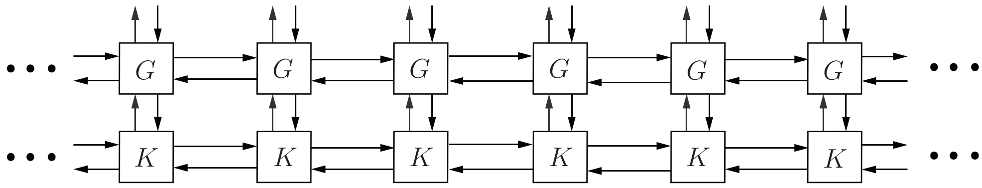


Figure 1.7: Distributed controller designed for a distributed plant

Among them, [8] introduced a novel multidimensional state space model to represent the interconnected dynamics of an LTSI system. Analysis and synthesis conditions are formulated in terms of LMIs, using the induced $\mathcal{L}_2$ norm as the performance criterion. To investigate the effectiveness of the framework proposed in [8], a simulation case study on the distributed control of a flexible beam has been performed in [33]. Accounting for the boundary conditions, non-uniform physical characteristics of the structure, etc., tools have been developed in [21] [34] to solve the control problem when the underlying system dynamics are not invariant with respect to temporal or spatial variables.

The distributed control scheme has been perceived as an effective and computationally attractive solution to tackle large-scale distributed systems. Among the various developed approaches, very few of them have been validated experimentally. This thesis is meant to fill in this gap by exploring the experimental implementation of the framework proposed in [8] on the constructed test structure.

### 1.2.3 Anti-Windup Compensator

In all physical systems, actuator capacities are limited by the inherent physical constraints and limitations of the actuators. In the presence of actuator saturation, any controller with slow or unstable dynamics exhibits a windup effect [35]: the established closed-loop performance suffers from deterioration, or even instability. The design of an effective anti-windup (AW) compensator for lumped systems has been an active field of research since 1970s. Only in the last decade, a more formal way with stability and performance specifications incorporated in the AW design has been established using $H_\infty$ optimal control [36]. In recent years, LMIs are employed as a tool to impose constraints on the design of an AW compensator [37] [38] [39], which significantly simplifies the computation of the global optimal solution into a convex optimization problem.

The windup effect can arise in distributed systems as well. Saturation on one actuator could easily lead to saturation on an array of interconnected actuators. Until now, very few works have addressed this issue thoroughly [40] [41]. Taking the inherent distributed dynamics of the plant and the controller into consideration, an appropriate AW scheme could effectively alleviate the degradation of the closed-loop performance caused by actuator saturation, thus being worth further research.

## 1.3 Scope and Main Contributions of this Thesis

This thesis focuses on the modelling, distributed identification and control of spatially-interconnected systems, with an application to an aluminium beam equipped with an array of collocated piezo actuator and sensor pairs. For a better understanding of the underlying physical laws of the test structure, it is meaningful to start with the physical modelling based on the knowledge of its properties and functionalities. Furthermore, the distributed framework proposed in [8] is employed in this thesis for the system analysis and distributed controller design. In order to apply the well-developed analysis and synthesis conditions developed in [8], a distributed model in multidimensional state space form needs to be identified first. Considered in this thesis are both the LTSI and LTSV systems. By slightly modifying the hardware, the test structure can realize the configurations required for both the LTSI and LTSV models. It is desired, that the controller inherits the interconnected structure of the plant as shown in Fig. 1.7. The distributed control problem of both the identified LTSI and LTSV models are addressed, and implemented experimentally. Keeping the physical limitations of the distributed actuators in mind, an appropriate AW scheme that accounts for the distributed nature of the plant and the controller, can effectively counteract the windup effect with a bound on the closed-loop performance guaranteed in the presence of actuator saturation.

The main contributions of this thesis are summarized as follows:

- The piezoelectric FE modelling approach is applied to model the coupled piezoelectric and mechanical behaviour of the piezo-actuated beam structure. With the combined implementation of the experimental modal analysis, an FE model that captures the structural dynamics of the real plant to a satisfactory degree is obtained.

- *Frequency response function* (FRF) is a mathematical representation of the relationship from an excitation at one location to the vibration response at the same or another location. It is demonstrated, that FRFs of even a homogeneous structure exhibit spatially-varying characteristics. A local LPV input/output identification technique for temporal systems is extended to spatio-temporal systems to model the FRF matrix as a spatial LPV model based on black-box identification.

- The multidimensional black-box identification techniques developed in [27] for LTSI models and [29] for spatial LPV models are for the first time implemented experimentally. Although the identified models capture the structural behaviour to a certain extent, dynamics at resonances are hardly identified. A new identification procedure is proposed to extract a distributed input/output model from the obtained FE model, yielding improved identification results.

- Distributed LTSI and LPV controllers for the LTSI and for the LTSV systems are designed, respectively, and experimentally implemented to suppress the vibratory motion of the actuated beam caused by the disturbance injection. To reduce the conservatism with the use of CLFs, the LPV controller design technique using PDLFs is extended from lumped systems to spatially-distributed systems with varying parameters. The performance of the designed controllers is evaluated experimentally.

- To alleviate the windup effect due to actuator saturation, a distributed AW scheme, that inherits the distributed pattern of the controlled system is proposed. The designed AW compensator can be implemented on top of an existing closed-loop system, with the global stability and a bound on $\mathcal{L}_2$ performance of the constrained system guaranteed.

## 1.4 Thesis Outline

This thesis consists of eight chapters. A brief overview of the content in each chapter is given below:

**Chapter 2** reviews the framework of spatially-interconnected systems. Definitions on the multidimensional signal and system norms are given as a preliminary. The multidimensional state space representations, that are employed throughout the work, proposed in [8] for LTSI systems, in [21] for LTSV systems, as well as their correspondent controllers, which inherit the distributed nature of the plant, are presented. The definitions of the well-posedness, exponential stability, and quadratic performance in the context of distributed systems are discussed. The analysis conditions for an LTSI system to be well-posed, exponentially stable, and with the imposed performance criteria satisfied are provided for both continuous and discrete systems.

**Chapter 3** takes physical aspects of the experimental structure into consideration, reviewing the functionality of piezoelectric patches as actuator and sensor, respectively. Linear constitutive equations are applied to analyse the linear dynamics of both the piezo actuators and sensors. The application of a piezoelectric FE modelling approach yields a theoretical FE model characterized in terms of mass and stiffness matrices, based on known and assumed knowledge on the physical properties of the actuated beam. To reduce the deviation between the theoretical FE model and test structure, experimental modal analysis is performed to update the mass and stiffness matrices at first, then the proportional-assumed damping matrix. Meanwhile, a direct feed-through effect is observed from actuators to collocated sensors.

Instead of exploring the inherent physics of a flexible structure using the FE modelling, **Chapter 4** identifies a structure through identifying its FRF matrix from the input/output measurements. It is demonstrated step by step, that even for a structure comprised of identical subsystems, its FRF matrix exhibits spatially-varying characteristics. A local LPV identification technique for temporal systems is extended to spatio-temporal systems to capture the spatially-varying properties of FRFs. Actuating and sensing at selected locations results in a set of measured FRFs, each being estimated as an LTI model using a least-squares-based identification technique. The application of the extended local LPV approach parametrizes the set of estimated LTI models as a spatial LPV model by defining the spatial coordinates of actuating and sensing locations as spatial scheduling parameters. The proposed approach allows to perform identification experiments at a small number of selected actuating and sensing locations, and parametrize a spatial LPV model. Then unknown FRFs at other locations can be easily approximated through interpolation. The proposed approach is tested experimentally.

Both the obtained FE model in Chapter 3 and the identified FRF matrix in spatial LPV representation in Chapter 4 treat the plant as a MIMO lumped system. **Chapter 5** deals with the identification problem in the context of spatially-distributed systems. A two-dimensional input/output model induced by the temporal and spatial discretization of governing PDEs is considered as the mathematical model for identification. It describes the dynamics of a spatially-discrete subsystem interacting with nearby subsystems. Black-box identification techniques for the identification of LTSI and LTSV models are briefly reviewed, and experimentally implemented. To improve the model accuracy, especially at resonant peaks, a new identification procedure which makes use of the FE model obtained in Chapter 3 is proposed. Both the identified LTSI and spatial LPV models preserve the two-dimensional input/output structure, and suggest a better representation of the plant dynamics than black-box identification.

Based on the input/output models identified in Chapter 5, **Chapter 6** solves the controller design problem for both the LTSI and LTSV systems. In order to employ the well-developed state-space based analysis and synthesis conditions, the experimentally identified input/output models are first converted into their multidimensional state space realizations. The construction of a multidimensional generalized plant for shaping the mixed sensitivity of the closed-loop system is discussed. The synthesis conditions of a distributed LTSI controller are briefly reviewed. Both a distributed and a decentralized controller are designed and implemented, with their performance compared experimentally. The synthesis conditions of temporal/spatial LPV controllers for LTSV systems are derived with the application of the *full block S-procedure* (FBSP), using both the CLFs and PDLFs. The experimental results demonstrate a superior performance of the LPV controller designed using PDLFs.

**Chapter 7** addresses a two-step distributed AW compensator design in the presence of actuator saturation in physical systems. A lumped AW scheme is first revisited. The definition of a mathematical tool – integral quadratic constraints (IQCs) [42] – and its application to the robust analysis of an LFT model with a nonlinear uncertainty is shortly recapped. Inspired by the lumped setup, a distributed AW scheme, which preserves the distributed nature of the plant and the controller, is proposed. The stability of the closed-loop subsystem in LFT form, with the nonlinear deadzone operator as uncertainty, is analysed using IQCs. The synthesis conditions are derived after applying the elimination lemma. The performance of the distributed AW compensator is illustrated using a simulation example, in comparison with a decentralized AW scheme.

In **Chapter 8**, conclusions to this thesis are drawn; and an outlook for future research is given.

# Chapter 2

# Spatially-Interconnected Systems

## 2.1 Introduction

In this chapter, relevant preliminary materials regarding spatially-interconnected systems are briefly reviewed. In Section 2.2, signal and system norms and shift operators in the context of spatially-interconnected systems are extended from their lumped counterparts. Instead of considering the distributed-parameter system as a large-scale lumped MIMO system, the distributed framework proposed in [8], where a spatially-distributed system can be seen as an array of interconnected subsystems, is presented in Section 2.3. The system dynamics are defined at the subsystem level using a multidimensional state space representation. Depending on the physical properties of subsystems, such a system can be either LTSI or LTSV, where subsystems in an LTSI system share identical dynamics, whereas the varying dynamics of an LTSV system can be captured using temporal/spatial-LPV models. It is desired that the controller inherits the distributed feature of the plant. The controller structures for both parameter-invariant and parameter-varying systems are given in Section 2.4. In Section 2.5, the well-posedness, exponential stability and quadratic performance are defined for spatially-interconnected systems, respectively. The analysis conditions that establish well-posedness, stability and performance specifications are stated in terms of LMIs.

## 2.2 Relevant Definitions

Unlike lumped systems, whose signals are functions of time only, spatially-distributed systems are multidimensional systems. For systems in $L$ spatial dimensions, involved signals are indexed by $L+1$ independent variables, e.g. signal $u(k, s_1, s_2, \ldots, s_L)$ with respect to discrete temporal variable $k$, and discrete spatial variables $s_1, s_2, \ldots, s_L$, where $s_i$ indexes the $i$-th spatial dimension. This work focuses on distributed systems of one spatial dimension, i.e. $u(k, s)$.

Signal norms for lumped systems measure the size of a signal over time, whereas system norms measure the gain of a system. These measures apply to multidimensional systems as well. The normed spaces, the signal and space norms, as well as the shift operators, have been extended to spatially-distributed systems in [8], accounting for both temporal and spatial variables.

**Definition 2.1 (Inner Product Space [5])** *An inner product on a linear vector space $V$ defined over complex or real filed $\mathcal{F}$ is a map*

$$< \cdot, \cdot >: V \times V \to \mathcal{F}. \tag{2.1}$$

**Definition 2.2 (Hilbert Space [5])** *A Hilbert space is an inner product space that is complete as a normed linear space under the induced norm.*

The spaces $l_2$ and $\mathcal{L}_2$ are Hilbert spaces under inner products. Provided $x(k, s)$—a function of discrete time $k$ and discrete space $s$, the spaces $l_2$ and $\mathcal{L}_2$ are defined by separating the spatial and temporal parts of the signal as follows:

**Definition 2.3 (Space $l_2$ [8])** *The space $l_2$ is the set of functions that the following quantity with fixed temporal variable $k = k_0$*

$$\sum_{s=-\infty}^{\infty} x^T(k_0, s)x(k_0, s) \tag{2.2}$$

*is bounded.*

The corresponding $l_2$ norm is defined as

$$\| x(k_0, s) \|_{l_2}^2 := \sum_{s=-\infty}^{\infty} x^T(k_0, s)x(k_0, s). \tag{2.3}$$

More intuitively, the boundness of space $l_2$ requires a finite shaded area in Fig. 2.1 at any instant in time. The boundness also implies the completeness of the norm space.

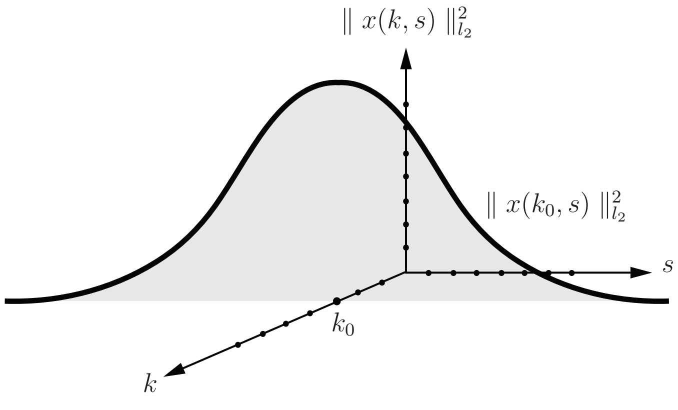


Figure 2.1: $l_2$ norm of $x(k, s)$ at a fixed time instant $k_0$

Provided that $x(k, s)$ is in $l_2$, the space $\mathcal{L}_2$ assesses the boundness of $x(k, s)$ over the whole positive time.

**Definition 2.4 (Space $\mathcal{L}_2$ [8])** *The space $\mathcal{L}_2$ is defined as the set of functions for which the following quantity*

$$\sum_{k=1}^{\infty} \sum_{s=-\infty}^{\infty} x^T(k, s)x(k, s) \tag{2.4}$$

*is bounded.*

The corresponding $\mathcal{L}_2$ norm is defined as

$$\| x(k, s) \|_{\mathcal{L}_2}^2 := \sum_{k=1}^{\infty} \sum_{s=-\infty}^{\infty} x^T(k, s)x(k, s). \tag{2.5}$$

Analogous to lumped systems, the induced $\mathcal{L}_2$ norm of a multidimensional system measures the system gain - the maximum ratio from the $\mathcal{L}_2$ norm of the output signal to the $\mathcal{L}_2$ norm of the input signal.

**Definition 2.5 (System Norm [8])** *The induced $\mathcal{L}_2$ norm of an operator $G$ is defined as*

$$\| G \|_{\mathcal{L}_2} := \sup_{x \neq 0, x \in \mathcal{L}_2} \frac{\| Gx \|_{\mathcal{L}_2}}{\| x \|_{\mathcal{L}_2}}. \tag{2.6}$$

The operator $G$ is said to be bounded on $\mathcal{L}_2$ if $\| G \|_{\mathcal{L}_2} < \infty$ holds.

**Definition 2.6 (Shift Operators [8])** *The temporal forward shift operator $\mathbf{T}$ is defined as*

$$\mathbf{T}x(k, s) = x(k + 1, s), \tag{2.7}$$

*whereas the spatial forward and backward shift operators $\mathbf{S}$ and $\mathbf{S}^{-1}$ act on signals in one spatial dimension as*

$$\mathbf{S}x(k, s) = x(k, s + 1), \quad \mathbf{S}^{-1}x(k, s) = x(k, s - 1). \tag{2.8}$$

## 2.3 Interconnected Systems

According to the framework proposed in [8], a spatially-distributed system is comprised of a number of interconnected subsystems exchanging information with their nearest neighbours as depicted in Fig. 2.2. The subsystems can either be identical or exhibit different dynamics, due to the physical properties, boundary conditions of the distributed system, etc. In this section, the multidimensional state space models that describe the dynamics of both the parameter-invariant and -varying systems are established.

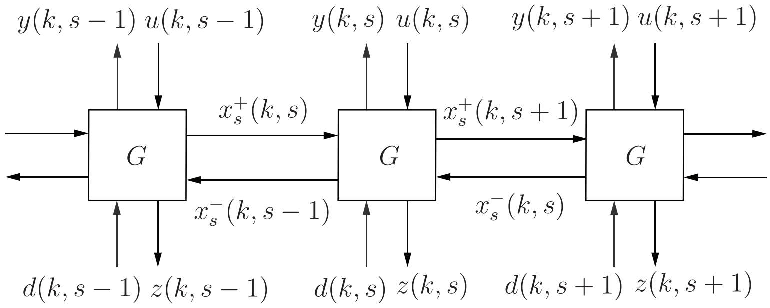


Figure 2.2: Part of a spatially-interconnected system

### 2.3.1 LTSI Systems

Distributed systems are considered LTSI, if the system dynamics are invariant under both temporal and spatial translations [6]. Instead of modelling a distributed system in a centralized manner, a localized model of small size is much easier to handle. The dynamics at any subsystem $s$ is represented in a multidimensional state space form

$$\left[\begin{array}{c} x_t(k+1,s) \\ x_s^+(k,s+1) \\ x_s^-(k,s-1) \\ \hdashline z(k,s) \\ y(k,s) \end{array}\right] = \left[\begin{array}{ccc:cc} A_{tt} & A_{ts}^+ & A_{ts}^- & B_{t,d} & B_{t,u} \\ A_{st}^+ & A_{ss}^{++} & A_{ss}^{+-} & B_{s,d}^+ & B_{s,u}^+ \\ A_{st}^- & A_{ss}^{-+} & A_{ss}^{--} & B_{s,d}^- & B_{s,u}^- \\ \hdashline C_{t,z} & C_{s,z}^+ & C_{s,z}^- & D_{zd} & D_{zu} \\ C_{t,y} & C_{s,y}^+ & C_{s,y}^- & D_{yd} & D_{yu} \end{array}\right] \left[\begin{array}{c} x_t(k,s) \\ x_s^+(k,s) \\ x_s^-(k,s) \\ \hdashline d(k,s) \\ u(k,s) \end{array}\right], \tag{2.9}$$

which contains the temporal state vector $x_t \in \mathbb{R}^{m_0}$, as well as the spatial state vectors $x_s^+ \in \mathbb{R}^{m_+}$ and $x_s^- \in \mathbb{R}^{m_-}$ in positive and negative directions, respectively, where $m_0$, $m_+$ and $m_-$ denote the size of temporal, and spatial state vectors in positive and negative directions, respectively. Subsystems communicate information with each other through spatial states, e.g. the spatial states $x_s^+(k,s)$ and $x_s^-(k,s)$ are the information sending from neighbours $s-1$ and $s+1$ to $s$, respectively. The disturbance signal $d \in \mathbb{R}^{n_d}$ and fictitious output $z \in \mathbb{R}^{n_z}$ are the input and output of the performance channel, respectively, whereas $y \in \mathbb{R}^{n_y}$ and $u \in \mathbb{R}^{n_u}$ are the measured output and exogenous input, respectively. The sizes of the respective signals are denoted by $n_d$, $n_z$, $n_y$ and $n_u$. The system matrices are identical for all subsystems in case of LTSI systems.

An ideal exchange of information among subsystems is assumed in (2.9), i.e. no noise is injected on the communication channel, and no data lost. Thus, the spatial inputs of one subsystem are the spatial outputs of neighbouring subsystems.

Define $\mathbf{\Delta}_m$ as an augmented operator containing both the temporal shift operator $\mathbf{T}$, and the spatial shift operators $\mathbf{S}$ and $\mathbf{S}^{-1}$ as

$$\mathbf{\Delta}_m := \begin{bmatrix} \mathbf{T}I_{m_0} & & \\ & \mathbf{S}I_{m_+} & \\ & & \mathbf{S}^{-1}I_{m_-} \end{bmatrix}, \tag{2.10}$$

with $m = (m_0, m_+, m_-)$. The state space realization (2.9) can be expressed in a compact way as

$$\begin{bmatrix} (\boldsymbol{\Delta}_m^G x^G)(k,s) \\ \hline z(k,s) \\ y(k,s) \end{bmatrix} = \left[\begin{array}{c|cc} A^G & B_d^G & B_u^G \\ \hline C_z^G & D_{zd}^G & D_{zu}^G \\ C_y^G & D_{yd}^G & D_{yu}^G \end{array}\right] \begin{bmatrix} x^G(k,s) \\ \hline d(k,s) \\ u(k,s) \end{bmatrix}. \tag{2.11}$$

The superscript $G$ specifies the plant model. This manner of representing referred systems will be applied throughout the work.

### 2.3.2 LTSV Systems

The assumptions of an LTSI system are often violated in real applications. Dynamics defined on subsystems could vary with respect to time, space, or both. The extended definition of LPV system provides a powerful framework for the modelling of time/space-varying systems, with the linear relationship between the inputs and the outputs still preserved. The multidimensional state space model (2.9), first developed for LTSI systems, is adapted to time/space-varying systems in [21] by allowing variations of the system matrices.

Let the temporal scheduling parameters be $\theta_t := [\theta_{t_1}, \theta_{t_2}, \ldots, \theta_{t_{n_t}}]$, and the spatial scheduling parameters $\theta_s := [\theta_{s_1}, \theta_{s_2}, \ldots, \theta_{s_{n_s}}]$, where $n_t$ and $n_s$ are the numbers of temporal and spatial scheduling parameters, respectively; both are assumed to be measurable in real time. Assume a functional dependence of the system matrices on bounded $\theta_t$ and $\theta_s$. The state space representation $G$ at subsystem $s$, that depends explicitly on $\theta_t$ and $\theta_s$, is written as

$$\begin{bmatrix} x_t(k+1,s) \\ x_s^+(k,s+1) \\ x_s^-(k,s-1) \\ \hline z(k,s) \\ y(k,s) \end{bmatrix} = \left[\begin{array}{ccc|cc} \mathcal{A}_{tt}(\theta_t,\theta_s) & \mathcal{A}_{ts}^+(\theta_t,\theta_s) & \mathcal{A}_{ts}^-(\theta_t,\theta_s) & \mathcal{B}_{t,d}(\theta_t,\theta_s) & \mathcal{B}_{t,u}(\theta_t,\theta_s) \\ \mathcal{A}_{st}^+(\theta_t,\theta_s) & \mathcal{A}_{ss}^{++}(\theta_t,\theta_s) & \mathcal{A}_{ss}^{+-}(\theta_t,\theta_s) & \mathcal{B}_{s,d}^+(\theta_t,\theta_s) & \mathcal{B}_{s,u}^+(\theta_t,\theta_s) \\ \mathcal{A}_{st}^-(\theta_t,\theta_s) & \mathcal{A}_{ss}^{-+}(\theta_t,\theta_s) & \mathcal{A}_{ss}^{--}(\theta_t,\theta_s) & \mathcal{B}_{s,d}^-(\theta_t,\theta_s) & \mathcal{B}_{s,u}^-(\theta_t,\theta_s) \\ \hline \mathcal{C}_{t,z}(\theta_t,\theta_s) & \mathcal{C}_{s,z}^+(\theta_t,\theta_s) & \mathcal{C}_{s,z}^-(\theta_t,\theta_s) & \mathcal{D}_{zd}(\theta_t,\theta_s) & \mathcal{D}_{zu}(\theta_t,\theta_s) \\ \mathcal{C}_{t,y}(\theta_t,\theta_s) & \mathcal{C}_{s,y}^+(\theta_t,\theta_s) & \mathcal{C}_{s,y}^-(\theta_t,\theta_s) & \mathcal{D}_{yd}(\theta_t,\theta_s) & \mathcal{D}_{yu}(\theta_t,\theta_s) \end{array}\right] \begin{bmatrix} x_t(k,s) \\ x_s^+(k,s) \\ x_s^-(k,s) \\ \hline d(k,s) \\ u(k,s) \end{bmatrix}. \tag{2.12}$$

Further assume that the functional dependence of the system matrices on scheduling parameters is rational, and that the temporal and spatial variations are decoupled, i.e. spatial properties of subsystems do not change in time. By pulling out the temporal and spatial uncertainties, the LPV system (2.12) can be written in an LFT representation

$$\begin{bmatrix} x_t(k+1,s) \\ x_s^+(k,s+1) \\ x_s^-(k,s-1) \\ \hline q^t(k,s) \\ q^s(k,s) \\ \hline z(k,s) \\ y(k,s) \end{bmatrix} = \left[\begin{array}{ccc|cc|cc} A_{tt} & A_{ts}^+ & A_{ts}^- & B_{t,p^t} & B_{t,p^s} & B_{t,d} & B_{t,u} \\ A_{st}^+ & A_{ss}^{++} & A_{ss}^{+-} & B_{s,p^t}^+ & B_{s,p^s}^+ & B_{s,d}^+ & B_{s,u}^+ \\ A_{st}^- & A_{ss}^{-+} & A_{ss}^{--} & B_{s,p^t}^- & B_{s,p^s}^- & B_{s,d}^- & B_{s,u}^- \\ \hline C_{t,q^t} & C_{s,q^t}^+ & C_{s,q^t}^- & D_{q^tp^t} & 0 & D_{q^td} & D_{q^tu} \\ C_{t,q^s} & C_{s,q^s}^+ & C_{s,q^s}^- & 0 & D_{q^sp^s} & D_{q^sd} & D_{q^su} \\ \hline C_{t,z} & C_{s,z}^+ & C_{s,z}^- & D_{zp^t} & D_{zp^s} & D_{zd} & D_{zu} \\ C_{t,y} & C_{s,y}^+ & C_{s,y}^- & D_{yp^t} & D_{yp^s} & D_{yd} & D_{yu} \end{array}\right] \begin{bmatrix} x_t(k,s) \\ x_s^+(k,s) \\ x_s^-(k,s) \\ \hline p^t(k,s) \\ p^s(k,s) \\ \hline d(k,s) \\ u(k,s) \end{bmatrix}, \tag{2.13}$$

and

$$\begin{bmatrix} p^t(k,s) \\ p^s(k,s) \end{bmatrix} = \begin{bmatrix} \Theta_t & \\ & \Theta_s \end{bmatrix} \begin{bmatrix} q^t(k,s) \\ q^s(k,s) \end{bmatrix} := \Upsilon^G \begin{bmatrix} q^t(k,s) \\ q^s(k,s) \end{bmatrix}, \tag{2.14}$$

with $p^t$ and $q^t \in \mathbb{R}^{n_{\Theta_t}}$, $p^s$ and $q^s \in \mathbb{R}^{n_{\Theta_s}}$, $\Theta_t \in \boldsymbol{\Theta}_t$ and $\Theta_s \in \boldsymbol{\Theta}_s$, where $p^t$ and $p^s$, $q^t$ and $q^s$ are the inputs and outputs of the temporal and spatial uncertainty channels, respectively. The decoupled temporal and spatial variations imply zero matrices $D_{q^t p^s}$ and $D_{q^s p^t}$. $\Theta_t$ and $\Theta_s$ are the structured temporal and spatial uncertainties of sizes $n_{\Theta_t}$ and $n_{\Theta_s}$ respectively. $\boldsymbol{\Theta}_t$ and $\boldsymbol{\Theta}_s$ are two compact sets with the uncertainties structured in diagonal matrices form, i.e.

$$\begin{aligned} \boldsymbol{\Theta}_t &= \{\Theta_t : \mathrm{diag}\{\theta_{t_1} I_{r_{\theta_{t1}}}, \ldots, \theta_{t_{n_t}} I_{r_{\theta_{tn_t}}}\}, |\theta_{t_i}| < 1, i = 1, \ldots, n_t\} \\ \boldsymbol{\Theta}_s &= \{\Theta_s : \mathrm{diag}\{\theta_{s_1} I_{r_{\theta_{s1}}}, \ldots, \theta_{s_{n_s}} I_{r_{\theta_{sn_s}}}\}, |\theta_{s_i}| < 1, i = 1, \ldots, n_s\}, \end{aligned} \tag{2.15}$$

where $r_{\theta_{ti}}$ and $r_{\theta_{si}}$ denote the multiplicity of scheduling parameters $\theta_{t_i}$ and $\theta_{s_i}$, respectively. A schematic LFT representation of the time/space-varying distributed system is shown in Fig. 2.3, where each subsystem can be seen as the interconnection of an LTSI model $G$ augmented by local feedback with its own temporal and spatial uncertainties.

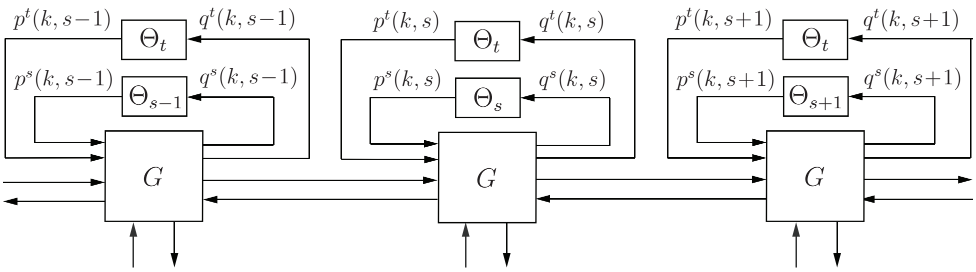


Figure 2.3: Distributed system with time/space-variations in LFT representation

The upper LFT description (2.13) and (2.14) in a compact form writes

$$\left[\begin{array}{c} (\boldsymbol{\Delta}_m^G x^G)(k,s) \\ \hdashline q^G(k,s) \\ \hdashline z(k,s) \\ y(k,s) \end{array}\right] = \left[\begin{array}{c:c:cc} A^G & B_p^G & B_d^G & B_u^G \\ \hdashline C_q^G & D_{qp}^G & D_{qd}^G & D_{qu}^G \\ \hdashline C_z^G & D_{zp}^G & D_{zd}^G & D_{zu}^G \\ C_y^G & D_{yp}^G & D_{yd}^G & D_{yu}^G \end{array}\right] \left[\begin{array}{c} x^G(k,s) \\ \hdashline p^G(k,s) \\ \hdashline d(k,s) \\ u(k,s) \end{array}\right], \tag{2.16}$$

with

$$p^G(k,s) = \Upsilon^G q^G(k,s). \tag{2.17}$$

Assume well-posedness of the interconnection between the LTSI model and uncertainties [43]. The explicit LPV form of (2.16) and (2.17) takes the form

$$\left[\begin{array}{c} (\boldsymbol{\Delta}_m^G x^G)(k,s) \\ \hdashline z(k,s) \\ y(k,s) \end{array}\right] = \left[\begin{array}{c:cc} \mathcal{A}^G(\Theta_t,\Theta_s) & \mathcal{B}_d^G(\Theta_t,\Theta_s) & \mathcal{B}_u^G(\Theta_t,\Theta_s) \\ \hdashline \mathcal{C}_z^G(\Theta_t,\Theta_s) & \mathcal{D}_{zd}^G(\Theta_t,\Theta_s) & \mathcal{D}_{zu}^G(\Theta_t,\Theta_s) \\ \mathcal{C}_y^G(\Theta_t,\Theta_s) & \mathcal{D}_{yd}^G(\Theta_t,\Theta_s) & \mathcal{D}_{yu}^G(\Theta_t,\Theta_s) \end{array}\right] \left[\begin{array}{c} x^G(k,s) \\ \hdashline d(k,s) \\ u(k,s) \end{array}\right]. \tag{2.18}$$

It can be recovered from (2.16) and (2.17) by applying the upper LFT definition (see Appendix C.1)

$$\begin{bmatrix} \mathcal{A}^G(\Theta_t,\Theta_s) & \mathcal{B}_d^G(\Theta_t,\Theta_s) & \mathcal{B}_u^G(\Theta_t,\Theta_s) \\ \mathcal{C}_z^G(\Theta_t,\Theta_s) & \mathcal{D}_{zd}^G(\Theta_t,\Theta_s) & \mathcal{D}_{zu}^G(\Theta_t,\Theta_s) \\ \mathcal{C}_y^G(\Theta_t,\Theta_s) & \mathcal{D}_{yd}^G(\Theta_t,\Theta_s) & \mathcal{D}_{yu}^G(\Theta_t,\Theta_s) \end{bmatrix} = \begin{bmatrix} A^G & B_d^G & B_u^G \\ C_z^G & D_{zd}^G & D_{zu}^G \\ C_y^G & D_{yd}^G & D_{yu}^G \end{bmatrix} + \begin{bmatrix} B_p^G \\ D_{zp}^G \\ D_{yp}^G \end{bmatrix} \Upsilon^G (I - D_{qp}^G \Upsilon^G) \begin{bmatrix} C_q^G & D_{qd}^G & D_{qu}^G \end{bmatrix}. \tag{2.19}$$

## 2.4 Controller Structure

A distributed controller that inherits the communication topology of the plant as shown in Fig. 2.4 is considered in this work. The distributed controller itself is a distributed system, interacting with nearby subsystems. The controller for an LTSI plant is assumed to be an LTSI system, whereas the stability of an LTSV system can only be guaranteed when its controller is properly gain-scheduled. This section presents the controller model structures, as well as the closed-loop state space models, for both the LTSI and LTSV models.

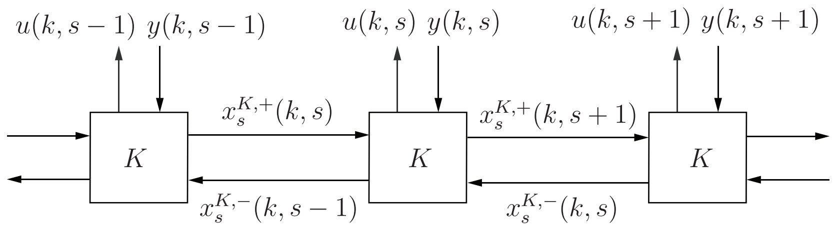


Figure 2.4: Part of a distributed controller

### 2.4.1 LTSI Systems

The distributed LTSI controller itself is an LTSI system as well. Its state space model at any subsystem $s$ admits a description

$$\begin{bmatrix} (\mathbf{\Delta}_m^K x^K)(k,s) \\ \hline u(k,s) \end{bmatrix} = \left[\begin{array}{c|c} A^K & B^K \\ \hline C^K & D^K \end{array}\right] \begin{bmatrix} x^K(k,s) \\ \hline y(k,s) \end{bmatrix}. \tag{2.20}$$

The resulting closed-loop system is depicted in Fig. 2.5, with a state space realization of a controlled subsystem

$$\begin{bmatrix} (\mathbf{\Delta}_m^L x^L)(k,s) \\ \hline z(k,s) \end{bmatrix} = \left[\begin{array}{c|c} A^L & B^L \\ \hline C^L & D^L \end{array}\right] \begin{bmatrix} x^L(k,s) \\ \hline d(k,s) \end{bmatrix}, \tag{2.21}$$

whose state vector is arranged in a way such that the temporal states, and the spatial states in positive and negative directions of the plant and the controller are grouped as

$$x^L = \left[ \begin{bmatrix} x_t^G \\ x_t^K \end{bmatrix}^T, \begin{bmatrix} x_s^{G,+} \\ x_s^{K,+} \end{bmatrix}^T, \begin{bmatrix} x_s^{G,-} \\ x_s^{K,-} \end{bmatrix}^T \right]^T. \tag{2.22}$$

The superscripts $G$, $K$ and $L$ indicate the plant, controller and closed-loop system, respectively.

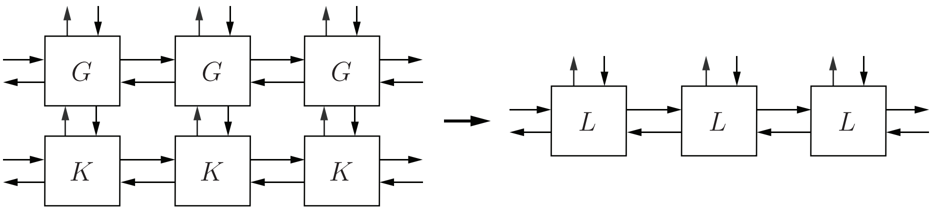


Figure 2.5: Controlled LTSI system

### 2.4.2 LTSV Systems

In lumped systems, an LTI controller often fails to realize an effective control if the plant exhibits varying dynamics. When it comes to distributed systems, a temporally/spatially-scheduled controller that inherits the distributed nature of the LTSV plant is desired to guarantee the stability and certain performance specifications of the controlled system.

The compact form of an explicit LPV controller takes the form

$$\begin{bmatrix} (\boldsymbol{\Delta}_m^K x^K)(k,s) \\ \hline u(k,s) \end{bmatrix} = \left[ \begin{array}{c|c} \mathcal{A}^K(\Theta_t^K, \Theta_s^K) & \mathcal{B}_y^K(\Theta_t^K, \Theta_s^K) \\ \hline \mathcal{C}_u^K(\Theta_t^K, \Theta_s^K) & \mathcal{D}_{uy}^K(\Theta_t^K, \Theta_s^K) \end{array} \right] \begin{bmatrix} x^K(k,s) \\ \hline y(k,s) \end{bmatrix}. \tag{2.23}$$

The interconnection of the LPV plant (2.18) and controller (2.23) yields an LPV closed-loop system

$$\begin{bmatrix} (\boldsymbol{\Delta}_m^L x^L)(k,s) \\ \hline z(k,s) \end{bmatrix} = \left[ \begin{array}{c|c} \mathcal{A}^L(\Theta_t^L, \Theta_s^L) & \mathcal{B}_d^L(\Theta_t^L, \Theta_s^L) \\ \hline \mathcal{C}_z^L(\Theta_t^L, \Theta_s^L) & \mathcal{D}_{zd}^L(\Theta_t^L, \Theta_s^L) \end{array} \right] \begin{bmatrix} x^L(k,s) \\ \hline d(k,s) \end{bmatrix}. \tag{2.24}$$

Provided an LFT representation of the plant subsystem (2.16) and (2.17), its LPV controller in LFT form which consists of the interconnection of an invariant system $K$ with own uncertainties $(\Theta_t^K, \Theta_s^K)$ is shown in Fig. 2.6. The compact state space representation of the LFT LPV controller at any subsystem $s$ is described as

$$\begin{bmatrix} (\boldsymbol{\Delta}_m^K x^K)(k,s) \\ \hline q^K(k,s) \\ \hline u(k,s) \end{bmatrix} = \left[ \begin{array}{c|c|c} A^K & B_p^K & B_y^K \\ \hline C_q^K & D_{qp}^K & D_{qy}^K \\ \hline C_u^K & D_{up}^K & D_{uy}^K \end{array} \right] \begin{bmatrix} x^K(k,s) \\ \hline p^K(k,s) \\ \hline y(k,s) \end{bmatrix}, \tag{2.25}$$

whose uncertainty channel $p^K(k,s) = \begin{bmatrix} p^{t,K}(k,s) \\ p^{s,K}(k,s) \end{bmatrix}$, $q^K(k,s) = \begin{bmatrix} q^{t,K}(k,s) \\ q^{s,K}(k,s) \end{bmatrix}$, and

$$p^K = \begin{bmatrix} \Theta_t^K & \\ & \Theta_s^K \end{bmatrix} q^K := \Upsilon^K q^K. \tag{2.26}$$

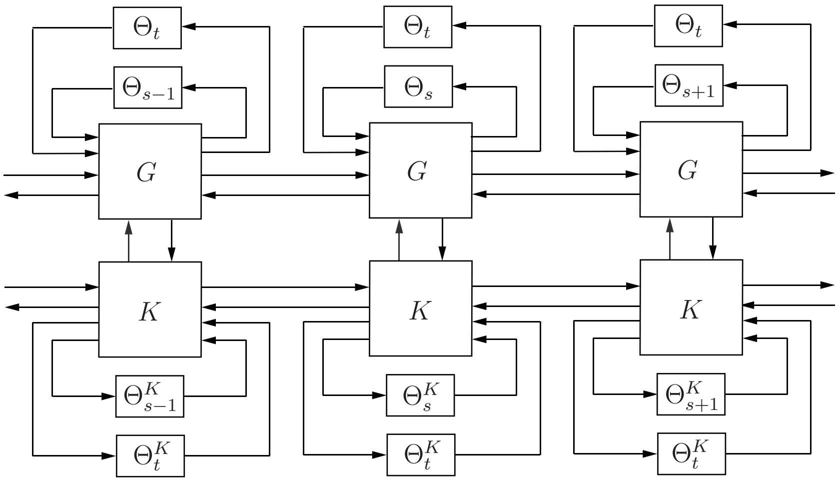


Figure 2.6: Interconnection between LFT plant subsystems and LFT controller subsystems

The interconnection between the plant subsystem (2.16) and (2.17), and the controller subsystem (2.25) and (2.26), leads to a closed-loop distributed system in LFT form as shown in Fig. 2.7 with augmented plant and controller uncertainties, where the dynamics of each controlled subsystem are governed by

$$\begin{bmatrix} (\mathbf{\Delta}_m^L x^L)(k,s) \\ \hdashline q^L(k,s) \\ \hdashline z(k,s) \end{bmatrix} = \left[\begin{array}{c:c:c} A^L & B_p^L & B_d^L \\ \hdashline C_q^L & D_{qp}^L & D_{qd}^L \\ \hdashline C_z^L & D_{zp}^L & D_{zd}^L \end{array}\right] \begin{bmatrix} x^L(k,s) \\ \hdashline p^L(k,s) \\ \hdashline d(k,s) \end{bmatrix}, \tag{2.27}$$

with

$$\begin{aligned} p^L(k,s) = \begin{bmatrix} p^{L,t}(k,s) \\ p^{L,s}(k,s) \end{bmatrix} &= \begin{bmatrix} p^{G,t}(k,s) \\ p^{K,t}(k,s) \\ \hdashline p^{G,s}(k,s) \\ p^{K,s}(k,s) \end{bmatrix} = \left[\begin{array}{cc:cc} \Theta_t & & & \\ & \Theta_t^K & & \\ \hdashline & & \Theta_s & \\ & & & \Theta_s^K \end{array}\right] \begin{bmatrix} q^{G,t}(k,s) \\ q^{K,t}(k,s) \\ \hdashline q^{G,s}(k,s) \\ q^{K,s}(k,s) \end{bmatrix} \\ &:= \begin{bmatrix} \Theta_t^L & \\ & \Theta_s^L \end{bmatrix} \begin{bmatrix} q^{L,t}(k,s) \\ q^{L,s}(k,s) \end{bmatrix} := \Upsilon^L q^L(k,s). \end{aligned} \tag{2.28}$$

*Remark*:

- Under certain assumptions, the controller uncertainty can be determined as a copy of the plant uncertainty, i.e. $\Upsilon^K = \Upsilon^G$, at the price of conservatism. The controller scheduling policy will be discussed in Chapter 6.

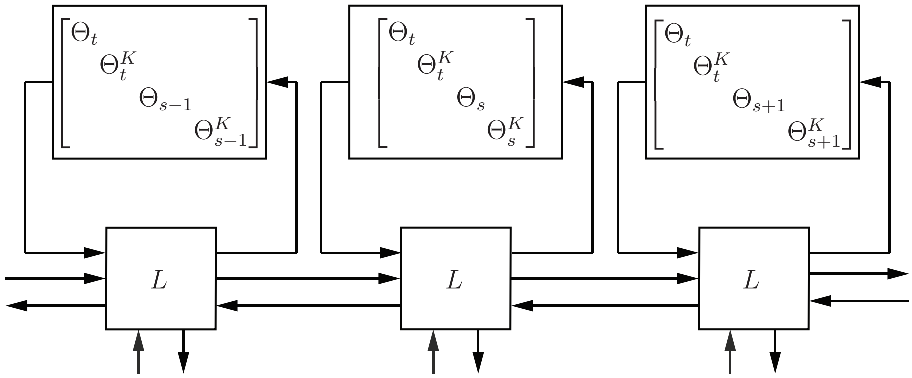


Figure 2.7: Controlled LTSV distributed system in LFT representation

## 2.5 Well-Posedness, Stability and Performance

Well-posedness, stability and performance are three major issues addressed in system analysis, which apply to spatially-interconnected systems as well. In [8], the three aspects are well defined for LTSI systems with continuous temporal and continuous spatial variables. Nevertheless, the experimentally identified plant models are normally discrete in both time and space. Meanwhile, most controllers can only be implemented digitally in practice. Thus, provided the state space realizations in Section 2.3 and 2.4 with discrete time and space, the bilinear transformation C.3 (see Appendix C) has to be performed to convert a discrete distributed system to its continuous counterpart, such that the analysis conditions developed in [8] can be applied. The continuous closed-loop matrices after conversion are denoted as $(\bar{A}^L, \bar{B}^L, \bar{C}^L, \bar{D}^L)$. From here on, the overhead bars above system matrices indicate a continuous system; otherwise discrete.

In this section, definitions of well-posedness, exponential stability and quadratic performance in the context of spatially-distributed systems are discussed. Analysis conditions for an LTSI system to be exponentially stable and satisfy the desired quadratic performance are provided. Conditions for LTSV systems will be discussed in Chapter 6 when it comes to the LPV controller design.

### 2.5.1 Well-Posedness

**Definition 2.7 (Well-Posedness [44])** *A feedback system is considered to be well-posed if all closed-loop transfer matrices are well-defined and proper. It is equivalent to: there exist unique and bounded solutions to the system equations when signals are injected anywhere.*

Well-posedness in a spatially-interconnected system implies the existence of bounded outputs at all subsystems, given any bounded noise $n^+$ in positive direction, $n^-$ in negative direction and disturbance $d$ injected in the loop as shown in Fig. 2.8.

**Theorem 2.1 ([8])** *A distributed system in the form of (2.21) is well-posed, if and only*

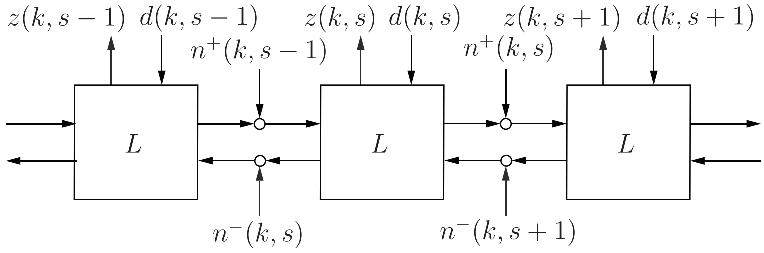


Figure 2.8: Distributed system with noise and disturbance injected

*if* $(\mathbf{\Delta}^L_{s,m} - A^L_{ss})$ *is invertible on space* $l_2$*, where* $\mathbf{\Delta}^L_{s,m}$ *and* $A^L_{ss}$ *are defined as*

$$\mathbf{\Delta}^L_{s,m} := \begin{bmatrix} \mathbf{S} I_{m^L_+} & \\ & \mathbf{S}^{-1} I_{m^L_-} \end{bmatrix}, \quad A^L_{ss} := \begin{bmatrix} A^{L,++}_{ss} & A^{L,+-}_{ss} \\ A^{L,-+}_{ss} & A^{L,--}_{ss} \end{bmatrix}, \tag{2.29}$$

*respectively.*

### 2.5.2 Exponential Stability and Quadratic Performance

Consider again the controlled system (2.21). Definitions of exponential stability, quadratic performance and structured Lyapunov functions in the context of distributed systems, as well as conditions for an LTSI system to be exponential stable and fulfil quadratic performance, are given below.

**Definition 2.8 (Exponential Stability)** *The discrete system (2.21) is said to be exponentially stable if there exist positive* $\alpha$ *and* $\beta$ *such that*

$$\| \mathbf{A}^n \|_{l_2} \leq \alpha e^{-\beta n}, \tag{2.30}$$

*where the operator* $\mathbf{A}$ *is defined [8] as* $\mathbf{A} := A^L_{tt} + \begin{bmatrix} A^{L,+}_{ts} & A^{L,-}_{ts} \end{bmatrix} (\mathbf{\Delta}^L_{s,m} - A^L_{ss})^{-1} \begin{bmatrix} A^{L,+}_{st} \\ A^{L,-}_{st} \end{bmatrix}$*;* $n$ *is a positive integer.*

Readers are referred to [8] regarding the stability condition for continuous systems. Condition (2.30) for discrete systems follows immediately.

**Definition 2.9 (Quadratic Performance)** *A stable closed-loop system (2.21) is said to have quadratic performance* $\gamma$*, if the induced* $\mathcal{L}_2$ *norm that maps* $d \in \mathcal{L}_2$ *to* $z \in \mathcal{L}_2$ *is bounded by* $\gamma > 0$*, i.e.* $\| z \|_{\mathcal{L}_2} < \gamma \| d \|_{\mathcal{L}_2}$*, which can be expressed in an integral quadratic form*

$$\sum_{k=1}^{\infty} \sum_{s=-\infty}^{\infty} [*]^T \begin{bmatrix} -\gamma I & 0 \\ 0 & \frac{1}{\gamma} I \end{bmatrix} \begin{bmatrix} d(k,s) \\ z(k,s) \end{bmatrix}^T \leq 0. \tag{2.31}$$

*When* $\gamma < 1$*, the system is said to be contractive.*

*Remark*:

- In this work, the constraint on the induced $\mathcal{L}_2$ norm of the performance channel is of interest. Rather general performance specifications can be imposed as suggested in [45]
$$\sum_{k=1}^{\infty}\sum_{s=-\infty}^{\infty}[*]^T\begin{bmatrix}Q_p & S_p\\ S_p^T & R_p\end{bmatrix}\begin{bmatrix}d(k,s)\\ z(k,s)\end{bmatrix}^T \leq 0. \tag{2.32}$$

**Definition 2.10 (Structured Lyapunov Matrix)** *The structured Lyapunov matrix set $\boldsymbol{\mathcal{X}}_m$ with decoupled temporal and spatial components is defined as*

$$\boldsymbol{\mathcal{X}}_m = \left\{X \in \mathbb{R}^{(m_0+m_++m_-)\times(m_0+m_++m_-)} \middle| X = X^T = \begin{bmatrix}X_t & \\ & X_s\end{bmatrix}, \det(X)\neq 0,\right.$$
$$\left. X_t \in \mathbb{R}^{m_0\times m_0} > 0\right\}. \tag{2.33}$$

In the following, the Lyapunov matrix set $\mathcal{X}_{\mathbf{m}}$ is always labelled with $m$ indexed by a superscript to specify the involved system, as well as compatible sizes of temporal and spatial components, e.g. $\boldsymbol{\mathcal{X}}_{m^L}$—the Lyapunov matrix of the closed-loop system.

Now we are ready to formulate the LMI conditions that establish both exponential stability and quadratic performance constraints on a discrete system and its continuous counterpart as follows.

**Theorem 2.2** *Assume that the interconnected system (2.21) is well-posed. The system is exponentially stable, and has quadratic performance $\gamma$, if and only if there exists a symmetric matrix $X \in \boldsymbol{\mathcal{X}}_{m^L}$, such that*

*(i) for discrete system:*

$$\begin{bmatrix}*\\ \hdashline *\end{bmatrix}^T\left[\begin{array}{cc:cc}-X & 0 & & \\ 0 & X & & \\ \hdashline & & -\gamma I & 0\\ & & 0 & \frac{1}{\gamma}I\end{array}\right]\left[\begin{array}{cccc}I & 0 & 0 & 0\\ 0 & I & 0 & 0\\ A_{st}^{L,-} & A_{ss}^{L,-+} & A_{ss}^{L,--} & B_{s,d}^{L,-}\\ A_{tt}^{L} & A_{ts}^{L,+} & A_{ts}^{L,-} & B_{t,d}^{L}\\ A_{st}^{L,+} & A_{ss}^{L,++} & A_{ss}^{L,+-} & B_{s,d}^{L,+}\\ 0 & 0 & I & 0\\ \hdashline 0 & 0 & 0 & I\\ C_{t,z}^{L} & C_{s,z}^{L,+} & C_{s,z}^{L,-} & D_{zd}^{L}\end{array}\right] < 0 \tag{2.34}$$

*(ii) for continuous system:*

$$\begin{bmatrix}*\\ \hdashline *\end{bmatrix}^T\left[\begin{array}{cc:cc}0 & X & & \\ X & 0 & & \\ \hdashline & & \frac{1}{\gamma}I & 0\\ & & 0 & -\gamma I\end{array}\right]\left[\begin{array}{cc}\bar{A}^L & \bar{B}_d^L\\ I & 0\\ \hdashline \bar{C}_z^L & \bar{D}_{zd}^L\\ 0 & I\end{array}\right] < 0 \tag{2.35}$$

**Proof** The proof of condition (2.34) is a simplified version of the one in [21], where an LMI condition that establishes exponential stability and quadratic performance of an LTSV system is derived. The proof of (2.35) is provided in [8]. ■

## 2.6 Summary

This introductory chapter has summarized some important definitions and results in the analysis of spatially-distributed systems. Definitions of signal and system norms in the context of multidimensional systems have been presented. An interconnected-system framework considered throughout this thesis has been introduced, where the distributed system is treated as the interconnection of an array of virtually-divided subsystems. A multidimensional state space model that defines the dynamics on subsystems has been provided both for parameter-invariant and -varying models. It is desired in a distributed control system, that the controller inherits the spatial structure of the plant. The distributed controllers for both LTSI and LTSV plants have been discussed. Definitions of well-posedness, stability and performance for spatially-distributed systems have been given, as well as the LMI conditions that establish the exponential stability and quadratic performance of an LTSI system.

# Chapter 3

# Physical Modelling

## 3.1 Introduction

Experimental structures similar to the one constructed – a long beam equipped with a large array of distributed actuators and sensors – to the best of the author's knowledge, have not been reported yet. Due to the lack of prior knowledge and experience, understanding the physical laws of both the flexible beam structure and attached actuator/sensor pairs individually and altogether provides important insights into the system behaviour. This chapter deals with the physical modelling of the 4.8 m long actuated aluminium beam.

Dynamics of multidimensional systems are often governed by PDEs—functions of multivariables and their partial derivatives. The governing PDEs of many continuum physics are available, e.g. the heat equation for the distribution of heat, Euler-Bernoulli equation for the vibration of beam-like structures, etc. Exact analytic solutions to complex PDEs may be difficult or even not possible to obtain. For this reason, numerical approaches are often applied to calculate approximated solutions. Three conventional techniques for solving PDEs numerically are: the finite difference (FD) method, the finite volume method and the FE method. One common feature of the three techniques is that PDEs are solved at discretized spatial locations—a finite approximation to the set of infinite continuous solutions. The approximated solution converges to the exact solution of a PDE, as the number of elements is increased.

Without prior knowledge of the governing PDE of the experimental structure, a piezoelectric FE approach that accounts for the distributed piezoelectric sensors and actuators is applied in this chapter to model the coupled electric and elastic behaviour, with both the aluminium beam and the attached piezo patches modelled based on one-dimension Euler-Bernoulli beam theory. The theoretical FE model is first obtained from known and assumed physical properties, yet it does not suffice for an accurate representation of the test structure, owing to the complexity of the structure. An essential step is to apply the *experimental modal analysis* to update the FE model using measurements, such that the discrepancy between the test structure and the obtained FE model is minimized.

The remainder of this chapter is organized as follows: Section 3.2 gives a short introduction to the direct and inverse piezoelectric effect, as well as the linear constitutive equations when a piezo patch functions as actuator and as sensor, respectively. Section 3.3 presents first the physical profiles of the piezo patches employed in this work. Under Euler-Bernoulli beam theory, the linear dynamics of a piezo patch as actuator and as sensor are illustrated in Section 3.3.2 and Section 3.3.3, respectively. In Section 3.4, a piezoelectric FE modelling approach [23] is applied to model the test structure in terms of its mass and stiffness matrices, based on given or assumed physical parameters. The obtained theoretical FE model is updated with the implementation of the *experimental modal analysis* in Section 3.5.

## 3.2 Piezoelectric Effect

Piezoelectric material possesses the ability to convert between mechanical and electrical energies. The conversion is a reversible process in materials that exhibit both the *direct piezoelectric effect* and the *inverse piezoelectric effect*. The direct piezoelectric effect – a phenomenon that certain crystalline materials generate an electric charge when an external force is applied – was first demonstrated by the brothers Pierre Curie and Jacques Curie in 1880 [46]. The inverse piezoelectric effect induces a deformation of the material with the application of an electric field parallel to the direction of polarization.

The most commonly used piezoelectric materials are Lead Zirconate Titanate (PZT) and Polyvinylidene Difluorid (PVDF) [47]. PZT is a ceramic material, composed of negative and positive ions. Each pair of positive and negative ions can be visualized as an electric dipole. Before poling, the dipoles are oriented randomly with the crystal exhibiting no piezoelectric effect. During poling, a strong electric field is applied to the material to force all dipoles to line up in nearly the same direction. After removing the electric field, the polarisation remains in the material, giving rise to the piezoelectricity. PZT materials are widely used as both actuators and sensors. Unlike the crystal structure of PZT, the other commonly used material PVDF is a polymer of molecule chains $CH_2-CF_2$. Depending on the poled direction, the positive hydrogen atoms are attracted to the negative side of the electric field, whereas the negative fluorine atoms are attracted to the positive side. PVDF is mainly used as sensor due to its high piezo-, pyro-, and ferroelectric properties [48]. In this work, piezoelectric components made of PZT materials are exclusively employed.

**Constitutive Equations**

Due to the presence of ferro-electricity, pyroelectricity or aging, piezoelectric materials may exhibit strong nonlinearities and hysteresis effect. Despite of that, the linear theory is commonly used to determine the piezoelectric properties of the poled ceramic material under certain conditions. The notations as in the *IEEE standard on piezoelectricity* [49] are used here to establish the coupled electrical and mechanical constitutive equations

$$S = s^E T + dE \tag{3.1}$$

$$D = dT + \epsilon^T E, \tag{3.2}$$

where $D$ denotes the electric displacement (electric charge per unit area, Coulomb/m$^2$), $E$ the electric field (V/m), $S$ the strain and $T$ the stress (N/m$^2$). Under the linear piezoelectricity theory, all coefficients are treated as constants: the piezoelectric constant $d$ in (3.1) relates the electric field to the strain without the presence of mechanical stress, whereas $s^E$ denotes the compliance when the electric field is constant; $\epsilon^T$ in (3.2) refers to the relative permittivity of the material when constant stress is applied. Note that the superscripts $E$ and $T$ in the context of *IEEE standard on piezoelectricity* denote that the applied electric field and stress are constant, respectively.

## 3.3 Piezoelectric Actuators/Sensors

This section introduces the physical profiles and linear dynamics of the piezo patches used as actuators and sensors, respectively. The governing equations are derived from the constitutive equations (3.1) and (3.2) according to the Euler-Bernoulli assumption.

### 3.3.1 Piezoelectric Patch Profile

The piezoelectric P-876 DuraAct$^{\text{TM}}$ patch transducers produced by the company Physik Instrumente (PI) are used to function either as actuators or sensors. The top view and cross section view of a patch transducer are drawn in Fig. 3.1. The piezoceramic layer is covered with two layers of electrodes, where positive or negative ions accumulate. The casing that wraps the electrodes is used for the electrical insulation. The effective area of a patch is determined by the electrodes, not the casing. Therefore, the width and length of the electrodes, $b_p$ and $l_p$, are considered to be effective.

The poling direction is aligned with the thickness direction, thus defined as axis 3. With the electric field applied parallel to the poling direction, the material PZT shrinks/expands along all 3 dimensions, with their shrinkage/expansion amplitudes governed by piezoelectric constants $d_{33}$, $d_{31}$ and $d_{32}$, respectively. The useful directions of shrinkage/expansion are normal to the direction of the electric field, e.g. axes 1 and 2. An isotropic behaviour of PZT in plane $1-2$ induces $d_{31} = d_{32}$, whereas an anisotropic behaviour in direction 3 indicates $d_{33} > d_{31} = d_{32}$.

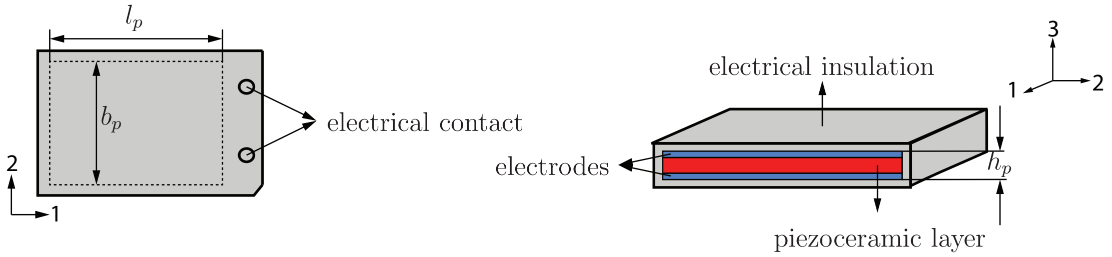


Figure 3.1: Left and right plots show the top view and the cross section view of the piezo patch, respectively.

The data sheet of the piezoelectric patch transducers used as actuators (P-876.A12, PI) and as sensors (P-876.A11, PI) are listed in Table 3.1 [50]. The patch model chosen for actuators has a larger voltage span than that for sensors, so that actuators could generate enough energy to excite the test structure.

| Model | P-876.A11 | P-876.A12 |
|---|---|---|
| Operating voltage (V) | -50 to 200 | -100 to 400 |
| Length (Electrodes) $l_p$ (mm) | 50 | 50 |
| Width (Electrodes) $b_p$ (mm) | 30 | 30 |
| Thickness $h_p$ (mm) | 0.4 | 0.5 |
| Young's modulus $c^E$ (GPa) | 16.4 | 23.3 |
| Relative permittivity $\epsilon^T$ | 1750 | 1750 |
| Piezoelectric constant $d_{31}$ ($d_{32}$) ($10^{-12}$m/V) | -180 | -180 |

Table 3.1: Some relevant physical parameters of piezo actuators and sensors

### 3.3.2 Functionality as Actuator

Consider the configuration in Fig. 3.2, where a piezoelectric patch is bonded on one side of a beam structure and connected with an input voltage. The longitudinal dimension of a beam structure (in this case, direction 1) is considerably larger than the other two dimensions. Assume the thickness of the piezo patch $h_p$ much smaller than that of the beam $h$, i.e. $h_p \ll h$, and its width $b_p$ constant. Applying a voltage to an actuator of constant width is equivalent to applying a pair of concentrated moments $M_p$ at the boundaries of the patch (or electrodes, more precisely) $x_a$ and $x_b$ as shown in Fig. 3.2. Thus, the inverse piezoelectric effect enables a piezo patch working as an actuator: when a voltage $\phi_i$ (or electric field $E_3$) in the direction of polarization is applied, the piezoelectric material expands/shrinks along the same direction (direction 3), and shrinks/expands along directions 1 and 2. With the negligence of the movement in direction 2 according to Euler-Bernoulli beam theory, the bending of the beam structure is caused by the expansion/shrinkage of the piezo patch in direction 1.

Furthermore, a linear relationship between the electric field $\phi_i$ as input and a pair of concentrated moments $M_p$ as output writes [51]

$$M_p = -c_p^E d_{31} b_p h \phi_i, \tag{3.3}$$

where $c_p^E$ is the Young's modulus of the piezo patch.

### 3.3.3 Functionality as Sensor

When a piezo patch is exclusively used as a sensor, the electrodes are short-circuited, so that a zero electric field is enforced, i.e. $\phi_i = 0$. Assume again a constant electrode width $b_p$. The direct piezoelectric effect induces electric charges accumulated on the electrodes,

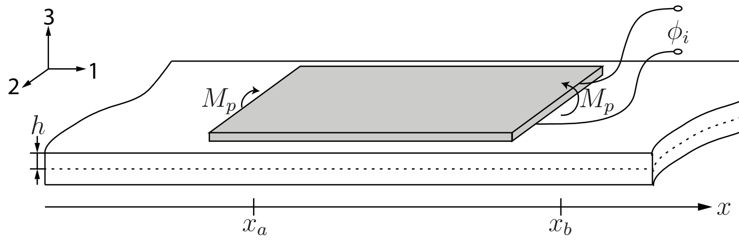


Figure 3.2: Piezoelectric materials function as an actuator

when the material is subject to deformation. A linear behaviour can be observed between the generated electric charges $q$ and the deformation as

$$q = -e_{31}hb_p(w'(x_b) - w'(x_a)), \tag{3.4}$$

where $w$ and $w'$ denote the transverse displacement and slope of the beam, respectively. $x_b$ and $x_a$ are the spatial coordinates at electrode boundaries along direction 1.

Depending on the surrounding electric circuits – whether the electrodes are connected to a charge amplifier or a current amplifier – the measured voltage exhibits different linear relationships. A general structure of a piezo sensor connected to an amplifier is depicted in Fig. 3.3. If the impedance $Z$ represents a resistance $R_e$, the surrounding circuits make a current amplifier, where the output voltage $\phi_o$ is proportional to the difference of the time derivative of slopes at electrode boundaries as

$$\phi_o = -R_e\dot{q} = R_e e_{31}hb_p(\dot{w}'(x_b) - \dot{w}'(x_a)). \tag{3.5}$$

If the impedance $Z$ represents a capacitor $C_a$ instead, the resulting charge amplifier yields a linear equation between the output voltage and the difference of slopes at electrode boundaries [51] as

$$\phi_o = -\frac{q}{C_a} = \frac{e_{31}hb_p}{C_a}(w'(x_b) - w'(x_a)). \tag{3.6}$$

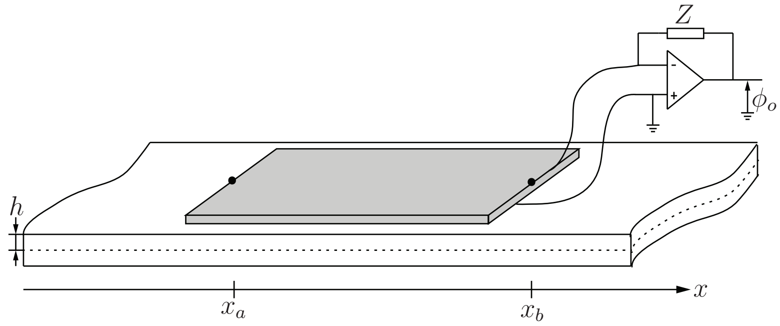


Figure 3.3: Piezoelectric materials function as a sensor

## 3.4 Piezoelectric Finite Element Modelling

The FE method ([22], [52]), as a computer modelling approach, has been employed extensively in the theoretical analysis of structural behaviour for decades. Nevertheless, the standard FE method accounts only for the dissipation of mechanical energy, not for the 'smart' structures with integrated piezoelectric sensors and actuators. The piezoelectric effect was first incorporated into the variational principle in [23]. In [24] the same theorem was derived by applying the principle of virtual displacement to a continuum under the influence of electrical and mechanical forces, where the tetrahedron serves as the most basic geometrical unit in modelling arbitrarily shaped continua. However, the tetrahedron elements are too thick and inefficient to model thin and large structures. A *piezoelectric FE approach* using thin piezoelectric solid elements with internal degrees of freedom (DOFs) was presented in [53]. This section applies the approach developed in [53] to model the piezo-actuated and -sensed test structure.

### 3.4.1 FE Discretization

Recall the schematic drawing of the experimental structure in Fig. 1.5. The experimental setup is constructed with following conditions fulfilled:

- The distances between any two neighbouring piezo pairs are identical, i.e. 250 mm.
- The distances between any two neighbouring springs are identical, i.e. 300 mm.
- The springs are located right in the middle between two neighbouring piezo pairs, such that the distances between any spring and its nearest piezo pairs are the same, i.e. 125 mm.

Consider both the locations where 17 springs are attached, and the boundaries of 16 piezo pairs as nodes. The suspended beam is virtually discretized into 48 elements with 49 nodes. Any beam segment between two neighbouring springs can be treated as the interconnection of three elements with four nodes as shown in Fig. 3.4:

- laminated element $e_2$ (between nodes 2 and 3): includes a pair of collocated piezo actuator/sensor and the clamped aluminium section.
- aluminium elements $e_1$ (between nodes 1 and 2) and $e_3$ (between nodes 3 and 4): with a spring attached to the left node of $e_1$ and the right node of $e_3$, respectively.

Due to the uniform configuration, the whole structure can be seen as a series connection of 16 identical beam segments, each an exact copy of the segment shown in Fig. 3.4. Thus, the FE modelling problem boils down to the modelling of elements $e_1$, $e_2$ and $e_3$.

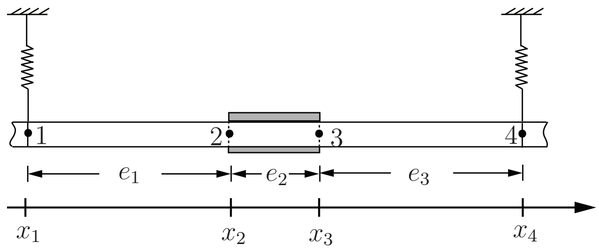


Figure 3.4: Beam segment between two neighbouring springs comprised of three elements

### 3.4.2 Modelling Based on Euler-Bernoulli Beam Theory

It has been suggested in [54] that beam theory is not accurate enough to model systems with collocated actuators and sensors due to the fact that the one-dimensional beam theory considers only the bending moment at elemental nodes, and neglects the torsional movement. Instead, shell theory has been proven to be a more suitable technique to model such a system. Nevertheless, recall the physical parameters of the structure: the length of the beam (4.8 m) is significantly larger than its width (40 mm) and thickness (3 mm); that implies a representative beam structure, whose transverse displacements dominate the vibratory dynamics. Thus, the one-dimensional beam theory could be appropriate for the FE modelling of the concerned structure here. Its validity will be examined in Section 3.5.

The simplest Euler-Bernoulli beam theory [55] assumes two DOFs at each node: the transverse displacement $w$ and its slope $w' = \frac{dw}{dx}$, where axis $x$ is along the longitudinal direction. An element of two nodes has four DOFs as shown in Fig. 3.5 (a). A vector $u^e$ that collects the nodal displacements at nodes 1 and 2 is denoted as

$$u^e = \begin{bmatrix} w_1 & w_1' & w_2 & w_2' \end{bmatrix}^T . \tag{3.7}$$

Meanwhile, external loads could act on nodes in form of transverse force $f$ and bending moment $M$ as shown in Fig. 3.5 (b), denoted as

$$p^e = \begin{bmatrix} f_1 & M_1 & f_2 & M_2 \end{bmatrix}^T . \tag{3.8}$$

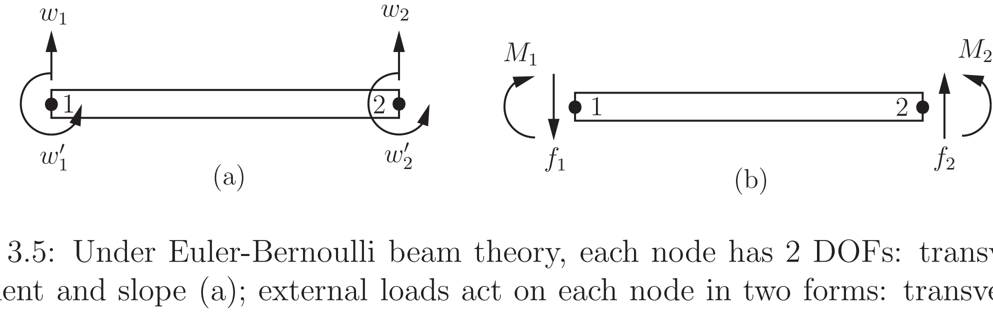


Figure 3.5: Under Euler-Bernoulli beam theory, each node has 2 DOFs: transverse displacement and slope (a); external loads act on each node in two forms: transverse force and moment (b).

The FE modelling of the given structure is realized in the following three steps.

**Elemental Formulation of Elements $e_1$ and $e_3$**

The FE formulations of elements $e_1$ and $e_3$ follow the classical FE modelling routine [22] that accounts for only the mechanical energy. Provided the nodal displacements $u^e$ (in this case, $u^{e_1}$ and $u^{e_3}$), the transverse displacement at any continuous location over the element, $w(x)$, with $x_1 \leq x \leq x_2$ for element $e_1$, and $x_3 \leq x \leq x_4$ for element $e_3$, can be determined through interpolation using a set of pre-chosen shape functions as

$$w(x) = N_u(x)u^e = \begin{bmatrix} N_u^{w_1} & N_u^{w'_1} & N_u^{w_2} & N_u^{w'_2} \end{bmatrix} \begin{bmatrix} w_1 \\ w'_1 \\ w_2 \\ w'_2 \end{bmatrix} \tag{3.9}$$

where $N_u(x)$, or $N_u$ for notational simplicity, denotes the shape functions, and meets the $C^1$ continuity requirement. The $C^1$ continuity is required, because both the transverse displacement $w$ and its spatial derivative $w'$ need to be continuous over the element. The shape functions often employed for the modelling of a beam element in terms of the dimensionless coordinate $\xi$ $(-1 \leq \xi \leq 1)$ are

$$N_u^{w_1} = \frac{1}{4}(1-\xi)^2(2+\xi) \tag{3.10}$$

$$N_u^{w'_1} = \frac{1}{8}l_e(1-\xi)^2(1+\xi) \tag{3.11}$$

$$N_u^{w_2} = \frac{1}{4}(1+\xi)^2(2-\xi) \tag{3.12}$$

$$N_u^{w'_2} = -\frac{1}{8}l_e(1+\xi)^2(1-\xi), \tag{3.13}$$

where $l_e$ denotes the length of the beam element. The four shape functions are shown in Fig. 3.6.

The FE modelling treats each element as a spring-mass-damper system. The governing equation of element $e_1$ or $e_3$ takes the form

$$M^e\ddot{u}^e + C^e\dot{u}^e + K_{uu}^e u^e = p^e, \tag{3.14}$$

where $e = e_1$ or $e = e_3$. The elemental displacements $u^e$ and external loads $p^e$ are defined in the same way as (3.7) and (3.8), respectively. The elemental mass matrix $M^e$ and stiffness matrix $K_{uu}^e$ are derived from the variational principle [52] as:

$$M^e = \int_{V_b^e} \rho_b N_u^T N_u dV_b^e \tag{3.15}$$

$$K_{uu}^e = \int_{V_b^e} B_u^T c_b^E B_u dV_b^e, \tag{3.16}$$

where $B_u$ is the spatial derivative of shape functions $N_u$, i.e.

$$B_u = N'_u.$$

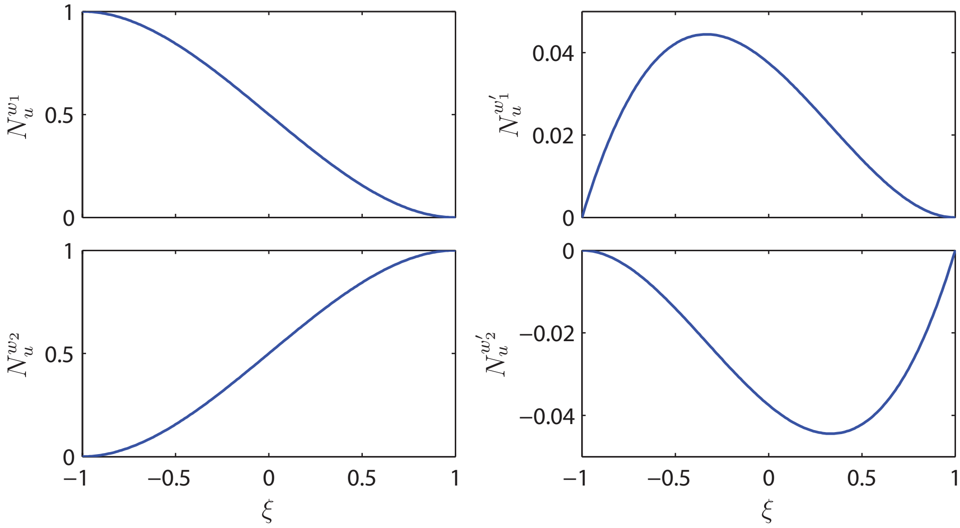


Figure 3.6: Shape functions used for the modelling of a beam element

The density, Young's modulus under constant electric field and volume of the aluminium beam element $e_1$ or $e_3$ are denoted by $\rho_b$, $c_b^E$, and $V_b^e$, respectively. Assume the identical spring stiffness $k_s$ at both elements. The stiffness matrix $K_{uu}^e$ computed in (3.16) is modified for $e_1$ and $e_3$ as

$$K_{uu}^{e_1}(1,1) = K_{uu}^{e_1}(1,1) + k_s \tag{3.17}$$

$$K_{uu}^{e_3}(3,3) = K_{uu}^{e_1}(3,3) + k_s, \tag{3.18}$$

respectively, due to the fact that the left node of $e_1$ and the right node of $e_3$ are attached to springs. The modelling of the damping matrix $C^e$ will be elaborately discussed in Section 3.5.

**Elemental Formulation of Element $e_2$**

The modelling of element $e_2$ involves the mechanical and piezoelectric energy transformation. As discussed in Section 3.3.2, the application of an input voltage $\phi_i^e$ to a piezo actuator is equivalent to the application of a pair of concentrated torques at the electrode boundaries. Thus both the external loads $p^e$ and the actuator can generate a mechanical motion of the element $e_2$. Skipping the derivation procedures [53], the governing equation that accounts for the conversion from electrical to mechanical energy at element $e_2$ writes

$$M^e\ddot{u}^e + C^e\dot{u}^e + K_{uu}^e u^e = p^e - K_{u\phi}^e \phi_i^e, \tag{3.19}$$

where the coupling stiffness matrix $K_{u\phi}^e$ relates the mechanical and electrical variables in piezo actuators.

On the other side, due to the direct piezoelectric effect, the mechanical deformation $u^e$ induces electrical charges $q^e$ on the electrodes of piezo sensors. The linear dynamics presented in Section 3.3.3 yields the sensor equation

$$q^e = K_{\phi u}^e u^e, \tag{3.20}$$

where the coupling stiffness matrix $K^e_{\phi u}$ relates the mechanical and electrical variables in piezo sensors.

Under the assumption that the electric potential is constant over a piezo patch, only one electrical DOF per patch is defined. More intuitively, $\phi^e_i$ and $q^e \in \mathbb{R}$ at any element. A charge amplifier is connected to the sensor electrodes to convert the generated electrical charges to voltage as (3.6). The output equation (3.20) is modified to

$$\phi^e_o = -\frac{K^e_{\phi u}}{C_a} u^e. \tag{3.21}$$

The elemental mass matrix $M^e$ and stiffness matrix $K^e_{uu}$ are constructed accounting for the collective contributions from the actuator, the sensor and the clamped aluminium beam section as

$$M^e = \int_{V_a} \rho_a N_u^T N_u dV_a + \int_{V_s} \rho_s N_u^T N_u dV_s + \int_{V_b^e} \rho_b N_u^T N_u dV_b^e \tag{3.22}$$

$$K^e_{uu} = \int_{V_a} B_u^T c_a^E B_u dV_a + \int_{V_s} B_u^T c_s^E B_u dV_s + \int_{V_b^e} B_u^T c_b^E B_u dV_b^e. \tag{3.23}$$

The shape functions and their derivatives $N_u$ and $B_u$ are defined in the same way as the FE modelling of elements $e_1$ and $e_3$. The density, Young's modulus under constant electric field and volume of the actuator and the sensor are denoted by $\rho_a$, $\rho_s$, $c_a^E$, $c_s^E$, $V_a$ and $V_s$, respectively, where the subscript $a$ indicates the actuator, $s$ the sensor parameters.

Consider (3.19) as the actuator equation, and (3.21) as the sensor equation. The elemental coupling matrices $K^e_{u\phi}$ and $K^e_{\phi u}$ are computed as

$$K^e_{u\phi} = \int_{V_a} B_u^T e_a^T B_{\phi a} dV_a \tag{3.24}$$

$$K^e_{\phi u} = \int_{V_s} B_{\phi s}^T e_s^T B_u dV_s. \tag{3.25}$$

The piezoelectric coupling coefficients $e_a^T$ and $e_s^T$ under constant stress are related to the Young's modulus under constant electric field by $e_a^T = d_{31} c_a^E$ and $e_s^T = d_{31} c_s^E$, respectively. It has been justified in [54] that, the constant electric potential over element $e_2$ yields $B_{\phi a} = 1/h_{pa}$ and $B_{\phi s} = 1/h_{ps}$, where $h_{pa}$ and $h_{ps}$ are the thicknesses of the piezo actuator and sensor, respectively.

**Globalization**

After the elemental formulation of the three fundamental elements in Fig. 3.4, the global FE model can be subsequently constructed by assembling the contribution from each element. The resulting global actuator and sensor equations are given by

$$\mathcal{M}\ddot{U} + \mathcal{C}\dot{U} + \mathcal{K}_{UU} U = P - \mathcal{K}_{U\Phi} \Phi_i \tag{3.26}$$

$$\Phi_o = -\frac{\mathcal{K}_{\Phi U} U}{C_a}, \tag{3.27}$$

where $U \in \mathbb{R}^{98}$, $\Phi_i \in \mathbb{R}^{16}$ and $\Phi_o \in \mathbb{R}^{16}$ are the global mechanical variables, input and output voltage, respectively. Matrices $\mathcal{M}$, $\mathcal{K}_{UU}$, $\mathcal{K}_{U\Phi}$, $\mathcal{K}_{\Phi U}$ and $\mathcal{C}$ are the global versions of their elemental counterparts.

Consider now a self-actuating and -sensing 'smart' system, i.e. $P = 0$. The actuator equation (3.26) is rewritten as

$$\mathcal{M}\ddot{U} + \mathcal{C}\dot{U} + \mathcal{K}_{UU}U = -\mathcal{K}_{U\Phi}\Phi_i. \tag{3.28}$$

*Remarks*:

Recall the single actuator equation (3.3) and sensor equation (3.6). To relate (3.3) to (3.28), and (3.6) to (3.27), the 3-element beam segment in Fig. 3.4 is taken as an example to avoid the demonstration of vectors of large sizes.

- With the application of an input voltage $\phi_i^{e_2}$ to the actuator of element $e_2$, a pair of moments $M_p^{e_2}$ are generated at nodes 2 and 3. The linear dynamics (3.3) can be rewritten for simplicity as $M_p^{e_2} = g_a\phi_i^{e_2}$, where $g_a$ is the simplified actuator constant. The computation of the coupling matrix $\mathcal{K}_{U\Phi}$ in (3.28) requires the computation of the actuator constant $g_a$, and mapping the generated moments to the correct positions in vector $\mathcal{K}_{U\Phi}\Phi$, i.e.

$$-\mathcal{K}_{U\Phi}\Phi = \begin{bmatrix} \cdots & \underbrace{0 \quad 0}_{\text{node 1}} & \underbrace{0 \quad g_a\phi_i^{e_2}}_{\text{node 2}} & \underbrace{0 \quad -g_a\phi_i^{e_2}}_{\text{node 3}} & \underbrace{0 \quad 0}_{\text{node 4}} & \cdots \end{bmatrix}^T \tag{3.29}$$

$$= \begin{bmatrix} \cdots & \underbrace{0 \quad 0}_{\text{node 1}} & \underbrace{0 \quad M_p^{e_2}}_{\text{node 2}} & \underbrace{0 \quad -M_p^{e_2}}_{\text{node 3}} & \underbrace{0 \quad 0}_{\text{node 4}} & \cdots \end{bmatrix}^T. \tag{3.30}$$

  Note that according to beam theory, nodes are in general subject to external loads in the form of transverse force and bending moment. On nodes 1 and 4 there are no external loads applied, whereas the piezo actuator induces zero transverse force and non-zero bending moments on nodes 2 and 3.

- Accoring to (3.6), output voltage $\phi_o^{e_2}$ is proportional to the slope difference at two electrode boundaries. i.e. $\phi_o^{e_2} = g_s(w'(3) - w'(2))$, where $g_s$ is the simplified sensor constant. Analogously, the term $\frac{\mathcal{K}_{\Phi U}}{C_a}$ in (3.27) picks the slopes at nodes 2 and 3 from the mechanical variable $U$, computing their difference as

$$\Phi_o = \begin{bmatrix} \cdots & \underbrace{g_s(w'(3) - w'(2))}_{\text{sensor } e_2} & \cdots \end{bmatrix}^T = \begin{bmatrix} \cdots & \underbrace{\phi_o^{e_2}}_{\text{sensor } e_2} & \cdots \end{bmatrix}^T. \tag{3.31}$$

## 3.5 Updating the FE Model Using the Experimental Modal Analysis

Although the FE model – in form of mass matrix, stiffness matrix, and two electromechanical coupling matrices – has been constructed based on given or assumed physical properties, it is unrealistic to expect that such a theoretical model accurately represents the dynamic behaviour of the test structure, owing to the presence of damping and uncertain nonlinearity of the structure. To reduce the discrepancy in between, experiments need to be designed and performed to extract modal information out of measurements. This process is called *experimental modal analysis*, which normally consists of three phases: test preparation, frequency response measurements, and modal parameter identification [56]. To measure a frequency response, an excitation is performed at one location on the structure, while the vibration response is measured at the same or another location. The dynamic relationship from excitation to response in frequency domain is known as FRF. A set of FRFs at all possible excitation and response locations constitutes an *FRF matrix*. As an example, 16 piezo actuators and 16 piezo sensors yield an FRF matrix of size $16 \times 16$.

Another important characteristic to describe the inherent structural dynamics are *modes*. Modes are a set of harmonic motions, and appear in an FRF as resonant peaks. Theoretically, the vibratory motion of an LTI structure can be expressed as the linear combination of an infinite number of modes. Each mode is characterized in terms of its natural frequency, damping factor and mode shape. Mode shapes are the displacement patterns when the structure vibrates at its natural frequencies. The three elements together – the natural frequency, damping factor and mode shape – are referred to as *modal parameters* or *modal data* that need to be extracted out of measured FRFs at each mode.

Updating the theoretical FE model based on identified modal parameters leads to a more accurate and reliable mathematical model. The updating process is realized in the following steps.

### 3.5.1 Performing Experiments to Obtain FRFs

The time domain data of FRFs is usually obtained by measuring the response to a hammer impulse or to certain excitation signals. In this work, two of the most common excitation tools - a hammer and an electromagnetic shaker - are used to produce excitation forces. The hammer produces an excitation force pulse at one selected location on the structure. A force transducer attached to the hammer tip feeds the force back to be measured. The vibratory responses of the structure are measured by 16 attached piezo sensors simultaneously. Instead of a wide range of frequencies, the structural behaviour at low frequencies is of more importance in this case, since the dominant modes of the test structure are mainly located at low frequencies. Therefore, a hammer tip made of rubber is used, so that the test structure is fully actuated at the low frequency range.

On the other hand, the electromagnetic shaker enables the excitation with various signals. The shaker is glued at one boundary (or tip) of the structure through a plastic stinger, with the applied force measured by a force transducer as shown in Fig. 3.7.

One common property using hammer or shaker excitation is the single-input and multiple-output configuration. With the actuating point fixed - either the hammer striking at one selected location on the surface, or the shaker exciting the tip of the beam, its vibratory motion is measured simultaneously by 16 piezo sensors. The resulting 16 measured FRFs

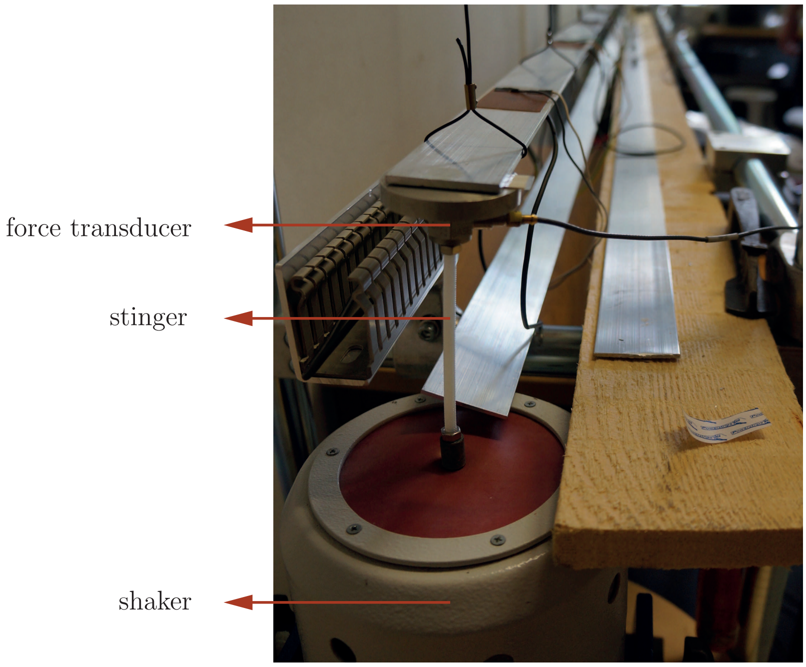


Figure 3.7: An electromagnetic shaker glued to one tip of the beam to generate excitation signals

fill up a column of the FRF matrix. Theoretically, those data are considered to be sufficient for the experimental modal analysis. In practice, in order to minimize the influence caused by operation errors, noisy measurements, etc., repeating experiments and averaging data in frequency domain plays an essential role. Fig. 3.8 shows the averaged FRFs at 4 out of 16 piezo sensor locations with the shaker exciting the tip of the beam. 20 loops of noise and 10 loops of chirp signals, with each loop 30 seconds long and of a bandwidth up to 30 Hz, are applied in sequence as excitation signals. The blue curves are the averaged FRFs of a 10-loop chirp excitation, whereas the red ones are the averaged FRFs of a 20-loop noise excitation.

With the measured FRFs available, the next step is to extract modal parameters (resonant frequencies, mode shapes and damping factors) at each mode. Prior to that, an essential question needs to be answered: how many authentic modes exist within the frequency range of interest. On one hand, some modes are difficult to be detected from some FRFs. On the other hand, not every peak on one FRF counts as a real mode. Those 'fake' modes may result from the structural nonlinearities, measurement noise, travelling waves, or other sources. In Fig. 3.8, several peaks but non-authentic modes can be detected, for example, peaks at 18.31 Hz and 19.65 Hz, yet the 'mode' shapes at above two frequencies exhibit the same pattern. A similar phenomenon can also be observed at 11.17 Hz and 12.33 Hz, 23.8 Hz and 25.12 Hz, and so on.

It has been demonstrated in [51], that the geometrical symmetry in a flexible structure leads to pairs of identical modes. However, due to the imperfection of symmetry or

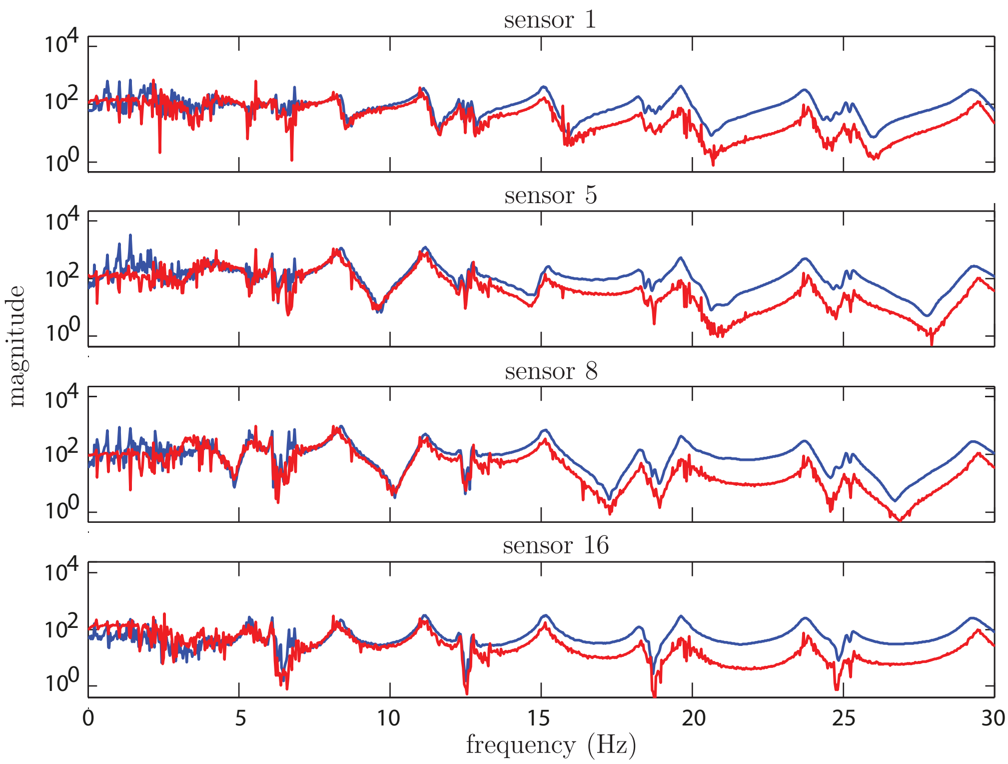


Figure 3.8: Measured FRFs from a shaker excitation at the tip of the beam to responses at 4 selected sensor locations. The blue curves are the averaged FRFs given a 10-loop chirp excitation, whereas the red ones are the averaged FRFs given a 20-loop noise excitation.

measurement errors, those pairs of identical modes become pairs of close modes, and can be counted only as one mode.

Taking these aspects into consideration, after the analysis of FRFs at various exciting and sensing locations, the first 10 modes below 30 Hz are finally determined, whose resonant frequencies are

$$\omega_m = [1.22^1, 1.968, 3.357, 5.249, 8.362, 11.29, 15.37, 19.78, 24.17, 29.95]\text{Hz}. \tag{3.32}$$

### 3.5.2 Updating the Mass and Stiffness Matrices

Provided known or assumed knowledge of physical properties of the structure, the FE model is characterised in terms of the mass and stiffness matrices as presented in Section 3.4.2. Consider that the solution of the governing equation (3.28) consists of a linear combination of mode shapes $\Omega$, i.e. $U(t) = \Omega x(t)$, where the vector $x(t)$ weights the contribution of modes at time $t$. The characteristic equation of (3.28)

$$(\mathcal{K}_{UU} - \omega^2 \mathcal{M})\Omega = 0 \tag{3.33}$$

[1]Due to the measurement noises at low frequencies, the first mode is difficult to be identified accurately.

solves its eigenvalue problem: natural frequencies $\omega$ and mode shapes $\Omega$. The purpose of updating the mass matrix $\mathcal{M}$ and the stiffness matrix $\mathcal{K}_{UU}$ is formulated as: after the update, the computed $\omega$ and $\Omega$ from (3.33) approximate the measured natural frequencies $\omega_m$ and mode shapes $\Omega_m$.

In past decades, various techniques have been developed in the structural engineering community to derive modal parameters from measured FRFs, e.g. peak picking, circle fit, global singular value decomposition (SVD) [57], and so on. The natural frequencies of the first 10 modes $\omega_m$ (3.32) have been determined by applying the simplest peak picking method, which is suitable for lightly damped systems with well-separated modes. The mode shapes $\Omega_m$ are the normalized displacement of 16 sensing locations at each picked natural frequency.

According to (3.22) and (3.23), the knowledge of structural properties determines the exactness of the computed mass and stiffness matrices. Although its geometrical dimensions (e.g. length, width, and thickness) are well-measurable, certain properties, like the Young's modulus of the beam $c_b^E$, the actuator $c_a^E$, and the sensor $c_s^E$, their densities $\rho_b$, $\rho_a$, and $\rho_s$, and the stiffness of the springs $k_s$, though provided by the manufacturer, are hardly known accurately. This constitutes the reason for the update.

Let $c_b^E$, $c_a^E$, $c_s^E$, $\rho_b$, $\rho_a$, $\rho_s$ and $k_s$ be the parameters to be updated, and arranged as a vector $\theta$. The cost function is defined as

$$V(\theta) = \frac{1}{2N} \sum e^T(\theta) e(\theta), \tag{3.34}$$

with

$$e(\theta) = [\omega(2) - \omega_m(2), \omega(3) - \omega_m(3), \ldots, \omega(10) - \omega_m(10)]^T, \tag{3.35}$$

where $N$ is the number of selected modes, i.e. $N = 9$. The error vector $e$ consists of the deviation between the measured natural frequencies and the ones calculated by (3.33) from 2nd to 10th modes. Note that the eigenvalue $\omega$ computed from (3.33) contains the natural frequencies of resonant modes, as well as the frequencies of rigid body modes. The correspondence between $\omega_m$ and $\omega$ in (3.35) can be detected by comparing the shape similarities between the computed eigenvectors $\Omega$ and measured mode shapes $\Omega_m$.

After the application of the standard Levenberg-Marquardt algorithm [58] to update the unknown parameter vector $\theta$ by minimizing the cost function (3.34), the comparison between the measured and updated natural frequencies is shown in Fig. 3.9. The comparison of mode shapes is shown in 3.10. The updated FE model demonstrates a good approximation to the dynamic characteristics of the test structure.

### 3.5.3 Updating the Damping Matrix

Unlike the mass and stiffness matrices, modelling of the damping matrix is challenging because the real damping model is not fully understood in the current state of the art [56] [57]. However, the characterization of damping is important in terms of making accurate predictions both in time and frequency domains. Proportional damping is a convenient

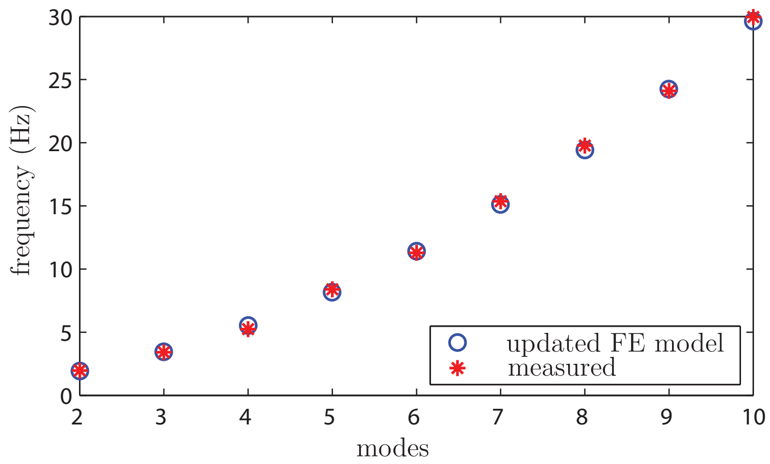


Figure 3.9: Comparison between the eigenvalues of the updated FE model (blue circle) and the measured natural frequencies (red asterisk) from modes 2 to 10

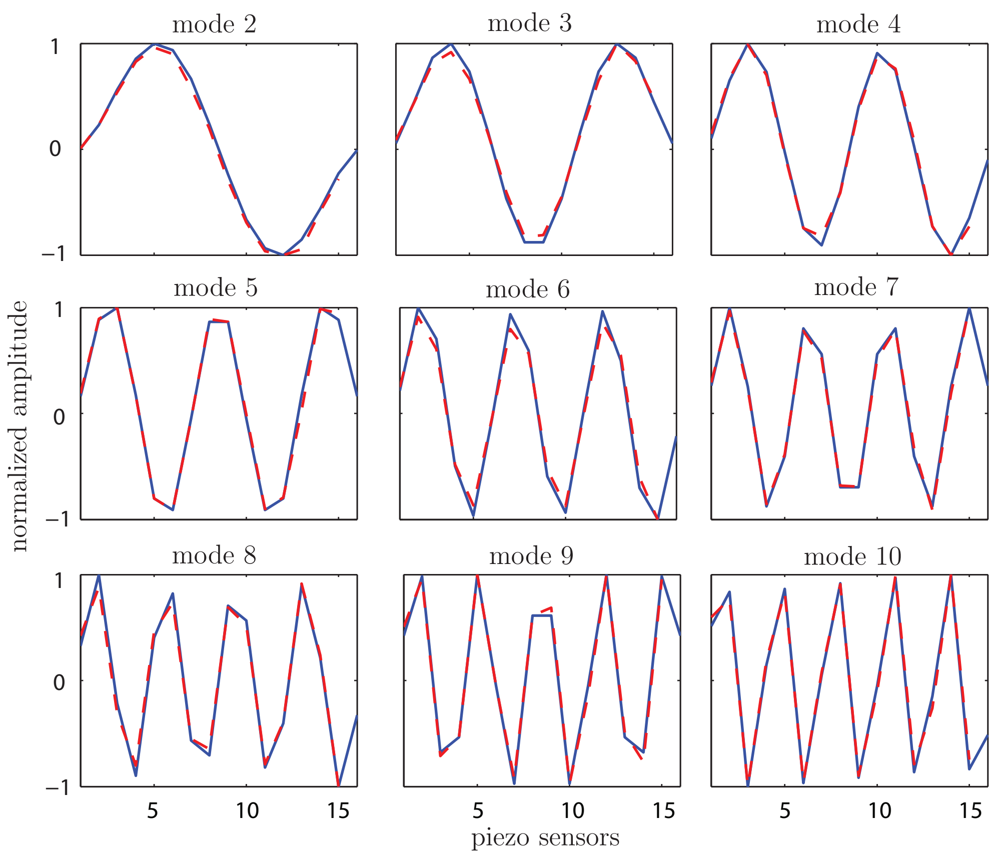


Figure 3.10: Comparison of normalized mode shapes from modes 2 to 10 between the updated FE model (blue solid line) and measurements (red dashed line)

but somewhat restricted damping model. Under the assumption of a proportional damping model, the damped model has the same mode shapes as its undamped counterpart, whereas the damped natural frequencies slightly deviate from the undamped ones when the structure is lightly damped. For a broader view regarding the damping identification procedure, readers are referred to [59] and [57]. For simplicity, a proportional viscous damping in the form of

$$\mathcal{C} = \alpha\mathcal{M} + \beta\mathcal{K}_{UU} \tag{3.36}$$

is assumed here, where the coefficients $\alpha$ and $\beta$ are to be estimated after updating the mass and stiffness matrices.

The Levenberg-Marquardt technique is applied again to estimate the unknown parameters $\alpha$ and $\beta$, such that the simulated damped FRFs approximate the measured ones. Fig. 3.11 shows the comparison of the measured and simulated damped FRFs at 4 out of 16 piezo sensors, with 10 loops of chirp excitations generated by the 8th piezo actuator. It can be seen that the main structural dynamics up to 30 Hz are well captured by the updated FE model, both at resonances and anti-resonances. It can also be observed that multiple peaks are measured at the frequencies where the FE model indicates only a single mode, e.g. near 20 and 25 Hz. It has been discussed in Section 3.5.1, that it may result from the structural nonlinearities, imperfect geometric symmetry, interference of travelling waves, etc. To explore the physical causes of this phenomenon is out the scope of this thesis. Nevertheless, possible sources that may result in the structural asymmetry are analysed as following:

- The piezo actuator/sensor pairs may be glued in an imperfect collocated pattern.
- The springs may not be centered exactly between two neighbouring piezo pairs.

Incorporating these subtle aspects into the FE modelling would make the modelling process cumbersome and tedious. The FE model after updating is considered to represent the test structure to a satisfactory degree.

### 3.5.4 Compensation of the Direct Feed-Through Effect

The FRF comparisons made in Fig. 3.11 are from the excitation at the 8th actuator to responses at non-collocated sensors. Now take a close look at the FRF from the 8th actuator to the 8th sensor as shown in Fig. 3.12 (a). It can be observed that a big gap exists between the measured and simulated FRFs over the whole frequency range, which may appear as a constant gain at the first sight. Actually, this discrepancy is the result of the direct feed-through effect (or fast dynamics) from actuators to their collocated sensors. After compensating the measurements at the 8th sensor with the fed-through input from its collocated actuator, i.e. $y(k,8) = y(k,8) + b_0 \cdot u(k,8)$, where $b_0$ denotes the feed-through constant, the simulation of the FE model is significantly improved as shown in Fig. 3.12 (b).

Although the existence of the direct feed-through effect within collocated piezo pairs has been detected, it remains still unknown whether the feed-through constants are identical at all 16 pairs. For this purpose, an experiment has been performed, where the 16 actuators are simultaneously actuated by an identical chirp signal up to 20 Hz. Then the

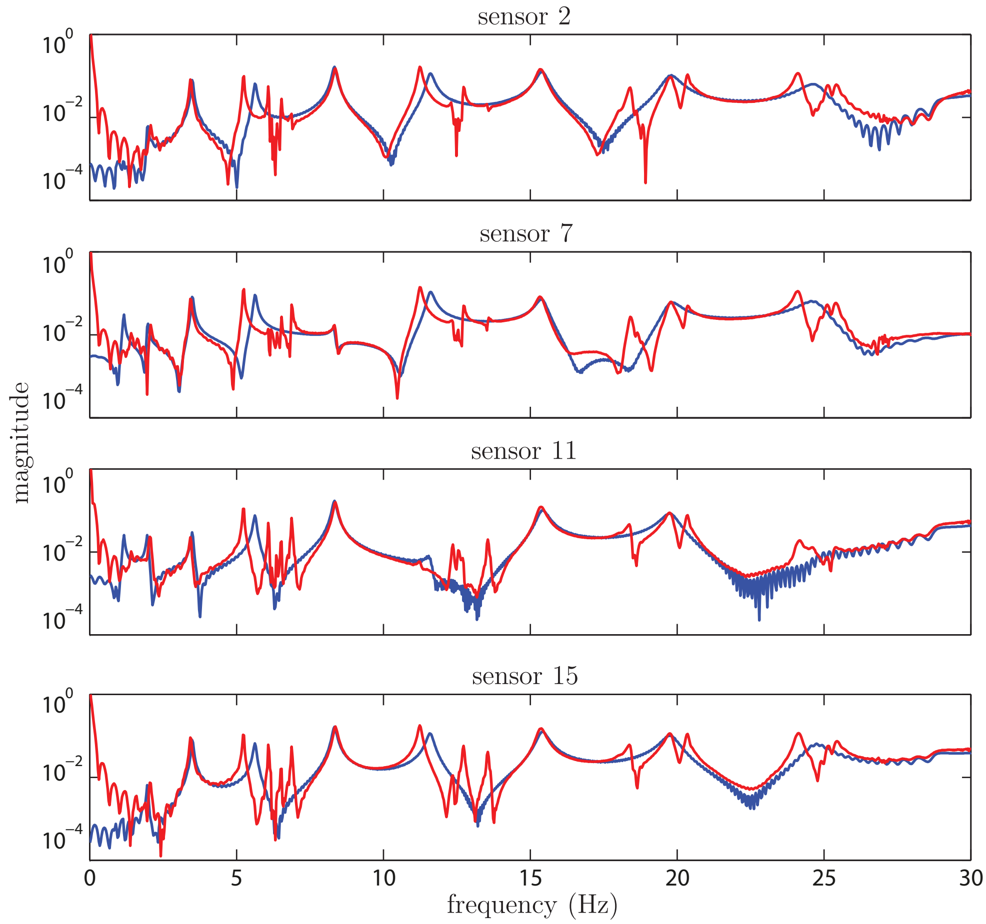


Figure 3.11: Comparison of simulated and measured FRFs at 4 selected piezo sensors given chirp excitation at the 8th piezo actuator. The blue curves are simulated FRFs using the updated FE model, whereas the red curves are the averaged FRFs out of the 10-loop measurements.

measurements at all 16 sensors are compensated with the fed-through input from their collocated actuators using the same feed-through constant as $y(k,i) = y(k,i) + b_0 \cdot u(k,i)$, $i = 1,\ldots,16$. Fig. 3.13 shows the comparison of measured and simulated FRFs between collocated actuators and sensors, after the compensation. It can be seen that the chosen feed-through constant fits quite well at some piezo pairs, e.g. pairs 8 and 15, but is slightly smaller or larger than its true value at other pairs, e.g. pairs 1 and 7, respectively. It can be concluded that the collocated actuator/sensor pairs may – due to their locations or variations in manufacturing – exhibit slightly different feed-through properties. A comparison of compensated sensor outputs to 16 (non-identical) noise excitations is shown in Fig. 3.14.

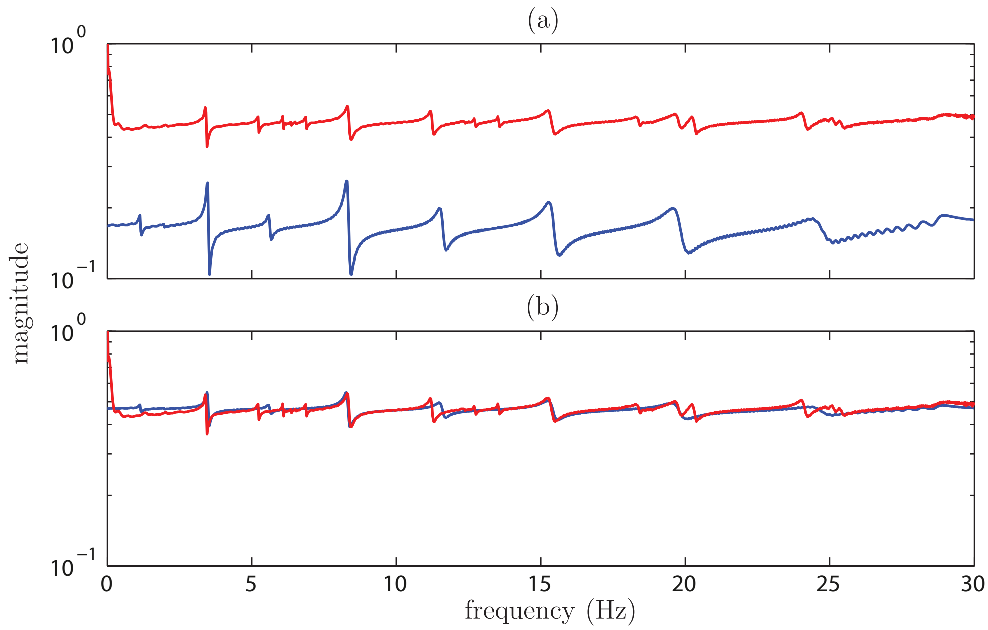


Figure 3.12: Comparison of simulated (blue) and measured (red) FRFs at the 8th sensor, given a chirp excitation at the 8th piezo actuator: (a) without considering the direct feed-through effect; (b) with the feed-through effect compensated.

## 3.6 Summary

In this chapter, the physical aspects of the test structure have been taken into account for physical modelling. The direct and inverse piezoelectric effects, which enable a piezo patch functioning as sensor and actuator, respectively, have been introduced. Despite of the presence of nonlinearites, linear constitutive equations that govern the dynamics of both a piezo actuator and a sensor have been discussed under the one-dimensional beam theory. Owing to the coupled mechanical and electric effect of the piezo-actuated and -sensed beam structure, a piezoelectric FE method has been applied to obtain a mathematical FE model based on the known or assumed physical parameters. In order to minimize the deviation between the theoretical FE model and test structure, the experimental modal analysis has been performed to update the FE model in terms of its mass, stiffness and damping matrices. A direct feed-through effect has been detected from piezo actuators to their collocated sensors. Experimental results have shown that the collocated actuator/sensor pairs exhibit slightly varying feed-through properties. The updated FE model accounting for the direct feed-through effect represents the true structural dynamics to a satisfactory degree.

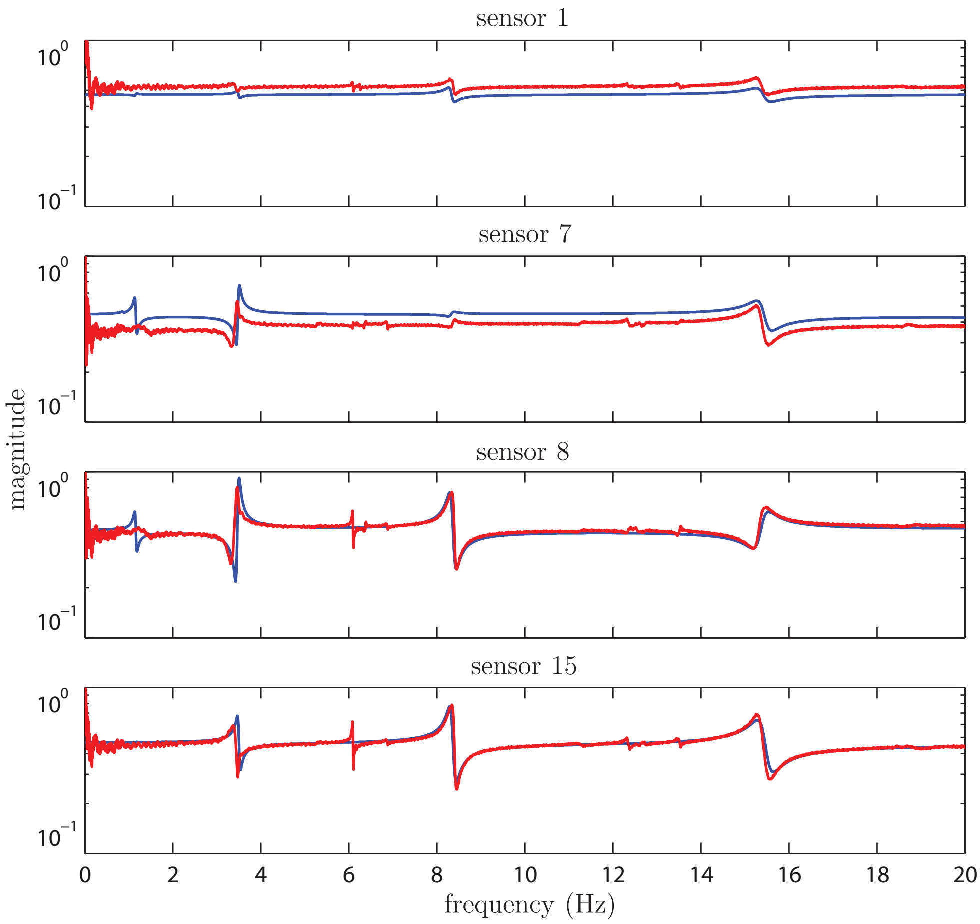


Figure 3.13: Comparison of simulated (blue) and measured (red) FRFs at 4 selected piezo sensors, given 16 identical chirp signals exciting 16 piezo actuators simultaneously. Measurements at sensors are compensated with the fed-through inputs from their collocated actuators by using the same feed-through constant for all piezo pairs.

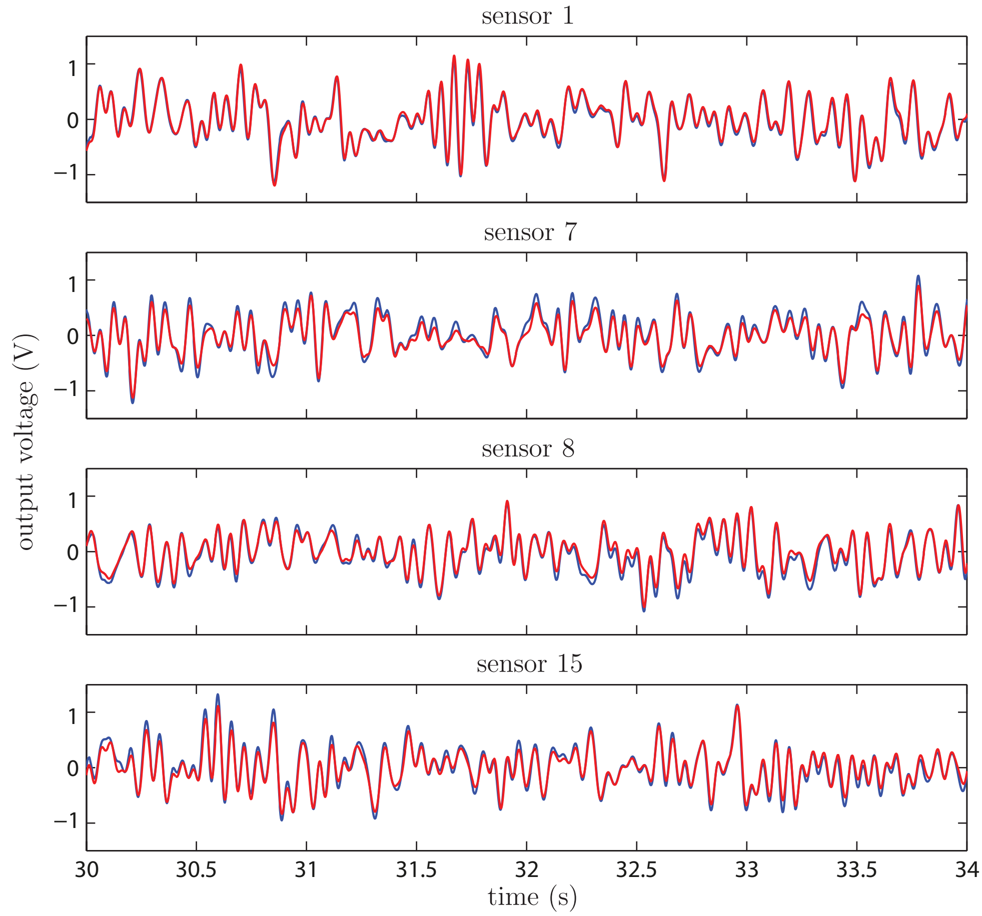


Figure 3.14: Comparison of simulated (blue) and measured (red) output voltages at 4 selected piezo sensors, given 16 noise signals exciting 16 piezo actuators simultaneously. The feed-through constants employed in the FE model are identical for all piezo pairs.

# Chapter 4

# Local LPV Identification of an FRF Matrix

## 4.1 Introdution

In Chapter 3, an FE-based modelling approach for the actuated structure accounting for the coupled mechanical and piezoelectricity effect has been presented. However, from a practical point of view, this approach can involve tremendous experimental work, particularly when a complex or a large-scale structure is encountered, where experiments at a large number of actuating and sensing locations need to be performed to capture the structural dynamics thoroughly. On the other hand, the lumped structure of the FE model is generally not suitable for a model-based controller design, due to its large system order.

Considering the combined FE method and experimental modal analysis as a white-box identification, this chapter addresses the above two issues of physical modelling, treating the structure as a black box and identifying its FRF matrix by directly modelling its input/output behaviour, without exploring the physical insights into the structural dynamics. It will be demonstrated that the FRF matrix of a structure even comprised of physically identical subsystems exhibits spatially-varying characteristics. A local LPV identification technique is extended from lumped systems to spatially-interconnected systems. The FRFs at selected actuating and sensing locations are first identified as a set of LTI models, then parametrized as a spatial LPV model with the application of the extended local approach. The FRFs at other locations can then be approximated through interpolation. In comparison to the physical modelling, the proposed approach facilitates the experimental work, at the price of a slightly deteriorated accuracy.

This chapter takes over results presented in [60], and is structured as follows: Section 4.2 recaps the black-box identification techniques for both LTI and LPV lumped systems, whose signals are functions of time. The local approach for a temporal LPV model identification is extended later in this chapter to spatially-distributed systems. Section 4.3 reviews the problems of current identification techniques and motivates the development of a new approach. Taking a simple five-spring-mass-damper system as an example, Section

4.4 explores the spatially-varying characteristics of its FRFs, and derives a compact spatial LPV representation of the FRF matrix. Section 4.5 validates the proposed approach on an experimental testbed. Two scenarios are implemented to test the accuracy and robustness of the proposed approach.

## 4.2 Preliminaries

Black-box identification of the FRF matrix relies on the input/output behaviour of the test structure. The least-squares based identification techniques for a temporal LPV model using both local and global approaches are briefly reviewed in this section.

### 4.2.1 Least-Squares Based Identification

The input/output behaviour of a system is identified by measuring the response of the plant to an excitation signal, where no physical insights into the plant dynamics are required. Consider a lumped linear data generating system with a sampling time $\Delta T$ as shown in Fig. 4.1, where $G(q_t)$ and $H(q_t)$ denote the discrete transfer function of the plant and of the noise model, respectively, $e(k)$ is a Gaussian white noise signal with zero mean at time instant $k\Delta T$, $v(k)$ is filtered noise, and $q_t$ the forward temporal shift operator, i.e. $q_t u(k) = u(k+1)$. The input/output representations of the plant and the noise model of an ARX (AutoRegressive with eXogeneous input) structure are:

$$G(q_t) = \frac{B(q_t)}{A(q_t)}, \quad H(q_t) = \frac{1}{A(q_t)}, \tag{4.1}$$

and

$$A(q_t) = 1 + \sum_{i_k=1}^{n_a} a_{i_k} q_t^{-i_k}, \quad B(q_t) = \sum_{j_k=1}^{n_b} b_{j_k} q_t^{-j_k}, \tag{4.2}$$

where $n_a$ and $n_b$ are the pre-chosen output and input orders, respectively.

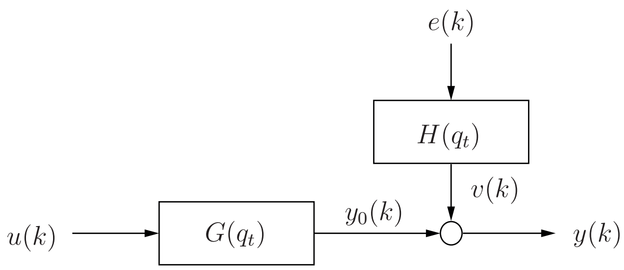


Figure 4.1: One-dimensional ARX model structure

The black-box identification problem is formulated as follows: Given an input and output data sequence $\{u(k),\ y(k)\}$, $k = 1, ..., N_k$, where $N_k$ is the number of measurements, coefficients $a_{i_k}$ and $b_{j_k}$ in $G(q_t)$ are to be estimated with the input and output orders $n_a$ and $n_b$ determined by trial and error, such that the cost function

$$J = \sum_{k=1}^{N_k} (y(k) - \hat{y}(k))^2 \tag{4.3}$$

is minimized. The measured output is denoted as $y(k)$, and the estimated output $\hat{y}(k)$ is computed by

$$\hat{y}(k) = -\sum_{i_k=1}^{n_a} a_{i_k} y(k - i_k) + \sum_{j_k=1}^{n_b} b_{j_k} u(k - j_k). \tag{4.4}$$

Restructure the difference equation (4.4) into regressor form

$$\hat{y}(k) = \phi^T(k) p, \tag{4.5}$$

with a regressor vector

$$\phi(k) = \begin{bmatrix} \left[\ \mathrm{cat}_{i_k} - y(k - i_k)\ \right]_{i_k=1:n_a} \\ \left[\ \mathrm{cat}_{j_k} u(k - j_k)\ \right]_{j_k=1:n_b} \end{bmatrix}, \tag{4.6}$$

and a parameter vector

$$p = \begin{bmatrix} \left[\ \mathrm{cat}_{i_k} a_{i_k}\ \right]_{i_k=1:n_a} \\ \left[\ \mathrm{cat}_{j_k} b_{j_k}\ \right]_{j_k=1:n_b} \end{bmatrix}, \tag{4.7}$$

where $\mathrm{cat}_{i_k}$ and $\mathrm{cat}_{j_k}$ denote the concatenation of the coefficients in $A(q_t)$ and $B(q_t)$, respectively. For example, a system of an input order 2 and an output order 1, i.e. $n_a = 2$ and $n_b = 1$, gives rise to a parameter vector $p = [a_1, a_2, b_1]^T$.

After constructing the data matrix $\Phi$ by augmenting the past inputs and outputs as

$$\Phi = [\phi(1), \phi(2), \cdots, \phi(N_k)]^T$$

and the output vector

$$Y = [y(1), y(2), \cdots, y(N_k)]^T,$$

where $\Phi \in \mathbb{R}^{N_k \times (n_a + n_b)}$, $Y \in \mathbb{R}^{N_k}$, the least squares approach solves the estimation problem by minimizing the cost function (4.3) with

$$p = (\Phi^T \Phi)^{-1} \Phi^T Y, \tag{4.8}$$

if $\Phi$ has full column rank.

### 4.2.2 LPV Input/Output Identification

The advantage of using LPV models to represent nonlinear systems is that linear modelling and control techniques can be extended. The difference equation of an LPV input/output representation can still be written in the form of (4.4), only that the coefficients $a$ and $b$ are time-varying and scheduled as functions of varying parameters $\theta_t(k)$, i.e.

$$\hat{y}(k) = -\sum_{i_k=1}^{n_a} a_{i_k}(\theta_t(k))y(k-i_k) + \sum_{j_k=1}^{n_b} b_{j_k}(\theta_t(k))u(k-j_k), \tag{4.9}$$

where the scheduling variable $\theta_t(k) \in \mathbb{R}$ varies in the interval $[\theta_{t,\min} \quad \theta_{t,\max}]$, and is assumed to be measurable online.

The linear regressor now takes the form

$$\hat{y}(k) = \phi^T(k)p(\theta_t(k)), \tag{4.10}$$

where

$$p(\theta_t(k)) = \begin{bmatrix} \left[\ \mathrm{cat}_{i_k} a_{i_k}(\theta_t(k))\ \right]_{i_k=1:n_a} \\ \left[\ \mathrm{cat}_{j_k} b_{j_k}(\theta_t(k))\ \right]_{j_k=1:n_b} \end{bmatrix}. \tag{4.11}$$

Although $p(\theta_t(k))$ can be chosen as any smooth function of $\theta_t(k)$, a polynomial function is often selected for the convenience of system analysis and controller synthesis at a later stage, i.e.

$$\hat{p}(\theta_t(k)) = \lambda_0 + \lambda_1\theta_t(k) + \lambda_2\theta_t(k)^2 + \cdots + \lambda_m\theta_t(k)^m, \tag{4.12}$$

where $\hat{p}(\theta_t(k))$ denotes the approximated coefficients using a polynomial basis function, $m$ the polynomial order chosen *a priori*; $\lambda_j \in \mathbb{R}^{n_a+n_b}$ $(j = 0, \ldots, m)$ are parameters to be estimated.

To identify the LPV model in the form of (4.10) with coefficients depending on scheduling parameters as described in (4.12), both local and global approaches are applicable. In the rest of this section, both identification approaches are shortly reviewed, with an emphasis on the local approach.

#### Local Approach

The local approach relies on the individual excitation at each operating point $\theta_t^i$ $(i = 1, \ldots, n_\theta)$ with $\theta_{t,\min} \leq \theta_t^i \leq \theta_{t,\max}$, and $n_\theta$ is the number of operating points at which a set of identification experiments are individually performed. The conventional procedure for identifying a temporal LPV model using a local approach proposed in [61] can be summarized into the following four steps:

1) Fix the scheduling variable at the first operating point $\theta_t(k) = \theta_t^1$ for all sampling instants $k$, and stimulate the system with an appropriately determined input signal. Given measured input/output data sequence and a pre-defined mathematical model, an LTI input/output model can be identified using the least squares technique. The estimated coefficients are denoted as $p(\theta_t^1) \in \mathbb{R}^{n_a+n_b}$.

2) Repeat step 1) at operating points $\theta_t^2$, $\theta_t^3$, ..., $\theta_t^{n_\theta}$ individually to obtain the estimated coefficient vectors $p(\theta_t^i)$ $(i = 2, \ldots, n_\theta)$.

3) Neglect the error caused by the use of the linear identification experiments, and assume that the estimated coefficients agree with their true values. The following LPV model identification problem can be formulated as: compute the polynomial coefficients $\lambda_j$ in (4.12), such that the cost function

$$J = \sum_{i=1}^{n_\theta} (p(\theta_t^i) - \hat{p}(\theta_t^i))^2, \tag{4.13}$$

which measures the differences between the estimated coefficients $p(\theta_t^i)$ in step 2) and the approximated coefficients $\hat{p}(\theta_t^i)$ using (4.12), is minimized at all chosen operating points.

Construct a matrix $\Lambda \in \mathbb{R}^{(n_a+n_b)\times m}$ containing all decision variables $\lambda_j$ $(j = 0, \ldots, m)$ as

$$\Lambda = \begin{bmatrix}\lambda_0 & \lambda_1 & \cdots & \lambda_m\end{bmatrix} = \begin{bmatrix} \lambda_{01} & \lambda_{11} & \cdots & \lambda_{m1} \\ \vdots & \vdots & & \vdots \\ \lambda_{0n_a} & \lambda_{1n_a} & \cdots & \lambda_{mn_a} \\ \lambda_{0(n_a+1)} & \lambda_{1(n_a+1)} & \cdots & \lambda_{m(n_a+1)} \\ \vdots & \vdots & & \vdots \\ \lambda_{0(n_a+n_b)} & \lambda_{1(n_a+n_b)} & \cdots & \lambda_{m(n_a+n_b)} \end{bmatrix}, \tag{4.14}$$

a matrix $\Delta_\theta \in \mathbb{R}^{m\times n_\theta}$ depending only on the operating points $\theta_t^i$ $(i = 1, \ldots, n_\theta)$

$$\Delta_\theta = \begin{bmatrix} 1 & 1 & \cdots & 1 \\ \theta_t^1 & \theta_t^2 & \cdots & \theta_t^{n_\theta} \\ \vdots & \vdots & & \vdots \\ (\theta_t^1)^m & (\theta_t^2)^m & \cdots & (\theta_t^{n_\theta})^m \end{bmatrix} \tag{4.15}$$

and a matrix $\mathcal{P} \in \mathbb{R}^{(n_a+n_b)\times n_\theta}$ by collecting the estimated $p(\theta_t^i)$ $(i = 1, \ldots, n_\theta)$ from steps 1) and 2)

$$\mathcal{P} = \begin{bmatrix} p(\theta_t^1) & p(\theta_t^2) & \ldots & p(\theta_t^{n_\theta}) \end{bmatrix}. \tag{4.16}$$

Then the matrix $\Lambda$ that minimizes the cost function (4.13) can be computed by solving the regressor form $\mathcal{P} = \Lambda\Delta_\theta$ for

$$\Lambda = (\mathcal{P}\Delta_\theta^T)(\Delta_\theta\Delta_\theta^T)^{-1}. \tag{4.17}$$

4) After the polynomial function (4.12) is determined, the LPV regressor form (4.10) allows to retrieve the dynamic behaviour at points between the chosen operating points, i.e. $\theta_t(k) \in [\theta_{t,\min} \quad \theta_{t,\max}]$ and $\theta_t(k) \neq \theta_t^i$ $(i = 1, \ldots, n_\theta)$, through interpolation.

*Remark:*

- It is demonstrated in [61] that the optimal choice of the polynomial degree $m = n_\theta - 1$ avoids over parametrization, and guarantees the accuracy of the LPV model with a proper size for further controller design.

### Global Approach

Instead of identifying the system dynamics at a set of fixed scheduling parameters using the local approach, the global approach allows to stimulate the system via one single experiment with a large number of operating points excited to determine the functional dependence ([62], [63]). In case of a polynomial dependence, conditions on persistency of excitation in terms of inputs and trajectories of scheduling parameters are discussed in [28], where the estimation problem is solved through the recursive least squares algorithms. In Chapter 5, the global approach will be applied for the identification of a two-dimensional LPV input/output model.

## 4.3 Problem Statement

It has been illustrated in Chapter 3 that the FE modelling discretizes a continuous structure into an array of interconnected subsystems, with the dynamics of each subsystem captured by a spring-mass-damper system. Consider a system as shown in Fig. 4.2. It consists of 5 spring-mass-damper systems, each governed by the equation of motion

$$f = m\ddot{y} + c\dot{y} + ky, \tag{4.18}$$

where $m$, $k$, and $c$ are the elemental (in this case, scalar) mass, stiffness and damping, respectively, $f$ is the exogenous force, and $y$ the mass deflection. The viscous damping $c$ represents the energy dissipation mechanisms, and it is typically not known exactly. For simplicity, a proportional damping

$$c = \alpha m + \beta k \tag{4.19}$$

is assumed, where $\alpha$ and $\beta$ are tunable coefficients. Let the global mass, stiffness and damping matrices be denoted as $\mathcal{M}$, $\mathcal{K}$, and $\mathcal{C}$, respectively. The global dynamics of the interconnected spring-mass-damper system are governed by

$$F = \mathcal{M}\ddot{Y} + \mathcal{C}\dot{Y} + \mathcal{K}Y, \tag{4.20}$$

where $F$ and $Y$ are the input force vector and the output deflection vector, respectively, i.e. $F = [f_1, f_2, f_3, f_4, f_5]^T$ and $Y = [y_1, y_2, y_3, y_4, y_5]^T$. A free-free boundary condition is fulfilled, as no restriction is applied to the boundary subsystems. It is obvious that each subsystem is capable of actuating and sensing.

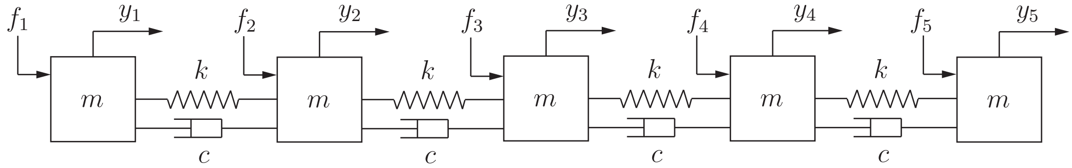


Figure 4.2: Interconnected spring-mass-damper system consisting of 5 subsystems

Assume that the mass, the stiffness, and the damping are identical for all subsystems. Let the values be $m = 1$ kg, $k = 10$ N/m, $\alpha = 10^{-3}$ and $\beta = 10^{-4}$. The global mass and stiffness matrices are

$$\mathcal{M} = \begin{bmatrix} 1 & 0 & 0 & 0 & 0 \\ 0 & 1 & 0 & 0 & 0 \\ 0 & 0 & 1 & 0 & 0 \\ 0 & 0 & 0 & 1 & 0 \\ 0 & 0 & 0 & 0 & 1 \end{bmatrix} \quad \mathcal{K} = \begin{bmatrix} 10 & -10 & 0 & 0 & 0 \\ -10 & 20 & -10 & 0 & 0 \\ 0 & -10 & 20 & -10 & 0 \\ 0 & 0 & -10 & 20 & -10 \\ 0 & 0 & 0 & -10 & 10 \end{bmatrix}, \tag{4.21}$$

respectively. The appication of the Laplace transform to (4.20) results in

$$G(s) = [\mathcal{M}s^2 + \mathcal{C}s + \mathcal{K}]^{-1}, \tag{4.22}$$

where $G(s)$ is the continuous MIMO transfer function matrix from $F$ to $Y$, or the so-called FRF matrix in the field of structural engineering. Its dimension is determined by the number of inputs and outputs, or in this context the number of spatially discretized subsystems.

The symmetric mass, damping and stiffness matrices imply a symmetric transfer function matrix $G(s)$, and further the structural reciprocity ([56], [64]) of a linear system: the transfer function from a single input at coordinate $i$ to the output at $j$ is the same as the transfer function from an input at $j$ to output at $i$. After the temporal discretization, the continuous and symmetric $G(s)$ is converted into

$$G(q_t) = \begin{bmatrix} G_{11}(q_t) & G_{12}(q_t) & G_{13}(q_t) & G_{14}(q_t) & G_{15}(q_t) \\ & G_{22}(q_t) & G_{23}(q_t) & G_{24}(q_t) & G_{25}(q_t) \\ & & G_{33}(q_t) & G_{34}(q_t) & G_{35}(q_t) \\ & \text{sym} & & G_{44}(q_t) & G_{45}(q_t) \\ & & & & G_{55}(q_t) \end{bmatrix}, \tag{4.23}$$

where the operator $G_{ij}(q_t)$ denotes the transfer function, or FRF, from the excitation at $j$ to response at $i$ $(i, j = 1, \ldots, 5)$, 'sym' the symmetric components in a matrix. When the coordinates of $i$ and $j$ coincide, i.e. $i = j$, the FRF is referred to as a *point* FRF, otherwise a *transfer* FRF. In the rest of this chapter, $G$ and $G_{ij}$ are used to denote the FRF matrix $G(q_t)$ and the operator $G_{ij}(q_t)$, respectively, for notational simplicity.

Both (4.20) and (4.23) describe the global dynamics of the system in Fig. 4.2. Now suppose that the elemental $m$, $k$, and $c$ are not known accurately, and need to be estimated. The modelling of (4.20) relies on the knowledge of system physics in terms of its mass, stiffness and damping matrices, and falls into the FE modelling that has been extensively discussed in Chapter 3. The obtained FE model is generally not suitable for a model-based controller synthesis, due to its generally high system order.

The conventional black-box identification of (4.23) relies on the input/output behaviour of the system. Each operator $G_{ij}$ is treated as an LTI system, and identified individually: given the single-input and single-output (SISO) data set $(u_j,\ y_i)$, $G_{ij}$ is identified by applying the least-squares method discussed in Section 4.2.1, where $n_a$ and $n_b$ determining the model structure are chosen *a priori*. Experiments and identification procedures are then repeatedly performed, until all upper triangular operators in (4.23) are estimated. Despite of its simplicity, the conventional black-box identification of (4.23) fails to be an effective approach due to the following two reasons:

1) The identification of any operator $G_{ij}$ in the FRF matrix requires the single excitation at subsystem $j$ and measured response of subsystem $i$. When a large-scale structure that consists of a large number of inputs and outputs is encountered, the experimental data acquisition process may become tremendous and tedious, in terms of repeating the experiments. The same is true for the estimation process.

2) For control engineers, system identification is performed to obtain an accurate mathematical model, whose structure is suitable for an effective controller design. It is desired in control of distributed parameter systems that the controller inherits the distributed structure of the plant, i.e.

$$K = \begin{bmatrix} K_{11} & K_{12} & K_{13} & K_{14} & K_{15} \\ & K_{22} & K_{23} & K_{24} & K_{25} \\ & & K_{33} & K_{34} & K_{35} \\ & \text{sym} & & K_{44} & K_{45} \\ & & & & K_{55} \end{bmatrix}. \tag{4.24}$$

Given the fact that each operator $G_{ij}$ in (4.23) is determined individually, so is the controller operator $K_{ij}$ in (4.24). The involved work makes the plant structure unfavourable from a practical point of view.

Driven by the above two drawbacks of the conventional black-box identification technique, a novel identification approach is needed. The identified model should preserve the accuracy achieved by the conventional technique to a certain extent. In addition, the resulting plant structure should lead to an efficient system identification and controller synthesis process, which involves a reasonable amount of effort, even when dealing with a complex or large-scale system.

## 4.4 LPV Identification of an FRF Matrix

To address the two issues related to the individual identification of the FRFs in (4.23), a spatial LPV model is proposed to capture the spatially-varying characteristics of the FRF matrix. To justify this approach, the system in Fig. 4.2 is taken as an example to demonstrate the varying properties of the FRFs, and how this variation leads to a spatial LPV representation.

### 4.4.1 Spatially-Varying Characteristics of FRFs

Due to the interconnection between subsystems through springs and dampers, the dynamics of the 5 subsystems in Fig. 4.2 are clearly not decoupled, but interacting with nearest neighbours. This interaction can be observed in terms of mode shapes, where the relative displacements of subsystems follow a certain pattern at resonant modes. The typical unforced mode shapes of the 5-node system in Fig. 4.2 at the first 3 natural frequencies are shown in Fig. 4.3. One important assumption can already be made: The dynamics of one subsystem have a functional dependence on its location within the interconnected system. If this assumption is true, the spatially-varying properties can be captured using an LPV model according to a certain spatial scheduling policy.

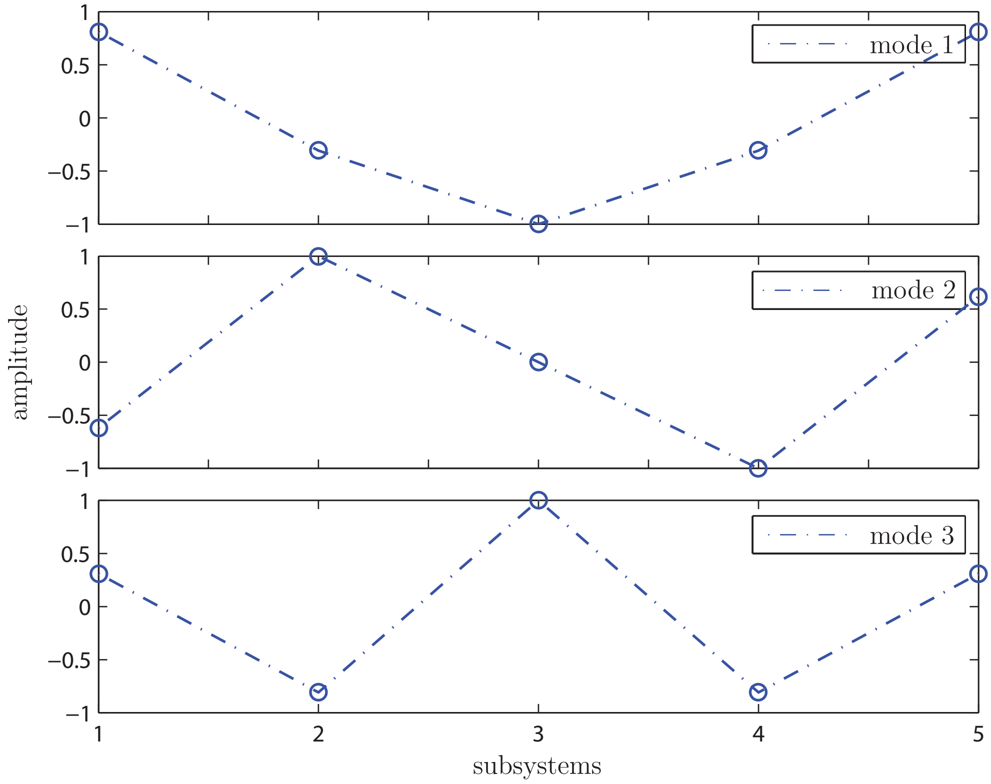


Figure 4.3: First 3 mode shapes of the five-spring-mass-damper system

Consider the diagonal terms in (4.23) at first, the so-called *point* FRFs, where the actuating and sensing subsystems coincide. If the spatial LPV characteristics can be established among the diagonal terms, it should be possible to use an LPV input/output model to generalize $G_{11}$, $G_{22}$, $G_{33}$, $G_{44}$, and $G_{55}$ as functions of the spatial coordinates. Introduce an extended notion of *operating points* in contrast to the lumped LPV sense. In this case, determine the spatial coordinate $s_i$, where the response is measured, as the spatial operating point $\theta_s^i$, i.e. $\theta_s^i = s_i$ $(i = 1, \ldots, 5)$. Let $\hat{p}_0(\theta_s^i)$ be a smooth function of $\theta_s^i$. The diagonal terms can be represented in LPV form as

$$G = \begin{bmatrix} G(\hat{p}_0(\theta_s^1)) & G_{12} & G_{13} & G_{14} & G_{15} \\ & G(\hat{p}_0(\theta_s^2)) & G_{23} & G_{24} & G_{25} \\ & & G(\hat{p}_0(\theta_s^3)) & G_{34} & G_{35} \\ & \text{sym} & & G(\hat{p}_0(\theta_s^4)) & G_{45} \\ & & & & G(\hat{p}_0(\theta_s^5)) \end{bmatrix}. \tag{4.25}$$

The spatial LPV model $G(\hat{p}_0(\theta_s^i))$ differs from (4.9) in terms of the scheduling parameters—time-varying in a lumped system, time/space-varying in a spatially-distributed system. The subscript 0 indicates the diagonal terms.

The true values of $p_0(\theta_s^i)$ can be first estimated by applying the conventional black-box identification technique to individually identify the LTI operators $G_{ii}$ ($i = 1, \ldots, 5$) as described in steps 1) and 2) in Section 4.2.2, except that the fixed operating points are spatial variables here. Approximate $p_0(\theta_s^i)$ with a polynomial function $\hat{p}_0(\theta_s^i)$ of $\theta_s^i$. An LPV representation of the 5 diagonal terms in (4.25) can then be easily derived following step 3) in Section 4.2.2. It is evident that if a solution to (4.17) exists, the approximated polynomial coefficients $\hat{p}_0(\theta_s^i)$ agree with the true values $p_0(\theta_s^i)$ ($i = 1, \ldots, 5$).

To explore the advantages of using an LPV model to generalize the diagonal terms (4.25), now assume that identification experiments can not be implemented at all operating points due to certain constraints. For example, the LTI operators $G_{11}$, $G_{33}$, $G_{44}$ and $G_{55}$ can be experimentally identified, whereas it is not possible to perform actuating and/or sensing at subsystem 2, so that $G_{22}$ needs to be determined without performing an experiment. This problem can be solved by first constructing an LPV model $G(\hat{p}_0(\theta_s^i))$ based on the information at operating points $\theta_s^1$, $\theta_s^3$, $\theta_s^4$ and $\theta_s^5$, then interpolating $\theta_s^2$ in $G(\hat{p}_0(\theta_s^i))$ to obtain $G_{22}$. Fig. 4.4 shows a comparison between two FRFs of $G_{22}$: one is its true value; the other one is simulated from $G(\hat{p}_0(\theta_s^2))$. Although the interpolated operator is lightly damped at the 2nd mode, the resonant peaks at other modes are well preserved. The main dynamics are captured in spite of a degraded accuracy. The modelling error may be attributed to a functional dependence of $\hat{p}_0(\theta_s^i)$ on $\theta_s^i$ of a higher complexity than the simple polynomial function assumed here.

The 1st off-diagonal terms are the *transfer* FRFs from the single excitation at subsystem $j = i+1$ to measured response at subsystem $i$ ($i = 1, \ldots, 4$). Applying similar procedures as above to identify operators $G_{i(i+1)}$ ($i = 1, \ldots, 4$) results in another set of LPV models $G(\hat{p}_1(\theta_s^i))$ ($i = 1, \ldots, 4$)

$$G = \begin{bmatrix} G_{11} & G(\hat{p}_1(\theta_s^1)) & G_{13} & G_{14} & G_{15} \\ & G_{22} & G(\hat{p}_1(\theta_s^2)) & G_{24} & G_{25} \\ & & G_{33} & G(\hat{p}_1(\theta_s^3)) & G_{35} \\ & \text{sym} & & G_{44} & G(\hat{p}_1(\theta_s^4)) \\ & & & & G_{55} \end{bmatrix}, \tag{4.26}$$

where the same scheduling policy as for the diagonal terms is employed, i.e., the spatial operating points are the spatial coordinates where the responses are measured.

The identified spatial LPV model also allows the interpolation of operating points where the identification experiments are not performed. Suppose that the response at subsystem 1

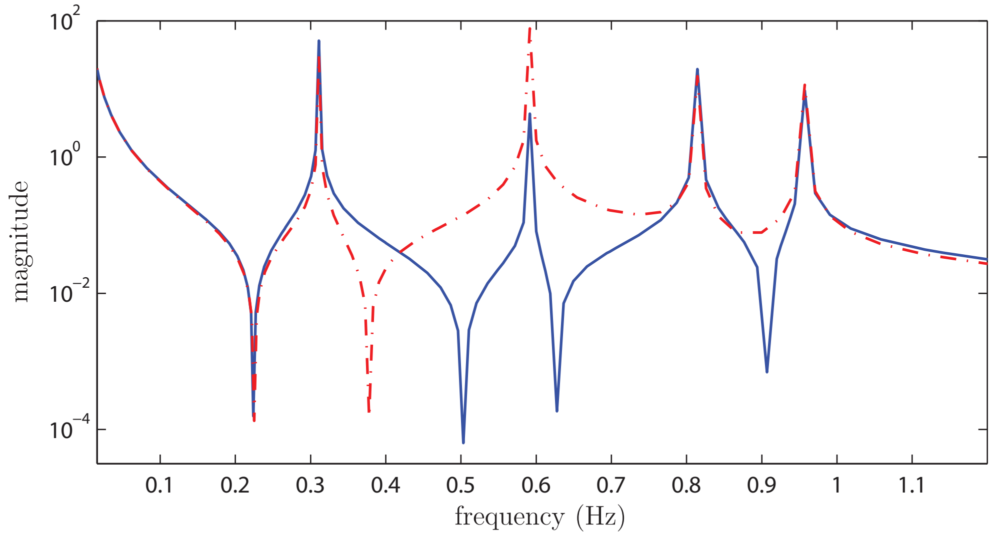


Figure 4.4: Comparison between two FRFs of $G_{22}$: the blue solid curve shows its true value; the red dotted curve is simulated by interpolating the LPV model $G(\hat{p}_0(\theta_s^i))$ with $\theta_s^2$.

can not be measured. The unknown operator $G_{12}$ is approximated by interpolating the LPV model, which is constructed from the identified local LTI systems $G_{23}$, $G_{34}$ and $G_{45}$, with a polynomial dependence of $\hat{p}_1(\theta_s^i)$ on $\theta_s^i$ $(i = 1, 2, 3, 4)$. The comparison between the true value and the simulation of $G_{12}$ as shown in Fig. 4.5 suggests a satisfactory accuracy of the LPV modelling.

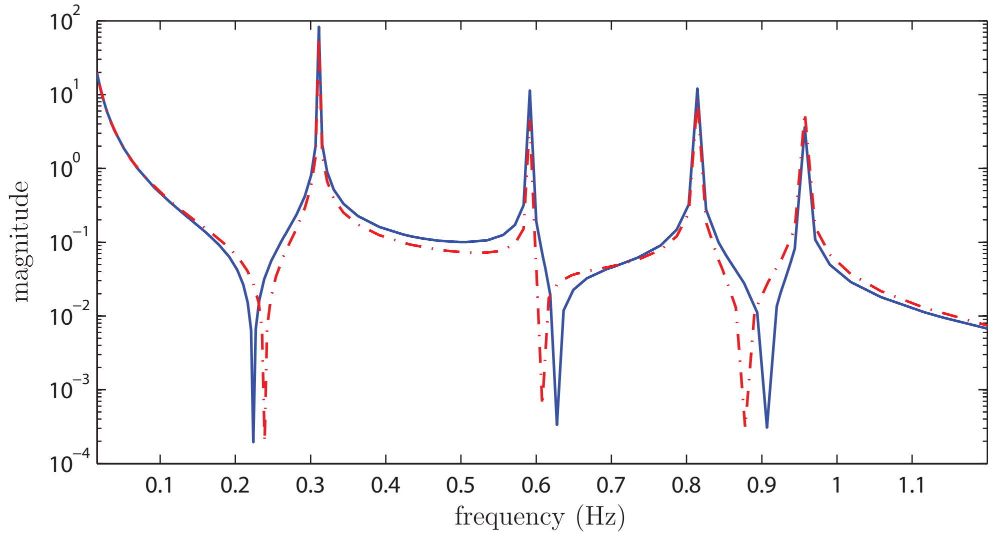


Figure 4.5: Comparison between two FRFs of $G_{12}$: the blue solid curve shows its true value; the red dotted curve is simulated by interpolating the LPV model $G(\hat{p}_1(\theta_s^i))$ with $\theta_s^1$.

Repeating the same procedures for the 2nd, 3rd and 4th off-diagonal operators, another three sets of spatial LPV models are accordingly derived—$G(\hat{p}_2(\theta_s^i))$ for $i = 1, 2, 3$, $G(\hat{p}_3(\theta_s^i))$ for $i = 1, 2$, and $G(\hat{p}_4(\theta_s^i))$ for $i = 1$, respectively. Finally, the transfer function matrix $G$ parametrized in a set of spatial LPV models is obtained as

$$G = \begin{bmatrix} G(\hat{p}_0(\theta_s^1)) & G(\hat{p}_1(\theta_s^1)) & G(\hat{p}_2(\theta_s^1)) & G(\hat{p}_3(\theta_s^1)) & G(\hat{p}_4(\theta_s^1)) \\ & G(\hat{p}_0(\theta_s^2)) & G(\hat{p}_1(\theta_s^2)) & G(\hat{p}_2(\theta_s^2)) & G(\hat{p}_3(\theta_s^2)) \\ & & G(\hat{p}_0(\theta_s^3)) & G(\hat{p}_1(\theta_s^3)) & G(\hat{p}_2(\theta_s^3)) \\ & \text{sym} & & G(\hat{p}_0(\theta_s^4)) & G(\hat{p}_1(\theta_s^4)) \\ & & & & G(\hat{p}_0(\theta_s^5)) \end{bmatrix}, \tag{4.27}$$

where the operating points are chosen to be the spatial coordinates of the locations where the responses are measured.

Certainly, (4.27) is not a unique way to explore the spatial-varying properties of the FRF matrix. Similar characteristics can also be detected when examining the rows of (4.23).

Operators on the first row of (4.23), $G_{1j}$ $(j = 1, \ldots, 5)$, denote the transfer function from a single input at subsystem $j$ $(j = 1, \ldots, 5)$ to the response at subsystem 1, respectively. Define a new scheduling policy as $\theta_s^j = s_j$—the spatial coordinate of a subsystem where an excitation is applied. The first row of (4.23) is represented in a spatial LPV form as

$$G = \begin{bmatrix} G(\hat{p}^1(\theta_s^1)) & G(\hat{p}^1(\theta_s^2)) & G(\hat{p}^1(\theta_s^3)) & G(\hat{p}^1(\theta_s^4)) & G(\hat{p}^1(\theta_s^5)) \\ & G_{22} & G_{23} & G_{24} & G_{25} \\ & & G_{33} & G_{34} & G_{35} \\ & \text{sym} & & G_{44} & G_{45} \\ & & & & G_{55} \end{bmatrix}, \tag{4.28}$$

where the superscript $\hat{p}^1(\theta_s^j)$ is used to distinguish it from $\hat{p}_1(\theta_s^i)$ in (4.26). In Fig. 4.6, the comparison between the true value of $G_{12}$ and the approximated one obtained by inserting $\theta_s^2$ into the LPV model $G(\hat{p}^1(\theta_s^i))$ calculated from $G_{11}$, $G_{13}$, $G_{14}$ and $G_{15}$, confirms the spatially-varying property among the operators on one row. Repeating the same procedures to the 2nd, 3rd and 4th rows in a sequel, the FRF matrix of an LPV form alternative to (4.27) is written as

$$G = \begin{bmatrix} G(\hat{p}^1(\theta_s^1)) & G(\hat{p}^1(\theta_s^2)) & G(\hat{p}^1(\theta_s^3)) & G(\hat{p}^1(\theta_s^4)) & G(\hat{p}^1(\theta_s^5)) \\ & G(\hat{p}^2(\theta_s^2)) & G(\hat{p}^2(\theta_s^3)) & G(\hat{p}^2(\theta_s^4)) & G(\hat{p}^2(\theta_s^5)) \\ & & G(\hat{p}^3(\theta_s^3)) & G(\hat{p}^3(\theta_s^4)) & G(\hat{p}^3(\theta_s^5)) \\ & \text{sym} & & G(\hat{p}^4(\theta_s^4)) & G(\hat{p}^4(\theta_s^5)) \\ & & & & G(\hat{p}^5(\theta_s^5)) \end{bmatrix}, \tag{4.29}$$

where the operating points are the spatial coordinates of subsystems at which the actuation is applied.

### 4.4.2 A Spatial LPV Representation

In Section 4.4.1, two alternative tests with different choices of operating points have been carried out to validate the assumption, that it is in principle feasible to model the

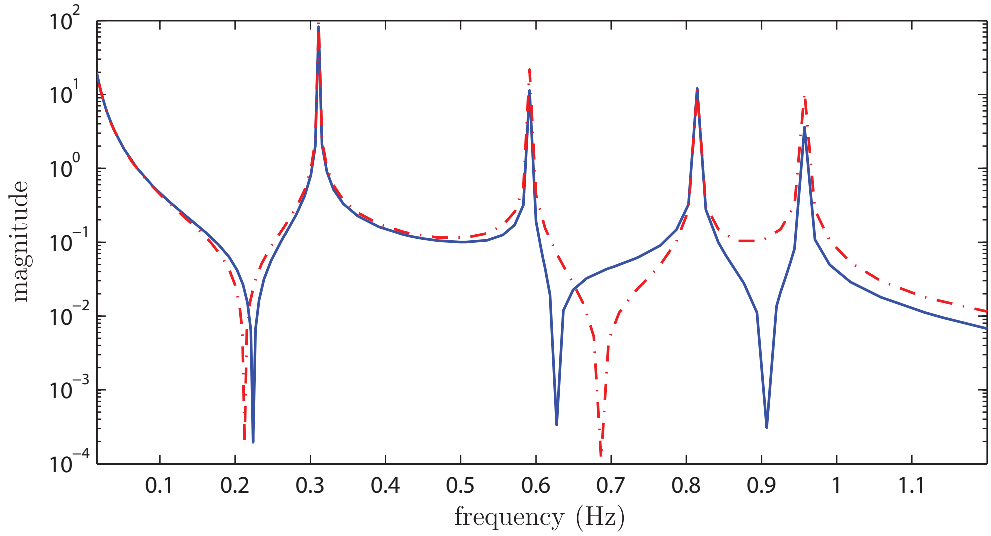


Figure 4.6: Comparison between two FRFs of $G_{12}$: the blue solid curve shows its true value; the red dotted curve is simulated by interpolating the LPV model $G(\hat{p}^1(\theta_s^i))$ with $\theta_s^2$.

input/output behaviour of a spatially-interconnected system as in Fig. 4.2 with a set of spatial LPV models. In this section, the above two intermediate results (4.27) and (4.29) are combined to derive a more compact spatial LPV representation of (4.23).

In (4.27), the spatial scheduling parameter is the spatial coordinate of the subsystem whose response is measured, i.e., $\theta_s^i = s_i$ in $G_{ij}$. On the other hand, the scheduling parameter in (4.29) is the spatial coordinate of the subsystem at which a single excitation is applied, i.e., $\theta_s^j = s_j$ in $G_{ij}$. Instead of using a scalar – either $s_i$ or $s_j$ – as the scheduling parameter, it can be expected that an LPV model which integrates both the input and output information, leads to a more compact model structure. Applying a new scheduling policy with $\theta_s^{ij} = [s_i \quad s_j]^T$, the spatial operating point determines any combination of input and output channels. Assume again a polynomial dependence of $\hat{p}(\theta_s^{ij})$ on $\theta_s^{ij}$, i.e.

$$\hat{p}(\theta_s^{ij}) = \lambda_0 + \lambda_1 \theta_s^{ij} + \lambda_2 (\theta_s^{ij})^2 + \cdots + \lambda_m (\theta_s^{ij})^m, \tag{4.30}$$

where $\lambda_k \in \mathbb{R}^{(n_a+n_b)\times n_\theta}$ $(k = 1, \ldots, m)$ is a matrix instead of a vector as in (4.14), whose column size agrees with the size of the vector exponential $(\theta_s^{ij})^m$. The FRF matrix (4.23) takes a compact LPV form

$$G = \begin{bmatrix} G(\hat{p}(\theta_s^{11})) & G(\hat{p}(\theta_s^{12})) & G(\hat{p}(\theta_s^{13})) & G(\hat{p}(\theta_s^{14})) & G(\hat{p}(\theta_s^{15})) \\ & G(\hat{p}(\theta_s^{22})) & G(\hat{p}(\theta_s^{23})) & G(\hat{p}(\theta_s^{24})) & G(\hat{p}(\theta_s^{25})) \\ & & G(\hat{p}(\theta_s^{33})) & G(\hat{p}(\theta_s^{34})) & G(\hat{p}(\theta_s^{35})) \\ & \text{sym} & & G(\hat{p}(\theta_s^{44})) & G(\hat{p}(\theta_s^{45})) \\ & & & & G(\hat{p}(\theta_s^{55})) \end{bmatrix}. \tag{4.31}$$

With the choice of $\theta_s^{ij}$ as the scheduling parameter, operator $G_{ij}(\hat{p}(\theta_s^{ij}))$ uniquely determines the transfer function from an input at subsystem $j$ to an output at $i$. The computation of the matrix $\Lambda = [\lambda_0, \lambda_1, \ldots, \lambda_m]$ follows the same pattern of (4.17).

If each subsystem in the interconnected five-spring-mass-damper system in Fig. 4.2 is equipped with sensing and actuating capability, the system has in total 15 operating points (by counting only the terms in the upper triangular matrix of (4.31)). Suppose now that excitation can not be applied at subsystem 2, whereas the responses at all 5 subsystems are measurable. Excluding two operating points $\theta_s^{12}$ and $\theta_s^{22}$, the spatial LPV identification is performed at the remaining 13 spatial operating points with polynomial order 12. The computation of $\Lambda$ is realized according to (4.17), where $\mathcal{P} = \left[p(\theta_s^{11}) \ldots p(\theta_s^{ij}) \ldots p(\theta_s^{55})\right]$, and

$$\Delta_\theta = \begin{bmatrix} \begin{bmatrix} 1 \\ 1 \end{bmatrix} & \cdots & \begin{bmatrix} 1 \\ 1 \end{bmatrix} & \cdots & \begin{bmatrix} 1 \\ 1 \end{bmatrix} \\ \begin{bmatrix} s_1 \\ s_1 \end{bmatrix} & \cdots & \begin{bmatrix} s_i \\ s_j \end{bmatrix} & \cdots & \begin{bmatrix} s_5 \\ s_5 \end{bmatrix} \\ \vdots & \vdots & \vdots & & \\ \begin{bmatrix} s_1 \\ s_1 \end{bmatrix}^{12} & \cdots & \begin{bmatrix} s_i \\ s_j \end{bmatrix}^{12} & \cdots & \begin{bmatrix} s_5 \\ s_5 \end{bmatrix}^{12} \end{bmatrix}. \tag{4.32}$$

The comparison between the true value and simulation of $G_{12}$ and $G_{22}$ is shown in Fig. 4.7 (a) and (b), respectively.

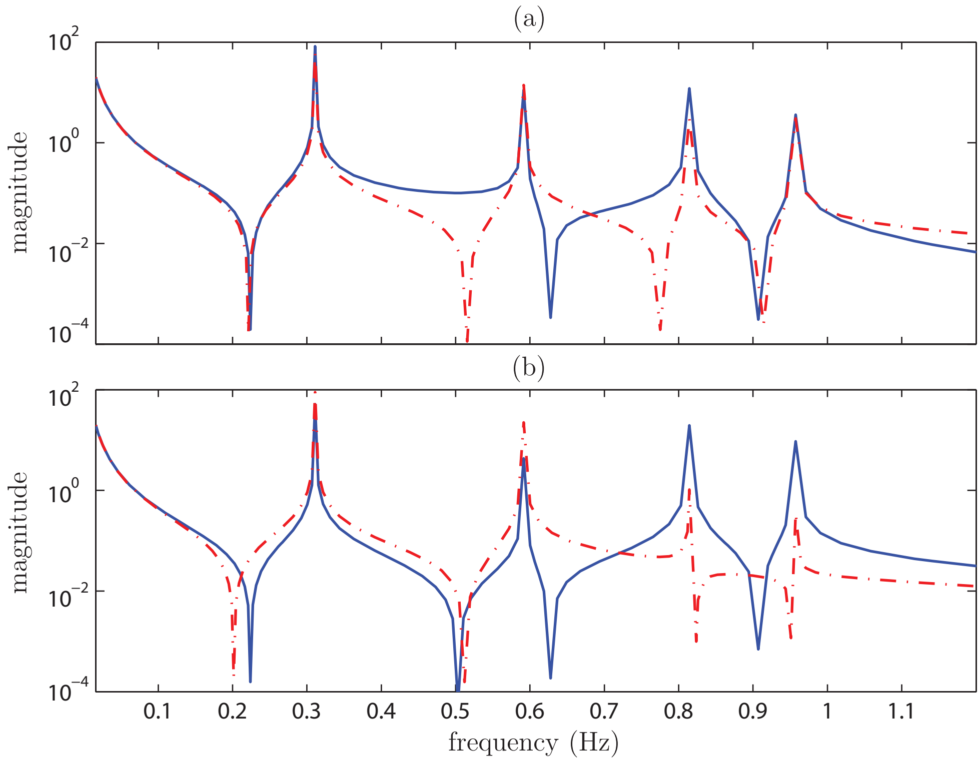


Figure 4.7: Comparison between the measured and simulated FRFs of $G_{12}$ in (a) and $G_{22}$ in (b): the blue solid curves show their true values; the red dotted curves are simulated by interpolating the LPV model $G_{ij}(\hat{p}(\theta_s^{ij}))$ with $\theta_s^{12}$ and $\theta_s^{22}$, respectively

*Remarks:*

- The benefits of using a spatial LPV model to parametrize the FRF matrix become more obvious when a large-scale system needs to be identified. Instead of performing the identification experiments at each spatial operating point, the spatial LPV structure allows to select some crucial points to perform the identification experiments, whereas the FRFs at other locations can be estimated through LPV interpolation.

- The spatial LPV plant model (4.31) leads to an efficient controller design process, where the controller inherits the spatial LPV structure as

$$K = \begin{bmatrix} K(\hat{p}(\theta_s^{11})) & K(\hat{p}(\theta_s^{12})) & K(\hat{p}(\theta_s^{13})) & K(\hat{p}(\theta_s^{14})) & K(\hat{p}(\theta_s^{15})) \\ & K(\hat{p}(\theta_s^{22})) & K(\hat{p}(\theta_s^{23})) & K(\hat{p}(\theta_s^{24})) & K(\hat{p}(\theta_s^{25})) \\ & & K(\hat{p}(\theta_s^{33})) & K(\hat{p}(\theta_s^{34})) & K(\hat{p}(\theta_s^{35})) \\ & \text{sym} & & K(\hat{p}(\theta_s^{44})) & K(\hat{p}(\theta_s^{45})) \\ & & & & K(\hat{p}(\theta_s^{55})) \end{bmatrix}. \tag{4.33}$$

- Since a vector exponential involves cross product terms, e.g. $(\theta_s^{ij})^2 = [s_i^2, s_j^2, s_i s_j]^T$, it may significantly increase the size of (4.32) and thus the computational burden of the optimization problem (4.17). Nevertheless, experience shows that even with an elementwise vector exponential, the identified LPV model demonstrates a satisfactory accuracy.

- It has been explained in [6] that the interaction between subsystems shows an exponential decay in space: the larger the distance between two subsystems, the smaller the impact. The implementation of *spatial truncation* leads to a 'localized' structure whose dynamics are close to the original system, but only influenced by the neighbouring subsystems. Therefore, when dealing with a system that consists of a large number of subsystems, instead of a full transfer function matrix $G$, a banded matrix

$$G' = \begin{bmatrix} * & \cdots & * & & & & \\ & * & \cdots & * & & 0 & \\ & & * & \cdots & * & & \\ & 0 & & * & \cdots & * & \\ & & & & * & \cdots & * \end{bmatrix} \tag{4.34}$$

  appears to be a more attractive structure from a practical point of view, after spatially truncating the operators $G_{ij}$ when $|s_j - s_i| > \bar{\gamma}$, where $\bar{\gamma}$ is the maximum allowable distance from input to output. The truncated FRF matrix coincides with the structure of a distributed system, in the sense that the response of one subsystem is determined by itself and its nearest neighbours.

- Increasing the number of the operating points at which the identification experiments are performed leads to a higher accuracy of the identified model at the cost of increased computational complexity. A compromise between the model accuracy and complexity needs to be achieved according to the requirements. On the other hand, given a fixed number of operating points, the optimization of their locations to achieve a maximum accuracy is discussed in [61] .

## 4.5 Experimental Results

To experimentally validate the proposed identification approach, another testbed as shown in Fig. 4.8 – an aluminium beam of 0.75 m length, 4 cm width, and 4 mm thickness, equipped with 5 collocated pairs of piezo actuators and sensors – has been employed. The attachment of the 5 piezo pairs virtually divides the test structure into 5 interconnected subsystems, with their spatial coordinates

$$s = [0.075, 0.225, 0.375, 0.525, 0.675]\text{m},$$

as shown in Fig. 4.9. The free-body condition is realized by suspending the beam with three springs in parallel.

Figure 4.8: Aluminium beam equipped with 5 pairs of collocated piezo actuators and sensors

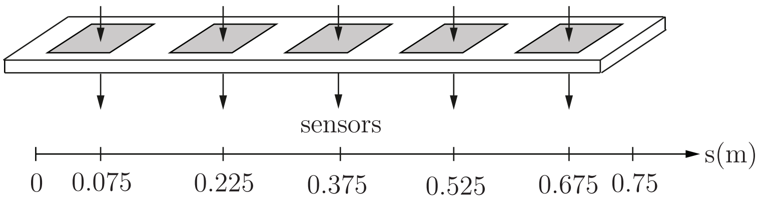


Figure 4.9: Distribution and spatial coordinates of the 5 piezo pairs

Experience shows that a chirp signal covering the resonant frequencies of interest works the best as an excitation signal. Knowing that the first two resonant frequencies of the structure are 35.05 and 96.08 Hz, a chirp signal sweeping the frequencies from 0 to 100 Hz with a sampling time $\Delta T = 0.001$ s is generated to excite each subsystem individually. The proposed identification technique is evaluated under two scenarios: 1. ideal case: actuating and sensing at all subsystems are possible; 2. non-ideal case: either actuating or sensing fails at certain subsystems, where the corresponding FRFs need to be estimated without performing identification experiments.

### 4.5.1 Ideal Case

In the ideal case, each subsystems is excited individually, while the responses at all 5 subsystems are measured simultaneously. Given the data set $(u_j, y_i)$ for $i, j = 1, 2, \ldots, 5$, the upper triangular operators $G_{ij}$ of (4.23) are first identified individually as a set of LTI models by means of the least-squares method discussed in Section 4.2.1. By trial and error, proper input and output orders are determined as $n_a = n_b = 10$. A polynomial dependence of $G(\hat{p}(\theta_s^{ij}))$ on $\theta_s^{ij}$ is assumed. An LPV model in the form of (4.31) is then identified to capture the spatially-varying characteristics of the FRF matrix. Fig. 4.10 shows the comparison between the measured and LPV approximated FRFs of the $5 \times 5$ matrix, which suggests a high accuracy of the LPV estimation.

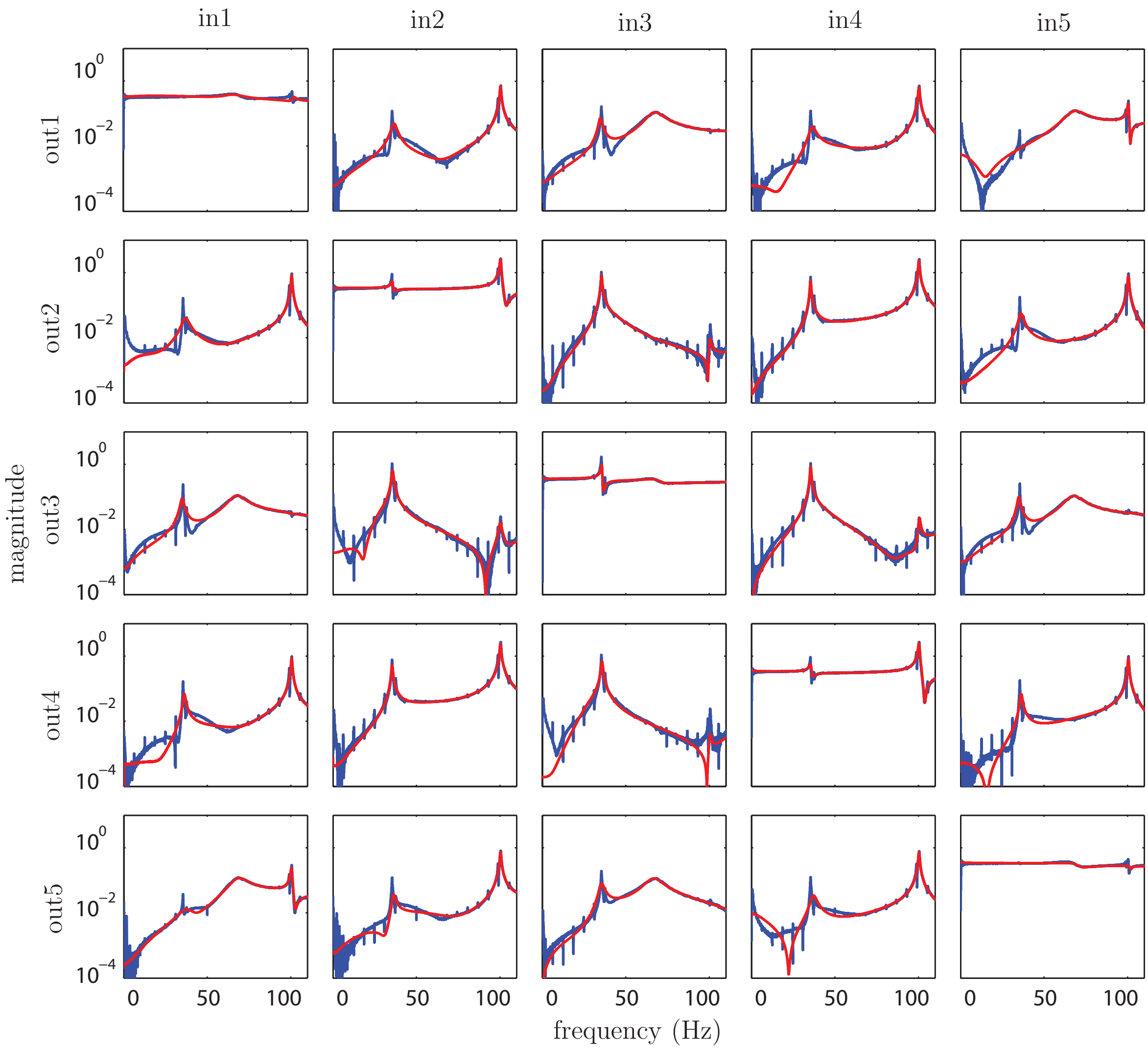


Figure 4.10: Comparison between the measured and LPV approximated FRFs of the $5 \times 5$ matrix: the blue curves are measured; the red ones are from the spatial LPV simulation.

### 4.5.2 Non-ideal Case

The non-ideal scenario is meant to test the reliability of the local LPV identification technique, when performing identification experiments at certain operating points is not possible.

Assume that the 3rd actuator is defect, i.e. the operators $G_{13}$, $G_{23}$ and $G_{33}$ in (4.23) can not be identified experimentally, but can be approximated, after a spatial LPV model $G(\hat{p}(\theta_s^{ij}))$ is constructed based on the information at available operating points. Fig. 4.11 shows the comparison between the measured and simulated FRFs of $G_{13}$ in (a), $G_{23}$ in (b) and $G_{33}$ in (c). Though some discrepancies exist, the structural dynamics at the first two modes are relatively well preserved.

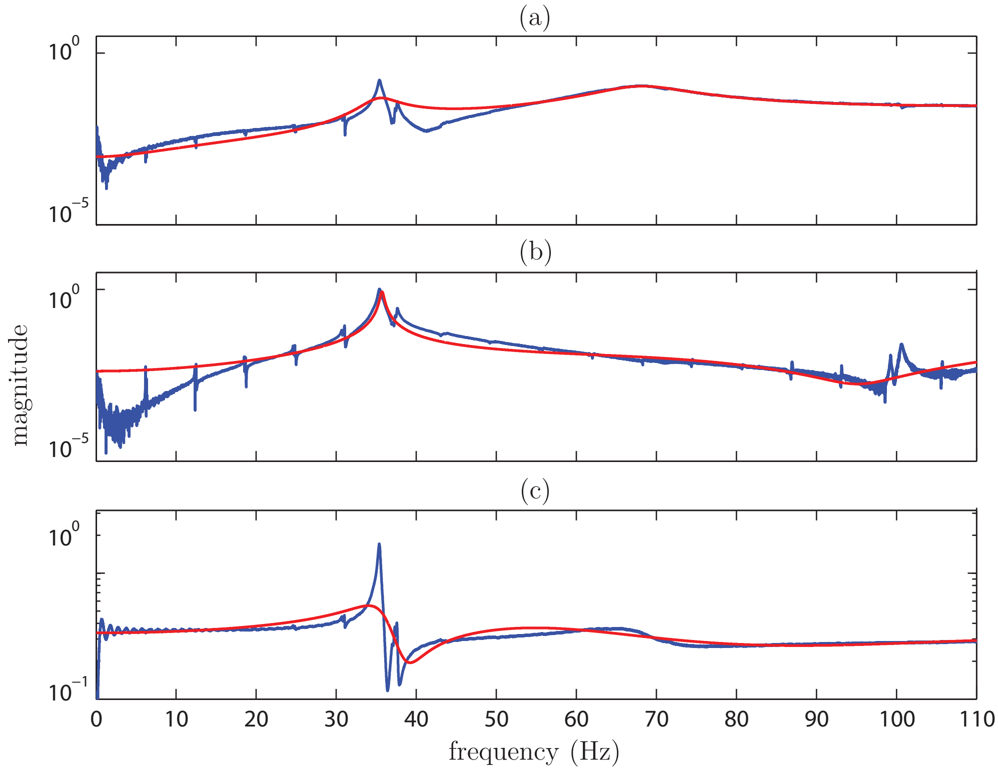


Figure 4.11: Comparison of the measured and simulated FRFs of $G_{13}$ in (a), $G_{23}$ in (b) and $G_{33}$ in (c): the blue curves are measured; the red curves are from interpolating the LPV model $G(\hat{p}(\theta_s^{ij}))$ with $\theta_s^{13}$, $\theta_s^{23}$, and $\theta_s^{33}$, respectively, assumed that the 3rd actuator fails.

## 4.6 Summary

This chapter has proposed a novel approach to identify the FRF matrix directly from the input/output behaviour of a test structure, to address two issues that arise from implementing the conventional black-box identification: 1. the individual identification of the FRFs in an FRF matrix requires performing identification experiments at a large number of actuating and sensing locations, when dealing with a large-scale or complex structure; 2. the structure of the identified FRF matrix is generally not suitable for controller design. It has been demonstrated step by step that the FRFs in an FRF matrix exhibit spatially-varying characteristics. A local LPV identification approach has been extended from lumped systems to spatially-distributed systems. The FRF matrix can then be parametrized as a spatial LPV model, which allows to approximate the FRFs at non-actuated/non-sensed locations through LPV interpolation. The proposed approach facilitates the experimental work by allowing to perform experiments at a relatively small number of selected actuating and sensing locations. Meanwhile, the LPV representation of the FRF matrix enables an efficient LPV controller design, if a controller that inherits the plant structure is required. The performance of the proposed approach has been experimentally demonstrated on an actuated beam. When actuating and/or sensing at certain locations is not possible, FRFs approximated through the LPV interpolation still preserve the main dynamics of the test structure.

# Chapter 5

# Distributed Identification

## 5.1 Introduction

Although Chapter 3 and Chapter 4 have dealt with the physical modelling and lumped identification of given test structures, respectively, the obtained models do not allow to work in the framework developed in Chapter 2. Thus a mathematical model that captures the distributed nature of a structure is needed, such that system analysis and controller synthesis conditions first developed in [8] can be applied.

It is well-known that the mechanical behaviour of structures is typically governed by PDEs. The FE method presented in Chapter 3 is one technique to solve for the approximated solutions to PDEs. In this chapter, an alternative numerical technique – the finite difference (FD) method – is discussed. The application of the FD method leads to a two-dimensional input/output model structure, which spatially discretizes the distributed-parameter system into interconnected subsystems, and defines the system dynamics on an individual subsystem of a small order. The resulting input/output model can then be converted into the state space form that lends itself to efficient, LMI-based synthesis of distributed control; it is thus used as the mathematical model for a distributed identification.

This chapter considers the distributed identification of both parameter-invariant and parameter-varying models. The input/output identification techniques developed in [27] for LTSI models and in [29] for spatial LPV models are implemented experimentally. A new identification approach that exploits the physical modelling results obtained in Chapter 3 is proposed here to improve the identification accuracy, with the desired mathematical model still preserved.

This chapter includes results reported in [65] and [66]. It is organized as follows: Section 5.2 derives the mathematical model for distributed identification by solving PDEs using the FD method. Section 5.3 briefly reviews the input/output identification techniques for both LTSI and spatial LPV models developed in [27] and [29], respectively, and tests them on the test structure. Section 5.4 develops an alternative identification procedure, which accounts for the physical properties of the test structure and experimentally demonstrates a better performance compared to black-box identification.

## 5.2 Mathematical Model for Identification

This section discusses the implementation of the FD method to solve for approximate solutions to the governing PDE of a beam structure. The resulting two-dimensional input/output model structure captures the dynamics of spatially-discrete subsystems interacting with nearest neighbours.

### 5.2.1 FD Method to Solve PDEs

The idea of the FD method is to replace the partial derivatives with approximations obtained by Taylor expansions around interest points. For example, the Taylor series of a function $u(x)$, that is infinitely differentiable at point $x_i$, is the power series

$$u(x_{i+1}) = u(x_i) + \frac{\Delta x}{1!}u'(x_i) + \frac{(\Delta x)^2}{2!}u''(x_i) + \ldots + \frac{(\Delta x)^n}{n!}u^{(n)}(x_i) + \ldots, \tag{5.1}$$

where $\Delta x = x_{i+1} - x_i$. Its first derivative can be expressed using the *forward* difference

$$u'(x_i) = \frac{u(x_{i+1}) - u(x_i)}{\Delta x} + \mathcal{O}(\Delta x), \tag{5.2}$$

the *backward* difference

$$u'(x_i) = \frac{u(x_i) - u(x_{i-1})}{\Delta x} + \mathcal{O}(\Delta x), \tag{5.3}$$

the *central* difference

$$u'(x_i) = \frac{u(x_{i+1}) - u(x_{i-1})}{2\Delta x} + \mathcal{O}((\Delta x)^2), \tag{5.4}$$

or the combination of the backward and forward difference methods—Crank-Nicolson scheme [67]. The *truncation error* – the difference between the numerical approximation and its exact value – is denoted by $\mathcal{O}(\cdot)$.

PDEs of one spatial dimension include the partial derivatives of signals – e.g. $u(t, x)$ – with respect to continuous time $t$ and space $x$. Replacing both the temporal and spatial derivatives with difference approximations results in a difference equation with respect to discrete time $k$ and discrete space $s$. Various combinations of the difference methods can be applied to replace the temporal and spatial derivatives, for example, forward-time forward-space (FTFS), backward-time central-space (BTCS), etc. Depending on how the solution $u(k, s)$ is calculated, the approximation can be categorized either as *explicit* scheme or *implicit* scheme.

An FD scheme is said to be explicit, if values at time instant $k$ depend only on values from the past. If the unknown values at $k$ are functions of both known quantities at $k-1$,

$k-2$, ..., and unknown quantities at $k$, the scheme is implicit. The implementation of different schemes may yield different results. One reason is that the round-off error that arises during calculation may lead to a blow up of the solution. A scheme is considered *convergent*, if its solution approximates the solution of the PDE, and the approximation improves as the sampling time and sampling space tend to zero.

Each scheme has its own benefits and drawbacks. A comparison can be carried out in terms of the following three aspects:

- Numerical stability: The implicit scheme is unconditionally stable, whereas the explicit scheme is stable only if a certain condition is fulfilled.
- Computation effort: The explicit scheme is easy to be implemented, and requires the least computation time, whereas the implicit scheme involves an intensive computational effort at each time step.
- Truncation error: The Crank-Nicolson scheme is most accurate for a small sampling time. The truncation error of the first-order derivative is quadratic over the sampling time/space in a Crank-Nicolson scheme, i.e. $\mathcal{O}((\Delta T)^2)$, $\mathcal{O}((\Delta X)^2)$, yet linear in an explicit scheme, i.e. $\mathcal{O}(\Delta T)$, $\mathcal{O}(\Delta X)$.

In this work, the explicit scheme is employed, accounting for its easy computation and real-time feasibility. Since the explicit scheme is only stable under certain conditions, the test of its numerical stability is required. Two mathematical tools – the *Courant-Friedrichs-Lewy (CFL) condition* and the *von Neumann analysis* – are available for this purpose.

The CFL condition developed by Courant, Friedrichs and Lewy [68], states a necessary (not sufficient) condition for an explicit FD scheme to be a stable approximation to a parabolic PDE by imposing a constraint on the *Courant number*. On the other hand, based on the Fourier decomposition of the round-off error, the von Neumann analysis results in necessary and sufficient conditions for the stability of an explicit FD scheme by imposing constraints on the temporal and spatial step sizes [69].

To illustrate the implementation of the explicit FD scheme to solve for approximated solutions to PDEs, as well as the numerical stability test, a PDE that governs the vibratory motion of a beam structure – the Euler-Bernoulli equation – is used as an example. The resulting difference equation after applying the FD method motivates the mathematical model for the distributed identification.

**Example 5.1 (Solving the Euler-Bernoulli Equation Using the FD Method)**
*The Euler-Bernoulli equation*

$$EI\frac{\partial^4 w(t,x)}{\partial x^4} + \rho A_o \frac{\partial^2 w(t,x)}{\partial t^2} = f(t,x) \tag{5.5}$$

*describes the dynamic relationship between the external force $f(t,x)$ and the transverse deflection $w(t,x)$, under the Euler-Bernoulli beam theory, where $E$, $I$, $\rho$, and $A_o$ denote the Young's modulus, second moment of area, density, and cross-section area, respectively.*

*Define the sampling time as $\Delta T$ and sampling space as $\Delta X$. Applying the central-time central-space (CTCS) FD method to (5.5) yields*

$$EI\frac{w(k,s-2)-4w(k,s-1)+6w(k,s)-4w(k,s+1)+w(k,s+2)}{(\Delta X)^4} + \rho A_o\frac{w(k+1,s)-2w(k,s)+w(k-1,s)}{(\Delta T)^2} = f(k,s). \tag{5.6}$$

*Performing the von Neumann stability analysis, the following requirement has to be fulfilled for a stable numerical solution to (5.6)*

$$\sqrt{\frac{EI}{\rho A_o}}\frac{\Delta T}{(\Delta X)^2} \leq \frac{1}{2}. \tag{5.7}$$

*Assume that stable and convergent solutions exist. Then $w(k,s)$ can be solved for explicitly in time from variables at spatial location $s$, neighbours $s-1$, $s-2$, $s+1$ and $s+2$ at time $k-1$ and $k-2$ as*

$$w(k,s) = -[a_{(1,-2)}w(k-1,s+2) + a_{(1,-1)}w(k-1,s+1) + a_{(1,0)}w(k-1,s) + a_{(1,1)}w(k-1,s-1) + a_{(1,2)}w(k-1,s-2) + a_{(2,0)}w(k-2,s)] + b_{(1,0)}f(k-1,s) \tag{5.8}$$

*with coefficients* $b_{(1,0)} = \frac{(\Delta T)^2}{\rho A_o}$, $a_{(1,0)} = -2 + \frac{6EI(\Delta T)^2}{\rho A_o(\Delta X)^4}$, $a_{(1,1)} = a_{(1,-1)} = -\frac{4EI(\Delta T)^2}{\rho A_o(\Delta X)^4}$, $a_{(1,2)} = a_{(1,-2)} = \frac{EI(\Delta T)^2}{\rho A_o(\Delta X)^4}$, $a_{(2,0)} = 1$.

*The dependence of $w(k,s)$ on temporally and spatially shifted inputs and outputs can be mapped onto two masks: input mask $M_u$ and output mask $M_y$ as shown in Fig. 5.1. Both masks are labelled by discretized temporal index $i_k$ and discretized spatial index $i_s$. Black dots indicate the involved temporally- and spatially-shifted inputs and outputs that contribute to the computation of $w(k,s)$, with their contributions weighed by the input and output coefficients $b_{(i_k,i_s)}$ and $a_{(i_k,i_s)}$, respectively. Alternatively, Fig. 5.1 can also be expressed as output and input sets, i.e.*

$$\begin{aligned} M_y &= \{(i_k,i_s) : (1,0),(1,1),(1,2),(1,-1),(1,-2),(2,0)\} \\ M_u &= \{(i_k,i_s) : (1,0)\}, \end{aligned}$$

*with the index of the output coefficients $(i_k,i_s) \in M_y$, and that of the input coefficients $(i_k,i_s) \in M_u$.*

**Initial and Boundary Conditions**

The solution to a PDE is generally not unique, but depending on its initial and boundary conditions. Thus, additional constraints must be specified on the initial status and domain boundary to obtain a unique solution. The Euler-Bernoulli equation is taken again as an example to illustrate some common boundary conditions.

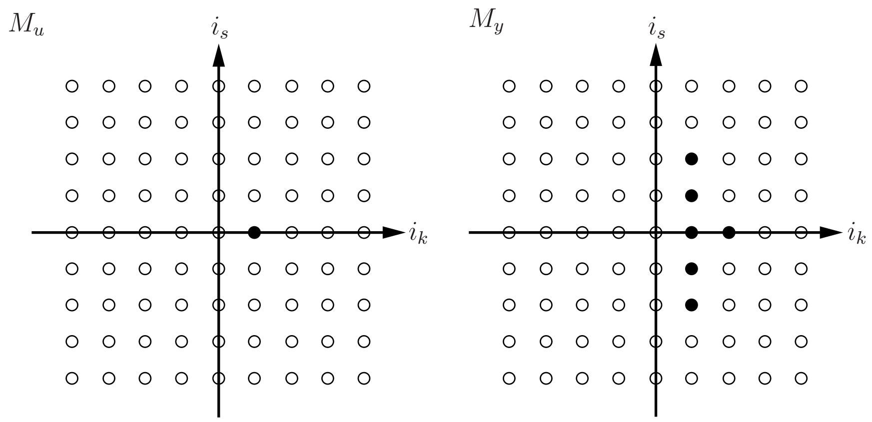


Figure 5.1: Input and output masks resulted from applying the CTCS FD method to solve the Euler-Bernoulli equation

**Example 5.2 (Common Boundary Conditions for the Euler-Bernoulli Equation)** *Denote the beam length as $l$. The boundary conditions for a free-free beam, where no restriction is applied to the boundary subsystems, and for a beam with one clamped end are defined as following:*

- *Free-free boundary condition at boundaries $x = 0, l$*

$$EI\frac{\partial^2 w(t,x)}{\partial x^2}|_{(x=0,l)} = 0, \quad EI\frac{\partial^3 w(t,x)}{\partial x^3}|_{(x=0,l)} = 0. \tag{5.9}$$

- *Clamped at one end, e.g. $x = 0$*

$$w(t,x)|_{(x=0)} = 0, \quad \frac{\partial w(t,x)}{\partial x}|_{(x=0)} = 0. \tag{5.10}$$

### 5.2.2 Two-Dimensional Input/Output Model Structure

Motivated by the two-dimensional difference equation (5.8), the lumped linear ARX model (4.4) has been extended to represent multidimensional systems in [27].

Define $u(k,s)$ as the discrete input signal applied to a two-dimensional discrete SISO data-generating system as shown in Fig. 5.2. The input/output dynamics of the plant model and the noise model take the form

$$A(q_t,q_s)y_0(k,s) = B(q_t,q_s)u(k,s) \tag{5.11}$$
$$A(q_t,q_s)v(k,s) = e(k,s), \tag{5.12}$$

where $e(k,s)$ represents a two-dimensional Gaussian white noise signal with zero mean, and $v(k,s)$ the filtered noise.

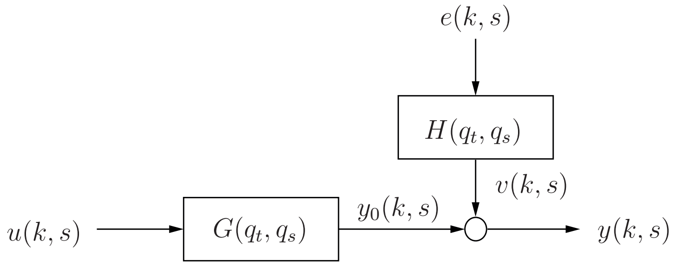


Figure 5.2: Two-dimensional ARX model structure

The polynomials $A$ and $B$ are

$$A(q_t, q_s) = 1 + \sum_{(i_k,i_s)\in M_y} a_{(i_k,i_s)} q_t^{-i_k} q_s^{-i_s} \tag{5.13}$$

$$B(q_t, q_s) = \sum_{(i_k,i_s)\in M_u} b_{(i_k,i_s)} q_t^{-i_k} q_s^{-i_s}, \tag{5.14}$$

where $q_t$ and $q_s$ are the temporal- and spatial-shift operators, respectively, e.g.

$$q_t^{-1} q_s^2 u(k,s) = u(k-1, s+2).$$

Given the predefined output and input masks $M_y$ and $M_u$—the so-called support regions in multidimensional digital signal processing [70], coefficients $a_{(i_k,i_s)}$ and $b_{(i_k,i_s)}$ impose weights on the respective outputs and inputs. Since a spatially-distributed system is causal in time and non-causal in space, the support region must be a subset of the first and fourth quadrants.

Insert (5.13)-(5.14) in (5.11)-(5.12). The output of subsystem $s$ at time instant $k$, i.e. $y(k,s)$, is determined by the difference equation

$$y(k,s) = -\sum_{(i_k,i_s)\in M_y} a_{(i_k,i_s)} y(k-i_k, s-i_s) + \sum_{(i_k,i_s)\in M_u} b_{(i_k,i_s)} u(k-i_k, s-i_s) + e(k,s), \tag{5.15}$$

which is a general form of (5.8). It defines the dynamics of a distributed system on a single subsystem of a small order, which can be easily reformulated in the form of the desired multidimensional state space model (2.9), once the input and output masks have been properly selected and the coefficients have been estimated. Taking (5.15) as the mathematical model for the distributed identification, Sections 5.3 and 5.4 present two identification techniques, as well as their experimental validation.

## 5.3 Black-Box Identification

As stated in Chapter 2, distributed systems consist of an array of interconnected subsystems. Let (5.15) represent the governing difference equation of subsystem $s$. The black-box identification problem can be formulated as: Given the model structure (5.15) and measured input and output data sequences $\{u(k,s), y(k,s)\}$, $k = 1, \ldots, N_k$, $s = 1, \ldots, N_s$, where $N_k$ and $N_s$ are the sizes of temporal and spatial measurements, respectively, find the proper input and output masks $M_u$ and $M_y$, and estimate their corresponding coefficients $b_{(i_k,i_s)}$ and $a_{(i_k,i_s)}$, such that the cost function

$$J = \sum_{s=1}^{N_s} \sum_{k=1}^{N_k} (y(k,s) - \hat{y}(k,s))^2 \tag{5.16}$$

is minimized, where $\hat{y}(k,s)$ denotes the estimated output.

This section considers not only the identification of LTSI models, but also spatial LPV models for systems with spatially-varying features. In [27], the simplest least-squares method is employed to identify a parametric model of an LTSI system. The identification of a spatial LPV model is presented in [29] by extending the input/output identification techniques for temporal LPV systems. Accounting for the precence of colored noise, techniques for improved identification are developed in [71], [72] and [73]. This section focuses on the application of the simplest least-squares based techniques developed in [27] and [29] for the identification of LTSI and spatial LPV models, respectively.

### 5.3.1 Identification of LTSI Models

LTSI models are used to represent distributed systems comprised of a number of identical subsystems, thus having identical coefficients $a_{(i_k,i_s)}$ and $b_{(i_k,i_s)}$ in (5.15) for all subsystems.

The input and output masks $M_u$ and $M_y$ are often unknown before the identification procedure is complete; they need to be updated by comparing various configurations. Provided an initial choice of the masks, the output can be estimated by rewriting the difference equation (5.15) into regressor form as

$$\hat{y}(k,s) = \phi^T(k,s)p, \tag{5.17}$$

where the parameter vector

$$p = \begin{bmatrix} \left[\ \mathrm{cat}_{i_k}\mathrm{cat}_{i_s} a_{(i_k,i_s)}\ \right]_{(i_k,i_s)\in M^y} \\ \left[\ \mathrm{cat}_{i_k}\mathrm{cat}_{i_s} b_{(i_k,i_s)}\ \right]_{(i_k,i_s)\in M^u} \end{bmatrix} \in \mathbb{R}^{n_p} \tag{5.18}$$

contains unknown coefficients. The symbol $\mathrm{cat}_{i_k}\mathrm{cat}_{i_s}$ means the concatenation of coefficients $a_{(i_k,i_s)}$ and $b_{(i_k,i_s)}$ with respect to $i_k$ and $i_s$ as a vector, with $(i_k, i_s)$ subject to sets $M^y$ and $M^u$, respectively. In the Euler-Bernoulli equation example, we have

$$p = [a_{(1,-2)}, a_{(1,-1)}, a_{(1,0)}, a_{(1,1)}, a_{(1,2)}, a_{(2,0)}, b_{(1,0)}]^T. \tag{5.19}$$

The data vector

$$\phi(k,s) = \begin{bmatrix} \left[\ -\mathrm{cat}_{i_k}\mathrm{cat}_{i_s} y(k-i_k, s-i_s)\ \right]_{(i_k,i_s)\in M^y} \\ \left[\ \mathrm{cat}_{i_k}\mathrm{cat}_{i_s} u(k-i_k, s-i_s)\ \right]_{(i_k,i_s)\in M^u} \end{bmatrix} \in \mathbb{R}^{n_\phi} \tag{5.20}$$

($n_\phi = n_p$ in this case) collects the measured input and output data indexed by chosen masks as well. The data vector corresponding to the parameter vector (5.19) is written as

$$\phi(k,s) = [-y(k-1,s+2), -y(k-1,s+1), -y(k-1,s), -y(k-1,s-1), \\ -y(k-1,s-2), -y(k-2,s), u(k-1,s)]^T.$$

The output vector $Y \in \mathbb{R}^{N_k N_s}$ and the regressor matrix $\Phi \in \mathbb{R}^{N_k N_s \times n_p}$ contain measurements at all temporal and spatial instants as

$$Y = [y(1,1), \cdots, y(N_k,1) \cdots, y(1,N_s), \cdots, y(N_k,N_s)]^T$$
$$\Phi = [\phi(1,1), \cdots, \phi(N_k,1) \cdots, \phi(1,N_s), \cdots, \phi(N_k,N_s)]^T.$$

The parameter vector $p$ that minimizes the cost function (5.16) is then computed as

$$p = (\Phi^T\Phi)^{-1}\Phi^T Y. \tag{5.21}$$

The masks can be modified after each trial, until a satisfactory estimation is achieved.

*Remarks*:

- The simplest least-squares based technique assumes white noise in the measured output, which may lead to a bias when coloured noise is present. Based on the initial results obtained using the least-squares method, an instrumental variable method can be then applied to obtain unbiased estimates. The reader is referred to [71] for a detailed discussion.
- The identification of a more realistic noise model having a Box-Jenkins structure instead of an ARX structure is proposed in [72].

### 5.3.2 Reasons to Use Spatial LPV Models

In [8], distributed systems comprised of either periodic or infinite interconnections of identical subsystems, are considered to be LTSI. In real applications, a system of an infinite length does not exist. Moreover, the building subsystems often do not share uniform physical properties. Examples are shown in Fig. 5.3 (a) for subsystems of various lengths, in (b) for subsystems of various thicknesses, and in (c) for subsystems of various widths. Those systems violate the assumption of an LTSI model. With the extension of temporal LPV notations to spatially-interconnected systems, spatial LPV models can be used to capture the spatially-varying dynamics, and still allow working in the distributed systems framework.

### 5.3.3 Identification of Spatial LPV Models

The mathematical model (5.15) can be applied not only to LTSI systems, but also to time/space-varying systems, if coefficients $a_{(i_k,i_s)}$ and $b_{(i_k,i_s)}$ are allowed to vary with respect to time and/or space. In this work, only spatially-varying systems are considered,

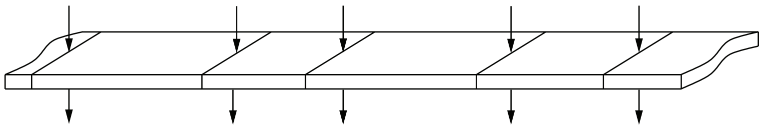


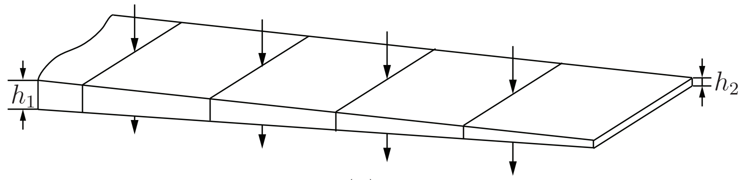


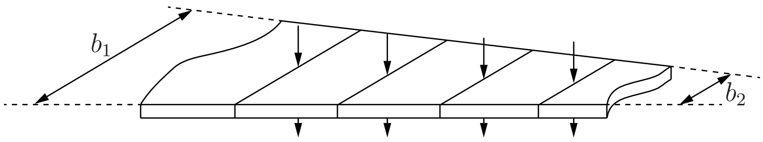


Figure 5.3: Examples of spatially-varying models: (a) subsystems of various lengths; (b) subsystems of various thicknesses; (c) subsystems of various widths.

i.e. coefficients are functions of spatial scheduling parameters $\theta_s$. In general, the dependence functions can be any smooth functions [74]. Assume that coefficients in (5.15) are polynomial functions of $\theta_s$ up to degree $m$ as

$$a_{(i_k,i_s)}(\theta_s) = \sum_{j=0}^{m} \alpha_{(i_k,i_s,j)}(\theta_s)^j \tag{5.22}$$

$$b_{(i_k,i_s)}(\theta_s) = \sum_{j=0}^{m} \beta_{(i_k,i_s,j)}(\theta_s)^j, \tag{5.23}$$

where $\alpha_{(i_k,i_s,j)}$ and $\beta_{(i_k,i_s,j)}$ $(j = 0, \cdots, m)$ are real constants to be estimated. The degree $m$, as well as input and output masks $M_u$ and $M_y$ are pre-defined variables, and to be updated after each trial. It should be self-evident, that the superscript $j$ in $(\theta_s)^j$ denotes the exponent, in $\theta_s^j$ the $j$-th spatial operating point.

Define a vector $\tau$ that consists of the powers of the scheduling parameters as

$$\tau = [1, \theta_s, \cdots, (\theta_s)^m]^T.$$

The counterpart of (5.17) for a spatial LPV model is written as

$$\hat{y}(k,s) = (\phi(k,s) \otimes \tau)^T \tilde{p}, \tag{5.24}$$

where $\phi(k,s) \in \mathbb{R}^{n_\phi}$ is defined in the same way as in (5.20). The parameter vector $\tilde{p} \in \mathbb{R}^{n_{\tilde{p}}}$ $(n_{\tilde{p}} = n_\phi(m+1))$ contains the unknown coefficients of polynomials $\alpha_{(i_k,i_s,j)}$ and $\beta_{(i_k,i_s,j)}$

as

$$\tilde{p} = \begin{bmatrix} \left[\ \mathrm{cat}_{i_k}\mathrm{cat}_{i_s}\mathrm{cat}_j\alpha_{(i_k,i_s,j)}\ \right]_{j=0:m,(i_k,i_s)\in M_y} \\ \left[\ \mathrm{cat}_{i_k}\mathrm{cat}_{i_s}\mathrm{cat}_j\beta_{(i_k,i_s,j)}\ \right]_{j=0:m,(i_k,i_s)\in M_u} \end{bmatrix}. \tag{5.25}$$

Introduce a new regressor vector $\eta(k,s) = \phi(k,s) \otimes \tau$, $\eta(k,s) \in \mathbb{R}^{n_{\tilde{p}}}$. The output vector $Y \in \mathbb{R}^{N_k N_s}$ and the regressor matrix $H \in \mathbb{R}^{N_k N_s \times n_{\tilde{p}}}$ are constructed from measurements as

$$\begin{aligned} Y &= [y(1,1), \cdots, y(N_k,1), \cdots, y(1,N_s), \cdots, y(N_k,N_s)]^T \\ H &= [\eta(1,1), \cdots, \eta(N_k,1), \cdots, \eta(1,N_s), \cdots, \eta(N_k,N_s)]^T. \end{aligned}$$

The parameter vector $\tilde{p}$ that minimizes the cost function (5.16) is then computed as

$$\tilde{p} = (HH^T)^{-1}HY. \tag{5.26}$$

*Remark:*

- Compared to the local approach for the LPV identification discussed in Chapter 4, which relies on the individual excitation of a single subsystem, the identification techniques presented here are considered as a global approach, due to the fact that all subsystems (or the spatial operating points) are excited simultaneously in one single experiment.

### 5.3.4 Experimental Identification

The experimental validation of black-box identification techniques for both LTSI and spatial LPV models is performed on the long test structure described in Section 1.1.2. 16 pairs of collocated actuators and sensors attached on the beam surface induce 16 spatially-discretized subsystems. The equal distances between two neighbouring pairs and the uniform physical properties of the structure suggest 16 identical subsystems, each equipped with sensing and actuating capabilities. The free-free boundary condition is assumed, when no restriction is applied at the beam ends. To test the identification technique for spatial LPV models, the same testbed can still be employed by intentionally deactivating a couple of actuator/sensor pairs at arbitrary locations. The resulting subsystems are not identical any more but spatially-varying due to varying distances between actuator/sensor pairs as shown in Fig. 5.3 (a).

**Identification of LTSI Models**

Identification experiments are performed by actuating the 16 actuators simultaneously with 16 out-of-phase chirp signals up to 15 Hz, which cover the first 6 resonant modes, i.e. $\omega = [1.22, 1.968, 3.357, 5.249, 8.362, 11.29]$ Hz. The sampling time is chosen as $\Delta T = 0.001$ s. After trial and error, the proper input and output masks are determined as shown in Fig. 5.4.

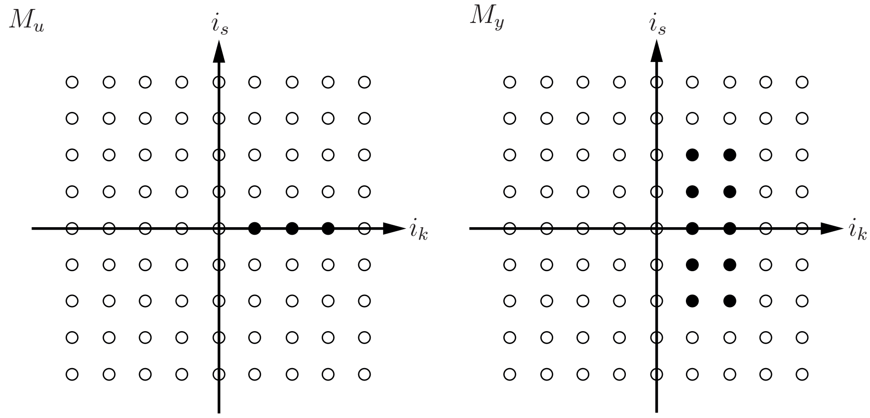


Figure 5.4: Input and output masks for the experimentally identified LTSI model using black-box identification

The comparison of the simulated and measured output voltages at 4 selected sensors is shown in Fig. 5.5, when the structure is excited by the same 16 (non-identical) noise signals as the ones used in Fig. 3.14. A good match between the identified model and the measurements can be observed.

**Identification of Spatial LPV Models**

Instead of the full usage of 16 actuator/sensor pairs, 6 pairs of them – pairs 3, 5, 9, 10, 12, 15 – are deactivated on purpose to allow varying distances between any two neighbouring subsystems. The resulting test structure exhibits spatially-varying properties.

The spatial coordinates of the remaining 10 pairs are

$$s = [0.15, 0.45, 1.05, 1.65, 1.95, 2.25, 3.15, 3.75, 4.05, 4.65] \quad \text{m}.$$

It is natural here to define the spatial coordinates as the spatial operating points, i.e. $\theta_s^i = s_i$ $(i = 1, \ldots, 10)$, after scaling the range down to [-1, 1]. Let $a_{(i_k,i_s)}(\theta_s)$ and $b_{(i_k,i_s)}(\theta_s)$ be first order polynomial functions of $\theta_s$. The proper input and output masks as shown in Fig. 5.6 are chosen. Fig. 5.7 shows the comparison of the simulated and measured output voltages at 4 piezo sensors, given 10 (non-identical) noise signals exciting the activated 10 piezo actuators. Although the identified spatial LPV model can follow the general trend of the structural behaviour to a certain extent, there is clearly still room for further improvement.

## 5.4 Identification based on the FE Modelling Results

Black-box identification is a quick and computationally efficient solution to identify a model from measurements based on its input/output behaviour. The experimental validation in Section 5.3.4 demonstrates that the identified models capture the structural dynamics to a certain extent, and also shows their difficulties in the identification around resonant frequencies. To improve the model accuracy, as well as the model-based controller

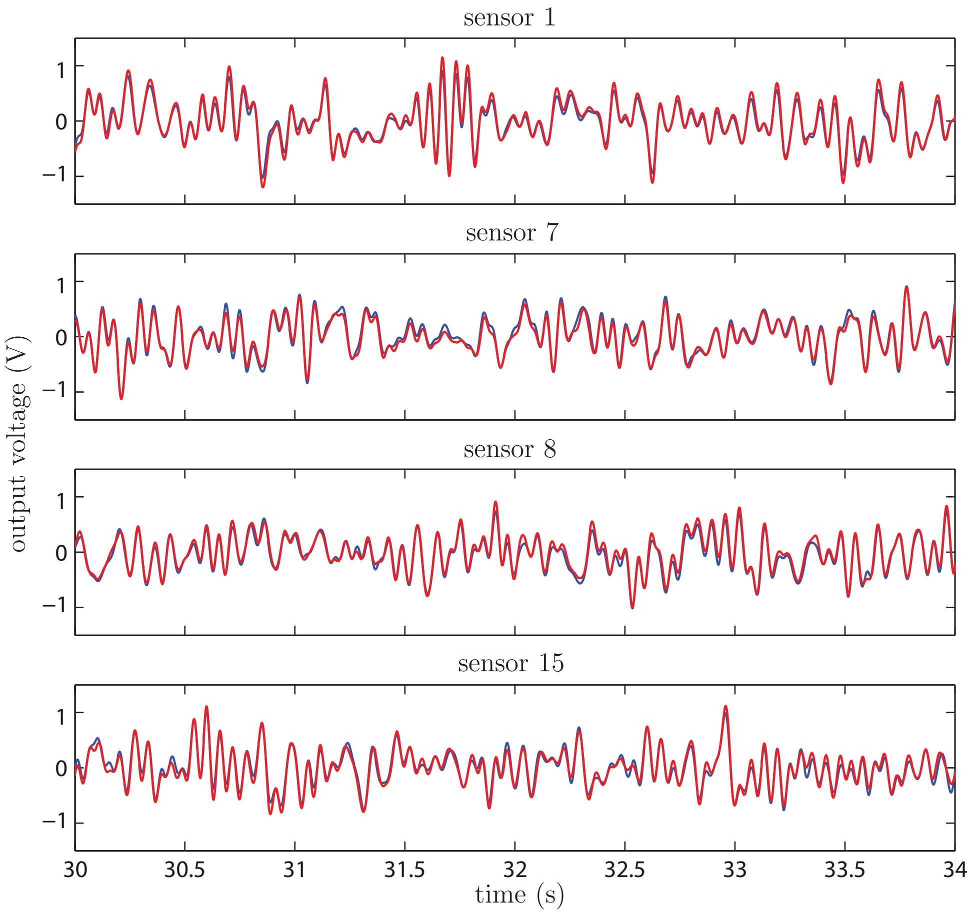


Figure 5.5: Comparison of the black-box simulated (blue) and measured (red) output voltages at 4 selected piezo sensors, given 16 (non-identical) noise signals exciting 16 piezo actuators simultaneously.

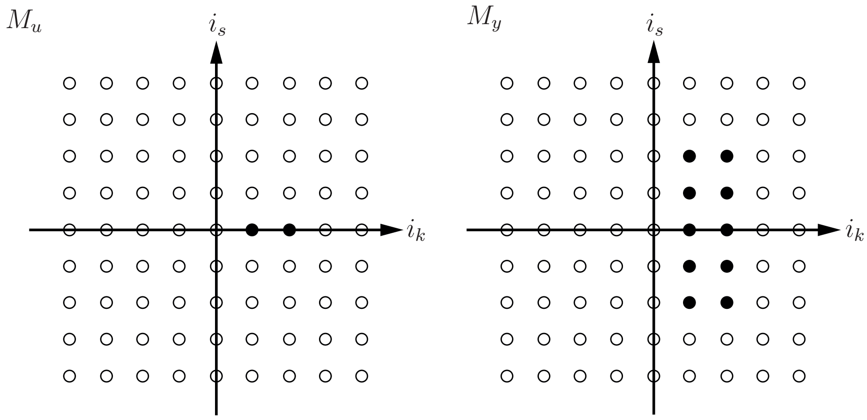


Figure 5.6: Input and output masks for the experimentally identified spatial LPV model using black-box identification

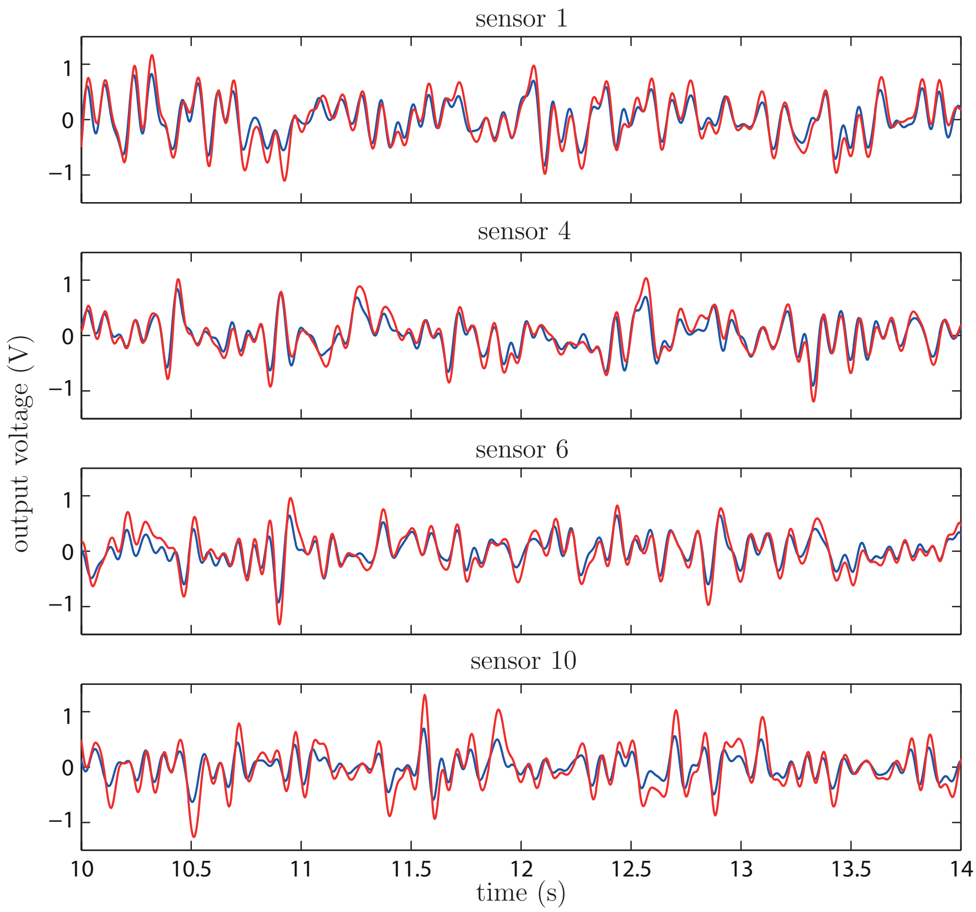


Figure 5.7: Comparison of the black-box simulated (blue) and measured (red) output voltages at 4 selected piezo sensors, given 10 noise signals exciting 10 piezo actuators simultaneously.

performance at a later stage (in Chapter 6), an alternative identification technique, that explores the physical meaning of the structure, and preserves the desired input/output model structure (5.15), is proposed in this section with the use of the FE modelling results achieved in Chapter 3.

It has been discussed that, although the obtained FE model exhibits a satisfactory performance in capturing the structural dynamics, it is generally not suitable for the further controller synthesis due to its large order and lumped structure. However, if it is possible to extract a distributed model in the form of (5.15) from the FE model, this may lead to a more accurate alternative to black-box identification.

Taking the physical properties of the test structure into consideration, Section 5.4.1 derives the input and output masks from its governing PDE. Provided the selected masks, Section 5.4.2 identifies the LTSI model by first constructing a 'lifted' state space model, then estimating coefficients $a_{(i_k,i_s)}$ and $b_{(i_k,i_s)}$ via exploiting the FE model obtained in Chapter 3. Section 5.4.3 follows a similar procedure to identify a spatial LPV model.

### 5.4.1 PDE-Based Selection of Masks

The Euler-Bernoulli equation (5.5) establishes the linear relationship between external forces and transverse displacements under Euler-Bernoulli beam theory. Recall the functionality of piezo patches as actuator and sensor described in Chapter 3: when the patch is used as an actuator, the input voltage is proportional to a pair of concentrated torques applied at the two electrode ends; as a sensor, the output voltage is proportional to the difference of the slopes at the two electrode ends. Thus (5.5) can not be taken directly as the governing PDE of the test structure. Nevertheless, it is possible to bring (5.5) into a shape that approximates this specific application.

First of all, the external force $f(k, s)$ can be approximated by $f \approx M_p''$ to bring the torque into the PDE as

$$EI\frac{\partial^4 w(t,x)}{\partial x^4} + \rho A\frac{\partial^2 w(t,x)}{\partial t^2} = \frac{\partial^2 M_p(t,x)}{\partial x^2}. \tag{5.27}$$

Differentiating both sides of (5.27) twice with respect to $x$ yields

$$EI\frac{\partial^4}{\partial x^4}(\frac{\partial^2 w(t,x)}{\partial x^2}) + \rho A\frac{\partial^2}{\partial t^2}(\frac{\partial^2 w(t,x)}{\partial x^2}) = \frac{\partial^4 M_p(t,x)}{\partial x^4}. \tag{5.28}$$

Knowing that the second local derivative of the transverse displacement approximates the curvature $\kappa$, i.e. $\kappa \approx w''$, (5.28) can then be expressed with respect to torque and curvature as

$$EI\frac{\partial^4 \kappa(t,x)}{\partial x^4} + \rho A\frac{\partial^2 \kappa(t,x)}{\partial t^2} = \frac{\partial^4 M_p(t,x)}{\partial x^4}. \tag{5.29}$$

Assume that the curvature $\kappa$ approximates the difference of the slopes, when the distance between two electrode ends – in other words, the length of a piezo patch – is small enough, i.e. $\kappa \approx w'' \approx \frac{w_a' - w_b'}{x_a - x_b}$, where $x_a$ and $x_b$ are the $x$ coordinates of the two electrode boundaries $a$ and $b$, respectively. Given the linear relationship between the output voltage $\phi_o$ and the difference of the slopes at the two electrode ends, i.e. $\phi_o = g_s(w_a' - w_b')$, $\phi_o$ is approximately proportional to the curvature $\kappa$ as well. Hence, a piezo pair of originally two nodes can be treated as a single node as shown in Fig. 5.8, where the input voltage $\phi_i$ is proportional to the applied torque $M_p$, while the output voltage $\phi_o$ approximates the curvature at the center of the electrodes.

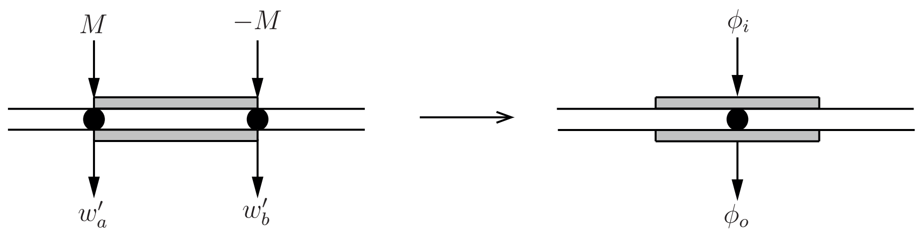


Figure 5.8: Two electrode nodes are approximated by one node with a single input (input voltage) and single output (output voltage) at the center of the electrodes

The CTCS FD method can be applied to (5.29) to solve for $\kappa(k,s)$. The input and output masks are shown in Fig. 5.9 with coefficients $a_{(1,2)} = a_{(1,-2)} = c_a$, $a_{(1,1)} = a_{(1,-1)} = -4c_a$, $a_{(1,0)} = -2 + 6c_a$, $a_{(2,0)} = 1$, $b_{(1,2)} = b_{(1,-2)} = c_b$, $b_{(1,1)} = b_{(1,-1)} = -4c_b$, and $b_{(1,0)} = 6c_b$, where $c_a = \frac{\Delta T^2 EI}{\Delta X^4 \rho A_o}$, and $c_b = \frac{\Delta T^2}{\Delta X^4 \rho A_o}$.

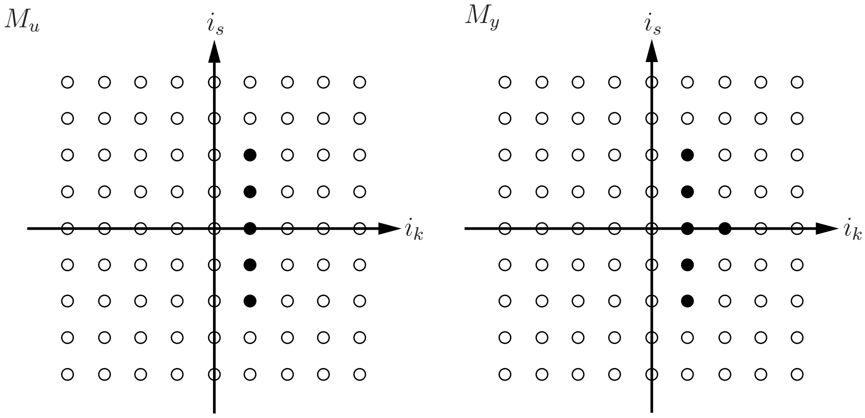


Figure 5.9: Input and output masks obtained by applying the CTCS FD method to solve PDE (5.29) with torque as input and curvature as output

Although (5.29) establishes the governing equation of a theoretical beam, with torque as input and curvature as output, aspects that are specific to the test structure and not yet modelled in (5.29) include:

- Damping. A simple proportional damping is assumed during the FE modelling. But the translation from the damped FE model back into its governing PDE is not known. To introduce damping into a PDE, terms that represent various types of energy dissipation mechanisms can be directly added [75], e.g.

$$(a)\alpha_0\frac{\partial\kappa}{\partial t}, \quad (b) - \alpha_1\frac{\partial^3\kappa}{\partial t\partial x^2}, \quad (c)\alpha_2\frac{\partial^5\kappa}{\partial t\partial x^4}, \tag{5.30}$$

  where $\alpha_0$, $\alpha_1$ and $\alpha_2$ are constant damping factors. The damping mechanism depends on the structure configuration and is not known exactly. Any choice of the damping mechanism may bring changes to the undamped input and output masks, and their coefficients accordingly.

- Suspension systems. It is desired that through attaching the test structure to a suspension system comprised of soft springs, the rigid body modes are separated from the the first bending mode by a ratio of 5 to 10 [9], such that the influence of springs on beam dynamics can be ignored. However, it is difficult to build a soft suspension system that fulfils this requirement for the long and thin aluminium beam used here. The computed suspension frequencies are 0.87 Hz and 0.92 Hz, while the first bending mode is 1.22 Hz. The suspension clearly interferes with the structural dynamics at the very low frequency range. Hence, apart from the actuated beam, the suspension system becomes part of the structure to be modelled, which is not included in the theoretical PDE.

To account for the unaddressed issues, an enlarged output mask as shown in Fig. 5.10 suggests a more complex model structure than Fig. 5.9. Both choices of masks in Fig. 5.9 and Fig. 5.10 will be tested and compared for both the LTSI model and the spatial LPV model identification.

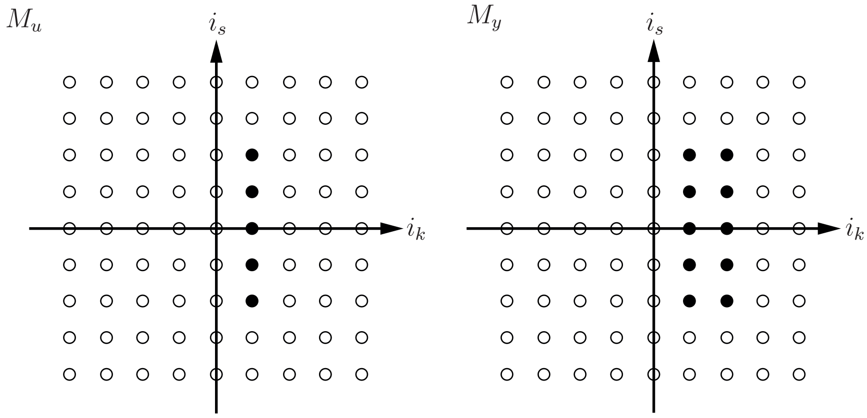


Figure 5.10: Input and (enlarged) output masks for the experimental identification

### 5.4.2 Identification of LTSI Models

With the input and output masks determined, coefficients $a_{(i_k,i_s)}$ and $b_{(i_k,i_s)}$ are constants and identical for all subsystems just like black-box identification. Consider first the masks in Fig. 5.9 and assume a symmetric contribution from the left and the right neighbouring subsystems, i.e. $a_1 = a_{(1,-2)} = a_{(1,2)}$, $a_2 = a_{(1,-1)} = a_{(1,1)}$, $a_3 = a_{(1,0)}$, $a_4 = a_{(2,0)}$, $b_1 = b_{(1,-2)} = b_{(1,2)}$, $b_2 = b_{(1,-1)} = b_{(1,1)}$, and $b_3 = b_{(1,0)}$, where $a_1$, $a_2$, $a_3$, $a_4$, $b_1$, $b_2$, and $b_3$ are coefficients to be estimated. The difference equation in the form of (5.15) is expanded as

$$\begin{aligned} y(k,s) = &- a_1[y(k-1,s-2) + y(k-1,s+2)] - a_2[y(k-1,s-1) + y(k-1,s+1)] \\ &- a_4[y(k-2,s-2) + y(k-2,s+2)] - a_5[y(k-2,s-1) + y(k-2,s+1)] \\ &+ b_1[u(k-1,s-2) + u(k-1,s+2)] + b_2[u(k-1,s-1) + u(k-1,s+1)] \\ &- a_3 y(k-1,s) - a_6 y(k-2,s) + b_3 u(k-1,s). \end{aligned} \tag{5.31}$$

To estimate the unknown coefficients, the FE model obtained in Chapter 3 is involved in the identification procedure as follows:

1. Construct a 'lifted' system. Given the difference equation (5.31), a state space model

of the overall system, or the so called 'lifted' system [76], is realized as

$$\begin{bmatrix} \breve{x}(k+1) \\ \breve{x}(k+2) \\ \hline \breve{y}(k+1) \end{bmatrix} = \left[\begin{array}{cc|c} 0 & I & 0 \\ \breve{A}_{21} & \breve{A}_{22} & \breve{B}_2 \\ \hline 0 & I & \breve{D} \end{array}\right] \begin{bmatrix} \breve{x}(k) \\ \breve{x}(k+1) \\ \hline \breve{u}(k+1) \end{bmatrix}. \tag{5.32}$$

The overhead $\breve{}$ indicates signals or system matrices of a lifted system. The state vector $\breve{x}(k)$ and the input vector $\breve{u}(k)$ contain the outputs and inputs of all 16 subsystems at time $k$ as

$$\breve{x}(k) = [y(k,1), y(k,2), \ldots, y(k,16)]^T,$$
$$\breve{u}(k) = [u(k,1), u(k,2), \ldots, u(k,16)]^T.$$

The system matrices $\breve{A}_{21}$, $\breve{A}_{22}$ and $\breve{B}_2$ retrieve the difference equation (5.31) at 16 spatial locations; each has the structure of a Toeplitz matrix as

$$\breve{A}_{21} = \begin{bmatrix} -a_4 & & & & & & \\ & -a_4 & & & & & \\ & & -a_4 & & & & \\ & & & -a_4 & & & \\ & & & & \ddots & & \\ & & & & & -a_4 & \\ & & & & & & -a_4 \end{bmatrix}, \breve{A}_{22} = \begin{bmatrix} -a_3 & -a_2 & -a_1 & & & & & & \\ -a_2 & -a_3 & -a_2 & -a_1 & & & & & \\ -a_1 & -a_2 & -a_3 & -a_2 & -a_1 & & & & \\ & -a_1 & -a_2 & -a_3 & -a_2 & -a_1 & & & \\ & & & & & \ddots & & & \\ & & & & & -a_1 & -a_2 & -a_3 & -a_2 \\ & & & & & & -a_1 & -a_2 & -a_3 \end{bmatrix}$$

$$\breve{B}_2 = \begin{bmatrix} b_3 & b_2 & b_1 & & & & & \\ b_2 & b_3 & b_2 & b_1 & & & & \\ b_1 & b_2 & b_3 & b_2 & b_1 & & & \\ & b_1 & b_2 & b_3 & b_2 & b_1 & & \\ & & & & \ddots & & & \\ & & & & b_2 & b_3 & b_2 & b_1 \\ & & & & & b_3 & b_2 & b_1 \end{bmatrix}. \tag{5.33}$$

The lifted state space model (5.32) differs from the multidimensional state space model (2.9) in the sense that (2.9) defines the system dynamics on an individual subsystem, where the exchange of information among subsystems is modelled as spatial states, whereas the lifted system (5.32) represents the overall dynamics as a MIMO LTI system, containing only temporal states.

2. Identify the system matrix $\breve{A} := \begin{bmatrix} 0 & I \\ \breve{A}_{21} & \breve{A}_{22} \end{bmatrix}$ using the Levenberg-Marquardt method [58] [77]. The dynamic properties of a system are determined by the eigenvalues of the system matrix, here $\breve{A}$. From a physical point of view, complex eigenvalues of the system matrix of a flexible structure determine the resonant frequencies, as well as damping factors at resonant modes. Thus, the system matrix $\breve{A}$ (or more specifically, $a_i$ $(i = 1, \ldots, 4)$) can be estimated by minimizing the difference of the computed eigenvalues between the FE model and the lifted system, without any

impact from the input matrix. Modes at low frequencies are considered to be more important than the high frequencies modes. Thus, higher weights are imposed on the low frequency modes during the identification. Fig. 5.11 shows the comparison of the first 10 resonant frequencies between the FE model and the estimated system matrix $\breve{A}$. Though modes start to diverge above the 8th mode, an accurate match below 15 Hz suggests a satisfactory estimation.

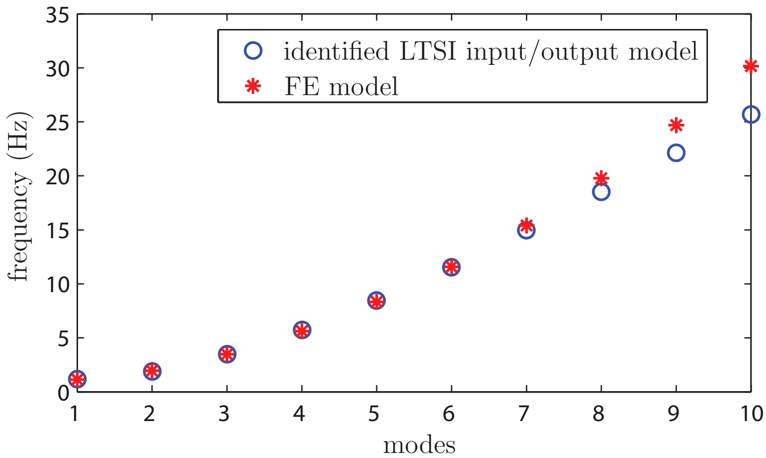


Figure 5.11: Comparison of the first 10 resonant frequencies between the identified lifted system and the FE model

3. Identify the input matrix $\breve{B} := [0 \quad \breve{B}_2^T]^T$. After the coefficients $a_i$ $(i = 1, \ldots, 4)$ in $\breve{A}$ have been determined, coefficients $b_j$ $(j = 1, \ldots, 3)$ can be estimated in either time or frequency domain. Here, coefficients $b_j$ are estimated by minimizing the difference of the computed FRFs between the lifted system and the FE model. Applying a chirp excitation at the 8th actuator, the comparison of the FRFs between the identified lifted system, the FE model and real measurements is shown in Fig. 5.12. Up to 15 Hz, a good agreement of the identified lifted system (or equivalently, the two-dimensional input/output model) with the FE model can be observed. The discrepancies compared to the real measurements have not been captured by the FE model, and therefore neither by the distributed input/output model.

*Remark:*

- In Section 3.5.4, a slight variation in the feed-through properties among 16 collocated piezo pairs has been observed, which implies a varying feed-through constant from subsystem to subsystem. By individually identifying the feed-through constant at each collocated pair could result in a more accurate plant model. However, the assumption of an LTSI model – the interconnected subsystems are identical – is then obviously violated. At the price of a slightly deteriorated accuracy, a feed-through constant that applies to all the subsystems and minimizes the average deviations is employed here, i.e. $\breve{D} = b_0 I$, where $I \in \mathbb{R}^{16\times16}$, and $b_0$ is the feed-through constant.

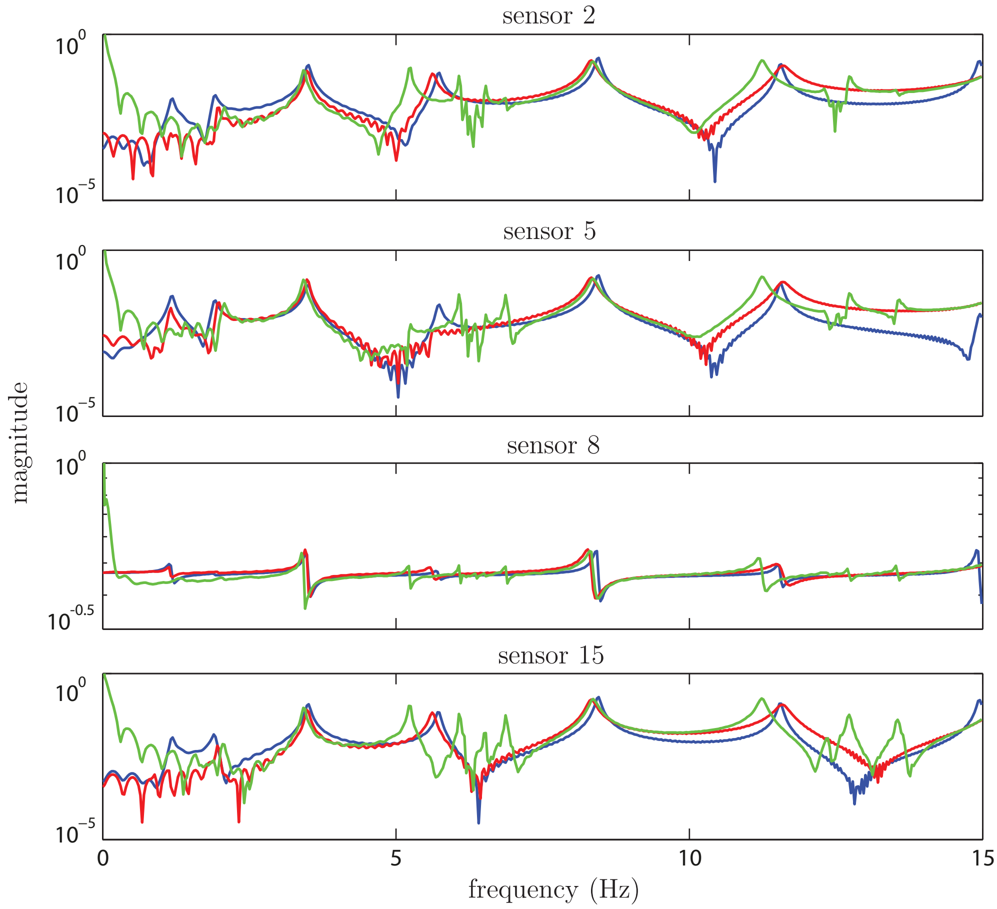


Figure 5.12: Comparison of the transfer FRFs at 4 selected sensors given a chirp excitation at the 8th actuator. The blue and red curves are computed from the identified lifted system and the FE model, respectively, whereas the green curves are from the real measurements.

### 5.4.3 Identification of Spatial LPV Models

The hardware configuration used in Section 5.3.4 to construct a spatially-varying system applies here as well. The identification of a spatial LPV model follows the same line as in Section 5.4.2, except that the coefficients $a_{(i_k,i_s)}$ and $b_{(i_k,i_s)}$ are now first order polynomial functions of spatial scheduling parameters $\theta_s \in [-1\ 1]$ as defined in (5.23), where $\alpha_{(i_k,i_s,j)}$ and $\beta_{(i_k,i_s,j)}$ are the coefficients to be estimated. Due to the non-uniform profiles of subsystems, the symmetry property of contributions made by the mirrored left and right neighbours is lost.

The lifted system in the form of (5.32) and the input and output masks in Fig. 5.9 apply to the spatial LPV model, except that matrices $\breve{A}_{21}$, $\breve{A}_{22}$ and $\breve{B}_2$ are now parameter-varying and constructed as

$$\breve{A}_{21}(\theta_s) = \begin{bmatrix} -a_{(2,0)}(\theta_s^1) & & & & \\ & -a_{(2,0)}(\theta_s^2) & & & \\ & & -a_{(2,0)}(\theta_s^3) & & \\ & & & \ddots & \\ & & & & -a_{(2,0)}(\theta_s^{10}) \end{bmatrix}$$

$$\breve{A}_{22}(\theta_s) = \begin{bmatrix} -a_{(1,0)}(\theta_s^1) & -a_{(1,-1)}(\theta_s^1) & -a_{(1,-2)}(\theta_s^1) & & & \\ -a_{(1,1)}(\theta_s^2) & -a_{(1,0)}(\theta_s^2) & -a_{(1,-1)}(\theta_s^2) & -a_{(1,-2)}(\theta_s^2) & & \\ -a_{(1,2)}(\theta_s^3) & -a_{(1,1)}(\theta_s^3) & -a_{(1,0)}(\theta_s^3) & -a_{(1,-1)}(\theta_s^3) & -a_{(1,-2)}(\theta_s^3) & \\ & & & & \ddots & \\ & & & -a_{(1,2)}(\theta_s^{10}) & -a_{(1,1)}(\theta_s^{10}) & -a_{(1,0)}(\theta_s^{10}) \end{bmatrix}$$

$$\breve{B}_{2}(\theta_s) = \begin{bmatrix} b_{(1,0)}(\theta_s^1) & b_{(1,-1)}(\theta_s^1) & b_{(1,-2)}(\theta_s^1) & & & \\ b_{(1,1)}(\theta_s^2) & b_{(1,0)}(\theta_s^2) & b_{(1,-1)}(\theta_s^2) & b_{(1,-2)}(\theta_s^2) & & \\ b_{(1,2)}(\theta_s^3) & b_{(1,1)}(\theta_s^3) & b_{(1,0)}(\theta_s^3) & b_{(1,-1)}(\theta_s^3) & b_{(1,-2)}(\theta_s^3) & \\ & & & & \ddots & \\ & & & b_{(1,2)}(\theta_s^{10}) & b_{(1,1)}(\theta_s^{10}) & b_{(1,0)}(\theta_s^{10}) \end{bmatrix}.$$

Although the hardware is reconfigured compared to the LTSI model—10 instead of 16 actuator/sensor pairs are actually activated, the test structure itself – the aluminium beam – remain unchanged, and so do the eigenvalues. The system matrix $\breve{A}$ can still be estimated by minimizing the difference of computed eigenvalues between the identified lifted system and the FE model.

Fig. 5.13 shows the comparison of the computed resonant frequencies between the identified LPV model and the FE model. An even better match than in Fig. 5.11 for an LTSI model identification has been achieved. This may be due to the fact that the introduction of more decision variables provides extra degrees of freedom in the estimation. After the $\breve{B}$ matrix being estimated, Fig. 5.14 is generated in the same way as Fig. 5.7. It can be easily seen, that the discrepancies between the simulated and measured subsystem responses in Fig. 5.14 are considerably reduced compared to Fig. 5.7.

*Remarks:*

- Similar procedures have been applied to identify more complex LTSI and spatial LPV models, by employing the enlarged masks in Fig. 5.10. The identification results do not show a significant improvement compared to the identified models using the masks in Fig. 5.9. Keep in mind that the identified models will be used for model-based controller design. Models of smaller sizes are therefore preferred.

- Under the assumption that the governing PDE of a spatially-distributed system is not known accurately, yet its FE model is available (which is realistic, because FE modelling has become a routine process in structural engineering for the analysis of test structures for decades), the proposed identification procedures fill the gap

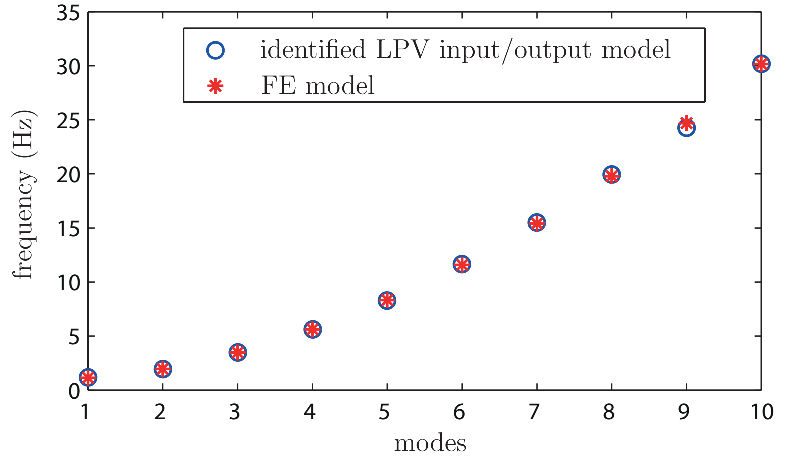


Figure 5.13: Comparison of the first 10 resonant frequencies between the identified LPV model and the FE model

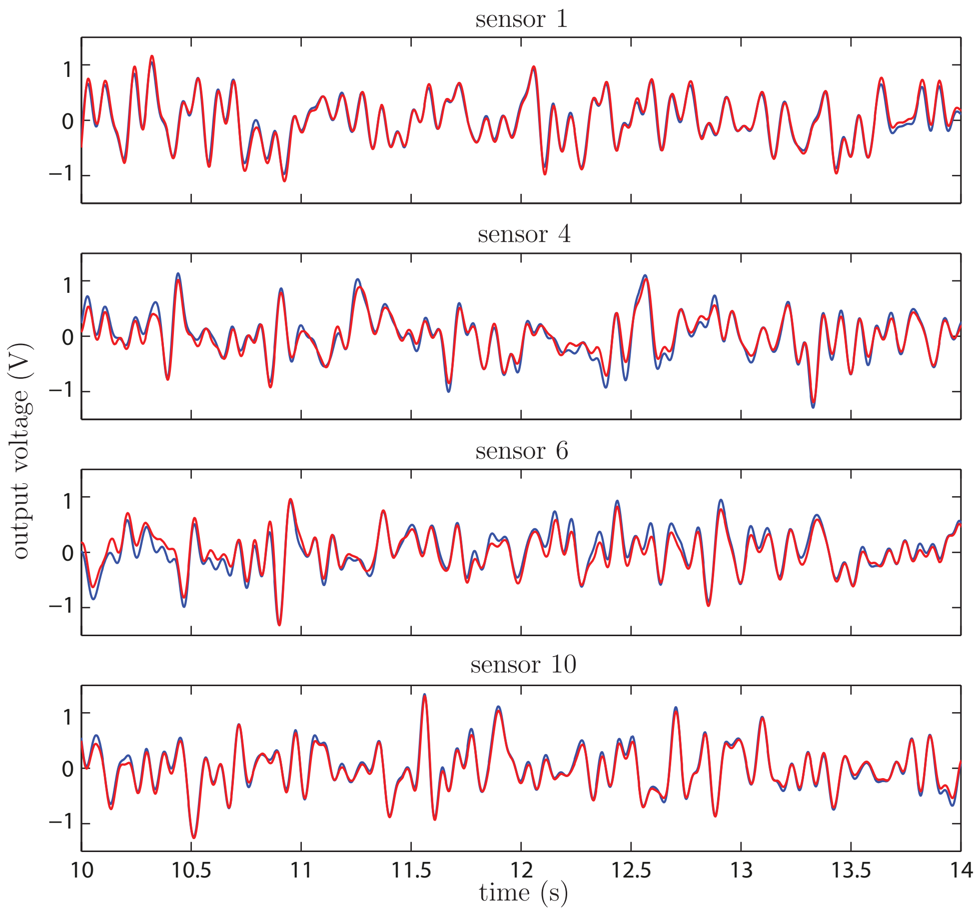


Figure 5.14: Comparison of the FE-based simulated (blue) and measured (red) output voltages at 4 selected piezo sensors, given 10 noise signals exciting 10 piezo actuators simultaneously.

between the FE modelling and distributed identification by extracting distributed models from the FE model.

- The identified input/output models are subject to the accuracy of the FE model. Structural dynamics which are not captured by the FE modelling can not be taken care of by the input/output model either.

## 5.5 Summary

This chapter has dealt with the distributed identification of both LTSI and spatial LPV models. A two-dimensional input/output model derived by applying the FD method to the governing PDE of a beam structure – the Euler-Bernoulli equation – defines the structural dynamics on spatially-discretized subsystems, and preserves the distributed nature of the flexible structure. Its general form is determined as the mathematical model for the distributed identification. The two-dimensional black-box identification techniques have been briefly reviewed and implemented on the test structure. The experimental validation demonstrated that the identified models represent the structural dynamics to a certain extent, but also display their difficulties in capturing the dynamics around resonant frequencies. For this reason, alternative identification procedures have been proposed by extracting distributed models from the FE model, with the desired model structure still maintained. Using the proposed procedures, a considerably improved agreement between measurements and identified models has been achieved in the experimental implementation.

# Chapter 6

# Distributed Controller Design

## 6.1 Introduction

This chapter deals with the controller design for both parameter-invariant and parameter-varying distributed systems. In many cases, a centralized controller fails to efficiently control a distributed system due to a high level of connectivity and computational burden caused by a large number of inputs and outputs. By inheriting the interconnected structure of the plant, distributed controller design at the subsystem level is much easier to handle.

In the last decade, distributed controller design has been studied by various researchers from different perspectives. A novel multidimensional state space framework, that addresses the system analysis and controller synthesis problem based on a single subsystem, has been proposed in [8]. Employing the state space model developed in [8], [30] takes a different path by solving the controller design problem of a 'lifted' system, which describes the overall dynamics by augmenting subsystems, using a sequentially semi-separable approach. Iterative algorithms are employed for a sub-optimal controller synthesis. A decomposition approach is proposed in [31] for interconnected systems, if the system matrices of these systems satisfy a certain structural property. Then it is possible to design a distributed controller which has the same interconnected pattern as the plant. Based on two-dimensional loop shaping concepts, [32] solves the controller design problem of a typical industrial spatially-distributed system – the papermaking machine – through decoupling the large-scale multi-variable system into a family of SISO design problems, one at each spatial frequency. In [78], an efficient and computationally tractable design method to optimize the design parameters of both the plant and the controller in a collocated structural system has been proposed using a norm upper bound approach.

In this work, the controller design problem is addressed in the framework developed in [8]. Given the experimentally identified input/output models in Chapter 5, their multidimensional state space representations are realized first. Analysis and synthesis conditions for the design of both distributed and decentralized controllers for LTSI systems are provided. The LPV control technique for lumped systems has been extended to address spatio-temporal systems in [21] using CLFs, under the assumption of an LFT-based dependence of the state space model on scheduling parameters. To reduce the conservatism incurred by the use of CLFs for parameter-varying systems with bounded variation rates, analysis and synthesis conditions using PDLFs for lumped systems are extended here to parameter-varying distributed systems. Experimental results validate the controller performance in terms of output disturbance rejection.

This chapter includes results reported in [79] and [80]. It is organized as follows: Section 6.2 converts the identified LTSI and spatial LPV input/output models into their state space representations. Section 6.3 presents a procedure for the construction of multidimensional generalized plants. Synthesis conditions for LTSI distributed controllers developed in [8] are recapped in Section 6.4, whereas conditions for decentralized controller design are provided in Section 6.4.2, with their performance evaluated experimentally in Section 6.4.3. The LPV controller design for time/space-varying systems is discussed in Section 6.5. Conditions for distributed LPV controller design using CLFs – less conservative than [21] – are given in Section 6.5.1. To further reduce the conservatism when an upper bound on the variation rate of scheduling parameters is known, the LPV control technique using PDLFs is extended from lumped systems to distributed systems in Section 6.5.2. Experimental results of closed-loop systems with controllers designed using both CLFs and PDLFs are demonstrated in Section 6.5.3.

## 6.2 Multidimensional State Space Realization

It has been justified in Chapter 5, that the test structure considered in this work can be described using a two-dimensional input/output model. A model-based controller can either be designed in input/output form of a fixed structure ([81], [82]), or in a state space framework. In this work, system analysis and controller synthesis are realized in state space framework. In order to apply the state-space based synthesis tools developed in [8], the realization of the identified input/output models into their multidimensional state space representations in the form of (2.9) is first required. The simple Euler-Bernoulli equation in Example 5.1 is used as an example here to illustrate the general procedures in multidimensional state space realization.

**Example 6.1 (State Space Realization of the Euler-Bernoulli Equation)** *After applying the FD method, the solution of the PDE (5.5) can be approximated by the difference equation (5.6). It states that the output of subsystem $s$ at time $k$ – $y(k,s)$ – is determined by the outputs of itself at time $k-1$ and $k-2$, the outputs of its neighbours $s-2$, $s-1$, $s+1$ and $s+2$ at time $k-1$, and its own input at $k-1$.*

*Follow the routines of constructing a lumped state space model in controller canonical form. Define the transverse displacement as output $y(k,s) = w(k,s)$, and the applied force as input $u(k,s) = f(k,s)$. The difference equation implies its transfer function model*

$$\frac{Y}{U} = \frac{B(q_t,q_s)}{A(q_t,q_s)} = \frac{b_{(1,0)}q_t}{q_t^2 + a_{(1,-2)}q_tq_s^2 + a_{(1,-1)}q_tq_s + a_{(1,0)}q_t + a_{(1,1)}q_tq_s^{-1} + a_{(1,2)}q_tq_s^{-2} + a_{(2,0)}}. \tag{6.1}$$

*Define a new variable* $V(q_t, q_s)$*, such that*

$$U = AV, \quad Y = BV, \tag{6.2}$$

*where* $U = AV$ *yields the input equation*

$$\begin{aligned} v(k+2,s) = &- a_{(1,-2)}v(k+1,s+2) - a_{(1,-1)}v(k+1,s+1) - a_{(1,0)}v(k+1,s) \\ &- a_{(1,1)}v(k+1,s-1) - a_{(1,2)}v(k+1,s-2) - a_{(2,0)}v(k,s) + u(k,s), \end{aligned}$$

*and* $Y = BV$ *the output equation*

$$y(k,s) = b_{(1,0)}v(k+1,s).$$

*Let the temporal state, and the positive and negative spatial state vectors be selected as*

$$x_t = \begin{bmatrix} v(k,s) \\ v(k+1,s) \end{bmatrix} \quad x_s^+ = \begin{bmatrix} v(k+1,s-2) \\ v(k+1,s-1) \end{bmatrix} \quad x_s^- = \begin{bmatrix} v(k+1,s+2) \\ v(k+1,s+1) \end{bmatrix}, \tag{6.3}$$

*respectively. The multidimensional state space model in controller canonical form is realized as*

$$\begin{bmatrix} x_t(k+1,s) \\ x_s^+(k,s+1) \\ x_s^-(k,s-1) \\ \hdashline y(k,s) \end{bmatrix} = \left[\begin{array}{cccccc:c} 0 & 1 & 0 & 0 & 0 & 0 & 0 \\ -a_{(2,0)} & -a_{(1,0)} & -a_{(1,2)} & -a_{(1,1)} & -a_{(1,-2)} & -a_{(1,-1)} & 1 \\ 0 & 0 & 0 & 1 & 0 & 0 & 0 \\ 0 & 1 & 0 & 0 & 0 & 0 & 0 \\ 0 & 0 & 0 & 0 & 0 & 1 & 0 \\ 0 & 1 & 0 & 0 & 0 & 0 & 0 \\ \hdashline 0 & b_{(1,0)} & 0 & 0 & 0 & 0 & 0 \end{array}\right] \begin{bmatrix} x_t(k,s) \\ x_s^+(k,s) \\ x_s^-(k,s) \\ \hdashline u(k,s) \end{bmatrix}. \tag{6.4}$$

Although the experimentally identified input/output models exhibit more complex dynamics than the simple Euler-Bernoulli equation, the realization of their state space models follows the similar line. The rest of this section converts the identified LTSI and spatial LPV models into their state space representations, considering models obtained using both black-box identification and the FE modelling results.

### 6.2.1 LTSI Models

The experimentally identified black-box LTSI model has the input and output masks shown in Fig. 5.4. Compared to the Euler-Bernoulli equation, the output of subsystem $s$ at time $k$, $y(k,s)$, additionally depends on the outputs of its neighbours at $k-2$ and its own input at $k-2$ and $k-3$. Thus define the temporal state, positive and negative spatial state vector as

$$x_t = \begin{bmatrix} v(k,s) \\ v(k+1,s) \\ v(k+2,s) \end{bmatrix} \quad x_s^+ = \begin{bmatrix} v(k+1,s-2) \\ v(k+1,s-1) \\ v(k+2,s-2) \\ v(k+2,s-1) \end{bmatrix} \quad x_s^- = \begin{bmatrix} v(k+1,s+2) \\ v(k+1,s+1) \\ v(k+2,s+2) \\ v(k+2,s+1) \end{bmatrix}, \tag{6.5}$$

respectively. A state space realization of the LTSI model takes the form

$$\begin{bmatrix} x_t(k+1,s) \\ x_s^+(k,s+1) \\ x_s^-(k,s-1) \\ \hdashline y(k,s) \end{bmatrix} = \left[\begin{array}{c:c} A^G & B^G \\ \hdashline C^G & D^G \end{array}\right] \begin{bmatrix} x_t(k,s) \\ x_s^+(k,s) \\ x_s^-(k,s) \\ \hdashline u(k,s) \end{bmatrix}, \tag{6.6}$$

with the system matrices given in Appendix (A.2) which are identical for all subsystems.

On the other hand, the FE-based LTSI model identified in Section 5.4 is endowed with physical meanings, and governed by the input and output masks shown in Fig. 5.9, where the output $y(k,s)$ depends on the past inputs applied on $s$, as well as on its neighbours $s-2$, $s-1$, $s+1$ and $s+2$. More intuitively, the black-box identified subsystem model interacts with nearby subsystems only through outputs, yet the FE-based model through both outputs and inputs. Thus the temporal state, positive and negative spatial state vectors are defined as

$$x_t = \begin{bmatrix} v(k,s) \\ v(k+1,s) \end{bmatrix} \quad x_s^+ = \begin{bmatrix} v(k+1,s-2) \\ v(k+1,s-1) \\ u(k+1,s-2) \\ u(k+1,s-1) \end{bmatrix} \quad x_s^- = \begin{bmatrix} v(k+1,s+2) \\ v(k+1,s+1) \\ u(k+1,s+2) \\ u(k+1,s+1) \end{bmatrix}, \tag{6.7}$$

respectively. Its state space realization takes the form of (6.6), with the system matrices expressed in Appendix (A.3).

### 6.2.2 Spatial LPV Models

Consider first the black-box identified spatial LPV model. Provided the input and output masks shown in Fig. 5.6, the application of the multidimensional Z-transformation to the LPV difference equation yields

$$\frac{Y}{U} = \frac{B(\theta_s, q_t, q_s)}{A(\theta_s, q_t, q_s)} = \frac{b_{(1,0)}(\theta_s)q_t + b_{(2,0)}(\theta_s)}{q_t^2 + a_{(1,-2)}(\theta_s)q_t q_s^2 + a_{(1,-1)}(\theta_s)q_t q_s + a_{(1,0)}(\theta_s)q_t + \ldots + a_{(2,2)}(\theta_s)q_s^{-2}}. \tag{6.8}$$

Compared to (6.1), the coefficients in (6.8) are not identical for all subsystems any more; instead they are varying from subsystem to subsystem. Black-box identification performed in Section 5.3.3 suggests that all coefficients in (6.8) are first order polynomials of the spatial scheduling parameter $\theta_s \in \mathbb{R}$.

Again introduce a new variable $V$ such that $U = AV$ and $Y = BV$ hold. The difference equation of $U = AV$ takes the form

$$\begin{aligned} v(k+2,s) =& -a_{(1,-2)}(\theta_s)v(k+1,s+2) - a_{(1,-1)}(\theta_s)v(k+1,s+1) - a_{(1,0)}(\theta_s)v(k+1,s) \\ & - a_{(1,1)}(\theta_s)v(k+1,s-1) - \ldots - a_{(2,2)}(\theta_s)v(k,s-2) + u(k,s) \\ =& -(\alpha_{(1,-2,0)} + \alpha_{(1,-2,1)}\theta_s)v(k+1,s+2) - (\alpha_{(1,-1,0)} + \alpha_{(1,-1,1)}\theta_s)v(k+1,s+1) \\ & - (\alpha_{(1,0,0)} + \alpha_{(1,0,1)}\theta_s)v(k+1,s) - (\alpha_{(1,1,0)} + \alpha_{(1,1,1)}\theta_s)v(k+1,s-1) \\ & - (\alpha_{(2,2,0)} + \alpha_{(2,2,1)}\theta_s)v(k,s-2) + u(k,s). \end{aligned} \tag{6.9}$$

Rearrange (6.9) by grouping all parameter-dependent terms together

$$\begin{aligned} v(k+2,s) = &-\alpha_{(1,-2,0)}v(k+1,s+2) - \alpha_{(1,-1,0)}v(k+1,s+1) - \alpha_{(1,0,0)}v(k+1,s) \\ &-\alpha_{(1,1,0)}v(k+1,s-1) - \ldots - \alpha_{(2,2,0)}v(k,s-2) + u(k,s) + p_1^s(k,s), \end{aligned}$$

where

$$\begin{aligned} p_1^s(k,s) &= \theta_s[-\alpha_{(1,-2,0)}v(k+1,s+2) - \alpha_{(1,-1,0)}v(k+1,s+1) - \alpha_{(1,0,0)}v(k+1,s) \\ &\quad - \alpha_{(1,1,0)}v(k+1,s-1) - \ldots - \alpha_{(2,2,0)}v(k,s-2)] \\ &= \theta_s q_1^s(k,s). \end{aligned} \tag{6.10}$$

Likewise, the difference equation of the output equation $Y = BV$ is written as

$$y(k,s) = \beta_{(1,0,0)}v(k+1,s) + \beta_{(2,0,0)}v(k,s) + p_2^s(k,s), \tag{6.11}$$

where

$$\begin{aligned} p_2^s(k,s) &= \theta_s[\beta_{(1,0,1)}v(k+1,s) + \beta_{(2,0,1)}v(k,s)] \\ &= \theta_s q_2^s(k,s). \end{aligned} \tag{6.12}$$

By pulling out the spatial uncertainties, the spatial LPV model can be represented in LFT form as shown in Fig. 6.1, which is a special case of the time/space-varying system shown in Fig. 2.3. Its LFT LPV state space model is given by

$$\begin{bmatrix} x_t(k+1,s) \\ x_s^+(k,s+1) \\ x_s^-(k,s-1) \\ \hline q^s(k,s) \\ \hline y(k,s) \end{bmatrix} = \left[\begin{array}{c|c|c} A^G & B_p^G & B_u^G \\ \hline C_q^G & D_{qp}^G & D_{qu}^G \\ \hline C_y^G & D_{yp}^G & D_{yu}^G \end{array}\right] \begin{bmatrix} x_t(k,s) \\ x_s^+(k,s) \\ x_s^-(k,s) \\ \hline p^s(k,s) \\ \hline u(k,s) \end{bmatrix}, \tag{6.13}$$

with the choices of vectors

$$x_t = \begin{bmatrix} v(k,s) \\ v(k+1,s) \end{bmatrix} \quad x_s^+ = \begin{bmatrix} v(k,s-2) \\ v(k,s-1) \\ v(k+1,s-2) \\ v(k+1,s-1) \end{bmatrix} \quad x_s^- = \begin{bmatrix} v(k,s+2) \\ v(k,s+1) \\ v(k+1,s+2) \\ v(k+1,s+1) \end{bmatrix}, \tag{6.14}$$

and the performance channel $p^s(k,s) = \begin{bmatrix} p_1^s(k,s) \\ p_2^s(k,s) \end{bmatrix}$, $q^s(k,s) = \begin{bmatrix} q_1^s(k,s) \\ q_2^s(k,s) \end{bmatrix}$, with

$$p^s(k,s) = \begin{bmatrix} \theta_s & \\ & \theta_s \end{bmatrix} q^s(k,s) = \Theta_s q^s(k,s). \tag{6.15}$$

The system matrices of (6.13) can be found in Appendix (A.6).

The explicit LPV form of the LFT LPV model (6.13) and (6.15) can be written as

$$\begin{bmatrix} x_t(k+1,s) \\ x_s^+(k,s+1) \\ x_s^-(k,s-1) \\ \hline y(k,s) \end{bmatrix} = \left[\begin{array}{c|c} \mathcal{A}^G(\Theta_s) & \mathcal{B}_u^G(\Theta_s) \\ \hline \mathcal{C}_y^G(\Theta_s) & \mathcal{D}_{yu}^G(\Theta_s) \end{array}\right] \begin{bmatrix} x_t(k,s) \\ x_s^+(k,s) \\ x_s^-(k,s) \\ \hline u(k,s) \end{bmatrix}, \tag{6.16}$$

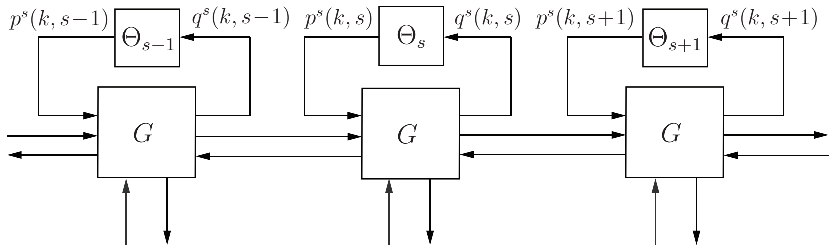


Figure 6.1: Spatially-varying distributed system in LFT representation

where the system matrices are scheduled by the structured spatial uncertainty $\Theta_s \in \mathbb{R}^{2\times 2}$, and can be recovered from (6.13) and (6.15) as

$$\begin{bmatrix} \mathcal{A}^G(\Theta_s) & \mathcal{B}_u^G(\Theta_s) \\ \mathcal{C}_y^G(\Theta_s) & \mathcal{D}_{yu}^G(\Theta_s) \end{bmatrix} = \begin{bmatrix} A^G & B_u^G \\ C_y^G & D_{yu}^G \end{bmatrix} + \begin{bmatrix} B_p^G \\ D_{yp}^G \end{bmatrix} \Theta_s (I - D_{qp}^G \Theta_s) \begin{bmatrix} C_q^G & D_{qu}^G \end{bmatrix}. \tag{6.17}$$

Analogous to the state space realization of the black-box identified spatial LPV model, the FE-based spatial LPV model identified in Section 5.4.3 has a state space representation given in Appendix (A.7) with the same choice of the states as in (6.7).

*Remarks*:

- It is demonstrated in [83] that, when converting a lumped LPV input/output model into a state space representation, the phenomenon of *dynamic dependence* arises: the resulting state space model depends on time-shifted versions of scheduling parameters. This phenomenon may also occur when converting a spatial LPV input/output model into state space form, where the resulting state space model depends on space-shifted scheduling parameters. To explore the property of dynamic dependence in a distributed LPV model, consider the observer canonical form of (6.16), whose output equation is expressed as $y(k,s) = x_t(k,s)$, and

$$\begin{aligned} y(k,s) = {} & \mathcal{A}_{tt}^G(\Theta_s)x_t(k-1,s) + \mathcal{A}_{ts}^{G,+}(\Theta_s)x_s^+(k-1,s) + \mathcal{A}_{ts}^{G,-}(\Theta_s)x_s^{G,-}(k-1,s) \\ & + \mathcal{B}_{t,u}^G(\Theta_s)u(k,s). \end{aligned} \tag{6.18}$$

  Replace $x_s^+(k-1,s)$ and $x_s^-(k-1,s)$ in (6.18) with

$$\begin{aligned} x_s^+(k-1,s) = {} & \mathcal{A}_{st}^{G,+}(\Theta_{s-1})x_t(k-1,s-1) + \mathcal{A}_{ss}^{G,++}(\Theta_{s-1})x_s^+(k-1,s-1) \\ & + \mathcal{A}_{ss}^{G,+-}(\Theta_{s-1})x_s^-(k-1,s-1) + \mathcal{B}_{s,u}^{G,+}(\Theta_s)u(k-1,s) \\ x_s^-(k-1,s) = {} & \mathcal{A}_{st}^{G,-}(\Theta_{s+1})x_t(k-1,s+1) + \mathcal{A}_{ss}^{G,-+}(\Theta_{s+1})x_s^+(k-1,s+1) \\ & + \mathcal{A}_{ss}^{G,--}(\Theta_{s+1})x_s^-(k-1,s+1) + \mathcal{B}_{s,u}^{G,-}(\Theta_s)u(k-1,s). \end{aligned}$$

  The computation of $y(k,s)$ depends on the scheduling parameter at $s$, i.e. $\Theta_s$, as well as on the space-shifted scheduling parameters at $s-1$ and $s+1$, i.e. $\Theta_{s-1}$ and

$\Theta_{s+1}$. That is the so-called dynamic dependence. However, this issue arises only when the block matrix

$$\left[\begin{array}{ccc:c} \mathcal{A}_{st}^{G,+}(\Theta_s) & \mathcal{A}_{ss}^{G,++}(\Theta_s) & \mathcal{A}_{ss}^{G,+-}(\Theta_s) & \mathcal{B}_{s,u}^{G,+}(\Theta_s) \\ \mathcal{A}_{st}^{G,-}(\Theta_s) & \mathcal{A}_{ss}^{G,-+}(\Theta_s) & \mathcal{A}_{ss}^{G,--}(\Theta_s) & \mathcal{B}_{s,u}^{G,-}(\Theta_s) \end{array}\right] \tag{6.19}$$

is gain-scheduled.

Recall the state space realization (6.4) of an LTSI model. An explicit LPV form of the spatial LPV model (6.16) can be constructed following the same pattern, where parameter-dependent coefficients $a_{(i_k,i_s)}(\theta_s)$ and $b_{(i_k,i_s)}(\theta_s)$ appear only in block matrices $\left[\begin{array}{ccc:c} \mathcal{A}_{tt}^{G}(\Theta_s) & \mathcal{A}_{ts}^{G,+}(\Theta_s) & \mathcal{A}_{ts}^{G,-}(\Theta_s) & \mathcal{B}_{t,u}^{G}(\Theta_s) \\ \mathcal{C}_{t,y}^{G,}(\Theta_s) & \mathcal{C}_{s,y}^{G,+}(\Theta_s) & \mathcal{C}_{s,y}^{G,-}(\Theta_s) & \mathcal{D}_{yu}^{G}(\Theta_s) \end{array}\right]$, leaving the block matrix (6.19) in (6.16) consisting of static terms—0 and 1, which indicate the signal flow between subsystems. Therefore, the phenomenon of dynamic dependence is not an issue in this specific application. The equivalence between the input/output LPV model and the converted state space model is not affected.

- The equivalence between the identified input/output model and the transformed multidimensional state space model has been validated by comparing their open-loop responses.

## 6.3 Construction of a Generalized Plant

The goal of designing a controller is to exponentially stabilize the controlled system and to impose a performance specification from the generalized disturbance $w$, which could be a combination of an input disturbance $d$, output noise $n$ and reference input $r$, to the fictitious controlled variable $z$, which measures the controller satisfying certain properties, e.g. with regard to the control error $e$, and the control effort $u$ [84]. The construction of a generalized plant for distributed systems does not differ much from lumped systems, except that the performance weightings can be either defined as multidimensional, involving both temporal and spatial dynamics, or purely temporal.

Note that a multidimensional weighting filter itself is a spatially-interconnected system. Although the two-dimensional loop shaping problem has been considered in [85] for a circulant system, how to construct and parametrize a multidimensional filter to specify certain performance requirements on a controlled distributed system is not known. Thus, one-dimensional temporal weighting filters are tuned and incorporated here in the spatio-temporal generalized plant.

Let the disturbance $d(k, s)$ be injected into the output of subsystem $s$ as shown in Fig. 6.2. Considered here is a controller design by shaping the mixed sensitivities: sensitivity to suppress the output disturbance, and control sensitivity to impose an upper bound on the control effort. The weighting filter $W_K$ used to shape the control sensitivity has a state space representation

$$\begin{aligned} x_1(k+1,s) &= A_1 x_1(k,s) + B_1 u(k,s) \\ z_1(k,s) &= C_1 x_1(k,s) + D_1 u(k,s), \end{aligned} \tag{6.20}$$

whereas the weighting filter to shape sensitivity $W_S$ is written as

$$\begin{aligned} x_2(k+1,s) &= A_2 x_2(k,s) + B_2 y(k,s) \\ z_2(k,s) &= C_2 x_2(k,s) + D_2 y(k,s). \end{aligned} \tag{6.21}$$

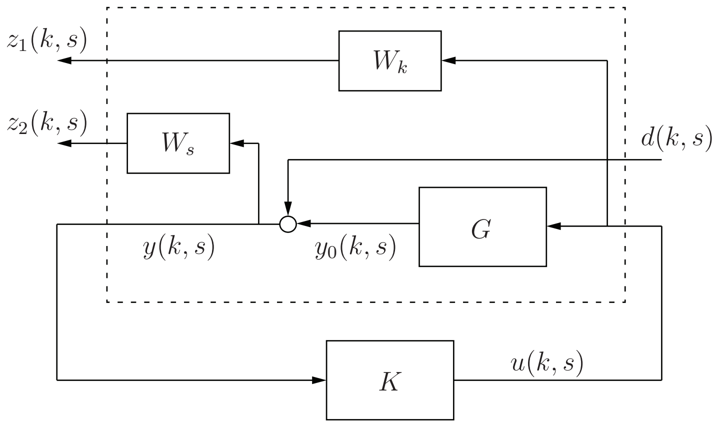


Figure 6.2: Generalized plant at the subsystem level of an LTSI model

The series interconnection of an LTSI plant model

$$\begin{bmatrix} x_t(k+1,s) \\ x_s^+(k,s+1) \\ x_s^-(k,s-1) \\ \hline y_0(k,s) \end{bmatrix} = \left[\begin{array}{c|cc} A^G & B_d^G & B_u^G \\ \hline C_y^G & D_{yd}^G & D_{yu}^G \end{array}\right] \begin{bmatrix} x_t(k,s) \\ x_s^+(k,s) \\ x_s^-(k,s) \\ \hline d(k,s) \\ u(k,s) \end{bmatrix}, \tag{6.22}$$

with shaping filters $W_K$ and $W_S$ incorporated, yields a generalized plant in the form of (2.11), whose algebraic expression is given by

$$\begin{bmatrix} x_t(k+1,s) \\ x_1(k+1,s) \\ x_2(k+1,s) \\ x_s^+(k,s+1) \\ x_s^-(k,s-1) \\ \hline z_1(k,s) \\ z_2(k,s) \\ y(k,s) \end{bmatrix} = \left[\begin{array}{ccccc|cc} A_{tt}^G & 0 & 0 & A_{ts}^{G,+} & A_{ts}^{G,-} & B_{t,d}^G & B_{t,u}^G \\ 0 & A_1 & 0 & 0 & 0 & 0 & B_1 \\ B_2 C_{t,y}^G & 0 & A_2 & B_2 C_{s,y}^{G,+} & B_2 C_{s,y}^{G,-} & B_2 D_{yd}^G & B_2 D_{yu}^G \\ A_{st}^{G,+} & 0 & 0 & A_{ss}^{G,++} & A_{ss}^{G,+-} & B_{s,d}^{G,+} & B_{s,u}^{G,+} \\ A_{st}^{G,-} & 0 & 0 & A_{ss}^{G,-+} & A_{ss}^{G,--} & B_{s,d}^{G,-} & B_{s,u}^{G,-} \\ \hline 0 & C_1 & 0 & 0 & 0 & 0 & D_1 \\ D_2 C_{t,y}^G & 0 & C_2 & D_2 C_{s,y}^{G,+} & D_2 C_{s,y}^{G,-} & D_2 D_{yd}^G & D_2 D_{yu}^G \\ C_{t,y} & 0 & 0 & C_{s,y}^+ & C_{s,y}^- & D_{yd} & D_{yu} \end{array}\right] \begin{bmatrix} x_t(k,s) \\ x_1(k,s) \\ x_2(k,s) \\ x_s^+(k,s) \\ x_s^-(k,s) \\ \hline d(k,s) \\ u(k,s) \end{bmatrix}. \tag{6.23}$$

Likewise, the generalized plant for the spatial LPV model shaped by LTI weighting filters has the form

$$
\left[\begin{array}{c}
x_t(k+1,s) \\ x_1(k+1,s) \\ x_2(k+1,s) \\ x_s^+(k,s+1) \\ x_s^-(k,s-1) \\ \hline q^s(k,s) \\ \hline z_1(k,s) \\ z_2(k,s) \\ y(k,s)
\end{array}\right]
=
\left[\begin{array}{ccccc|c|cc}
A_{tt}^G & 0 & 0 & A_{ts}^{G,+} & A_{ts}^{G,-} & B_{t,p^s}^G & B_{t,d}^G & B_{t,u}^G \\
0 & A_1 & 0 & 0 & 0 & 0 & 0 & B_1 \\
B_2C_{t,y}^G & 0 & A_2 & B_2C_{s,y}^{G,+} & B_2C_{s,y}^{G,-} & B_2D_{yp^s}^G & B_2D_{yd}^G & B_2D_{yu}^G \\
A_{st}^{G,+} & 0 & 0 & A_{ss}^{G,++} & A_{ss}^{G,+-} & B_{s,p^s}^{G,+} & B_{s,d}^{G,+} & B_{s,u}^{G,+} \\
A_{st}^{G,-} & 0 & 0 & A_{ss}^{G,-+} & A_{ss}^{G,--} & B_{s,p^s}^{G,-} & B_{s,d}^{G,-} & B_{s,u}^{G,-} \\ \hline
C_{t,q^s} & 0 & 0 & C_{s,q^s}^+ & C_{s,q^s}^- & D_{q^sp^s} & D_{q^sd} & D_{q^su} \\ \hline
0 & C_1 & 0 & 0 & 0 & 0 & 0 & D_1 \\
D_2C_{t,y}^G & 0 & C_2 & D_2C_{s,y}^{G,+} & D_2C_{s,y}^{G,-} & D_2D_{yp^s}^G & D_2D_{yd}^G & D_2D_{yu}^G \\
C_{t,y} & 0 & 0 & C_{s,y}^+ & C_{s,y}^- & D_{yp^s} & D_{yd} & D_{yu}
\end{array}\right]
\left[\begin{array}{c}
x_t(k,s) \\ x_1(k,s) \\ x_2(k,s) \\ x_s^+(k,s) \\ x_s^-(k,s) \\ \hline p^s(k,s) \\ \hline d(k,s) \\ u(k,s)
\end{array}\right],
$$

with $p^s = \Theta_s q^s$.

## 6.4 Controller Synthesis for LTSI Models

It is desired that the controller shares the interconnected structure of the plant. The control design objective for an LTSI model (2.11) is to find a controller in the form of (2.20), such that the closed-loop system (2.21) is well-posed, exponentially stable and satisfies a given quadratic performance condition as defined in Section 2.5. In this chapter, synthesis conditions for continuous systems developed in [8] are revisited. Conditions for discrete systems can be easily derived from [21]. Given the generalized plant (6.23) discrete in time and space, a bilinear transformation has to be applied to convert the discrete system to its continuous equivalence.

The following assumptions are made for controller design:

(i) $(\bar{A}^G, \bar{B}_u^G, \bar{C}_y^G)$ is stabilizable and detectable.

(ii) $\bar{D}_{yu}^G = 0$.

In this specific application, the second assumption is obviously violated due to the direct feed-through effect within the collocated piezo pairs. Nevertheless, the non-zero $\bar{D}_{yu}^G$ can be absorbed in $\bar{B}_u^G$ through postfiltering, such that assumption (ii) holds. Alternatively, the controller can be first designed under this assumption, then mapped via *loop shifting* to account for a non-zero $\bar{D}_{yu}^G$. Section 6.4.1 addresses this issue in detail. Consequently, the assumption $\bar{D}_{yu}^G = 0$ can be made without loss of generality.

### 6.4.1 Analysis and Synthesis Conditions

The analysis condition for continuous systems – Theorem 2.2 (ii) – involves the realization of the closed-loop system $L$ whose state vector is partitioned into temporal, positive and negative spatial state vectors as shown in (2.22), leading to the system matrices of a controlled system constructed from the plant and controller matrices as

$$\left[\begin{array}{c:c} \bar{A}^L & \bar{B}^L \\ \hdashline \bar{C}^L & \bar{D}^L \end{array}\right] = \left[\begin{array}{cccccc:c} \bar{A}^G_{tt} & 0 & \bar{A}^{G,+}_{ts} & 0 & \bar{A}^{G,-}_{ts} & 0 & \bar{B}^G_{t,d} \\ 0 & 0 & 0 & 0 & 0 & 0 & 0 \\ \bar{A}^{G,+}_{st} & 0 & \bar{A}^{G,++}_{ss} & 0 & \bar{A}^{G,+-}_{ss} & 0 & \bar{B}^{G,+}_{s,d} \\ 0 & 0 & 0 & 0 & 0 & 0 & 0 \\ \bar{A}^{G,-}_{st} & 0 & \bar{A}^{G,-+}_{ss} & 0 & \bar{A}^{G,--}_{ss} & 0 & \bar{B}^{G,-}_{s,d} \\ 0 & 0 & 0 & 0 & 0 & 0 & 0 \\ \hdashline \bar{C}^G_{t,z} & 0 & \bar{C}^{G,+}_{s,z} & 0 & \bar{C}^{G,-}_{s,z} & 0 & \bar{D}^G_{zd} \end{array}\right] + \left[\begin{array}{cccc} 0 & 0 & 0 & \bar{B}^G_{t,u} \\ I & 0 & 0 & 0 \\ 0 & 0 & 0 & \bar{B}^{G,+}_{s,u} \\ 0 & I & 0 & 0 \\ 0 & 0 & 0 & \bar{B}^{G,-}_{s,u} \\ 0 & 0 & I & 0 \\ \hdashline 0 & 0 & 0 & \bar{D}^L_{zu} \end{array}\right] \left[\begin{array}{c:c} \bar{A}^K & \bar{B}^K \\ \hdashline \bar{C}^K & \bar{D}^K \end{array}\right]$$
$$\times \left[\begin{array}{cccccc:c} 0 & I & 0 & 0 & 0 & 0 & 0 \\ 0 & 0 & 0 & I & 0 & 0 & 0 \\ 0 & 0 & 0 & 0 & 0 & I & 0 \\ \bar{C}^G_{t,y} & 0 & \bar{C}^{G,+}_{s,y} & 0 & \bar{C}^{G,-}_{s,y} & 0 & \bar{D}^G_{yd} \end{array}\right]. \tag{6.24}$$

However, the partition of positive and negative spatial state vectors of the controller remains unknown until the synthesis is complete. Therefore, the closed-loop system needs to be restructured such that the state vectors of the plant and the controller are grouped separately, i.e.

$$x^{\tilde{L}}(k,s) = \begin{bmatrix} x^G(k,s) \\ x^K(k,s) \end{bmatrix}, \tag{6.25}$$

where the subscript $\tilde{L}$ indicates a permuted closed-loop system. The resulting system matrices in contrast to (6.24) are given by

$$\left[\begin{array}{c:c} \bar{A}^{\tilde{L}} & \bar{B}^{\tilde{L}} \\ \hdashline \bar{C}^{\tilde{L}} & \bar{D}^{\tilde{L}} \end{array}\right] = \left[\begin{array}{cc:c} \bar{A}^G & 0 & \bar{B}^G_d \\ 0 & 0 & 0 \\ \hdashline \bar{C}^G_z & 0 & \bar{D}^G_{zd} \end{array}\right] + \left[\begin{array}{cc} 0 & \bar{B}^G_u \\ I & 0 \\ \hdashline 0 & \bar{D}^G_{zu} \end{array}\right] \left[\begin{array}{c:c} \bar{A}^K & \bar{B}^K \\ \hdashline \bar{C}^K & \bar{D}^K \end{array}\right] \left[\begin{array}{cc:c} 0 & I & 0 \\ \bar{C}^G_y & 0 & \bar{D}^G_{yd} \end{array}\right]. \tag{6.26}$$

The closed-loop Lyapunov matrix that accounts for the permutation of the closed-loop system (6.26) is rearranged from $X^L \in \boldsymbol{\mathcal{X}}_{m^L}$ to $X^{\tilde{L}}$ [8], where

$$X^L = \left[\begin{array}{c:c} X^L_t & \\ \hdashline & X^L_s \end{array}\right] = \left[\begin{array}{cc:cc} X^G_t & X^{GK}_t & & \\ (X^{GK}_t)^T & X^K_t & & \\ \hdashline & & X^G_s & X^{GK}_s \\ & & (X^{GK}_s)^T & X^K_s \end{array}\right], \tag{6.27}$$

$$X^{\tilde{L}} = \left[\begin{array}{cc:cc} X^G_t & & X^{GK}_t & \\ & X^G_s & & X^{GK}_s \\ \hdashline (X^{GK}_t)^T & & X^K_t & \\ & (X^{GK}_s)^T & & X^K_s \end{array}\right]. \tag{6.28}$$

The analysis condition Theorem 2.2 (ii) is equivalent to the condition in the following theorem.

**Theorem 6.1 ([8])** *Assume that the interconnected system (2.21) is well-posed. The system is exponentially stable, and has quadratic performance $\gamma$, if and only if there exists a symmetric matrix $X^{\tilde{L}}$, such that*

$$\begin{bmatrix} * \\ \hdashline * \end{bmatrix}^T \left[\begin{array}{cc:cc} 0 & X^{\tilde{L}} & & \\ X^{\tilde{L}} & 0 & & \\ \hdashline & & \frac{1}{\gamma}I & 0 \\ & & 0 & -\gamma I \end{array}\right] \left[\begin{array}{cc} \bar{A}^{\tilde{L}} & \bar{B}_d^{\tilde{L}} \\ I & 0 \\ \hdashline \bar{C}_z^{\tilde{L}} & \bar{D}_{zd}^{\tilde{L}} \\ 0 & I \end{array}\right] < 0. \tag{6.29}$$

Applying the elimination lemma (see Appendix C.1) to (6.29) yields corresponding synthesis conditions.

**Theorem 6.2** *There exists a distributed controller in the form of (2.20) that guarantees exponential stability and a quadratic performance $\gamma$ of the closed-loop system (2.21), if and only if there exist symmetric matrices $R$, $S \in \boldsymbol{\mathcal{X}}_{m^G}$, such that*

$$N_R^T \begin{bmatrix} * \\ \hdashline * \end{bmatrix}^T \left[\begin{array}{cc:cc} 0 & R & & \\ R & 0 & & \\ \hdashline & & \frac{1}{\gamma}I & 0 \\ & & 0 & -\gamma I \end{array}\right] \left[\begin{array}{cc} (\bar{A}^G)^T & (\bar{C}_z^G)^T \\ I & 0 \\ \hdashline (\bar{B}_d^G)^T & (\bar{D}_{zd}^G)^T \\ 0 & I \end{array}\right] N_R < 0 \tag{6.30}$$

$$N_S^T \begin{bmatrix} * \\ \hdashline * \end{bmatrix}^T \left[\begin{array}{cc:cc} 0 & S & & \\ S & 0 & & \\ \hdashline & & \frac{1}{\gamma}I & 0 \\ & & 0 & -\gamma I \end{array}\right] \left[\begin{array}{cc} \bar{A}^G & \bar{B}_d^G \\ I & 0 \\ \hdashline \bar{C}_z^G & \bar{D}_{zd}^G \\ 0 & I \end{array}\right] N_S < 0 \tag{6.31}$$

$$\begin{bmatrix} R_t & I \\ I & S_t \end{bmatrix} \geq 0, \tag{6.32}$$

*where* $N_R = \ker[(\bar{B}_u^G)^T \quad (\bar{D}_{zu}^G)^T]$, $N_S = \ker[\bar{C}_y^G \quad \bar{D}_{yd}^G]$.

**Controller Construction**

After LMIs (6.30)-(6.32) have been solved for matrices $R$ and $S$, the temporal and spatial components of the Lyapunov matrix can be constructed via performing an SVD of $I - RS$, i.e.

$$M_t N_t^T = I - R_t S_t, \quad M_s N_s^T = I - R_s S_s, \tag{6.33}$$

then

$$X_t^L = \begin{bmatrix} S_t & I \\ N_t^T & 0 \end{bmatrix}^{-1} \begin{bmatrix} I & R_t \\ 0 & M_t^T \end{bmatrix} \quad X_s^L = \begin{bmatrix} S_s & I \\ N_s^T & 0 \end{bmatrix}^{-1} \begin{bmatrix} I & R_s \\ 0 & M_s^T \end{bmatrix} \quad X^L = \begin{bmatrix} X_t^L & \\ & X_s^L \end{bmatrix}. \tag{6.34}$$

Restructure the Lyapunov matrix $X^L$ in the form of $X^{\tilde{L}}$ in (6.28). Given the system matrices of the permuted closed-loop system (6.26), the LMI condition (6.29) depends now on the unknown controller matrices in an affine way. The controller is obtained by solving (6.29) for the controller matrices $\left[\begin{array}{c:c} \bar{A}^K & \bar{B}^K \\ \hdashline \bar{C}^K & \bar{D}^K \end{array}\right]$.

Note that the designed controller is still continuous both in time and space. To implement it digitally, the bilinear transformation C.3 (see Appendix C) needs to be performed to convert it back to its discrete counterpart.

**Addressing a Non-Zero $\mathbf{\bar{D}^G_{yu}}$**

The controller is designed under the assumption $\bar{D}^G_{yu} = 0$. To take care of non-zero $\bar{D}^G_{yu}$, two possible ways are provided here:

- Loop shifting [8]: after the controller matrices are computed from (6.29), the non-zero $\bar{D}^G_{yu}$ is taken care of by applying the following transformation:

$$\left[\begin{array}{c|c} \bar{A}^K & \bar{B}^K \\ \hline \bar{C}^K & \bar{D}^K \end{array}\right] \rightarrow \left[\begin{array}{c|c} \bar{A}^K - \bar{B}^K \bar{D}^G_{yu}(I + \bar{D}^K \bar{D}^G_{yu})^{-1} \bar{C}^K & \bar{B}^K (I + \bar{D}^G_{yu} \bar{D}^K)^{-1} \\ \hline (I + \bar{D}^K \bar{D}^G_{yu})^{-1} \bar{C}^K & (I + \bar{D}^K \bar{D}^G_{yu})^{-1} \bar{D}^K \end{array}\right]. \tag{6.35}$$

- Postfiltering: add a postfilter $W_f$ to the plant output as shown in Fig. 6.3.

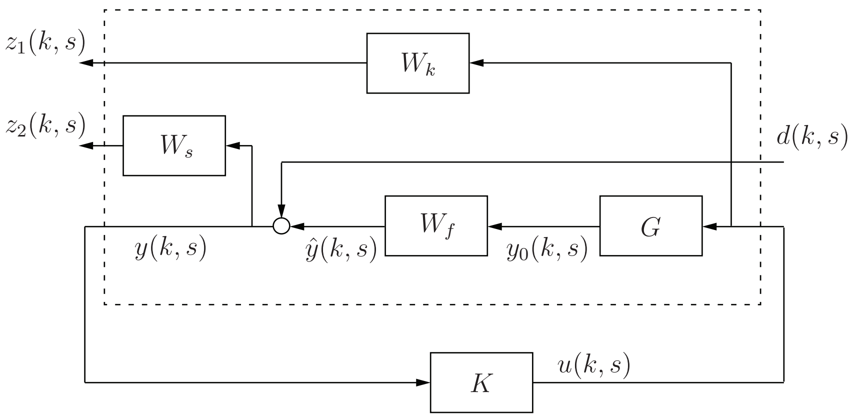


Figure 6.3: Generalized plant at the subsystem level after incorporating a postfilter

Let a realization of the postfilter be described as

$$x_f(k+1, s) = A_f x_f(k, s) + B_f y_0(k, s) \tag{6.36}$$

$$\hat{y}(k, s) = C_f x_f(k, s), \tag{6.37}$$

which is chosen as a low-pass filter with cut-off frequency well beyond the bandwidth of the controlled system. The plant model (6.6) with a postfilter incorporated takes the form

$$\left[\begin{array}{c} x_t(k+1, s) \\ x_f(k+1, s) \\ x_s^+(k, s+1) \\ x_s^-(k, s-1) \\ \hline \hat{y}(k, s) \end{array}\right] = \left[\begin{array}{cccc|c} A^G_{tt} & 0 & A^{G,+}_{ts} & A^{G,-}_{ts} & B^G_{t,u} \\ B_f C^G_{t,y} & A_f & B_f C^{G,+}_{s,y} & B_f C^-_{s,y} & B_f D^G_{yu} \\ A^{G,+}_{st} & 0 & A^{G,++}_{ss} & A^{G,+-}_{ss} & B^{G,+}_{s,u} \\ A^{G,-}_{st} & 0 & A^{G,-+}_{ss} & A^{G,--}_{ss} & B^{G,-}_{s,u} \\ \hline 0 & C_f & 0 & 0 & 0 \end{array}\right] \left[\begin{array}{c} x_t(k, s) \\ x_f(k, s) \\ x_s^+(k, s) \\ x_s^-(k, s) \\ \hline u(k, s) \end{array}\right], \tag{6.38}$$

where assumption (ii) ($\bar{D}^G_{yu} = 0$) is fulfilled.

### 6.4.2 Decentralized Controller Design

Decentralized controllers differ from distributed controllers in the sense that no information exchange takes place between controller subsystems, as shown in Fig. 6.4. Decentralized controllers thus exhibit only temporal dynamics.

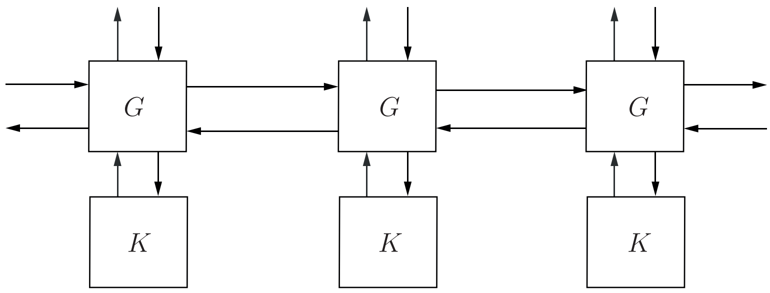


Figure 6.4: Part of a decentralized system

Consider the structure of a decentralized controller on subsystem $s$

$$\begin{bmatrix} x^K(k+1,s) \\ \hdashline u(k,s) \end{bmatrix} = \left[\begin{array}{c:c} A^K & B^K \\ \hdashline C^K & D^K \end{array}\right] \begin{bmatrix} x^K(k,s) \\ \hdashline y(k,s) \end{bmatrix}. \tag{6.39}$$

Synthesis conditions (6.30)-(6.32) for distributed controller design apply to the design of decentralized controllers, except for the Lyapunov matrix $X \in \hat{\boldsymbol{\mathcal{X}}}_m$, where

$$\hat{\boldsymbol{\mathcal{X}}}_m = \left\{ X \in \mathbb{R}^{(m_0+m_++m_-)\times(m_0+m_++m_-)} \middle| X = X^T = \begin{bmatrix} X_t & \\ & 0 \end{bmatrix}, X_t \in \mathbb{R}^{m_0\times m_0} > 0 \right\}. \tag{6.40}$$

By imposing the condition that spatial Lyapunov matrices are zero, the resulting controller realizes a decentralized control scheme.

### 6.4.3 Experimental Results

To test the controller performance, 16 identical chirp signals of amplitude 4 V and bandwidth up to 20 Hz are injected into the loop as output disturbances as shown in Fig. 6.2. Without any feedback control, the open-loop output is the injected disturbances, i.e. $y(k,s) = d(k,s)$.

Both a distributed and a decentralized controller have been designed for performance comparison. The controller design is realized by modifying the Multidimensional Toolbox [86] to meet the specific requirements. Provided the black-box identified LTSI model, the designed distributed controller is of temporal order $m_0^K = 6$, and of spatial order $m_+^K = m_-^K = 4$, whereas the decentralized controller is of order $m_0^K = 5$.

Fig. 6.5 shows the comparison of measured outputs over time at two selected sensors between open-loop response, the closed-loop response with a distributed controller, and the closed-loop response with a decentralized controller. Both controllers attenuate the disturbances down to certain extents. It is obvious that the distributed controller outperforms the decentralized one by significantly reducing the vibratory amplitudes. Fig. 6.6 shows the comparison of controlled FRFs using distributed and decentralized controllers. Over the considered frequency range, a better disturbance rejection achieved by the distributed controller can be observed as well. Evidently, the exchange of information between subsystems leads to a more efficient control scheme.

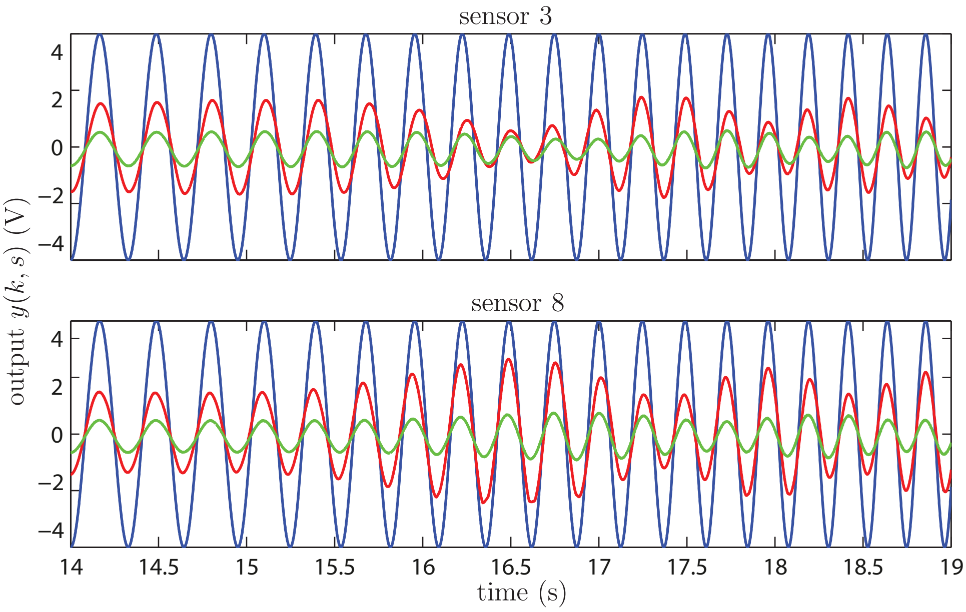


Figure 6.5: With output disturbances injected, comparison of measured outputs over time between open-loop response (blue curve), closed-loop response with a distributed LTSI controller (green curves), and closed-loop response with a decentralized LTSI controller (red curves)

*Remarks*:

- The online computation of the controller outputs can only be realized in a centralized manner. Recall the spatial-state equation of the controller

$$\mathbf{\Delta}^K_{s,m} x^K_s(k,s) = A^K_{st} x^K_t(k,s) + A^K_{ss} x^K_s(k,s) + B^K_s y(k,s). \tag{6.41}$$

  Moving terms involving spatial states $x^K_s(k,s)$ to the left generates

$$(\mathbf{\Delta}^K_{s,m} - A^K_{ss}) x^K_s(k,s) = A^K_{st} x^K_t(k,s) + B^K_s y(k,s). \tag{6.42}$$

  Note that after solving for the controller matrices from (6.29), the spatial state vector may lose its physical meanings, i.e. subsystems may not communicate directly through their inputs and/or outputs. Thus the computation of the controller output can not be realized on a single-subsystem basis based on the information it receives from its neighbours.

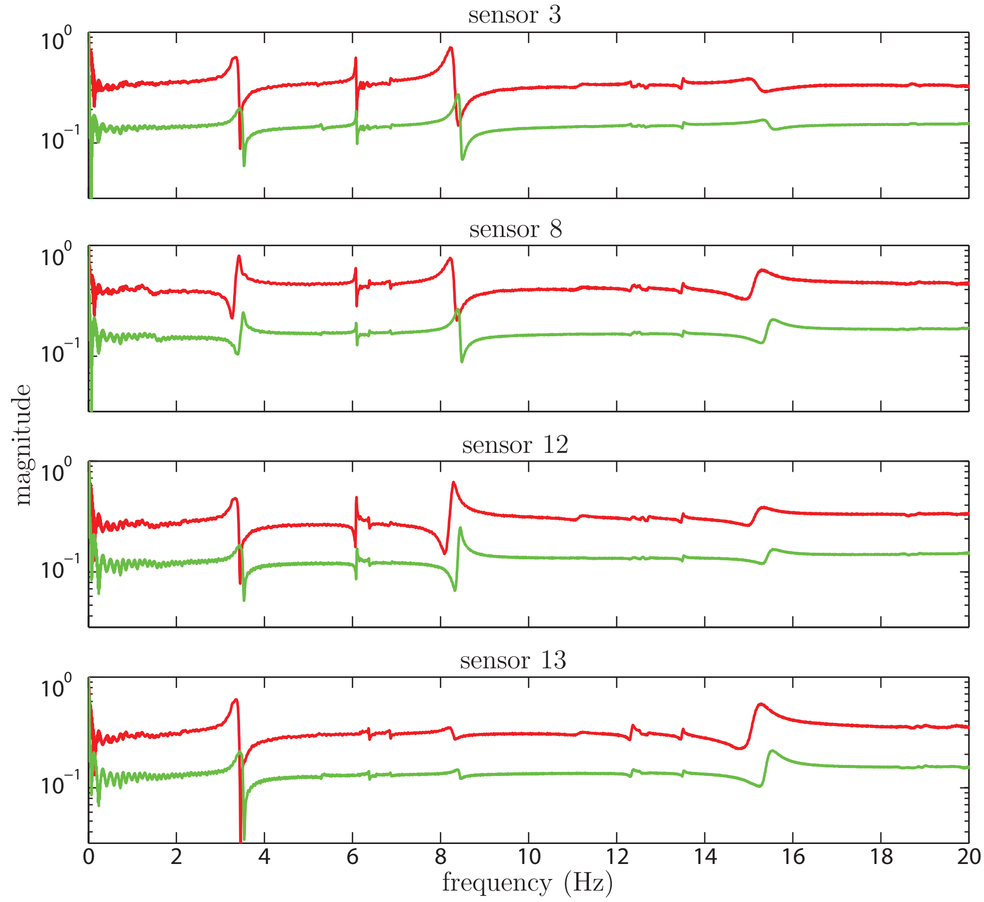


Figure 6.6: Comparison of FRFs from injected output disturbances to collocated output between closed-loop response with distributed LTSI controllers (green curves), and closed-loop response with decentralized LTSI controllers (red curves)

To the author's knowledge, the only way to compute it, is to construct a global version of (6.42) that includes the entire spatial states from all controller subsystems as

$$(\mathbf{I}_{16} \otimes \mathbf{\Delta}^K_{s,m} - \mathbf{I}_{16} \otimes A^K_{ss})x^K_s(k,\cdot) = (\mathbf{I}_{16} \otimes A^K_{st})x^K_t(k,\cdot) + (\mathbf{I}_{16} \otimes B^K_s)y(k,\cdot), \quad (6.43)$$

where $x^K_s(k,\cdot) \in \mathbb{R}^{16(m^K_+ + m^K_-)}$, $x^K_t(k,\cdot) \in \mathbb{R}^{16m^K_0}$, and $y(k,\cdot) \in \mathbb{R}^{16}$ denote the augmented spatial, temporal state vectors and plant outputs at all 16 subsystems, respectively. Then solve the spatial states at each time instant by

$$x^K_s(k,\cdot) = (\mathbf{I}_{16} \otimes \mathbf{\Delta}^K_{s,m} - \mathbf{I}_{16} \otimes A^K_{ss})^{-1}[(\mathbf{I}_{16} \otimes A^K_{st})x^K_t(k,\cdot) + (\mathbf{I}_{16} \otimes B^K_s)y(k,\cdot)]. \quad (6.44)$$

- Given the FE model derived in Chapter 3, attempts have been made to design a centralized $H_\infty$ controller for comparison. However, it is not possible for Matlab to solve the synthesis problem for a system of order 196.
- Difficulties have been encountered in the controller synthesis using the FE-based input/output model obtained in Section 5.4, despite of the fact that a better match

to the plant dynamics has been achieved by the FE-based model than by the black-box identified model. This may attribute to the presence of the direct feed-through effect in the FE-based model, which is approximated in the black-box identification as fast dynamics.

## 6.5 Controller Synthesis for Temporal/Spatial LPV Models

The gain scheduling control methodology guarantees stability and performance over a wide range of varying parameters. Extending analysis and synthesis approaches for temporal LPV systems to parameter-varying spatially-interconnected systems leads to a high performance and computationally attractive control scheme. In this section, the controller design problem for distributed systems subject to temporal/spatial variations is studied. Inheriting the spatial structure of the plant, distributed controllers are synthesized using both CLFs and PDLFs and implemented experimentally. Advantages of using PDLFs will become clear when compared with the controller performance using CLFs.

It is assumed that

(i) $(\bar{\mathcal{A}}^G(\Theta_t,\Theta_s), \bar{\mathcal{B}}_u^G(\Theta_t,\Theta_s), \bar{\mathcal{C}}_y^G(\Theta_t,\Theta_s))$ is stabilizable and detectable for all $\Theta_t \in \mathbf{\Theta}_t$ and $\Theta_s \in \mathbf{\Theta}_s$.

(ii) $[\bar{\mathcal{C}}_y^G(\Theta_t,\Theta_s) \quad \bar{\mathcal{D}}_{yd}^G(\Theta_t,\Theta_s)]$ and $[(\bar{\mathcal{B}}_u^G)^T(\Theta_t,\Theta_s) \quad (\bar{\mathcal{D}}_{zu}^G)^T(\Theta_t,\Theta_s)]$ have full row rank for all $\Theta_t \in \mathbf{\Theta}_t$ and $\Theta_s \in \mathbf{\Theta}_s$.

(iii) $\bar{\mathcal{D}}_{zd}^G(\Theta_t,\Theta_s) = 0$ and $\bar{\mathcal{D}}_{yu}^G(\Theta_t,\Theta_s) = 0$.

The first two assumptions guarantee the existence of a stabilizing output feedback controller, whereas the third one is assumed for simplicity. Two methods have been discussed in Section 6.4.1 to address non-zero $\bar{\mathcal{D}}_{yu}^G(\Theta_t,\Theta_s)$.

A powerful tool, the FBSP [45], plays an important role in the derivation of synthesis conditions for LFT LPV systems.

**Theorem 6.3 (Full Block S-Procedure)** *Let $\Theta \in \mathbf{\Theta}$ represent the varying parameters. Assume a rational parameter dependence of $\mathcal{G}(\Theta) \in \mathbb{R}^{m\times n}$ on $\Theta$. Let*

$$\mathcal{G}(\Theta) = \Theta \star \begin{bmatrix} G_{11} & G_{12} \\ G_{21} & G_{22} \end{bmatrix} = G_{22} + G_{21}\Theta(I - G_{11}\Theta)^{-1}G_{12} \tag{6.45}$$

*be an LFT representation. For a given matrix $M \in \mathbb{R}^{m\times m}$, the following two conditions are equivalent:*

*(i) The quadratic matrix inequality*

$$\mathcal{G}^T(\Theta)M\mathcal{G}(\Theta) < 0 \tag{6.46}$$

*holds $\forall\Theta \in \mathbf{\Theta}$.*

*(ii)* *There exists a full-block multiplier* $\Pi$ *such that*

$$[*]^T \left[\begin{array}{c|c} \Pi & \\ \hline & M \end{array}\right] \left[\begin{array}{cc} G_{11} & G_{12} \\ I & 0 \\ \hline G_{21} & G_{22} \end{array}\right] < 0, \tag{6.47}$$

*and* $\forall \Theta \in \boldsymbol{\Theta}$

$$[*]^T \Pi \begin{bmatrix} I \\ \Theta \end{bmatrix} \geq 0. \tag{6.48}$$

**Proof** The proof of Theorem 6.3 is provided in [14]. ∎

Theorem 6.3 states that the nonlinear matrix inequality (6.46) is equivalent to a set of two LMIs: the main condition (6.47) that contains the constant matrices from the LFT representation of $\mathcal{G}(\Theta)$; and a multiplier condition (6.48) that involves the varying parameters $\Theta$. The use of the FBSP for the derivation of synthesis conditions is discussed in Section 6.5.1 using CLFs, and in Section 6.5.2 using PDLFs. The performance of designed controllers is demonstrated experimentally in Section 6.5.3.

### 6.5.1 Analysis and Synthesis Conditions Using CLFs

In the state-space framework developed in [8], distributed systems with temporal/spatial variations can be expressed in explicit LPV form (2.12). A rational dependence of system matrices on scheduling parameters allows an equivalent LFT representation (2.13) and (2.14). Using the small-gain theorem, the design of a gain-scheduled $H_\infty$ controller in LFT form can be recast in terms of LMIs [11]. A distributed controller design for parameter-dependent spatially-interconnected systems using CLFs has been studied in [21], where synthesis conditions are derived based on a specific choice of multipliers. Here, rather general and less conservative conditions are given using the FBSP. Note that the use of CLFs allows for arbitrary fast parameter-variation rates.

Consider a gain-scheduled closed-loop system in the form of (2.24) whose state vector is structured as in (2.22). It can be viewed as an LTSI system subject to temporal/spatial uncertainties from the plant $\Upsilon^G$ and from the controller $\Upsilon^K$ as

$$\left[\begin{array}{c|c} \bar{\mathcal{A}}^L(\Theta_t^L, \Theta_s^L) & \bar{\mathcal{B}}_d^L(\Theta_t^L, \Theta_s^L) \\ \hline \bar{\mathcal{C}}_z^L(\Theta_t^L, \Theta_s^L) & \bar{\mathcal{D}}_{zd}^L(\Theta_t^L, \Theta_s^L) \end{array}\right] = \begin{bmatrix} \Upsilon^G & \\ & \Upsilon^K \end{bmatrix} \star \left[\begin{array}{c|cc} \bar{D}_{qp}^L & \bar{C}_q^L & \bar{D}_{qd}^L \\ \hline \bar{B}_p^L & \bar{A}^L & \bar{B}_d^L \\ \bar{D}_{zp}^L & \bar{C}_z^L & \bar{D}_{zd}^L \end{array}\right] := \Upsilon^L \star \left[\begin{array}{c|cc} \bar{D}_{qp}^L & \bar{C}_q^L & \bar{D}_{qd}^L \\ \hline \bar{B}_p^L & \bar{A}^L & \bar{B}_d^L \\ \bar{D}_{zp}^L & \bar{C}_z^L & \bar{D}_{zd}^L \end{array}\right],$$

where the uncertainties $\Upsilon^G$ and $\Upsilon^K$ are defined as in (2.14) and (2.26), respectively.

Define the multiplier set $\boldsymbol{\mathcal{Y}}_{(n_{\Theta_t}, n_{\Theta_s})}$ as

$$\boldsymbol{\mathcal{Y}}_{(n_{\Theta_t}, n_{\Theta_s})} = \left\{ \Pi \in \mathbb{R}^{2(n_{\Theta_t}+n_{\Theta_s}) \times 2(n_{\Theta_t}+n_{\Theta_s})} \middle| \Pi = \Pi^T = \begin{bmatrix} \Pi_{11} & \Pi_{12} \\ \Pi_{12}^T & \Pi_{22} \end{bmatrix}, \Pi_{ij} = \begin{bmatrix} \Pi_{ij}^t & \\ & \Pi_{ij}^s \end{bmatrix}, \right.$$
$$\left. \Pi_{ij}^t \in \mathbb{R}^{n_{\Theta_t} \times n_{\Theta_t}}, \Pi_{ij}^s \in \mathbb{R}^{n_{\Theta_s} \times n_{\Theta_s}}, \Pi_{ij}^t \Theta_t = \Theta_t \Pi_{ij}^t, \Pi_{ij}^s \Theta_s = \Theta_s \Pi_{ij}^s, i, j = 1, 2 \right\}.$$

The analysis condition – Theorem 2.2 (ii) – for LTSI systems is extended to distributed LPV systems in the following result.

**Theorem 6.4** *Assume that the controlled system (2.27) and (2.28) is well-posed. The system is exponentially stable and has quadratic performance $\gamma$, for any $(\Theta_t^L, \Theta_s^L) \in (\boldsymbol{\Theta}_t^L, \boldsymbol{\Theta}_t^L)$, if one of following two conditions is satisfied:*

*(i)* *There exists a symmetric matrix $X^L \in \boldsymbol{\mathcal{X}}_{m^L}$, such that*

$$\begin{bmatrix} * \\ \hdashline * \end{bmatrix}^T \left[\begin{array}{cc:cc} 0 & X^L & & \\ X^L & 0 & & \\ \hdashline & & \frac{1}{\gamma}I & 0 \\ & & 0 & -\gamma I \end{array}\right] \left[\begin{array}{cc} \bar{\mathcal{A}}^L(\Theta_t^L, \Theta_s^L) & \bar{\mathcal{B}}_d^L(\Theta_t^L, \Theta_s^L) \\ I & 0 \\ \hdashline \bar{\mathcal{C}}_z^L(\Theta_t^L, \Theta_s^L) & \bar{\mathcal{D}}_{zd}^L(\Theta_t^L, \Theta_s^L) \\ 0 & I \end{array}\right] < 0. \tag{6.49}$$

*(ii)* *There exists a symmetric matrix $X^L \in \boldsymbol{\mathcal{X}}_{m^L}$ and a symmetric multiplier $\Pi^L \in \boldsymbol{\mathcal{Y}}_{(n_{\Theta_t^L}, n_{\Theta_s^L})}$, such that*

$$\begin{bmatrix} * \\ \hdashline * \\ \hdashline * \end{bmatrix}^T \left[\begin{array}{cc:c:cc} 0 & X^L & & & \\ X^L & 0 & & & \\ \hdashline & & \Pi^L & & \\ \hdashline & & & \frac{1}{\gamma}I & 0 \\ & & & 0 & -\gamma I \end{array}\right] \left[\begin{array}{ccc} \bar{A}^L & \bar{B}_p^L & \bar{B}_d^G \\ I & 0 & 0 \\ \hdashline \bar{C}_q^L & \bar{D}_{qp}^L & \bar{D}_{qd}^L \\ 0 & I & 0 \\ \hdashline \bar{C}_z^L & \bar{D}_{zp}^L & \bar{D}_{zd}^L \\ 0 & 0 & I \end{array}\right] < 0, \tag{6.50}$$

*and*

$$\begin{bmatrix} * \\ \hdashline * \end{bmatrix}^T \Pi^L \begin{bmatrix} I \\ \hdashline \Upsilon^L \end{bmatrix} > 0, \tag{6.51}$$

*where $n_{\Theta_t^L}$ and $n_{\Theta_s^L}$ denote the sizes of temporal and spatial uncertainties of the closed-loop system, respectively.*

Condition (ii) is the result after applying the FBSP to (6.49) with extra constraints imposed on the multiplier structure, in addition to the symmetry required by the FBSP.

Just like the derivation of synthesis conditions for LTSI systems, the elimination lemma can not be directly applied to conditions (6.50) and (6.51), due to the unknown partition of the controller spatial state vector. The restructured state vector $x^{\tilde{L}} = [(x^G)^T \quad (x^K)^T]^T$ requires the permutation of the system matrices, Lyapunov matrices, as well as the multiplier $\Pi^L$. The permuted multiplier $\Pi^{\tilde{L}}$ has the form

$$\Pi^{\tilde{L}} = \left[\begin{array}{cccc:cccc} \Pi_{11}^{G,t} & & \Pi_{11}^{GK,t} & & \Pi_{12}^{G,t} & & \Pi_{12}^{GK,t} & \\ & \Pi_{11}^{G,s} & & \Pi_{11}^{GK,s} & & \Pi_{12}^{G,s} & & \Pi_{12}^{GK,s} \\ (\Pi_{11}^{GK,t})^T & & \Pi_{11}^{K,t} & & \Pi_{12}^{KG,t} & & \Pi_{12}^{K,t} & \\ & (\Pi_{11}^{GK,s})^T & & \Pi_{11}^{K,s} & & \Pi_{12}^{KG,s} & & \Pi_{12}^{K,s} \\ \hdashline & & & & \Pi_{22}^{G,t} & & \Pi_{22}^{GK,t} & \\ & & & & & \Pi_{22}^{G,s} & & \Pi_{22}^{GK,s} \\ & \text{sym} & & & (\Pi_{22}^{GK,t})^T & & \Pi_{22}^{K,t} & \\ & & & & & (\Pi_{22}^{GK,s})^T & & \Pi_{22}^{K,s} \end{array}\right]. \tag{6.52}$$

Theorem 6.4 (ii) is equivalent to the following results.

**Theorem 6.5** *The controlled system (2.27) and (2.28) is well-posed, exponentially stable and has quadratic performance $\gamma$ if there exists $X^{\tilde{L}}$ in the form of (6.28), and a multiplier $\Pi^{\tilde{L}}$ in the form of (6.52), such that*

$$\begin{bmatrix} * \\ \hdashline * \\ \hdashline * \end{bmatrix}^T \left[\begin{array}{cc:c:cc} 0 & X^{\tilde{L}} & & & \\ X^{\tilde{L}} & 0 & & & \\ \hdashline & & \Pi^{\tilde{L}} & & \\ \hdashline & & & \frac{1}{\gamma}I & 0 \\ & & & 0 & -\gamma I \end{array}\right] \left[\begin{array}{ccc} \bar{A}^{\tilde{L}} & \bar{B}_p^{\tilde{L}} & \bar{B}_d^{G} \\ I & 0 & 0 \\ \hdashline \bar{C}_q^{\tilde{L}} & \bar{D}_{qp}^{\tilde{L}} & \bar{D}_{qd}^{\tilde{L}} \\ 0 & I & 0 \\ \hdashline \bar{C}_z^{\tilde{L}} & \bar{D}_{zp}^{\tilde{L}} & \bar{D}_{zd}^{\tilde{L}} \\ 0 & 0 & I \end{array}\right] < 0 \tag{6.53}$$

$$\begin{bmatrix} * \\ \hdashline * \end{bmatrix}^T \Pi^{\tilde{L}} \left[\begin{array}{cc} I & \\ & I \\ \hdashline \Upsilon^G & \\ & \Upsilon^K \end{array}\right] > 0. \tag{6.54}$$

Controller synthesis conditions can then be further developed by applying the elimination lemma to (6.53) and (6.54).

**Theorem 6.6** *Consider a distributed system in LFT form as in (2.16) and (2.17). There exists a distributed controller in the form of (2.25) and (2.26), that guarantees well-posedness, exponential stability and quadratic performance $\gamma$ of the closed-loop systems (2.27) and (2.28), if there exist symmetric matrices $R$, $S \in \boldsymbol{\mathcal{X}}_{m^G}$, and symmetric multipliers $\Pi_R$, $\Pi_S \in \boldsymbol{\mathcal{Y}}_{(n_{\Theta_t^G}, n_{\Theta_s^G})}$, that satisfy*

$$N_R^T \begin{bmatrix} * \\ \hdashline * \\ \hdashline * \end{bmatrix}^T \left[\begin{array}{cc:c:cc} 0 & R & & & \\ R & 0 & & & \\ \hdashline & & \Pi_R & & \\ \hdashline & & & \frac{1}{\gamma}I & 0 \\ & & & 0 & -\gamma I \end{array}\right] \left[\begin{array}{ccc} (\bar{A}^G)^T & (\bar{C}_q^G)^T & (\bar{C}_z^G)^T \\ I & 0 & 0 \\ \hdashline (\bar{B}_p^G)^T & (\bar{D}_{qp}^G)^T & (\bar{D}_{zp}^G)^T \\ 0 & I & 0 \\ \hdashline (\bar{B}_d^G)^T & (\bar{D}_{qd}^G)^T & (\bar{D}_{zd}^G)^T \\ 0 & 0 & I \end{array}\right] N_R < 0 \tag{6.55}$$

$$N_S^T \begin{bmatrix} * \\ \hdashline * \\ \hdashline * \end{bmatrix}^T \left[\begin{array}{cc:c:cc} 0 & S & & & \\ S & 0 & & & \\ \hdashline & & \Pi_S & & \\ \hdashline & & & \frac{1}{\gamma}I & 0 \\ & & & 0 & -\gamma I \end{array}\right] \left[\begin{array}{ccc} \bar{A}^{G} & \bar{B}_p^{G} & \bar{B}_d^{G} \\ I & 0 & 0 \\ \hdashline \bar{C}_q^{G} & \bar{D}_{qp}^{G} & \bar{D}_{qd}^{G} \\ 0 & I & 0 \\ \hdashline \bar{C}_z^{G} & \bar{D}_{zp}^{G} & \bar{D}_{zd}^{G} \\ 0 & 0 & I \end{array}\right] N_S < 0 \tag{6.56}$$

$$\begin{bmatrix} R_t & I \\ I & S_t \end{bmatrix} \geq 0, \tag{6.57}$$

*and for any $\Theta_t \in \boldsymbol{\Theta}_t$, $\Theta_s \in \boldsymbol{\Theta}_s$*

$$[*]^T \Pi_R \begin{bmatrix} I \\ \Upsilon^G \end{bmatrix} \geq 0 \qquad [*]^T \Pi_S \begin{bmatrix} I \\ \Upsilon^G \end{bmatrix} \geq 0, \tag{6.58}$$

*where* $N_R = \ker\left[(\bar{B}_u^G)^T \quad (\bar{D}_{qu}^G)^T \quad (\bar{D}_{zu}^G)^T\right]$, $N_S = \ker\left[\bar{C}_y \quad \bar{D}_{yp}^G \quad \bar{D}_{yd}^G\right]$.

### Multiplier Structures

Solving (6.58) involves an infinite number of constraints on gridding points within the variation space $\Theta_t \times \Theta_s$. Imposing additional constraints on the multipliers reduces condition (6.58) into a finite number of LMIs. The first LMI in (6.58) is equivalent to

$$\Pi_{R11} + \Pi_{R12}\Upsilon^G + \Upsilon^G\Pi_{R12}^T + \Upsilon^G\Pi_{R22}\Upsilon^G \geq 0. \tag{6.59}$$

Under the assumption $\Pi_{R22} < 0$, solving (6.59) can be reduced to solving

$$\Pi_{R11} + \Pi_{R12}\Upsilon^G + \Upsilon^G\Pi_{R12}^T \geq 0. \tag{6.60}$$

A similar constraint is imposed on $\Pi_S$ as well. Then condition (6.58) is affine with respect to $\Upsilon^G$. Instead of checking (6.58) over the whole variation range, it suffices to check only at the vertices of a convex hull that contains the Cartesian product $\Theta_t \times \Theta_s$, i.e.

$$[*]^T \Pi_R \begin{bmatrix} I \\ \hat{\Upsilon}_i^G \end{bmatrix} \geq 0, \quad [*]^T \Pi_S \begin{bmatrix} I \\ \hat{\Upsilon}_i^G \end{bmatrix} \geq 0, \quad i = 1, 2, \ldots, 2^{2(n_t+n_s)}, \tag{6.61}$$

with $\Pi_{R22} < 0$ and $\Pi_{S22} < 0$, where $\hat{\Upsilon}_i^G$ denotes the vertices of the admissible set, and $n_t$ and $n_s$ are the numbers of temporal and spatial scheduling parameters $\theta_t$ and $\theta_s$, respectively.

Furthermore, at the price of additional conservatism, condition (6.58) can be rendered trivially fulfilled and eliminated by using $(D, G)$-scaling [87]. That is achieved by imposing

$$\Pi_{R11} = -\Pi_{R22} > 0, \quad \Pi_{R12} = -\Pi_{R12}^T; \tag{6.62}$$

$$\Pi_{S11} = -\Pi_{S22} > 0, \quad \Pi_{S12} = -\Pi_{S12}^T. \tag{6.63}$$

Under the assumption that $|\theta_{t_i}| < 1$ and $|\theta_{s_i}| < 1$, the multiplier condition (6.58) is trivially fulfilled. Therefore, it is adequate to consider only (6.55)-(6.57) for the existence of the searched controller.

Results presented in [21] are a special case of Theorem 6.6 with the use of a more conservative $D$-scaling, i.e.

$$\Pi_{R11} = -\Pi_{R22} > 0, \quad \Pi_{R12} = 0; \tag{6.64}$$

$$\Pi_{S11} = -\Pi_{S22} > 0, \quad \Pi_{S12} = 0. \tag{6.65}$$

### Controller Scheduling Policy and Controller Construction

Imposing structural constraints on the multipliers reduces computational complexity at the expense of conservatism. Using $(D, G)$- or $D$-scaling, condition (6.54) is trivially fulfilled when the controller is scheduled in the same way as the plant, i.e. $\Upsilon^K = \Upsilon^G$. The imposed multiplier structure induces conservatism. The use of the full block multipliers leads to less conservative results, but requires the construction of a more complex controller scheduling subspace as explained in [43].

After Lyapunov matrices $R$ and $S$, multipliers $\Pi_R$ and $\Pi_S$ have been computed, the controller can either be constructed using closed-loop formulas, see [21] and [14], or solved from the analysis conditions (6.53) and (6.54). The closed-loop Lyapunov function $X^{\tilde{L}}$ is computed in the same way as in the LTSI case (6.33) and (6.34). A general procedure of constructing the closed-loop multiplier $\Pi^L$ is provided in [43]. Nevertheless, when $D$-scaling is imposed on the multipliers $\Pi_R$ and $\Pi_S$ for simplicity, i.e. $\Pi_R = \text{diag}\{\Pi_{R11}, -\Pi_{R11}\}$ and $\Pi_S = \text{diag}\{\Pi_{S11}, -\Pi_{S11}\}$, the closed-loop multiplier $\Pi^L$ can be constructed in the same way as the closed-loop Lyapunov matrix [11], i.e.

$$P_t Q_t^T = I - \Pi_{R11}^t \Pi_{S11}^t, \quad P_s Q_s^T = I - \Pi_{R11}^s \Pi_{S11}^s, \tag{6.66}$$

then

$$\Pi^{L,t} = \begin{bmatrix} \Pi_{S11}^t & I \\ Q_t^T & 0 \end{bmatrix}^{-1} \begin{bmatrix} I & \Pi_{R11}^t \\ 0 & P_t^T \end{bmatrix}, \quad \Pi^{L,s} = \begin{bmatrix} \Pi_{S11}^s & I \\ Q_s^T & 0 \end{bmatrix}^{-1} \begin{bmatrix} I & \Pi_{R11}^s \\ 0 & P_s^T \end{bmatrix}. \tag{6.67}$$

The resulting closed-loop multiplier $\Pi^L$ inherits the structure of $D$-scaling, i.e.

$$\Pi^L = \left[\begin{array}{cc:cc} \Pi^{L,t} & 0 & & \\ 0 & \Pi^{L,s} & & \\ \hdashline & & -\Pi^{L,t} & 0 \\ & & 0 & -\Pi^{L,s} \end{array}\right]. \tag{6.68}$$

The permuted multiplier $\Pi^{\tilde{L}}$ takes the form of (6.52), with $\Pi_{12}^L = \Pi_{21}^L = 0$. The unknown and constant controller matrices in LFT representation in the form of (2.25) can then be easily solved from (6.53).

### 6.5.2 Synthesis Conditions Using PDLFs

The use of CLFs to design LPV controllers allows an infinite rate of parameter variations and results in conservatism, when an upper bound on the variation rate exists. The smaller the bounds, the more conservative is the use of CLFs. This section extends the controller design approach in [14] for temporal LFT systems to distributed LFT LPV systems using PDLFs.

Define $\partial\mathcal{X}(\Theta_t, \Theta_s)$ as the variation rate of a Lyapunov function $\mathcal{X}(\Theta_t, \Theta_s) \in \boldsymbol{\mathcal{X}}_m$. Assume that the varying dynamics of the temporal and spatial variables are decoupled, then

$$\partial\mathcal{X}(\Theta_t, \Theta_s) = \begin{bmatrix} \partial_t \mathcal{X}_t(\Theta_t) & \\ & \partial_s \mathcal{X}_s(\Theta_s) \end{bmatrix}, \tag{6.69}$$

where $\partial_t$ and $\partial_s$ denote the derivatives with respect to time and space, respectively. Let the set of temporal and spatial variation rates of uncertainties be denoted by $(\boldsymbol{\Xi}_t, \boldsymbol{\Xi}_s)$, such that $(\Theta_t, \Theta_s) \in (\boldsymbol{\Theta}_t, \boldsymbol{\Theta}_s)$, and $(\partial_t\Theta_t, \partial_s\Theta_s) \in (\boldsymbol{\Xi}_t, \boldsymbol{\Xi}_s)$.

After incorporating the parameter-dependent Lyapunov functions, the system analysis conditions are formulated as follows.

**Theorem 6.7** *Assume that the controlled system (2.27) and (2.28) is well-posed. The system is exponentially stable and has quadratic performance $\gamma$, if one of following two conditions is satisfied:*

*(i)* *There exists a Lyapunov matrix $\mathcal{X}^{\tilde{L}}(\Theta_t^{\tilde{L}}, \Theta_s^{\tilde{L}})$ in the form of (6.28) with respect to permuted closed-loop uncertainties $(\Theta_t^{\tilde{L}}, \Theta_s^{\tilde{L}})$, such that for any $(\Theta_t^{\tilde{L}}, \Theta_s^{\tilde{L}}) \in (\boldsymbol{\Theta}_t^{\tilde{L}}, \boldsymbol{\Theta}_s^{\tilde{L}})$, $(\partial_t\Theta_t^{\tilde{L}}, \partial_s\Theta_s^{\tilde{L}}) \in (\boldsymbol{\Xi}_t^{\tilde{L}}, \boldsymbol{\Xi}_s^{\tilde{L}})$*

$$\begin{bmatrix} * \\ \hdashline * \end{bmatrix}^T \left[\begin{array}{cc:cc} 0 & \mathcal{X}^{\tilde{L}}(\Theta_t^{\tilde{L}}, \Theta_s^{\tilde{L}}) & & \\ \mathcal{X}^{\tilde{L}}(\Theta_t^{L}, \Theta_s^{L}) & -\partial\mathcal{X}^{\tilde{L}}(\Theta_t^{\tilde{L}}, \Theta_s^{\tilde{L}}) & & \\ \hdashline & & \frac{1}{\gamma}I & 0 \\ & & 0 & -\gamma I \end{array}\right] \left[\begin{array}{cc} \bar{\mathcal{A}}^{\tilde{L}}(\Theta_t^{\tilde{L}}, \Theta_s^{\tilde{L}}) & \bar{\mathcal{B}}_d^{\tilde{L}}(\Theta_t^{\tilde{L}}, \Theta_s^{\tilde{L}}) \\ I & 0 \\ \hdashline \bar{\mathcal{C}}_z^{\tilde{L}}(\Theta_t^{\tilde{L}}, \Theta_s^{\tilde{L}}) & \bar{\mathcal{D}}_{zd}^{\tilde{L}}(\Theta_t^{\tilde{L}}, \Theta_s^{\tilde{L}}) \\ 0 & I \end{array}\right] < 0, \tag{6.70}$$

*where $(\boldsymbol{\Theta}_t^{\tilde{L}}, \boldsymbol{\Theta}_s^{\tilde{L}})$ are the sets of permuted closed-loop uncertainties.*

*(ii)* *There exist Lyapunov matrices $\mathcal{R}(\Theta_t, \Theta_s)$, $\mathcal{S}(\Theta_t, \Theta_s) \in \boldsymbol{\mathcal{X}}_{m^G}$, such that for any $(\Theta_t, \Theta_s) \in (\boldsymbol{\Theta}_t, \boldsymbol{\Theta}_s)$, $(\partial_t\Theta_t, \partial_s\Theta_s) \in (\boldsymbol{\Xi}_t, \boldsymbol{\Xi}_s)$*

$$[*]^T \begin{bmatrix} * \\ \hdashline * \end{bmatrix}^T \left[\begin{array}{cc:cc} 0 & \mathcal{R}(\Theta_t, \Theta_s) & & \\ \mathcal{R}(\Theta_t, \Theta_s) & -\partial\mathcal{R}(\Theta_t, \Theta_s) & & \\ \hdashline & & \frac{1}{\gamma}I & 0 \\ & & 0 & -\gamma I \end{array}\right] \left[\begin{array}{cc} (\bar{\mathcal{A}}^G)^T(\Theta_t, \Theta_s) & (\bar{\mathcal{C}}_z^G)^T(\Theta_t, \Theta_s) \\ I & 0 \\ \hdashline (\bar{\mathcal{B}}_d^G)^T(\Theta_t, \Theta_s) & (\bar{\mathcal{D}}_{zd}^G)^T(\Theta_t, \Theta_s) \\ 0 & I \end{array}\right]$$
$$\times \mathcal{N}_R(\Theta_t, \Theta_s) < 0, \tag{6.71}$$

$$[*]^T \begin{bmatrix} * \\ \hdashline * \end{bmatrix}^T \left[\begin{array}{cc:cc} 0 & \mathcal{S}(\Theta_t, \Theta_s) & & \\ \mathcal{S}(\Theta_t, \Theta_s) & \partial\mathcal{S}(\Theta_t, \Theta_s) & & \\ \hdashline & & \frac{1}{\gamma}I & 0 \\ & & 0 & -\gamma I \end{array}\right] \left[\begin{array}{cc} \bar{\mathcal{A}}^G(\Theta_t, \Theta_s) & \bar{\mathcal{B}}_d^G(\Theta_t, \Theta_s) \\ I & 0 \\ \hdashline \bar{\mathcal{C}}_z^G(\Theta_t, \Theta_s) & \bar{\mathcal{D}}_{zd}^G(\Theta_t, \Theta_s) \\ 0 & I \end{array}\right]$$
$$\times \mathcal{N}_S(\Theta_t, \Theta_s) < 0, \tag{6.72}$$

$$\begin{bmatrix} \mathcal{R}_t(\Theta_t) & I \\ I & \mathcal{S}_t(\Theta_t) \end{bmatrix} \geq 0, \tag{6.73}$$

*where*

$$\mathcal{N}_R(\Theta_t, \Theta_s) = \ker \left[ (\bar{\mathcal{B}}_u^G)^T(\Theta_t, \Theta_s) \quad (\bar{\mathcal{D}}_{zu}^G)^T(\Theta_t, \Theta_s) \right], \tag{6.74}$$
$$\mathcal{N}_S(\Theta_t, \Theta_s) = \ker \left[ \bar{\mathcal{C}}_y^G(\Theta_t, \Theta_s) \quad \bar{\mathcal{D}}_{yd}^G(\Theta_t, \Theta_s) \right]. \tag{6.75}$$

Condition (ii) is the result of applying the elimination lemma to (6.70).

To solve the infinite set of LMIs (6.71)-(6.73), two commonly used approaches are

1. gridding [18], where inequalities are solved at grid points that cover the range of parameter variation and rates $(\boldsymbol{\Theta}_t, \boldsymbol{\Theta}_s) \times (\boldsymbol{\Xi}_t, \boldsymbol{\Xi}_s)$;

2. LFT LPV synthesis, which relies on the application of S-procedure [88], or the extended version - FBSP.

Considered here is LFT LPV controller synthesis. Assume a quadratic form of the Lyapunov matrices $\mathcal{R}(\Theta_t, \Theta_s)$ and $\mathcal{S}(\Theta_t, \Theta_s)$, and bring the parameter-varying system matrices and null spaces in their LFT representations, respectively. After performing the multiplications of LFT systems, conditions (6.71)-(6.73) can be rewritten as

$$[*]^T \left[\begin{array}{cc|cc} 0 & P & & \\ P & 0 & & \\ \hline & & \frac{1}{\gamma}I & 0 \\ & & 0 & -\gamma I \end{array}\right] \left(\Omega \star \begin{bmatrix} G_{P11} & G_{P12} \\ G_{P21} & G_{P22} \end{bmatrix}\right) < 0 \tag{6.76}$$

$$[*]^T \left[\begin{array}{cc|cc} 0 & Q & & \\ Q & 0 & & \\ \hline & & \frac{1}{\gamma}I & 0 \\ & & 0 & -\gamma I \end{array}\right] \left(\Omega \star \begin{bmatrix} G_{Q11} & G_{Q12} \\ G_{Q21} & G_{Q22} \end{bmatrix}\right) < 0 \tag{6.77}$$

$$[*]^T \left[\begin{array}{cc|cc} P_t & 0 & & \\ 0 & Q_t & & \\ \hline & & 0 & I \\ & & I & 0 \end{array}\right] \left(\begin{bmatrix} \Theta_t & \\ & \Theta_t \end{bmatrix} \star \begin{bmatrix} G_{11} & G_{12} \\ G_{21} & G_{22} \end{bmatrix}\right) \geq 0, \tag{6.78}$$

where $P,\ Q \in \boldsymbol{\mathcal{X}}_{m^G}$; the augmented plant uncertainty $\Omega$ arises from the LFT multiplication in (6.71) and (6.72), and is defined as $\Omega = \mathrm{diag}\{\partial\Upsilon^G, \Upsilon^G, \Upsilon^G, \Upsilon^G, \Upsilon^G\}$. The derivation from (6.71)-(6.73) to (6.76)-(6.78), and the algebraic expressions of the constant matrices in (6.76)-(6.78) can be found in Appendix B. It is easy to see that the quadratic matrix inequalities (6.76)-(6.78) are now in the form of (6.46). Applying the FBSP to each of them results in the following synthesis conditions.

**Theorem 6.8** *Consider an LTSV system (2.16) and (2.17) with its parameter variation and rate sets* $(\boldsymbol{\Theta}_t, \boldsymbol{\Theta}_s)$ *and* $(\Xi_t, \Xi_s)$*, respectively. There exists a distributed LPV controller in the form of (2.23), that guarantees well-posedness, exponential stability and quadratic performance* $\gamma$ *of the closed-loop system (2.24), if there exist matrices* $P,\ Q \in \boldsymbol{\mathcal{X}}_{m^G}$*, multipliers* $\Pi_P,\ \Pi_Q \in \boldsymbol{\mathcal{Y}}_{(5n_{\Theta_t^G}, 5n_{\Theta_s^G})}$ *and* $\Pi \in \boldsymbol{\mathcal{Y}}_{(2n_{\Theta_t^G}, 2n_{\Theta_t^G})}$*, that satisfy*

$$\left[\begin{array}{c} * \\ \hline * \end{array}\right]^T \left[\begin{array}{c|cc|cc} \Pi_P & & & & \\ \hline & 0 & P & & \\ & P & 0 & & \\ \hline & & & \frac{1}{\gamma}I & 0 \\ & & & 0 & -\gamma I \end{array}\right] \left[\begin{array}{cc} G_{P11} & G_{P12} \\ I & 0 \\ \hline G_{P21} & G_{P22} \end{array}\right] < 0, \tag{6.79}$$

$$\left[\begin{array}{c} * \\ \hline * \end{array}\right]^T \left[\begin{array}{c|cc|cc} \Pi_Q & & & & \\ \hline & 0 & Q & & \\ & Q & 0 & & \\ \hline & & & \frac{1}{\gamma}I & 0 \\ & & & 0 & -\gamma I \end{array}\right] \left[\begin{array}{cc} G_{Q11} & G_{Q12} \\ I & 0 \\ \hline G_{Q21} & G_{Q22} \end{array}\right] < 0, \tag{6.80}$$

$$\begin{bmatrix} * \\ \hdashline * \end{bmatrix}^T \left[\begin{array}{c:cc:cc} -\Pi & & & & \\ \hdashline & P_t & 0 & & \\ & 0 & Q_t & & \\ \hdashline & & & 0 & I \\ & & & I & 0 \end{array}\right] \left[\begin{array}{cc} G_{11} & G_{12} \\ I & 0 \\ \hdashline G_{21} & G_{22} \end{array}\right] \geq 0, \tag{6.81}$$

*and* $\forall(\Theta_t, \Theta_s) \in (\boldsymbol{\Theta}_t, \boldsymbol{\Theta}_s)$, $(\partial_t\Theta_t, \partial_s\Theta_s) \in (\boldsymbol{\Xi}_t, \boldsymbol{\Xi}_s)$

$$[*]^T \Pi_P \begin{bmatrix} I \\ \Omega \end{bmatrix} \geq 0, \tag{6.82}$$

$$[*]^T \Pi_Q \begin{bmatrix} I \\ \Omega \end{bmatrix} \geq 0, \tag{6.83}$$

$$\begin{bmatrix} * \\ \hdashline * \end{bmatrix}^T \Pi \left[\begin{array}{cc} I & \\ & I \\ \hdashline \Theta_t & \\ & \Theta_t \end{array}\right] > 0. \tag{6.84}$$

**Proof** The proof of Theorem 6.8 can be found in Appendix B. ■

**Controller Construction**

Discussions on the multiplier structures in Section 6.5.1 for the controller design using CLFs apply when PDLFs are used. If the quadratic LFT matrix functions $\mathcal{R}(\Theta_t, \Theta_s)$ and $\mathcal{S}(\Theta_t, \Theta_s)$ have been found after solving (6.79)–(6.84), to the author's knowledge, the LPV controller can only be constructed using explicit formulas, see [14] and [18]. Nevertheless, due to the use of gain-scheduled Lyapunov functions, the implementation of the designed controller in the form of (2.23) requires the real-time measurement of the parameter variation rates. Under the assumption of decoupled temporal and spatial variations, the derivatives of spatial parameters can be measured off-line and remain unchanged on-line. However, it is often difficult to estimate the temporal variation rate. Thus, in order to remove the controller dependence on $\partial_t\Theta_t$, only one of the Lyapunov matrices $\mathcal{R}(\Theta_t, \Theta_s)$ or $\mathcal{S}(\Theta_t, \Theta_s)$ is defined as parameter-varying [13], e.g. let $R$ be constant and $\mathcal{S}(\Theta_t, \Theta_s)$ be parameter-dependent. For the sake of brevity, the argument $(\Theta_t, \Theta_s)$ of a parameter-dependent matrix is left out in the following equations, e.g. a calligraphic $\mathcal{A}$ is short for $\mathcal{A}(\Theta_t, \Theta_s)$, whereas $R$ stands for a constant matrix. The continuous LPV controller is obtained as

$$\begin{aligned}
\mathcal{N} &= I - \mathcal{S}R, \\
\mathcal{F} &= -\,[(\bar{\mathcal{D}}^G_{zu})^T \bar{\mathcal{D}}^G_{zu}]^{-1} \times [\gamma(\bar{\mathcal{B}}^G_u)^T R^{-1} + (\bar{\mathcal{D}}^G_{zu})^T \bar{\mathcal{C}}^G_z], \\
\mathcal{L} &= -\,[\gamma\mathcal{S}^{-1}(\bar{\mathcal{C}}^G_y)^T + \bar{\mathcal{B}}_d(\bar{\mathcal{D}}^G_{yd})^T] \times [\bar{\mathcal{D}}^G_{yd}(\bar{\mathcal{D}}^G_{yd})^T]^{-1}, \\
\bar{\mathcal{A}}^K &= -\,\mathcal{N}^{-1}\big((\bar{\mathcal{A}}^G)^T + \mathcal{S}[\bar{\mathcal{A}}^G + \bar{\mathcal{B}}^G_u\mathcal{F} + \mathcal{L}\bar{\mathcal{C}}^G_y]R + \gamma^{-1}\mathcal{S}[\bar{\mathcal{B}}^G_d + \mathcal{L}\bar{\mathcal{D}}^G_{yd}](\bar{\mathcal{B}}^G_d)^T \\
&\qquad + \gamma^{-1}(\bar{\mathcal{C}}^G_z)^T[\bar{\mathcal{C}}^G_z + \bar{\mathcal{D}}^G_{zu}\mathcal{F}]R\big), \\
\bar{\mathcal{B}}^K &= \mathcal{N}^{-1}\mathcal{S}\mathcal{L}, \\
\bar{\mathcal{C}}^K &= \mathcal{F}R, \\
\bar{\mathcal{D}}^K &= 0.
\end{aligned}$$

### 6.5.3 Experimental Results

The experimental setup is modified as a spatially-varying system by deactivating six actuator/sensor pairs just as for the LPV model identification in Chapter 5. The control objective is defined in the same way as in the LTSI case in Section 6.4.3—suppressing parallel injected output disturbances. Based on the black-box identified spatial LPV model, distributed controllers using both CLFs and PDLFs have been designed by shaping mixed sensitivities, and have been validated experimentally.

- Distributed controller using CLFs: Multipliers with $D$-scalings are used. The resulting controller is of temporal order $m_0^K = 5$, and of spatial order $m_+^K = m_-^K = 4$.
- Distributed controller using PDLFs: Multipliers with $D$-scalings are used. Due to the spatial variation of the subsystem, the parameter-dependent Lyapunov matrix is a function of spatial uncertainties. A quadratic Lyapunov matrix can be written in LFT form as

$$
\begin{aligned}
R(\Theta_s) &= \begin{bmatrix} R_t & \\ & R_s(\Theta_s) \end{bmatrix} = T_R^T(\Theta_s) P T_R(\Theta_s) = [*]^T \left[\begin{array}{c:c} P_t & \\ \hdashline & P_s \end{array}\right] \left[\begin{array}{c:c} I & \\ \hdashline & T_{R_s}(\Theta_s) \end{array}\right] \\
&= [*]^T \left[\begin{array}{c:c} P_t & \\ \hdashline & P_s \end{array}\right] \left[\begin{array}{c:c} I & \\ \hdashline & \Theta_s \star \begin{bmatrix} T_{R_s11} & T_{R_s12} \\ T_{R_s21} & T_{R_s22} \end{bmatrix} \end{array}\right] = [*]^T \left[\begin{array}{c:c} P_t & \\ \hdashline & P_s \end{array}\right] \left( \Theta_s \star \left[\begin{array}{c:cc} T_{R_s11} & 0 & T_{R_s12} \\ \hdashline 0 & I & 0 \\ T_{R_s21} & 0 & T_{R_s22} \end{array}\right] \right).
\end{aligned}
\tag{6.85}
$$

  Let $R_s(\Theta_s)$ be a first order polynomial in $\Theta_s$, i.e. $R_s(\Theta_s) = P_0 + P_1\Theta_s$, which yields the following selection

$$
P_s = \begin{bmatrix} 0 & P_1/2 \\ P_1/2 & P_0 \end{bmatrix}, \quad \begin{bmatrix} T_{R_s11} & T_{R_s12} \\ T_{R_s21} & T_{R_s22} \end{bmatrix} = \left[\begin{array}{c:c} 0 & I \\ \hdashline I & 0 \\ 0 & I \end{array}\right]. \tag{6.86}
$$

  The obtained controller is of temporal order $m_0^K = 4$, and of spatial order $m_+^K = m_-^K = 4$.

Fig. 6.7 shows the comparison of the experimental responses in time domain between open loop and closed-loop system with controllers designed using both PDLFs and CLFs. Fig. 6.8 shows the comparison in frequency domain—FRFs from injected output disturbance to collocated output. The distributed controller designed using PDLFs improves the closed-loop performance significantly at most of the subsystems, especially in the low frequency range. Provided the knowledge of the upper bound on the spatial variation rate, the conservatism caused by the use of CLFs is largely reduced by the use of PDLFs. The improved experimental results confirm the benefits of using PDLFs.

## 6.6 Summary

This chapter has addressed the distributed controller design problem for both LTSI and LTSV systems, where a controller inheriting the distributed nature of the plant is desired.

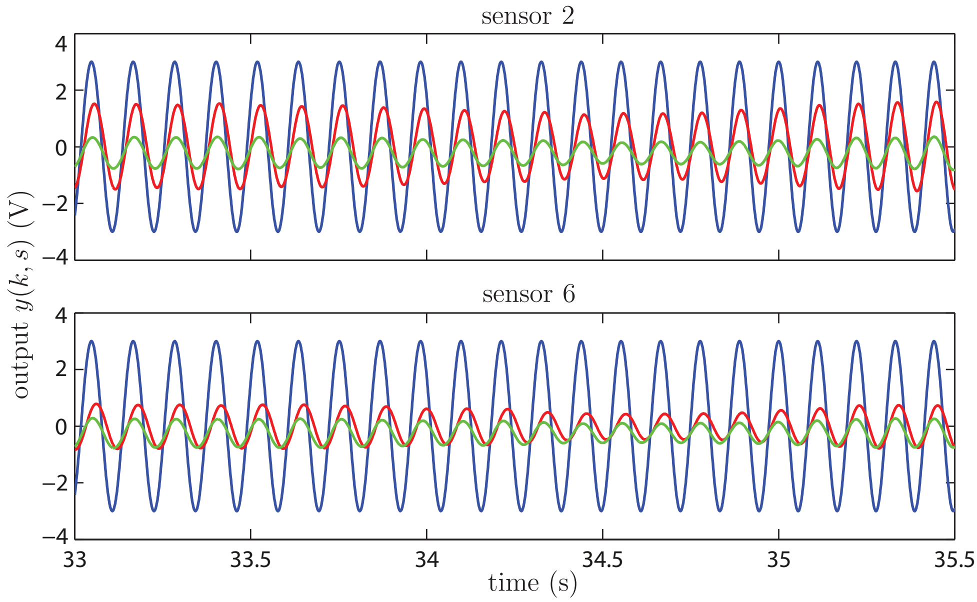


Figure 6.7: With output disturbances injected, comparison of measured outputs over time between open-loop response(blue curve), closed-loop response with PDLFs (green curves), and closed-loop response with CLFs (red curves)

The input/output models identified in Chapter 5 have been first converted into their multidimensional state space representations, such that the state-space based controller design techniques can be applied. The procedures for constructing a generalized plant for shaping the mixed sensitivities of the spatio-temporal system have been discussed. Analysis and synthesis conditions for a distributed LTSI controller design have been briefly reviewed and implemented on the test structure to suppress the injected disturbance. The performance of the obtained distributed controller has been compared with that of a decentralized controller. The experimental results confirm that with the information exchange between subsystems, an improved overall performance has been achieved. For LTSV systems, the distributed LPV controller design using CLFs has been considered. To reduce the conservatism due to the bounded variation rates of the scheduling parameters, the LPV controller design techniques using PDLFs originally developed for temporal systems have been extended here to multidimensional systems. The designed LPV controllers using both CLFs and PDLFs have been tested experimentally. The less conservative LPV controller designed using PDLFs has demonstrated a superior performance in terms of suppressing the injected disturbance.

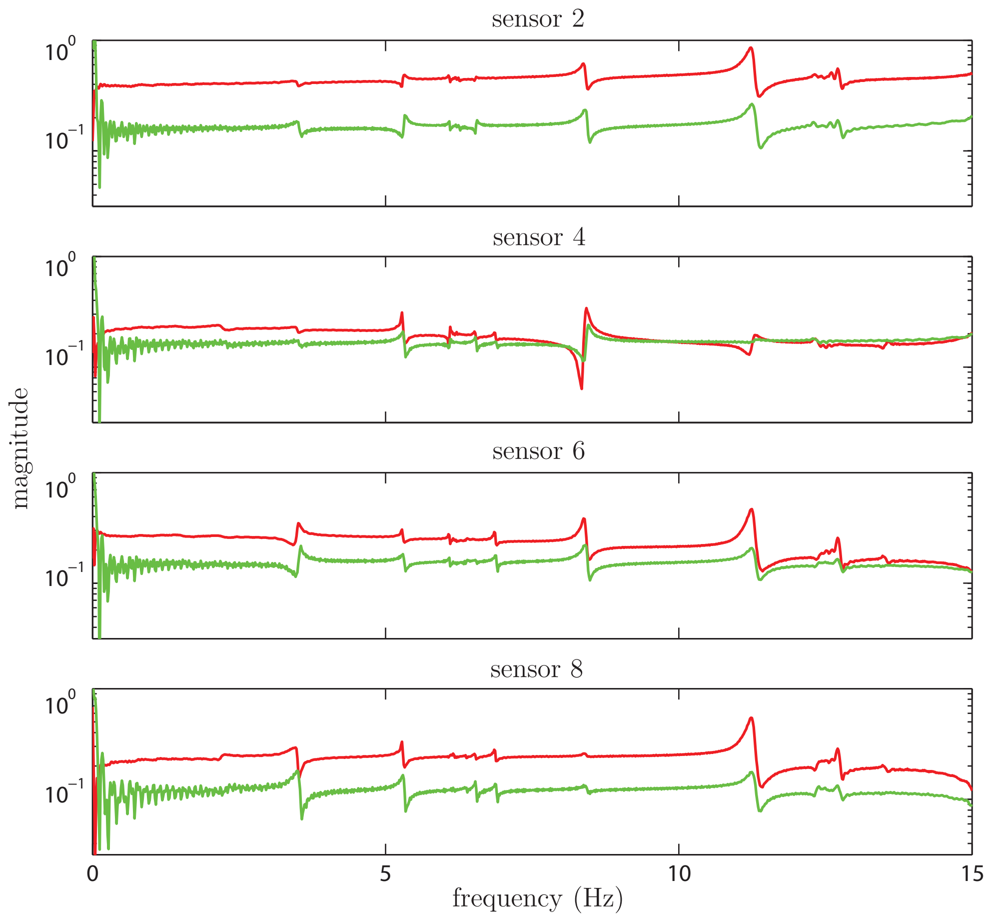


Figure 6.8: Comparison of FRFs from injected output disturbance to collocated output between closed-loop response with PDLFs (green curves), and closed-loop response with CLFs (red curves)

# Chapter 7

# Distributed Anti-Windup Compensator Design

## 7.1 Introduction

Actuator saturation often occurs in physical systems. The constrained control behaviour is usually not captured when solving the controller design problem as described in Chapter 6. In the presence of limitations on the actuator capacity, the established closed-loop performance suffers from deterioration, or even instability. For this reason, anti-windup (AW) compensators are often considered in real applications to counteract the effects of actuator saturation.

Over the last decades, AW compensator design has been addressed in numerous works by applying various approaches. A linear conditioning scheme that augments a system with a linear transfer function as the AW compensator, which results from the right coprime factorisation of the plant, is proposed in [36], aiming at driving the saturated system back to the intended linear behaviour as quickly as possible. In [39], provided that stability is guaranteed for a constrained system, performance can be tuned by minimizing the $\mathcal{L}_2$ gain using a static compensator. This approach is further developed in [37] [89] with a compensator of order greater than or equal to that of the plant. AW compensators that handle the controller saturation as well as plant uncertainties are considered in [38]. In [42], a more general and potentially less conservative framework for the robust analysis of nonlinearities is developed, which is applied to solve the AW compensator design problem in [90] and [91]. The common feature of the aforementioned works is a two-step approach, where the synthesis problems are solved separately, one after the other, for the controller and the AW compensator. Different from the conventional two-step approach, [92] computes the controller and the AW compensator in one step with one goal, where the gridding method is employed to solve the resulting nonlinear inequalities.

Among the existing works, very few deal with the saturation problem of distributed parameter systems. In [40], a robust AW compensator for the reaction-diffusion equation is presented. The centralized scheme may encounter difficulties when applied to a large scale system. Instead of a large model describing the system dynamics in a centralized manner, a localized model of smaller size is much easier to handle. Working in the distributed system framework developed in [8], [41] proposes a distributed AW compensator for an open-water channel control system, which boils down to the search for a static gain value that guarantees Lyapunov stability.

Inspired by the work in [41], [89] and [37], this chapter proposes an AW compensator design using a two-step approach for LTSI systems. The designed AW compensator can be implemented on top of an existing closed-loop system, with global stability and a bound on $\mathcal{L}_2$ performance of the augmented system guaranteed. The tool developed in [42] – the IQC approach – is employed to impose constraints on the nonlinear saturation operator, such that the analysis and synthesis conditions can be formulated in terms of LMIs.

This chapter includes results reported in [93]. The rest of this chapter is organized as follows: Section 7.2 recaps a lumped AW architecture, and the framework of IQCs, with an emphasis on its application to the saturation/deadzone operator, and robust analysis. Section 7.3 extends the AW scheme for lumped systems to spatially-interconnected systems. In Section 7.3.1, stability analysis via IQCs is applied to constrained distributed systems. Synthesis conditions for an AW compensator are derived in Section 7.3.2. A decentralized AW scheme is designed for comparison in Section 7.4. Simulation results obtained on an actuated Euler-Bernoulli beam demonstrate the performance of both the distributed and the decentralized AW schemes in Section 7.5.

## 7.2 Preliminary

This section recaps the working principle of a lumped AW scheme with full-order dynamics. A mathematical tool – IQCs – that is often used to analyse the robust stability of a feedback system with nonlinear uncertainties is reviewed here, and will be employed later for the derivation of system analysis conditions.

### 7.2.1 AW Scheme for Lumped Systems

The two-step AW design, also referred to as control of constrained systems [94], consists of two steps:

1. Design a linear controller $K$, such that when $|u| \leq \bar{u}$, where $\bar{u}$ is the maximum capacity of the physical actuators, stability and a performance bound are guaranteed on the closed-loop system.
2. Design a linear AW compensator $\Psi$, such that when $|u| > \bar{u}$, the achieved stability and performance from step 1 are preserved to a certain extent.

The AW framework for lumped systems proposed in [89] is shown in Fig. 7.1. When actuator saturation does not occur, $u = u_0$ holds; otherwise, the AW compensator $\Psi$ is activated and generates two compensation signals: $v_1 \in \mathbb{R}^{n_u}$ is added to the controller output, while $v_2 \in \mathbb{R}^{n_y}$ enters the controller as part of the controlled input, i.e., $y = y_0 + v_2$. The state space realization of the AW compensator suggested in [89]

$$\begin{bmatrix} x^{\Psi}(k+1) \\ \hline \begin{bmatrix} v_1(k) \\ v_2(k) \end{bmatrix} \end{bmatrix} = \left[\begin{array}{c|c} A^{\Psi} & B^{\Psi} \\ \hline C^{\Psi} & D^{\Psi} \end{array}\right] \begin{bmatrix} x^{\Psi}(k) \\ \hline e(k) \end{bmatrix}, \tag{7.1}$$

where $e = \tilde{u} - u$, possesses full-order dynamics, and allows more degrees of freedom than a static compensator. The saturation operator is defined as

$$u = \mathrm{sat}(u_0 + v_1) = \mathrm{sat}(\tilde{u}), \tag{7.2}$$

where $\mathrm{sat}(\tilde{u}) = \mathrm{sign}(\tilde{u}) * \min\{\bar{u}, |\tilde{u}|\}$.

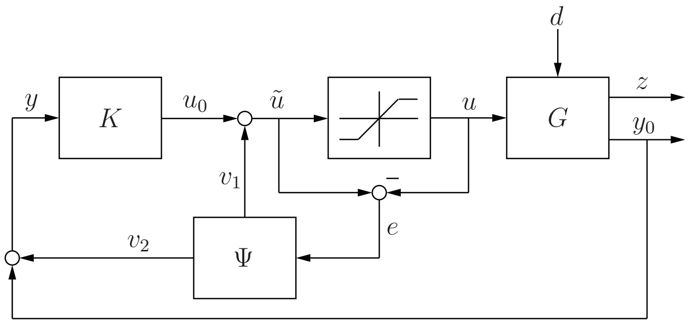


Figure 7.1: AW scheme proposed for lumped systems in [89]

### 7.2.2 Robust Analysis Using IQCs

IQCs [42] can be used to analyse systems with various types of uncertainties. It describes the behaviour of a system in the frequency domain in terms of an integral constraint on the Fourier transformations of the input/output signals [95].

Let $\mathbb{R}H_\infty$ be the set of proper, stable and rational functions with real coefficients, $L_2^l(0,\infty)$ be the space of square integrable signals, i.e., a signal $f(t) \in L_2^l(0,\infty)$, if its energy

$$\| f(t) \|_2 = \int_0^\infty \| f(\tau) \|^2 \, d\tau \tag{7.3}$$

is bounded. The definition of IQCs is given as follows.

**Definition 7.1 (IQC [42])** *Two signals $w \in L_2^m(0,\infty)$ and $v \in L_2^l(0,\infty)$ are said to satisfy the IQC defined by a Hermitian-valued function $\Pi$, where $\Pi : j\mathbb{R} \to \mathbb{C}^{(l+m)\times(l+m)}$, if*

$$\int_{-\infty}^{\infty} \begin{bmatrix} \hat{v}(jw) \\ \hat{w}(jw) \end{bmatrix}^* \Pi(jw) \begin{bmatrix} \hat{v}(jw) \\ \hat{w}(jw) \end{bmatrix} dw \geq 0, \tag{7.4}$$

*where $\hat{v}(jw)$ and $\hat{w}(jw)$ are the Fourier transformations of $v$ and $w$, respectively.*

Provided a proper choice of the multiplier $\Pi$, IQCs can be used to describe relations between signals. For example, with the multiplier $\Pi = \begin{bmatrix} I & 0 \\ 0 & -I \end{bmatrix}$, (7.4) defines $\| w \|_2 \leq \| v \|_2$.

**Multiplier for Saturation/Deadzone Operator**

With the definition of the saturation operator given, the deadzone operator is defined as $e = \mathrm{dz}(\tilde{u}) = u - \mathrm{sat}(u)$; both of them are nonlinear operators. By allowing additional conservatism, the saturation and deadzone operators can be over-bounded by a linear operator – sector [0 1] – as shown in Fig. 7.2.

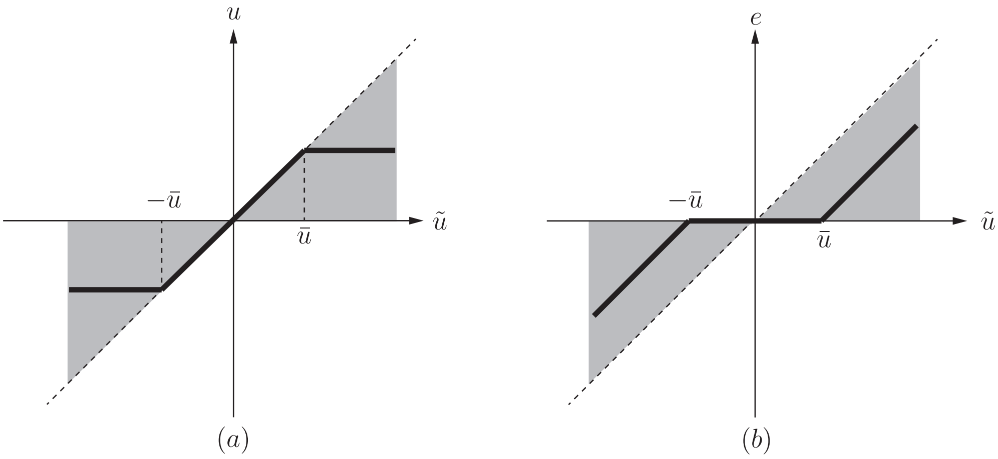


Figure 7.2: Sector [0 1] bounds a saturation operator (a) and a deadzone operator (b)

Consider now only the deadzone function. The fact that the deadzone operator is bounded by a sector [0 1] implies that for any positive definite symmetric matrix $\tilde{W} \in \mathbb{R}^{n_u \times n_u}$, the condition

$$e^T \tilde{W}(\tilde{u} - e) \geq 0 \tag{7.5}$$

holds, which can be reformulated as a quadratic matrix inequality as

$$2e^T \tilde{W} \tilde{u} - 2e^T \tilde{W} e \geq 0, \tag{7.6}$$

$$e^T \tilde{W} \tilde{u} + \tilde{u}^T \tilde{W} e - 2e^T \tilde{W} e \geq 0, \tag{7.7}$$

$$[*]^T \begin{bmatrix} -2\tilde{W} & \tilde{W} \\ \tilde{W} & 0 \end{bmatrix} \begin{bmatrix} e \\ \tilde{u} \end{bmatrix} \geq 0. \tag{7.8}$$

Therefore a static multiplier $\Pi := \begin{bmatrix} -2\tilde{W} & \tilde{W} \\ \tilde{W} & 0 \end{bmatrix}$ can be used to cast the nonlinear deadzone function into a quadratic constraint.

**Stability Analysis**

The characterization of a nonlinear operator in terms of (7.4) makes sense only when the involved signals are bounded, such that their square integral exists. Thus, stability analysis on the feedback loop as shown in Fig. 7.3 is required.

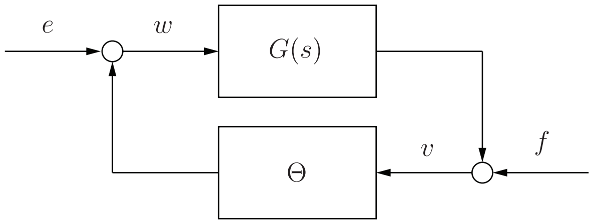


Figure 7.3: Output feedback loop, where $\Theta$ can be a linear or nonlinear bounded operator.

It is assumed that $G(s) \in \mathbb{R}H_\infty^{l\times m}$ is an LTI operator, and $\Theta$ is a bounded operator that maps from $L_{2e}^l(0,\infty)$ to $L_{2e}^m(0,\infty)$, and can be used to describe nonlinear components of a system. Noise or disturbances are injected through $e$ and $f$; both are square integrable on finite intervals. Without loss of generality, assume $e = 0$ in Fig. 7.3, so that $w = \Theta(v)$.

The stability of the feedback loop can be stated as follows [42].

**Theorem 7.1** *The feedback interconnection of $G(s)$ and $\Theta$ is stable, where $G(s) \in \mathbb{R}H_\infty^{l\times m}$, and $\Theta$ is a bounded causal operator, if*

*(i) for every $\zeta \in [0,1]$, the interconnection of $G(s)$ and $\zeta\Theta$ is well-posed;*

*(ii) for every $\zeta \in [0,1]$, the IQC defined by $\Pi$ is satisfied by $\zeta\Theta$;*

*(iii) there exists $\epsilon > 0$ such that*

$$\begin{bmatrix} G(j\omega) \\ I \end{bmatrix}^* \Pi(j\omega) \begin{bmatrix} G(j\omega) \\ I \end{bmatrix} \le -\epsilon I, \quad \forall \omega \in \mathbb{R}. \tag{7.9}$$

The multiplier $\Pi(j\omega)$ can be parametrized to describe various nonlinear operators. It can be defined either static or dynamic. The well-posedness in condition (i) can be verified through the invertibility of $I - \zeta G\Theta$. Finding dynamic multipliers that fulfil condition (ii) is not trivial and will be further discussed in Section 7.3.1. Under the assumption that $\Pi(j\omega)$ is a rational function with no poles on the imaginary axis, condition (iii) can be cast into a quadratic problem, and further into LMIs with the application of Kalman-Yakubovic-Popov (KYP) Lemma (see Appendix C.2) as follows.

Consider the transfer function $G(j\omega) := C(j\omega I - A)^{-1}B + D$, and a frequency-independent multiplier $\Pi(jw) = M$. The left side of (7.9) can be expressed in terms of $G$ and $M$ as

$$\begin{bmatrix} G(j\omega) \\ I \end{bmatrix}^* M \begin{bmatrix} G(j\omega) \\ I \end{bmatrix} = \begin{bmatrix} (j\omega I - A)^{-1}B \\ I \end{bmatrix}^* \left( \begin{bmatrix} C^T & 0 \\ D^T & I \end{bmatrix} M \begin{bmatrix} C & D \\ 0 & I \end{bmatrix} \right) \begin{bmatrix} (j\omega I - A)^{-1}B \\ I \end{bmatrix}. \tag{7.10}$$

According to [96], with the application of the KYP lemma, (7.10) is equivalent to: there exists a positive and symmetric matrix $X$, and a positive scalar $\mu$, such that

$$\begin{bmatrix} A^T X + XA & XB \\ B^T X & 0 \end{bmatrix} + \begin{bmatrix} C^T & 0 \\ D^T & I \end{bmatrix} \mu M \begin{bmatrix} C & D \\ 0 & I \end{bmatrix} < 0. \tag{7.11}$$

## 7.3 Distributed AW Compensator Scheme

Analogous to the distributed pattern of the controller, it is desired that the AW compensator also reflects the distributed structure of the closed-loop system. The local exchange of saturation information may lead to a better allocation of control effort among subsystems. Inspired by the AW scheme for lumped systems in Fig. 7.1, an AW scheme for distributed systems in Fig. 7.4 is proposed, where the distributed plant $G$, the controller $K$, and the AW compensator $\Psi$ interact with neighbouring subsystems and share a common communication topology. For the clarity of presentation, all involved signals in Fig. 7.4 are indexed only by their spatial variables.

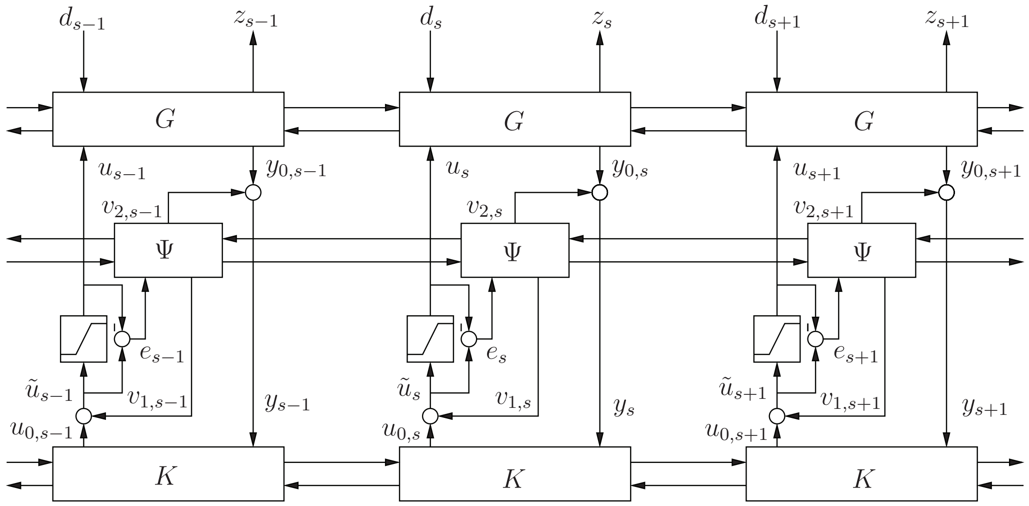


Figure 7.4: Distributed structure of the proposed AW compensator

The compact state space models of the plant and the controller that account for the integrated AW compensator are slightly modified from (2.11) and (2.20) to

$$\begin{bmatrix} (\boldsymbol{\Delta}_m^G x^G)(k,s) \\ \hdashline z(k,s) \\ y_0(k,s) \end{bmatrix} = \left[\begin{array}{c:cc} A^G & B_d^G & B_u^G \\ \hdashline C_z^G & D_{zd}^G & D_{zu}^G \\ C_y^G & D_{yd}^G & D_{yu}^G \end{array}\right] \begin{bmatrix} x^G(k,s) \\ \hdashline d(k,s) \\ u(k,s) \end{bmatrix}, \tag{7.12}$$

$$\begin{bmatrix} (\boldsymbol{\Delta}_m^K x^K)(k,s) \\ \hdashline u_0(k,s) \end{bmatrix} = \left[\begin{array}{c:c} A^K & B^K \\ \hdashline C^K & D^K \end{array}\right] \begin{bmatrix} x^K(k,s) \\ \hdashline y(k,s) \end{bmatrix}, \tag{7.13}$$

respectively. The distributed AW compensator $\Psi$ at subsystem $s$ is realized as

$$\begin{bmatrix} x_t^\Psi(k+1,s) \\ x_s^{\Psi,+}(k,s+1) \\ x_s^{\Psi,-}(k,s-1) \\ \hdashline \begin{bmatrix} v_1(k,s) \\ v_2(k,s) \end{bmatrix} \end{bmatrix} = \left[\begin{array}{ccc:c} A_{tt}^\Psi & A_{ts}^{\Psi,+} & A_{ts}^{\Psi,-} & B_t^\Psi \\ A_{st}^{\Psi,+} & A_{ss}^{\Psi,++} & A_{ts}^{\Psi,+-} & B_s^{\Psi,+} \\ A_{st}^{\Psi,-} & A_{ss}^{\Psi,+-} & A_{ts}^{\Psi,--} & B_s^{\Psi,-} \\ \hdashline C_{v_1,t}^\Psi & C_{v_1,s}^{\Psi,+} & C_{v_1,s}^{\Psi,-} & D_{v_1e}^\Psi \\ C_{v_2,t}^\Psi & C_{v_2,s}^{\Psi,+} & C_{v_2,s}^{\Psi,-} & D_{v_1e}^\Psi \end{array}\right] \begin{bmatrix} x_t^\Psi(k,s) \\ x_s^{\Psi,+}(k,s) \\ x_s^{\Psi,-}(k,s) \\ \hdashline e(k,s) \end{bmatrix}, \tag{7.14}$$

whose compact form writes

$$\begin{bmatrix} (\boldsymbol{\Delta}_m^{\Psi} x^{\Psi})(k,s) \\ \hdashline \begin{bmatrix} v_1(k,s) \\ v_2(k,s) \end{bmatrix} \end{bmatrix} = \left[\begin{array}{c:c} A^{\Psi} & B^{\Psi} \\ \hdashline C^{\Psi} & D^{\Psi} \end{array}\right] \begin{bmatrix} x^{\Psi}(k,s) \\ \hdashline e(k,s) \end{bmatrix}. \tag{7.15}$$

Note that although (7.1) and (7.15) appear similar, they fall into to two classes of systems: (7.1), as a lumped system, exhibits only temporal dynamics; (7.15) is a spatio-temporal system, whose signals are two-dimensional with respect to time and space.

*Remarks*:

- When no saturation occurs, the system in Fig. 7.4 retrieves the behaviour of the unconstrained closed-loop system in Fig. 2.5.
- The compensator scheme in Fig. 7.4 is a distributed version of Fig. 7.1: cutting off the communication channels between the plant, the controller, and the AW compensator subsystems leads to a number of dynamically decoupled systems, each including lumped $G$, $K$ and $\Psi$—an exact copy of Fig. 7.1.

Among the dynamic components in Fig. 7.4, the plant dynamics $G$ are assumed to be known, usually through system identification, whereas the controller $K$ is designed independently of the AW compensator $\Psi$ by solving the synthesis conditions described in Section 6.4.1. Provided the state space realizations of the plant subsystem (7.12) and controller subsystem (7.13), replacing the controller input $y(k,s)$ with $y_0(k,s) + v_2(k,s)$, the control effort $u(k,s)$ with $u_0(k,s)+v_1(k,s)-e(k,s)$, and pulling the plant subsystem $G$ and its controller $K$ together, give rise to the closed-loop subsystem $L$ whose input signals are $d(k,s)$, $e(k,s)$, and a vector $v(k,s)$ that consists of the compensator outputs $v(k,s) := \begin{bmatrix} v_1(k,s)^T & v_2(k,s)^T \end{bmatrix}^T$, and outputs are $z(k,s)$ and $\tilde{u}(k,s) = u_0(k,s) + v_1(k,s)$. The state space representation of the closed-loop subsystem $L$ is written as

$$\begin{bmatrix} (\boldsymbol{\Delta}_m^{L} x^{L})(k,s) \\ \hdashline z(k,s) \\ \tilde{u}(k,s) \end{bmatrix} = \left[\begin{array}{c:ccc} A^{L} & B_d^{L} & B_e^{L} & B_v^{L} \\ \hdashline C_z^{L} & D_{zd}^{L} & D_{ze}^{L} & D_{zv}^{L} \\ C_{\tilde{u}}^{L} & D_{\tilde{u}d}^{L} & D_{\tilde{u}e}^{L} & D_{\tilde{u}v}^{L} \end{array}\right] \begin{bmatrix} x^{L}(k,s) \\ \hdashline d(k,s) \\ e(k,s) \\ v(k,s) \end{bmatrix}, \tag{7.16}$$

whose state vector $x^L(k,s)$ is arranged as (2.22) by separating temporal, positive and negative spatial states. Recall the definition of a deadzone function that maps from $\tilde{u}$ to $e$. Replacing the saturation function with a deadzone function allows to restructure the distributed system in Fig. 7.4 in a compact way as shown in Fig. 7.5.

For the purpose of system analysis, Fig. 7.5 can be further restructured by pulling the AW compensator $\Psi$ and the closed-loop subsystem $L$ together into one block $P$ as shown in Fig. 7.6. Then the resulting distributed system can be seen as the interconnection of LTSI subsystem $P$ with an uncertainty in the form of a deadzone operator.

As mentioned in Section 7.2.2, the deadzone operator is a memoryless nonlinear operator, which can be over-bounded by the sector [0 1]. The replacement of the deadzone operator

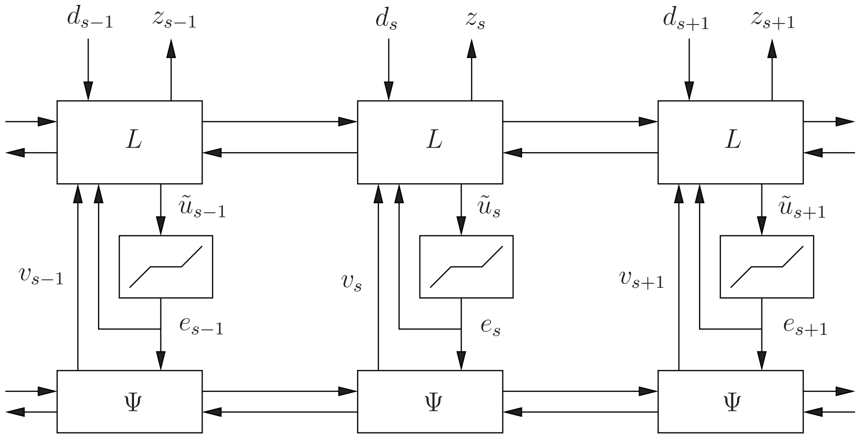


Figure 7.5: Compact form of the constrained system obtained by pulling the plant and the controller into one block

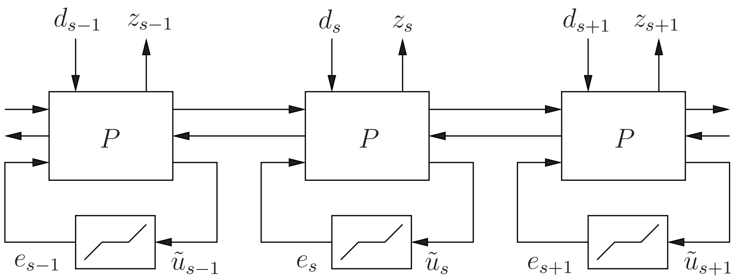


Figure 7.6: Constrained closed-loop system in a compact form with the deadzone operator as the uncertainty

in the uncertainty block by the sector [0 1] operator yields the lower LFT representation (see Appendix C.2) of subsystems as shown in Fig. 7.7, where $\Theta_s$ denotes the linear sector [0 1] and takes values from 0 to 1.

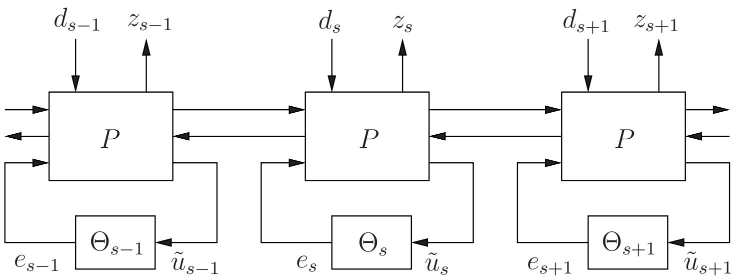


Figure 7.7: Constrained closed-loop system in a compact form with the sector [0 1] as the uncertainty

The subsystem $P$ contains the interactive dynamics of $G$, $K$ and $\Psi$, and is realized in

LFT form as

$$\begin{bmatrix} (\mathbf{\Delta}_m^P x^P)(k,s) \\ \hline z(k,s) \\ \tilde{u}(k,s) \end{bmatrix} = \left[\begin{array}{c|cc} A^P & B_d^P & B_e^P \\ \hline C_z^P & D_{zd}^P & D_{ze}^P \\ C_{\tilde{u}}^P & D_{\tilde{u}d}^P & D_{\tilde{u}e}^P \end{array}\right] \begin{bmatrix} x^P(k,s) \\ \hline d(k,s) \\ e(k,s) \end{bmatrix} \tag{7.17}$$

$$e(k,s) = \Theta_s \tilde{u}(k,s), \tag{7.18}$$

whose state vector is grouped as

$$x^P = \left[ \begin{bmatrix} x_t^L \\ x_t^\Psi \end{bmatrix}^T, \begin{bmatrix} x_{s+}^L \\ x_{s+}^\Psi \end{bmatrix}^T, \begin{bmatrix} x_{s-}^L \\ x_{s-}^\Psi \end{bmatrix}^T \right]^T. \tag{7.19}$$

With the matrices of subsystem $L$ known, after grouping the unknown AW parameters together, the system matrices of subsystem $P$ can be decomposed as

$$\left[\begin{array}{cccccc|cc} A_{tt}^L & 0 & A_{ts}^{L,+} & 0 & A_{ts}^{L,-} & 0 & B_{t,d}^L & B_{t,e}^L \\ 0 & 0 & 0 & 0 & 0 & 0 & 0 & 0 \\ A_{st}^{L,+} & 0 & A_{ss}^{L,++} & 0 & A_{ss}^{L,+-} & 0 & B_{s,d}^{L,+} & B_{s,e}^{L,+} \\ 0 & 0 & 0 & 0 & 0 & 0 & 0 & 0 \\ A_{st}^{L,-} & 0 & A_{ss}^{L,-+} & 0 & A_{ss}^{L,--} & 0 & B_{s,d}^{L,-} & B_{s,e}^{L,-} \\ 0 & 0 & 0 & 0 & 0 & 0 & 0 & 0 \\ \hline C_{t,z}^L & 0 & C_{s,z}^{L,+} & 0 & C_{s,z}^{L,-} & 0 & D_{zd}^L & D_{ze}^L \\ C_{t,\tilde{u}}^L & 0 & C_{s,\tilde{u}}^{L,+} & 0 & C_{s,\tilde{u}}^{L,-} & 0 & D_{\tilde{u}d}^L & D_{\tilde{u}e}^L \end{array}\right] + \left[\begin{array}{cccc} 0 & 0 & 0 & B_{t,v}^L \\ I & 0 & 0 & 0 \\ 0 & 0 & 0 & B_{s,v}^{L,+} \\ 0 & I & 0 & 0 \\ 0 & 0 & 0 & B_{s,v}^{L,-} \\ 0 & 0 & I & 0 \\ \hline 0 & 0 & 0 & D_{zv}^L \\ 0 & 0 & 0 & D_{\tilde{u}v}^L \end{array}\right] \left[\begin{array}{c|c} A^\Psi & B^\Psi \\ \hline C^\Psi & D^\Psi \end{array}\right] \left[\begin{array}{cccccc|cc} 0 & I & 0 & 0 & 0 & 0 & 0 & 0 \\ 0 & 0 & 0 & I & 0 & 0 & 0 & 0 \\ 0 & 0 & 0 & 0 & 0 & I & 0 & 0 \\ 0 & 0 & 0 & 0 & 0 & 0 & 0 & I \end{array}\right]. \tag{7.20}$$

### 7.3.1 Analysis Conditions

Theorem 7.1 states conditions for a lumped feedback loop in Fig. 7.3 to be stable. Replace the LTI operator $G(s)$ in Fig. 7.3 with the LTSI subsystem $P$ in Fig. 7.6, the uncertainty block $\Theta$ with $\Theta_s$. The stability theorem 7.1 can be extended to spatially distributed systems as follows.

**Theorem 7.2** *Assume that the distributed plant $G$ in (7.12), the distributed controller $K$ in (7.13) and the distributed AW compensator $\Psi$ in (7.15) are given. The interconnected system (7.17) and (7.18) is well-posed, exponentially stable and satisfies quadratic performance $\gamma$, if there exists a symmetric positive definite matrix $W \in \mathbb{R}^{n_u \times n_u}$ and a real matrix $X^P \in \boldsymbol{\mathcal{X}}_{m^P}$, such that*

$$\begin{bmatrix} * \\ \hline * \\ \hline * \end{bmatrix}^T \left[\begin{array}{cc|cc|cc} 0 & X^P & & & & \\ X^P & 0 & & & & \\ \hline & & -\gamma I & 0 & & \\ & & 0 & \frac{1}{\gamma} I & & \\ \hline & & & & -2W & W \\ & & & & W & 0 \end{array}\right] \left[\begin{array}{ccc} I & 0 & 0 \\ \bar{A}^P & \bar{B}_d^P & \bar{B}_e^P \\ \hline 0 & I & 0 \\ \bar{C}_z^P & \bar{D}_{zd}^P & \bar{D}_{ze}^P \\ \hline 0 & 0 & I \\ \bar{C}_{\tilde{u}}^P & \bar{D}_{\tilde{u}d}^P & \bar{D}_{\tilde{u}e}^P \end{array}\right] < 0 \tag{7.21}$$

*holds.*

**Proof** Consider now the state space realization (7.17) of subsystem $P$. Impose a worst-case gain $\gamma$ on the performance channel $d \rightarrow z$. After applying the KYP lemma C.2 (see Appendix C), condition (iii) in Theorem 7.1 is equivalent to the existence of a Lyapunov matrix $X^P \in \boldsymbol{\mathcal{X}}_{m^P}$, and a positive scalar $\mu$ ([42] [97]), such that

$$\begin{bmatrix} (\bar{A}^P)^T X^P + X^P \bar{A}^P & X^P \bar{B}_d^P & X^P \bar{B}_e^P \\ (\bar{B}_d^P)^T X^P & 0 & 0 \\ (\bar{B}_e^P)^T X^P & 0 & -I \end{bmatrix} + \frac{1}{\gamma^2} \begin{bmatrix} (\bar{C}_z^P)^T \\ (\bar{D}_{zd}^P)^T \\ (\bar{D}_{ze}^P)^T \end{bmatrix} \begin{bmatrix} \bar{C}_z^P & \bar{D}_{zd}^P & \bar{D}_{ze}^P \end{bmatrix}$$
$$+ \begin{bmatrix} (\bar{C}_{\tilde{u}}^P)^T & 0 \\ (\bar{D}_{\tilde{u}d}^P)^T & 0 \\ (\bar{D}_{\tilde{u}e}^P)^T & I \end{bmatrix} \mu M \begin{bmatrix} \bar{C}_{\tilde{u}}^P & \bar{D}_{\tilde{u}d}^P & \bar{D}_{\tilde{u}e}^P \\ 0 & 0 & I \end{bmatrix} < 0, \tag{7.22}$$

where the static multiplier that characterizes the sector [0 1] operator is selected as

$$M = \begin{bmatrix} 0 & \tilde{W} \\ \tilde{W} & -2\tilde{W} \end{bmatrix}. \tag{7.23}$$

Provided that the upper left term in the chosen multiplier is positive semi-definite, condition (ii) in Theorem 7.1 is always fulfilled for $\zeta = 0$. Meanwhile, the negative semi-definiteness of the lower right terms turns (7.4) into a convex problem. Therefore, it suffices to check condition (ii) only at $\zeta = 1$ [42], which is trivially fulfilled. Thus, stability of the well-posed interconnected system between subsystem $P$ and a deadzone operator $\Psi$ has been established.

Finally, with the change of variable $W = \mu\tilde{W}$, (7.22) can be written in a quadratic inequality form as (7.21). ■

*Remarks*:

- According to the sector condition, (7.5) should hold for any positive symmetric matrices $\tilde{W}$ (or $W$). Defining $W$ as a variable in (7.21) allows extra degrees of freedom in the minimization of $\gamma$.
- Despite the conservatism of a sector-based boundary [98], sector [0 1] is widely applied in control engineering to impose constraints on a deadzone/saturation operator. The conservatism could be reduced with the use of dynamic (frequency-dependent) multipliers [99] [100].

### 7.3.2 Synthesis Conditions

With the analysis conditions developed in Theorem 7.2, synthesis conditions for a distributed AW compensator $\Psi$ can be easily obtained by applying the elimination lemma not to (7.21) directly, but to the permuted version of (7.21), due to the same argument as made during the derivation of the controller synthesis conditions in Chapter 6, i.e., the sizes of positive and negative spatial states of the compensator remain unknown until the synthesis is complete. Instead of a closed-loop realization as in (7.20), a restructured state space model with the state vector defined as $x^{\tilde{P}}(k,s) = \begin{bmatrix} x^L(k,s) \\ x^\Psi(k,s) \end{bmatrix}$ is given by

$$\left[\begin{array}{c|cc} A^{\tilde{P}} & B_d^{\tilde{P}} & B_e^{\tilde{P}} \\ \hline C_z^{\tilde{P}} & D_{zd}^{\tilde{P}} & D_{ze}^{\tilde{P}} \\ C_{\tilde{u}}^{\tilde{P}} & D_{\tilde{u}d}^{\tilde{P}} & D_{\tilde{u}e}^{\tilde{P}} \end{array}\right] = \left[\begin{array}{cc|cc} A^L & 0 & B_d^L & B_e^L \\ 0 & 0 & 0 & 0 \\ \hline C_z^L & 0 & D_{zd}^L & D_{ze}^L \\ C_{\tilde{u}}^L & 0 & D_{\tilde{u}d}^L & D_{\tilde{u}e}^L \end{array}\right] + \left[\begin{array}{cc} 0 & B_v^L \\ I & 0 \\ \hline 0 & D_{zv}^L \\ 0 & D_{\tilde{u}v}^L \end{array}\right] \left[\begin{array}{c|c} A^\Psi & B^\Psi \\ \hline C^\Psi & D^\Psi \end{array}\right] \underbrace{\left[\begin{array}{cc|cc} 0 & I & 0 & 0 \\ 0 & 0 & 0 & I \end{array}\right]}_{Q}. \tag{7.24}$$

The Lyapunov matrix $X^P \in \boldsymbol{\mathcal{X}}_{m^P}$ is accordingly permuted in the same way as in (6.28), i.e.

$$X^{\tilde{P}} = \left[\begin{array}{cc|cc} X_t^L & & X_t^{L\Psi} & \\ & X_s^L & & X_s^{L\Psi} \\ \hline (X_t^{L\Psi})^T & & X_t^\Psi & \\ & (X_s^{L\Psi})^T & & X_s^\Psi \end{array}\right]. \tag{7.25}$$

Theorem 7.2 is equivalent to: The interconnected system (7.17) and (7.18) is well-posed, exponentially stable and satisfies quadratic performance $\gamma$, if there exists a symmetric positive definite matrix $W \in \mathbb{R}^{n_u \times n_u}$ and a real matrix $X^{\tilde{P}}$ in the form of (7.25), such that

$$\left[\begin{array}{c} * \\ \hline * \\ \hline * \end{array}\right]^T \left[\begin{array}{cc|cc|cc} 0 & X^{\tilde{P}} & & & & \\ X^{\tilde{P}} & 0 & & & & \\ \hline & & -\gamma I & 0 & & \\ & & 0 & \frac{1}{\gamma} I & & \\ \hline & & & & -2W & W \\ & & & & W & 0 \end{array}\right] \left[\begin{array}{ccc} I & 0 & 0 \\ \bar{\mathcal{A}}^{\tilde{P}} & \bar{\mathcal{B}}_d^{\tilde{P}} & \bar{\mathcal{B}}_e^{\tilde{P}} \\ \hline 0 & I & 0 \\ \bar{\mathcal{C}}_z^{\tilde{P}} & \bar{\mathcal{D}}_{zd}^{\tilde{P}} & \bar{\mathcal{D}}_{ze}^{\tilde{P}} \\ \hline 0 & 0 & I \\ \bar{\mathcal{C}}_{\tilde{u}}^{\tilde{P}} & \bar{\mathcal{D}}_{\tilde{u}d}^{\tilde{P}} & \bar{\mathcal{D}}_{\tilde{u}e}^{\tilde{P}} \end{array}\right] < 0. \tag{7.26}$$

Inheriting the distributed fashion of the controller design, a local AW compensator is to be designed based on a single subsystem, and copied to all other subsystems in case of an LTSI system. Conditions for the design of a distributed AW compensator can be derived as follows.

**Theorem 7.3** *There exists a distributed AW compensator $\Psi$ in (7.15), that guarantees well-posedness, exponential stability and quadratic performance $\gamma$ of the constrained closed-loop system (7.17) and (7.18), if there exist a symmetric positive definite matrix $W \in \mathbb{R}^{n_u \times n_u}$ and $R$, $S \in \boldsymbol{\mathcal{X}}_{m^L}$, that satisfy*

$$\left[\begin{array}{c} * \\ \hline * \end{array}\right]^T \left[\begin{array}{cc|cc} 0 & S & & \\ S & 0 & & \\ \hline & & -\gamma I & 0 \\ & & 0 & \frac{1}{\gamma} I \end{array}\right] \left[\begin{array}{cc} I & 0 \\ \bar{A}^L & \bar{B}_d^L \\ \hline 0 & I \\ \bar{C}_z^L & \bar{D}_{zd}^L \end{array}\right] < 0, \tag{7.27}$$

$$N_R^T \begin{bmatrix} * \\ * \\ * \end{bmatrix}^T \left[\begin{array}{cc:cc:cc} 0 & R & & & & \\ R & 0 & & & & \\ \hdashline & & -\frac{1}{\gamma}I & 0 & & \\ & & 0 & \gamma I & & \\ \hdashline & & & & 0 & W^{-1} \\ & & & & W^{-1} & 2W^{-1} \end{array}\right] \left[\begin{array}{ccc} -(\bar{A}^L)^T & -(\bar{C}_z^L)^T & -(\bar{C}_{\tilde{u}}^L)^T \\ I & 0 & 0 \\ \hdashline -(\bar{B}_d^L)^T & -(\bar{D}_{zd}^L)^T & -(\bar{D}_{\tilde{u}d}^L)^T \\ 0 & I & 0 \\ \hdashline -(\bar{B}_e^L)^T & -(\bar{D}_{ze}^L)^T & -(\bar{D}_{\tilde{u}e}^L)^T \\ 0 & 0 & I \end{array}\right] N_R > 0, \quad (7.28)$$

$$\begin{bmatrix} R_t & I \\ I & S_t \end{bmatrix} > 0, \quad (7.29)$$

*where* $N_R = \ker \left[ (\bar{B}_v^L)^T \ (\bar{D}_{zv}^L)^T \ (\bar{D}_{\tilde{u}v}^L)^T \right]$.

**Proof** The proof of this theorem follows from [43], by applying the elimination lemma to (7.21). ■

*Remark:*

- Condition (7.27) differs from the conventional form of the matrix inequality after applying dualization lemma [43], which contains additional multiplications with null space $N_s^T$ from left and $N_s$ from right. Condition (7.27) is actually the result after multiplying with $N_s^T$ and $N_s$. This is due to the fact that the null space of matrix $Q$ in (7.24) does not depend on any system matrix. Thus neither does its null space $N_s$. After the multiplication, $W$ drops out from (7.27).

After matrices $R$ and $S$ have been computed, the Lyapunov matrix $X$ and the AW compensator $\Psi$ can be subsequently obtained from (7.26) by following the controller reconstruction procedure provided in Section 6.4.1.

## 7.4 Decentralized AW Compensator Design

Cutting off the communication channels between AW compensators results in a decentralized AW scheme as shown in Fig. 7.8.

The decentralized AW compensator contains only temporal states, thus takes the form of the lumped state space representation in (7.1). Analogous to the handling of decentralized controller, analysis condition (7.21) or (7.26), and synthesis conditions (7.27)-(7.29) can be applied to solve for the decentralized AW compensator as well, except that the spatial components in Lyapunov matrix $X^P$ are restricted to be zero matrices as in (6.40).

## 7.5 Simulation Results

After the analysis and synthesis conditions for a distributed AW compensator design being developed, attempts have been made to design an AW compensator for the experiment

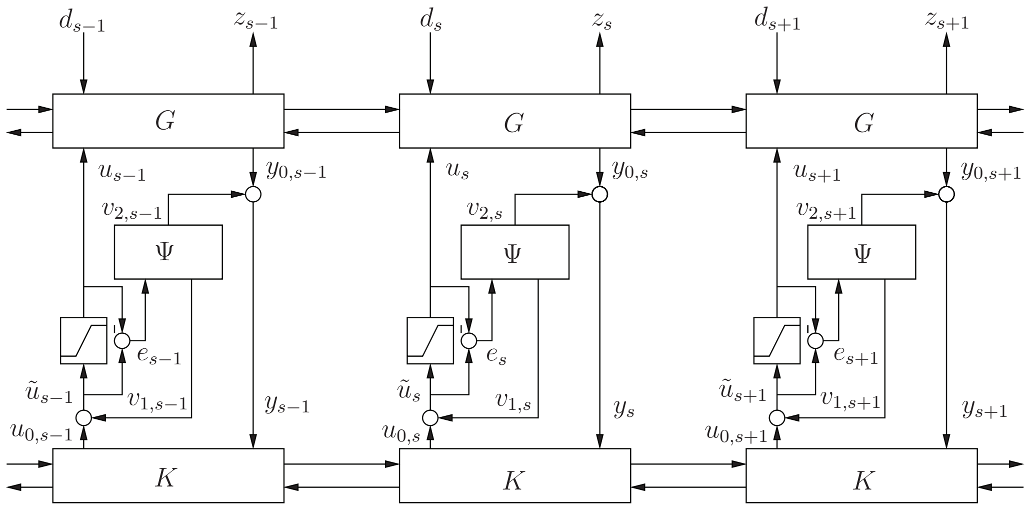


Figure 7.8: Decentralized AW scheme

setup. However, due to the large order of the augmented subsystem, Matlab fails to solve the problem numerically. Instead, an Euler-Bernoulli beam as shown in Fig. 7.9, whose dynamics are governed by the PDF (5.5) of smaller order is used again as an example to demonstrate how the occurrence of the windup effect affects the established closed-loop performance, as well as how a distributed and a decentralized AW scheme counteract it.

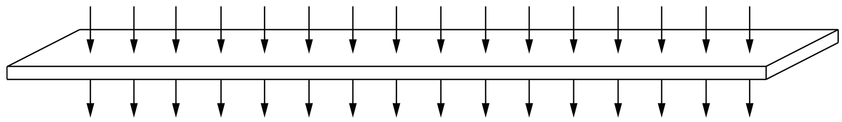

Figure 7.9: Aluminium beam with free-free boundary condition equipped with 16 pairs of actuators and sensors

**Example 7.1 (AW Compensation for the Euler-Bernoulli Beam)** *Here, the performance of the AW compensator in terms of input disturbance rejection is tested. Excite the subsystems with 16 identical chirp signals of amplitude 5 N up to 10 Hz simultaneously as input disturbances. The open-loop response of the beam is shown in Fig. 7.10.*

*Following the controller design procedures in Section 6.4.1, a distributed controller is obtained and implemented. The achieved closed-loop response without actuator constraints is shown in Fig. 7.11; it can be observed as the nominal performance. The vibratory motion of the beam caused by the input disturbance is damped to a significantly smaller scale. Fig. 7.12 shows the comparison between the control effort and injected disturbance at subsystem 8, which clearly indicates that an effective active vibration control counteracts the external disturbance by generating a control signal with the same frequency but opposite phase.*

*Now suppose that all actuators are subject to the constraint $u \in [-4 \quad 4]$ N. It is obvious that the required control input in Fig. 7.12 exceeds the actuation limits. Fig. 7.13 shows*

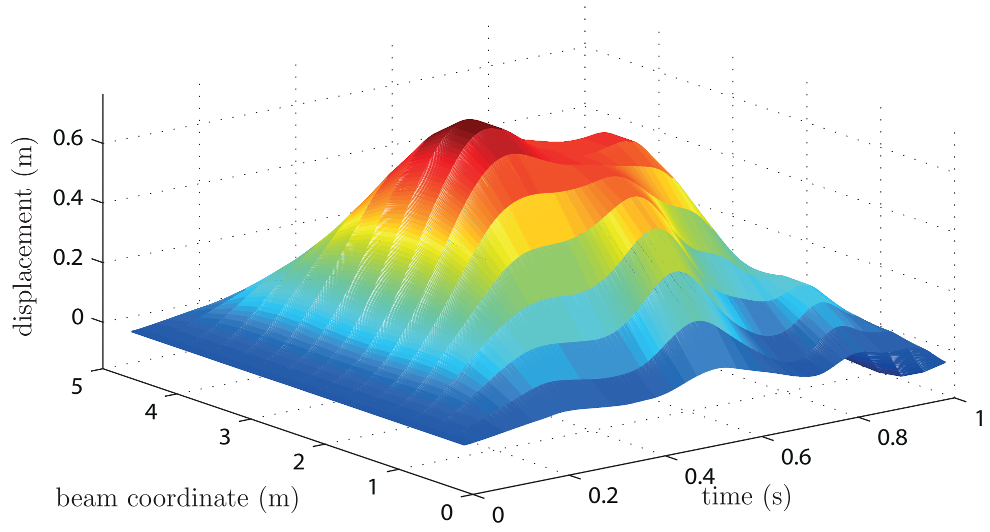


Figure 7.10: Open-loop response to 16 parallel chirp signals up to 10 Hz as input disturbances

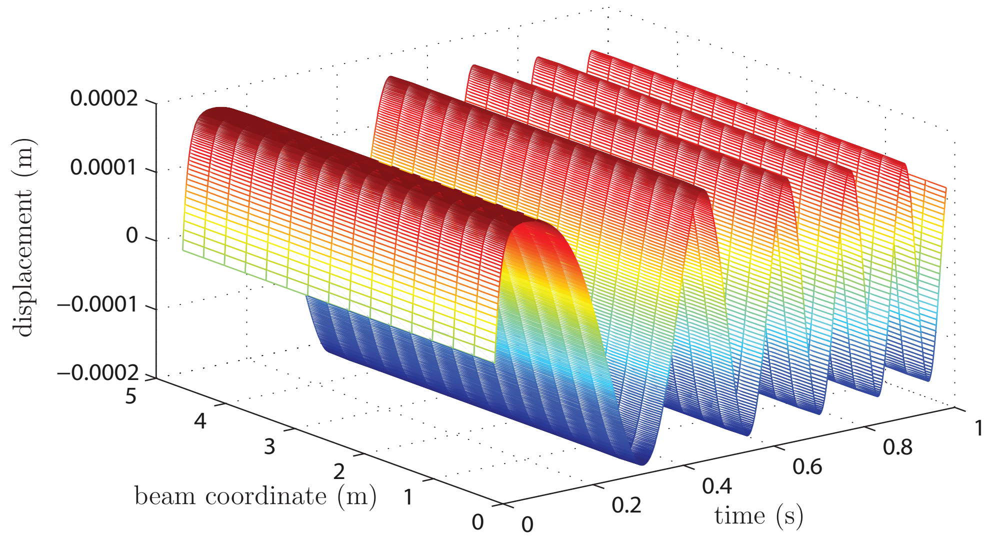


Figure 7.11: Closed-loop response to 16 parallel chirp signals up to 10 Hz as input disturbances without actuator constraints

*the closed-loop performance achieved by the same controller with actuator constraints. Although worse than Fig. 7.11, it is still better than the open-loop response. The windup effect can be observed in Fig. 7.14, where in (a) the controller output* $u_0(k, 8)$ *is winded up to a considerably high level, whereas (b) shows the control signal after saturation.*

*Fig. 7.15 shows the closed-loop response with the distributed AW scheme, and Fig. 7.17 with the decentralized AW scheme. The distributed AW compensator improves the performance, compared to Fig. 7.13, but not to the level of the nominal closed-loop performance in Fig. 7.11—in principle, any AW scheme can hardly recover the unconstrained per-*

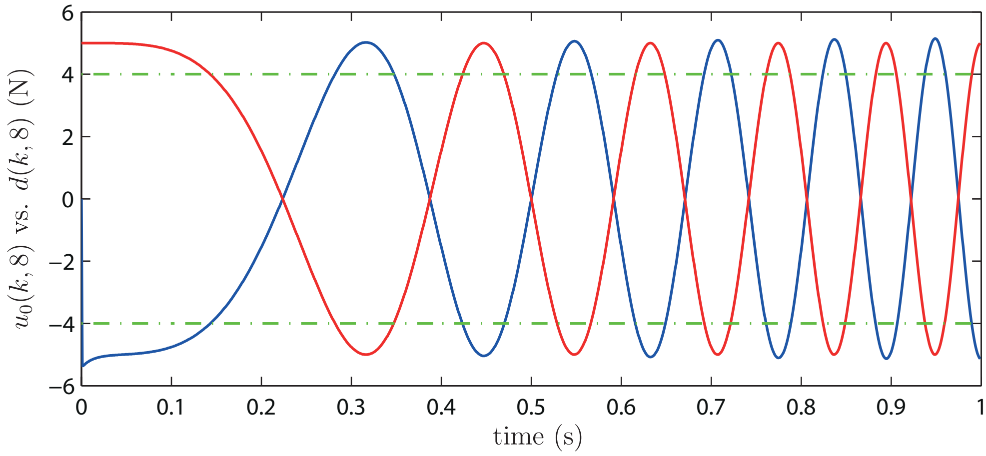


Figure 7.12: Control effort (blue curve) and input disturbance (red curve) at subsystem 8, without actuator constraints. The required control effort exceeds the max. and min. actuation limits (green lines).

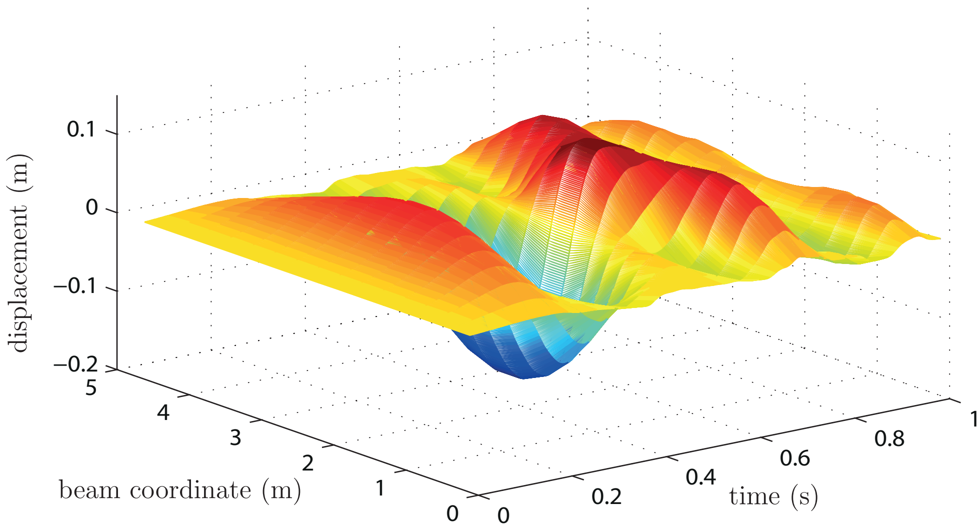


Figure 7.13: Closed-loop response to 16 parallel chirp signals up to 10 Hz as input disturbances with actuator constraints imposed, without AW implemented

*formance. Fig. 7.16 shows how the attenuation of saturated control effort is realized by the distributed AW scheme. The counteracting of distributed AW output $v_1$ against the excessive controller output $u_0$, effectively brings the saturated system behaviour back to its linear range. With the information exchanging between subsystems, the control effort can be better allocated to counteract the saturation effects. The decentralized compensator in Fig. 7.17 clearly destabilizes the system. However, it should be noted that this is not the general case. For a fair comparison in this work, the same shaping filters have been employed to tune the decentralized and distributed AW compensator design. It turns out that the decentralized AW compensator destabilizes the constrained system.*

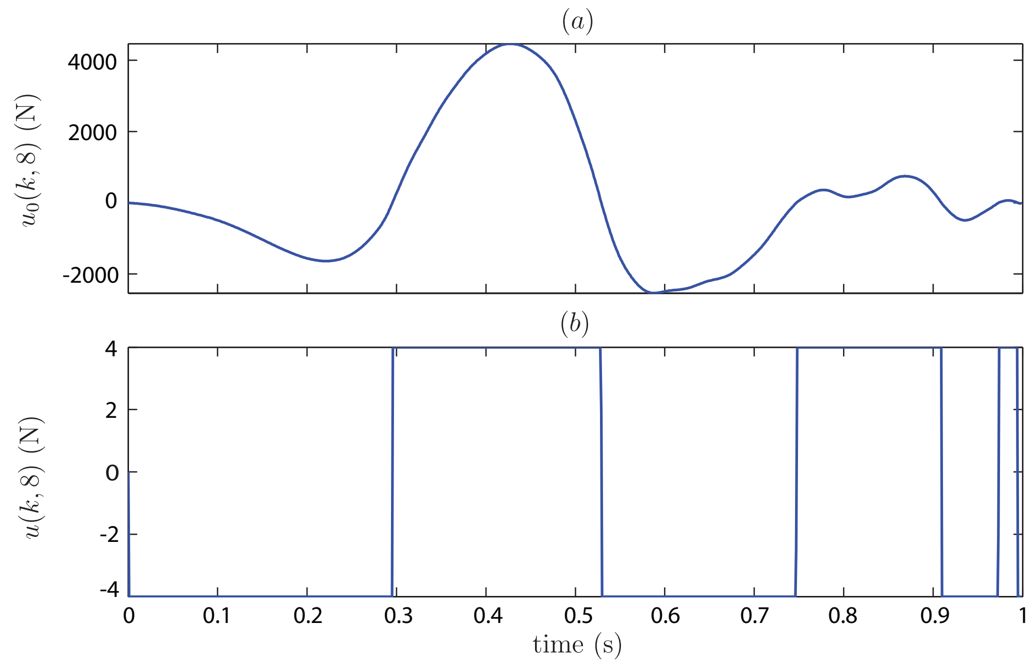


Figure 7.14: Controller output $u_0(k, s)$ in $(a)$ and saturated control effort $u(k, s)$ in $(b)$ at subsystem 8 with actuator constraints imposed

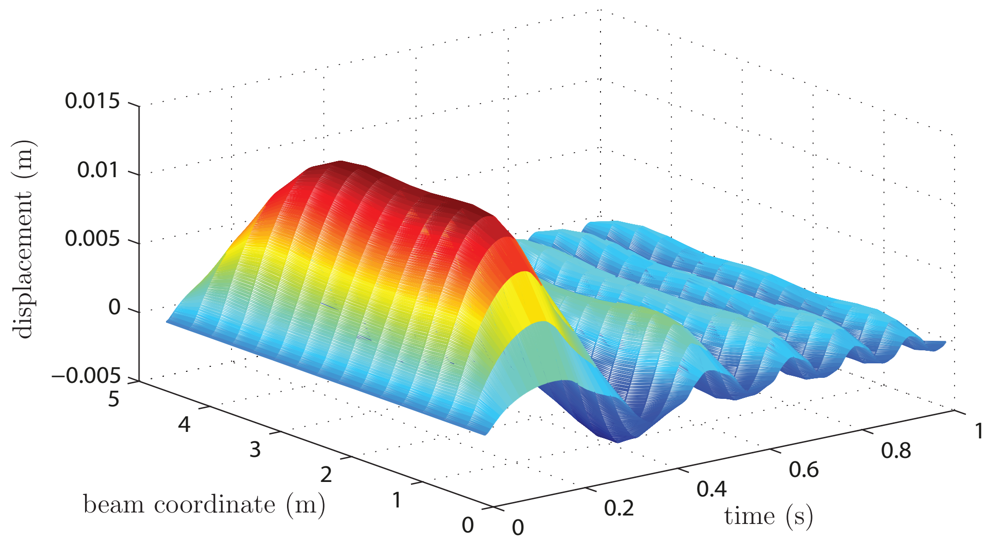


Figure 7.15: Closed-loop response to 16 parallel chirp signals up to 10 Hz as input disturbances with actuator constraints imposed, with a distributed AW compensator implemented

## 7.6 Summary

This chapter has proposed a two-step approach for the distributed AW compensator design to counteract the actuator saturation that often occurs in physical systems. A

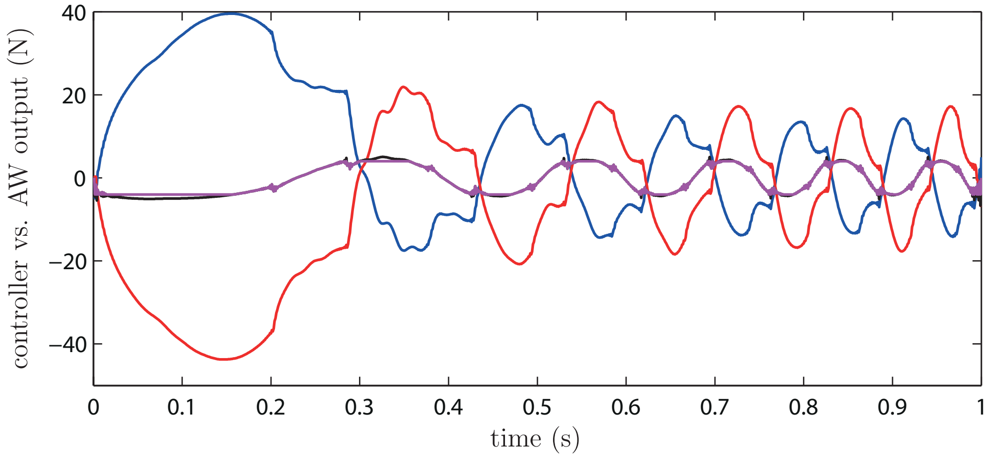


Figure 7.16: Output $v_1(k,8)$ (red curve) of the distributed AW compensator counteracts the winded controller output $u_0(k,8)$ (blue curve) at patch 8, resulting an attenuated sum $\tilde{u}(k,8) = u_0(k,8) + v_1(k,8)$ (black curve). The saturated control effort $u(k,8)$ (magenta curve) is the actual input of the plant subsystem 8.

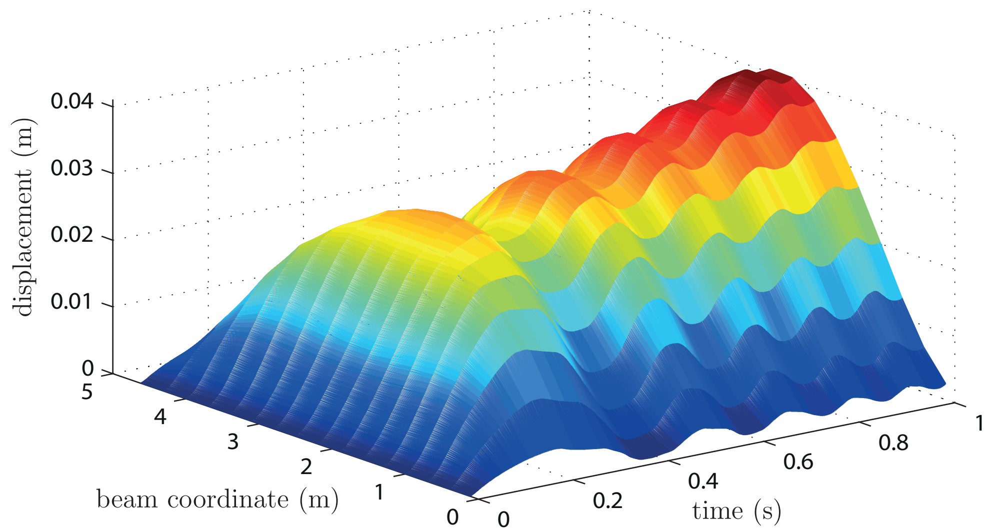


Figure 7.17: Closed-loop response to 16 parallel chirp signals up to 10 Hz as input disturbances with actuator constraints imposed, with a decentralized AW compensator implemented

lumped AW scheme employed as the building block of the distributed AW compensator has been first introduced. To cope with the nonlinear saturation/deadzone operator, a powerful tool – IQCs – has been briefly reviewed, as well as the choice of the multipliers and the application of IQCs for the stability analysis of a feedback system subject to a bounded linear/nonlinear uncertainty. A distributed AW scheme has been proposed, which inherits the spatial structure of the controlled distributed system. IQCs have been employed to impose constraints on the nonlinear saturation/deadzone operator as the uncertainty, such that the compensator design problem can be cast in terms of LMIs. The proposed distributed AW scheme has been compared with a decentralized AW scheme; both designed compensators have been tested in simulation to address the saturation problem of a beam structure governed by the Euler-Bernoulli equation. The simulation results demonstrated that by enforcing the communication between subsystems in the distributed AW scheme, the control effort can be more efficiently allocated to counteract the saturation effects than in the decentralized one.

# Chapter 8

# Conclusions and Outlook

This thesis has studied physical modelling, identification, controller and AW compensator design of spatially-distributed systems. An aluminium beam equipped with an array of collocated piezo actuator/sensor pairs has been constructed as a representative spatially-distributed system for experimental use. The aim is to realize an effective model-based controller design to achieve given performance specifications on the closed-loop system. The state space framework developed in [8] provides the foundation of the thesis. New methods have been developed to address problems arising during implementation.

A physical model has been constructed in Chapter 3 using a piezoelectric FE modelling approach, which incorporates an array of piezo actuators and sensors into the modelling. The obtained theoretical FE model has been updated by performing the experimental modal analysis. A good match between the updated FE model and measured structural dynamics has been achieved. Possible reasons for unmodeled effects have been analysed. A direct feed-through phenomenon has been observed between collocated actuators and sensors.

Physical modelling by means of exploring the underlying physical laws may become difficult if the plant dynamics get complex. Chapter 4 has proposed an approach to identify the FRF matrix directly from the input/output behaviour of the plant. Provided FRF measurements at a small number of selected actuating and sensing locations, a local LPV identification technique for spatio-temporal systems has been proposed to parametrize the FRF matrix as a spatial LPV model, allowing to approximate FRFs at unmeasured actuation or sensing locations. The proposed method thus alleviates tedious experimental work in case of a complex structure. Experimental results demonstrate the feasibility of this approach.

Considering a spatially-distributed system as the interconnection of an array of subsystems, Chapter 5 addressed the identification problem in a distributed framework. The two-dimensional least-squares based estimation methods developed in [27] for LTSI models and in [29] for LTSV models have been experimentally implemented. To improve the identification accuracy especially at resonances, a new identification procedure has been developed by making use of the FE modelling results obtained in Chapter 3. The identified models provide a better representation of the real structural dynamics than the black-box models.

Analysis and synthesis conditions for spatially-invariant systems proposed in [8] have been implemented experimentally in Chapter 6 for the first time to suppress the structural vibration of an actuated beam. The closed-loop performance of the distributed controller has been compared to that of a decentralized controller. The information exchange within a distributed controller allows each subsystem to obtain information about the status of its neighbours; it helps to achieve an improved overall performance. The LPV controller design technique using PDLFs has been extended from lumped systems to LTSV systems. Spatial LPV controllers have been designed for the test structure which consists of spatially-varying subsystems using both CLFs and PDLFs. The experimental comparison confirms that, with the reduced conservatism, an LPV controller designed using PDLFs outperforms the corresponding one using CLFs.

Chapter 7 has dealt with the actuator saturation problem that often occurs in a physical system. A distributed AW scheme has been proposed, that preserves the distributed nature of the plant and the designed controller. IQCs have been applied to analyse the robust stability of the saturated system. A distributed AW compensator has been synthesized using the Euler-Bernoulli beam as an example. Its performance has been compared in simulation with that of a decentralized AW scheme. Due to the more efficient allocation of control effort among subsystems, the distributed AW scheme recovers the closed-loop performance better than the decentralized one in the presence of actuator saturation.

**Outlook**

Aspects that should be taken into consideration in future research are summarized as follows:

- The experimental identification of distributed systems often requires a large spatial order to achieve an accurate approximation of the test structure. Experience shows that, after the implementation of the controller synthesis procedure, the obtained controller has normally the same order as the generalized plant. Furthermore, if a distributed AW scheme is built on top of them to counteract actuator saturation, the AW compensator has a size of both the plant and the controller. The large system order imposes numerical challenges on the search for optimal solutions when solving synthesis LMIs: either the LMIs can not be handled by the LMI solvers; or the results are sensitive to numerical errors. Therefore, keeping the model order as small as possible can be essential for LMI solvers to find a feasible and reliable solution. Taking the coupled temporal and spatial dynamics into consideration, structure-preserving model reduction [101] is one interesting option to simplify a multidimensional model.

- In this work, the construction of a generalized plant for controller synthesis is based on the use of one-dimensional shaping filters by only shaping the temporal dynamics of the closed-loop system. Although it has demonstrated its performance to a certain extent in terms of disturbance rejection, the power of robust controller design through shaping sensitivities has not been fully explored in multidimensional systems. It has been mentioned that the use of two-dimensional shaping filters may potentially lead to an improved performance, where the filter itself is a distributed system. To find the appropriate parametrization of a two-dimensional shaping filter which imposes desired constraints on the closed-loop system is not a trivial task. It leaves room for further research on the impact of the use of two-dimensional shaping filters.

- Before applying the well-developed state-space based synthesis conditions in [8], the experimentally identified input/output model needs to be realized in state space representation. Alternatively, analysis and synthesis conditions could be directly derived and implemented in input/output form. Two main advantages of employing input/output synthesis are:
  - It has been discussed in Section 6.4.3 that after solving for the controller matrices, the online computation of the controller outputs can only be realized in a centralized manner as depicted in Fig. 1.6. In contrast, a distributed controller in input/output form allows to implement the online computation in a 'real' distributed architecture as shown in Fig. 1.2 (c), where subsystems communicate with each other through inputs and/or outputs.
  - It has been mentioned in Section 6.2.2 that the equivalence between the spatial LPV input/output model and its state space representation is not influenced by the dynamic dependence on the scheduling parameters in this specific application. Nevertheless, when it is not this case, the complexity in terms of realizing an equivalent state space model can increase significantly. This motivates the development of synthesis techniques that can design temporal/spatial LPV controllers directly from the identified input/output LPV models. Relevant methods have been developed for lumped systems, e.g. [102], [82], etc. A distributed fixed-structure controller design approach for LTSI systems is proposed in [103].
- This thesis works on the modelling, identification and controller design of an experimental setup, with an array of piezo actuators and sensors attached in a collocated pattern. It has been studied in [51], that the use of collocated actuator/sensor pairs for a lightly damped flexible structure leads to alternating poles and zeros near the imaginary axis. This property guarantees the asymptotic stability of the controlled system against disturbances and uncertainties; thus it is recommended. It has been observed in Chapter 3, that a direct feed-through effect exists between collocated actuators and sensors. Although the sensor measurements could be compensated using a feed-through constant, the presence of the direct feed-through effect caused several difficulties in identification and controller design.
  - It has been demonstrated that the feed-through constants slightly vary from patch to patch. The use of an identical feed-through constant for all subsystems brings inaccuracy into the modelling and identification. On the other hand, the use of varying feed-through constants violates the LTSI assumption.

- The controller is designed to suppress the structural vibration caused by the disturbance injection. Due to the presence of the feed-through effect, sensor measurements are dominated by the fed-through actuation input. To separate the signal that is actually caused by structural vibration (in this case, proportional to curvature) from sensor measurements requires an accurate knowledge of the feed-through behaviour at each pair.
- The direct feed-through effect could be the reason for the encountered synthesis problem when a distributed controller is to be designed based on the FE-based identified model. Singular perturbations [104] can be considered as a solution to address this issue by modelling the direct feed-through effect as fast dynamics.

Therefore, it could be mostly helpful to avoid these problems by placing actuator/sensor pairs in a modified 'collocated' way. Two possible options to attach one actuator/sensor pair are shown in Fig. 8.1, where in (a), the actuator and sensor are attached next to each other in the width direction, and in (b) in the length direction of the beam. Nevertheless, it has been validated in [51], that the classical beam theory does not suffice to model the configuration (a). Instead, the Kirchhoff shell theory that accounts for the membrane strain is required. On the other hand, the piezo pair in configuration (b) actuates and senses at slightly deviated locations in the length direction of the beam. However, if the length of the beam is significantly larger than the length of the piezo patch, the small location deviation could be ignored. The assumption that subsystems are equipped with actuating and sensing capabilities is still fulfilled.

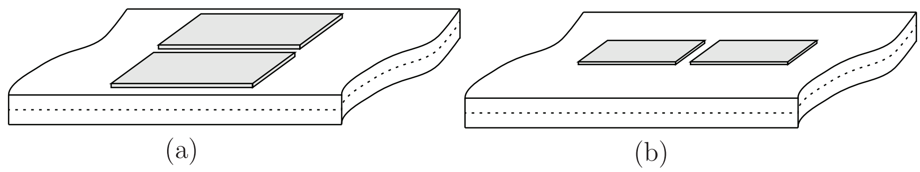


Figure 8.1: Possible options for the placement of a pair of 'collocated' piezo patches to avoid the direct feed-through effect: (a) an actuator and a sensor are attached next to each other in the width direction, (b) in the length direction of the beam.

# Appendix A

# State Space Realization of Identified Models

## A.1 LTSI Models

A state space realization of the experimentally identified LTSI models takes the form

$$\left[\begin{array}{c} x_t(k+1,s) \\ x_s^+(k,s+1) \\ x_s^-(k,s-1) \\ \hline y(k,s) \end{array}\right] = \left[\begin{array}{c|c} A^G & B^G \\ \hline C^G & D^G \end{array}\right] \left[\begin{array}{c} x_t(k,s) \\ x_s^+(k,s) \\ x_s^-(k,s) \\ \hline u(k,s) \end{array}\right]. \tag{A.1}$$

The system matrices of the black-box identified model are

$$\left[\begin{array}{ccccccccccc|c}
0 & 1 & 0 & 0 & 0 & 0 & 0 & 0 & 0 & 0 & 0 & 0 \\
0 & 0 & 1 & 0 & 0 & 0 & 0 & 0 & 0 & 0 & 0 & 0 \\
0 & -a_{(2,0)} & -a_{(1,0)} & -a_{(2,2)} & -a_{(2,1)} & -a_{(1,2)} & -a_{(1,1)} & -a_{(2,-2)} & -a_{(2,-1)} & -a_{(1,-2)} & -a_{(1,-1)} & 1 \\
0 & 0 & 0 & 0 & 1 & 0 & 0 & 0 & 0 & 0 & 0 & 0 \\
0 & 1 & 0 & 0 & 0 & 0 & 0 & 0 & 0 & 0 & 0 & 0 \\
0 & 0 & 0 & 0 & 0 & 0 & 1 & 0 & 0 & 0 & 0 & 0 \\
0 & 0 & 1 & 0 & 0 & 0 & 0 & 0 & 0 & 0 & 0 & 0 \\
0 & 0 & 0 & 0 & 0 & 0 & 0 & 1 & 0 & 0 & 0 & 0 \\
0 & 1 & 0 & 0 & 0 & 0 & 0 & 0 & 0 & 0 & 0 & 0 \\
0 & 0 & 0 & 0 & 0 & 0 & 0 & 0 & 0 & 0 & 1 & 0 \\
0 & 0 & 1 & 0 & 0 & 0 & 0 & 0 & 0 & 0 & 0 & 0 \\
\hline
b_{(3,0)} & b_{(2,0)} & b_{(1,0)} & 0 & 0 & 0 & 0 & 0 & 0 & 0 & 0 & 0
\end{array}\right], \tag{A.2}$$

whereas the system matrices of the FE-based LTSI model are

$$\left[\begin{array}{cccccccccc|c} 0 & 1 & 0 & 0 & 0 & 0 & 0 & 0 & 0 & 0 & 0 \\ -a_{(2,0)} & -a_{(1,0)} & -a_{(1,2)} & -a_{(1,1)} & b_{(1,2)} & b_{(1,1)} & -a_{(1,-2)} & -a_{(1,-1)} & b_{(1,-2)} & b_{(1,-1)} & b_{(1,0)} \\ 0 & 0 & 0 & 1 & 0 & 0 & 0 & 0 & 0 & 0 & 0 \\ 0 & 1 & 0 & 0 & 0 & 0 & 0 & 0 & 0 & 0 & 0 \\ 0 & 0 & 0 & 0 & 0 & 1 & 0 & 0 & 0 & 0 & 0 \\ 0 & 0 & 0 & 0 & 0 & 0 & 0 & 0 & 0 & 0 & 1 \\ 0 & 0 & 0 & 0 & 0 & 0 & 0 & 1 & 0 & 0 & 0 \\ 0 & 1 & 0 & 0 & 0 & 0 & 0 & 0 & 0 & 0 & 0 \\ 0 & 0 & 0 & 0 & 0 & 0 & 0 & 0 & 0 & 1 & 0 \\ 0 & 0 & 0 & 0 & 0 & 0 & 0 & 0 & 0 & 0 & 1 \\ \hline 0 & 1 & 0 & 0 & 0 & 0 & 0 & 0 & 0 & 0 & 0 \end{array}\right]. \tag{A.3}$$

## A.2 Spatial LPV Models

A state space realization of the spatial LPV model in LFT representation is given by

$$\begin{bmatrix} x_t(k+1,s) \\ x_s^+(k,s+1) \\ x_s^-(k,s-1) \\ \hline q_1^s(k,s) \\ q_2^s(k,s) \\ \hline y(k,s) \end{bmatrix} = \left[\begin{array}{c|c|c} A^G & B_p^G & B_u^G \\ \hline C_q^G & D_{qp}^G & D_{qu}^G \\ \hline C_y^G & D_{yp}^G & D_{yu}^G \end{array}\right] \begin{bmatrix} x_t(k,s) \\ x_s^+(k,s) \\ x_s^-(k,s) \\ \hline p_1^s(k,s) \\ p_2^s(k,s) \\ \hline u(k,s) \end{bmatrix}, \tag{A.4}$$

with

$$\begin{bmatrix} p_1^s(k,s) \\ p_2^s(k,s) \end{bmatrix} = \begin{bmatrix} \theta_s & \\ & \theta_s \end{bmatrix} \begin{bmatrix} q_1^s(k,s) \\ q_2^s(k,s) \end{bmatrix}. \tag{A.5}$$

The system matrices of the black-box identified spatial LPV model are

$$\left[\begin{array}{cccccccccc|cc|c} 0 & 1 & 0 & 0 & 0 & 0 & 0 & 0 & 0 & 0 & 0 & 0 & 0 \\ -\alpha_{(2,0,0)} & -\alpha_{(1,0,0)} & -\alpha_{(2,2,0)} & -\alpha_{(2,1,0)} & -\alpha_{(1,2,0)} & -\alpha_{(1,2,0)} & -\alpha_{(2,-2,0)} & -\alpha_{(2,-1,0)} & -\alpha_{(1,-2,0)} & -\alpha_{(1,-1,0)} & 1 & 0 & 1 \\ 0 & 0 & 0 & 1 & 0 & 0 & 0 & 0 & 0 & 0 & 0 & 0 & 0 \\ 1 & 0 & 0 & 0 & 0 & 0 & 0 & 0 & 0 & 0 & 0 & 0 & 0 \\ 0 & 0 & 0 & 0 & 0 & 1 & 0 & 0 & 0 & 0 & 0 & 0 & 0 \\ 0 & 1 & 0 & 0 & 0 & 0 & 0 & 0 & 0 & 0 & 0 & 0 & 0 \\ 0 & 0 & 0 & 0 & 0 & 0 & 1 & 0 & 0 & 0 & 0 & 0 & 0 \\ 1 & 0 & 0 & 0 & 0 & 0 & 0 & 0 & 0 & 0 & 0 & 0 & 0 \\ 0 & 0 & 0 & 0 & 0 & 0 & 0 & 0 & 0 & 1 & 0 & 0 & 0 \\ 0 & 1 & 0 & 0 & 0 & 0 & 0 & 0 & 0 & 0 & 0 & 0 & 0 \\ \hline -\alpha_{(2,0,1)} & -\alpha_{(1,0,1)} & -\alpha_{(2,2,1)} & -\alpha_{(2,1,1)} & -\alpha_{(1,2,1)} & -\alpha_{(1,2,1)} & -\alpha_{(2,-2,1)} & -\alpha_{(2,-1,1)} & -\alpha_{(1,-2,1)} & -\alpha_{(1,-1,1)} & 0 & 0 & 0 \\ \beta_{(2,0,1)} & \beta_{(1,0,1)} & 0 & 0 & 0 & 0 & 0 & 0 & 0 & 0 & 0 & 0 & 0 \\ \hline \beta_{(2,0,0)} & \beta_{(1,0,0)} & 0 & 0 & 0 & 0 & 0 & 0 & 0 & 0 & 0 & 1 & 0 \end{array}\right] \tag{A.6}$$

whereas the system matrices of the FE-based spatial LPV model are

$$\left[\begin{array}{cccccccccc:cc:c}
0 & 1 & 0 & 0 & 0 & 0 & 0 & 0 & 0 & 0 & 0 & 0 & 0 \\
-\alpha_{(2,0,0)} & -\alpha_{(1,0,0)} & -\alpha_{(1,2,0)} & -\alpha_{(1,2,0)} & \beta_{(1,2,0)} & \beta_{(1,2,0)} & -\alpha_{(1,-2,0)} & -\alpha_{(1,-1,0)} & \beta_{(1,-2,0)} & \beta_{(1,-1,0)} & 1 & 0 & 1 \\
0 & 0 & 0 & 1 & 0 & 0 & 0 & 0 & 0 & 0 & 0 & 0 & 0 \\
0 & 1 & 0 & 0 & 0 & 0 & 0 & 0 & 0 & 0 & 0 & 0 & 0 \\
0 & 0 & 0 & 0 & 0 & 1 & 0 & 0 & 0 & 0 & 0 & 0 & 0 \\
0 & 0 & 0 & 0 & 0 & 0 & 0 & 0 & 0 & 0 & 0 & 0 & 1 \\
0 & 0 & 0 & 0 & 0 & 0 & 0 & 1 & 0 & 0 & 0 & 0 & 0 \\
0 & 1 & 0 & 0 & 0 & 0 & 0 & 0 & 0 & 0 & 0 & 0 & 0 \\
0 & 0 & 0 & 0 & 0 & 0 & 0 & 0 & 0 & 1 & 0 & 0 & 0 \\
0 & 0 & 0 & 0 & 0 & 0 & 0 & 0 & 0 & 0 & 0 & 0 & 1 \\
\hdashline
-\alpha_{(2,0,1)} & -\alpha_{(1,0,1)} & -\alpha_{(1,2,1)} & -\alpha_{(1,2,1)} & \beta_{(1,2,1)} & \beta_{(1,2,1)} & -\alpha_{(1,-2,1)} & -\alpha_{(1,-1,1)} & \beta_{(1,-2,1)} & \beta_{(1,-1,1)} & 0 & 0 & 0 \\
0 & \beta_{(1,0,1)} & 0 & 0 & 0 & 0 & 0 & 0 & 0 & 0 & 0 & 0 & 0 \\
\hdashline
0 & \beta_{(1,0,0)} & 0 & 0 & 0 & 0 & 0 & 0 & 0 & 0 & 0 & 1 & 0
\end{array}\right]. \tag{A.7}$$

# Appendix B

# Proof of Theorem 6.8

**Proof** Assume a quadratic LFT form of $\mathcal{R}(\Theta_t, \Theta_s)$ and $\mathcal{S}(\Theta_t, \Theta_s)$, i.e.

$$\mathcal{R}(\Theta_t,\Theta_s) = \mathcal{T}_R^T(\Theta_t,\Theta_s) P \mathcal{T}_R(\Theta_t,\Theta_s) = [*]^T \left[\begin{array}{c:c} P_t & \\ \hdashline & P_s \end{array}\right] \left[\begin{array}{c:c} \mathcal{T}_{R_t}(\Theta_t) & \\ \hdashline & \mathcal{T}_{R_s}(\Theta_s) \end{array}\right]$$

$$= [*]^T \left[\begin{array}{c:c} P_t & \\ \hdashline & P_s \end{array}\right] \left[\begin{array}{c:c} \Theta_t \star \begin{bmatrix} T_{R_t 11} & T_{R_t 12} \\ T_{R_t 21} & T_{R_t 22} \end{bmatrix} & \\ \hdashline & \Theta_s \star \begin{bmatrix} T_{R_s 11} & T_{R_s 12} \\ T_{R_s 21} & T_{R_s 22} \end{bmatrix} \end{array}\right]$$

$$= [*]^T \left[\begin{array}{c:c} P_t & \\ \hdashline & P_s \end{array}\right] \left( \Upsilon \star \left[\begin{array}{cc:cc} T_{R_t 11} & & T_{R_t 12} & \\ & T_{R_s 11} & & T_{R_s 12} \\ \hdashline T_{R_t 21} & & T_{R_t 22} & \\ & T_{R_s 21} & & T_{R_s 22} \end{array}\right] \right) = [*]^T \left[\begin{array}{c:c} P_t & \\ \hdashline & P_s \end{array}\right] \left( \Upsilon \star \left[\begin{array}{c:c} R_{11} & R_{12} \\ \hdashline R_{21} & R_{22} \end{array}\right] \right). \tag{B.1}$$

Likewise,

$$\mathcal{S}(\Theta_t,\Theta_s) = \mathcal{T}_S^T(\Theta_t,\Theta_s) Q \mathcal{T}_S(\Theta_t,\Theta_s) = [*]^T \left[\begin{array}{c:c} Q_t & \\ \hdashline & Q_s \end{array}\right] \left( \Upsilon \star \left[\begin{array}{cc:cc} T_{S_t 11} & & T_{S_t 12} & \\ & T_{S_s 11} & & T_{S_s 12} \\ \hdashline T_{S_t 21} & & T_{S_t 22} & \\ & T_{S_s 21} & & T_{S_s 22} \end{array}\right] \right)$$

$$= [*]^T \left[\begin{array}{c:c} Q_t & \\ \hdashline & Q_s \end{array}\right] \left( \Upsilon \star \left[\begin{array}{c:c} S_{11} & S_{12} \\ \hdashline S_{21} & S_{22} \end{array}\right] \right). \tag{B.2}$$

Then all factors in condition (6.71) can be expressed in LFT representation as

$$\left[\begin{array}{cc} (\bar{\mathcal{A}}^G)^T(\Theta_t,\Theta_s) & (\bar{\mathcal{C}}_z^G)^T(\Theta_t,\Theta_s) \\ I & 0 \\ \hdashline (\bar{\mathcal{B}}_d^G)^T(\Theta_t,\Theta_s) & (\bar{\mathcal{D}}_{zd}^G)^T(\Theta_t,\Theta_s) \\ 0 & I \end{array}\right] = \Upsilon \star \left[\begin{array}{c:cc} (\bar{D}_{qp}^G)^T & (\bar{B}_p^G)^T & (\bar{D}_{zp}^G)^T \\ \hdashline (\bar{C}_q^G)^T & (\bar{A}^G)^T & (\bar{C}_z^G)^T \\ 0 & I & 0 \\ (\bar{D}_{qd}^G)^T & (\bar{B}_d^G)^T & (\bar{D}_{zd}^G)^T \\ 0 & 0 & I \end{array}\right] = \Upsilon \star \begin{bmatrix} M_{R11} & M_{R12} \\ M_{R21} & M_{R22} \end{bmatrix}, \tag{B.3}$$

$$\mathcal{N}_R(\Theta_t,\Theta_s) = \ker\left(\Upsilon \star \left[\begin{array}{c|cc} (\bar{D}^G_{qp})^T & (\bar{B}^G_p)^T & (\bar{D}^G_{zp})^T \\ \hline (\bar{D}^G_{qu})^T & (\bar{B}^G_u)^T & (\bar{D}^G_{zu})^T \end{array}\right]\right) = \Upsilon \star \begin{bmatrix} N_{R11} & N_{R12} \\ N_{R21} & N_{R22} \end{bmatrix}, \qquad \text{(B.4)}$$

$$\begin{bmatrix} 0 & \mathcal{R}(\Theta_t,\Theta_s) & 0 & 0 \\ \mathcal{R}(\Theta_t,\Theta_s) & -\partial\mathcal{R}(\Theta_t,\Theta_s) & 0 & 0 \\ 0 & 0 & \frac{1}{\gamma}I & 0 \\ 0 & 0 & 0 & -\gamma I \end{bmatrix} = [*]^T \begin{bmatrix} 0 & P & 0 & 0 \\ P & 0 & 0 & 0 \\ 0 & 0 & \frac{1}{\gamma}I & 0 \\ 0 & 0 & 0 & -\gamma I \end{bmatrix} \begin{bmatrix} \mathcal{T}_R(\Theta_t,\Theta_s) & -\partial\mathcal{T}_R(\Theta_t,\Theta_s) & 0 & 0 \\ 0 & \mathcal{T}_R(\Theta_t,\Theta_s) & 0 & 0 \\ 0 & 0 & I & 0 \\ 0 & 0 & 0 & I \end{bmatrix}, \qquad \text{(B.5)}$$

whose right factor is decomposed

$$\begin{aligned} \begin{bmatrix} \mathcal{T}_R(\Theta_t,\Theta_s) & -\partial\mathcal{T}_R(\Theta_t,\Theta_s) & 0 & 0 \\ 0 & \mathcal{T}_R(\Theta_t,\Theta_s) & 0 & 0 \\ 0 & 0 & I & 0 \\ 0 & 0 & 0 & I \end{bmatrix} &= \begin{bmatrix} \partial\Upsilon & & \\ & \Upsilon & \\ & & \Upsilon \end{bmatrix} \star \left[\begin{array}{ccc|cccc} 0 & 0 & R_{11} & 0 & R_{12} & 0 & 0 \\ R_{11} & R_{11} & 0 & -R_{12} & 0 & 0 & 0 \\ 0 & 0 & R_{11} & 0 & R_{12} & 0 & 0 \\ \hline -R_{21} & -R_{21} & 0 & R_{22} & 0 & 0 & 0 \\ 0 & 0 & R_{21} & 0 & R_{22} & 0 & 0 \\ 0 & 0 & 0 & 0 & 0 & I & 0 \\ 0 & 0 & 0 & 0 & 0 & 0 & I \end{array}\right] \\ &= \begin{bmatrix} \partial\Upsilon & & \\ & \Upsilon & \\ & & \Upsilon \end{bmatrix} \star \begin{bmatrix} L_{R11} & L_{R12} \\ L_{R21} & L_{R22} \end{bmatrix}. \end{aligned} \qquad \text{(B.6)}$$

Combine the LFT representations (B.3), (B.4) and (B.6). Condition (6.71) can be written as

$$[*]^T \begin{bmatrix} 0 & P & 0 & 0 \\ P & 0 & 0 & 0 \\ 0 & 0 & \frac{1}{\gamma}I & 0 \\ 0 & 0 & 0 & -\gamma I \end{bmatrix} \left(\begin{bmatrix} \partial\Upsilon & & \\ & \Upsilon & \\ & & \Upsilon \end{bmatrix} \star \begin{bmatrix} L_{R11} & L_{R12} \\ L_{R21} & L_{R22} \end{bmatrix}\right) \left(\Upsilon \star \begin{bmatrix} M_{R11} & M_{R12} \\ M_{R21} & M_{R22} \end{bmatrix}\right) \left(\Upsilon \star \begin{bmatrix} N_{R11} & N_{R12} \\ N_{R21} & N_{R22} \end{bmatrix}\right) < 0. \qquad \text{(B.7)}$$

After performing the star products, (B.7) becomes

$$[*]^T \begin{bmatrix} 0 & P & 0 & 0 \\ P & 0 & 0 & 0 \\ 0 & 0 & \frac{1}{\gamma}I & 0 \\ 0 & 0 & 0 & -\gamma I \end{bmatrix} \left(\begin{bmatrix} \partial\Upsilon & & & & \\ & \Upsilon & & & \\ & & \Upsilon & & \\ & & & \Upsilon & \\ & & & & \Upsilon \end{bmatrix} \star \begin{bmatrix} G_{P11} & G_{P12} \\ G_{P21} & G_{P22} \end{bmatrix}\right) < 0, \qquad \text{(B.8)}$$

where

$$\left[\begin{array}{c|c} G_{P11} & G_{P12} \\ \hline G_{P21} & G_{P22} \end{array}\right] = \left[\begin{array}{ccc|c} L_{R11} & L_{R12}M_{R21} & L_{R12}M_{R22}N_{R21} & L_{R12}M_{R22}N_{R22} \\ 0 & M_{R11} & M_{R12}N_{R21} & M_{R12}N_{R22} \\ 0 & 0 & N_{R11} & N_{R12} \\ \hline L_{R21} & L_{R22}M_{R21} & L_{R22}M_{R22}N_{R21} & L_{R22}M_{R22}N_{R22} \end{array}\right]. \qquad \text{(B.9)}$$

Applying similar procedures to (6.72) yields

$$[*]^T \begin{bmatrix} 0 & Q & 0 & 0 \\ Q & 0 & 0 & 0 \\ 0 & 0 & \frac{1}{\gamma}I & 0 \\ 0 & 0 & 0 & -\gamma I \end{bmatrix} \left( \begin{bmatrix} \partial\Upsilon & & & & \\ & \Upsilon & & & \\ & & \Upsilon & & \\ & & & \Upsilon & \\ & & & & \Upsilon \end{bmatrix} \star \begin{bmatrix} G_{Q11} & G_{Q12} \\ G_{Q21} & G_{Q22} \end{bmatrix} \right) < 0, \tag{B.10}$$

where

$$\left[\begin{array}{c:c} G_{Q11} & G_{Q12} \\ \hdashline G_{Q21} & G_{Q22} \end{array}\right] = \left[\begin{array}{ccc:c} L_{S11} & L_{S12}M_{S21} & L_{S12}M_{S22}N_{S21} & L_{S12}M_{S22}N_{S22} \\ 0 & M_{S11} & M_{S12}N_{S21} & M_{S12}N_{S22} \\ 0 & 0 & N_{S11} & N_{S12} \\ \hdashline L_{S21} & L_{S22}M_{S21} & L_{S22}M_{S22}N_{S21} & L_{S22}M_{S22}N_{S22} \end{array}\right] \tag{B.11}$$

with

$$\begin{bmatrix} \bar{\mathcal{A}}^G(\Theta_t,\Theta_s) & \bar{\mathcal{B}}_d^G(\Theta_t,\Theta_s) \\ I & 0 \\ \bar{\mathcal{C}}_z^G(\Theta_t,\Theta_s) & \bar{\mathcal{D}}_{zd}^G(\Theta_t,\Theta_s) \\ 0 & I \end{bmatrix} = \Upsilon \star \left[\begin{array}{c:cc} \bar{D}_{qp}^G & \bar{C}_q^G & \bar{D}_{qd}^G \\ \hdashline \bar{B}_p^G & \bar{A}^G & \bar{B}_d^G \\ 0 & I & 0 \\ \bar{D}_{zp}^G & \bar{C}_z^G & \bar{D}_{zd}^G \\ 0 & 0 & I \end{array}\right] = \Upsilon \star \begin{bmatrix} M_{S11} & M_{S12} \\ M_{S21} & M_{S22} \end{bmatrix}, \tag{B.12}$$

$$\mathcal{N}_S(\Theta_t,\Theta_s) = \ker\left(\Upsilon \star \left[\begin{array}{c:cc} \bar{D}_{qp}^G & \bar{C}_p^G & \bar{D}_{qd}^G \\ \hdashline \bar{D}_{yp}^G & \bar{C}_y^G & \bar{D}_{yd}^G \end{array}\right]\right) = \Upsilon \star \begin{bmatrix} N_{S11} & N_{S12} \\ N_{S21} & N_{S22} \end{bmatrix}, \tag{B.13}$$

and

$$\begin{bmatrix} 0 & \mathcal{S}(\Theta_t,\Theta_s) & 0 & 0 \\ \mathcal{S}(\Theta_t,\Theta_s) & \partial\mathcal{S}(\Theta_t,\Theta_s) & 0 & 0 \\ 0 & 0 & \frac{1}{\gamma}I & 0 \\ 0 & 0 & 0 & -\gamma I \end{bmatrix} = [*]^T \begin{bmatrix} 0 & Q & 0 & 0 \\ Q & 0 & 0 & 0 \\ 0 & 0 & \frac{1}{\gamma}I & 0 \\ 0 & 0 & 0 & -\gamma I \end{bmatrix} \begin{bmatrix} \mathcal{T}_S(\Theta_t,\Theta_s) & \partial\mathcal{T}_S(\Theta_t,\Theta_s) & 0 & 0 \\ 0 & \mathcal{T}_S(\Theta_t,\Theta_s) & 0 & 0 \\ 0 & 0 & I & 0 \\ 0 & 0 & 0 & I \end{bmatrix}, \tag{B.14}$$

whose right factor is decomposed as

$$\begin{aligned} \begin{bmatrix} \mathcal{T}_S(\Theta_t,\Theta_s) & \partial\mathcal{T}_S(\Theta_t,\Theta_s) & 0 & 0 \\ 0 & \mathcal{T}_S(\Theta_t,\Theta_s) & 0 & 0 \\ 0 & 0 & I & 0 \\ 0 & 0 & 0 & I \end{bmatrix} &= \begin{bmatrix} \partial\Upsilon & & \\ & \Upsilon & \\ & & \Upsilon \end{bmatrix} \star \left[\begin{array}{ccc:cccc} 0 & 0 & S_{11} & 0 & S_{12} & 0 & 0 \\ S_{11} & S_{11} & 0 & S_{12} & 0 & 0 & 0 \\ 0 & 0 & S_{11} & 0 & S_{12} & 0 & 0 \\ \hdashline S_{21} & S_{21} & 0 & S_{22} & 0 & 0 & 0 \\ 0 & 0 & S_{21} & 0 & S_{22} & 0 & 0 \\ 0 & 0 & 0 & 0 & 0 & I & 0 \\ 0 & 0 & 0 & 0 & 0 & 0 & I \end{array}\right] \\ &= \begin{bmatrix} \partial\Upsilon & & \\ & \Upsilon & \\ & & \Upsilon \end{bmatrix} \star \begin{bmatrix} L_{S11} & L_{S12} \\ L_{S21} & L_{S22} \end{bmatrix}. \end{aligned} \tag{B.15}$$

Analogously, applying the FBSP to (6.73) yields

$$[*]^T \begin{bmatrix} P_t & 0 & 0 & 0 \\ 0 & Q_t & 0 & 0 \\ 0 & 0 & 0 & I \\ 0 & 0 & I & 0 \end{bmatrix} \begin{bmatrix} \mathcal{T}_{R_t}(\Theta_t) & 0 \\ 0 & \mathcal{T}_{S_t}(\Theta_t) \\ I & 0 \\ 0 & I \end{bmatrix} \geq 0, \tag{B.16}$$

$$[*]^T \begin{bmatrix} P_t & 0 & 0 & 0 \\ 0 & Q_t & 0 & 0 \\ 0 & 0 & 0 & I \\ 0 & 0 & I & 0 \end{bmatrix} \left( \begin{bmatrix} \Theta_t & \\ & \Theta_t \end{bmatrix} \star \begin{bmatrix} G_{11} & G_{12} \\ G_{21} & G_{22} \end{bmatrix} \right) \geq 0, \tag{B.17}$$

where

$$\left[\begin{array}{c:c} G_{11} & G_{12} \\ \hdashline G_{21} & G_{22} \end{array}\right] = \left[\begin{array}{cc:cc} T_{R_t 11} & 0 & T_{R_t 12} & 0 \\ 0 & T_{S_t 11} & 0 & T_{S_t 12} \\ \hdashline T_{R_t 21} & 0 & T_{R_t 22} & 0 \\ 0 & T_{S_t 21} & 0 & T_{S_t 22} \\ 0 & 0 & I & 0 \\ 0 & 0 & 0 & I \end{array}\right]. \tag{B.18}$$

Thus, conditions (6.71) - (6.73) can be written in LFT form as (6.77) - (6.78). Applying the FBSP results synthesis conditions (6.79) - (6.84). ■

# Appendix C

# Auxiliary Technical Material

## C.1 Hardware and Software Description

| Quantity | Type | Description | Producer |
|---|---|---|---|
| 16 | P-876.A11 | PZT as sensor | Physik Instrumente |
| 16 | P-876.A12 | PZT as actuator | Physik Instrumente |
| 16 | E-835 | PZT driver module | Physik Instrumente |
| 1 | NI6353 | Analog input card | National Instruments |
| 1 | NI6723 | Analog output card | National Instruments |
| 1 | Labview | Real-time system | National Instruments |

Table C.1: Hardware and software description

## C.2 Upper and Lower LFT

For appropriately dimensioned matrices $K$ and $M = \begin{bmatrix} M_{11} & M_{12} \\ M_{21} & M_{22} \end{bmatrix}$ and assuming its inverse exists, the upper LFT is defined as

$$F_u(M, K) = M_{22} + M_{21}K(I - M_{11}K)^{-1}M_{12}. \tag{C.1}$$

Similarly, the lower LFT is defined as

$$F_l(M, K) = M_{11} + M_{12}K(I - M_{22}K)^{-1}M_{21}. \tag{C.2}$$

## C.3 Bilinear Transformation

Let $m_0$, $m_+$, $m_-$ indicate the sizes of the temporal, positive and negative spatial state vectors, respectively, and define $H = \mathrm{diag}\{I_{m_0}, I_{m_+}, -I_{m_-}\}$. The discrete state space model (2.11) (discrete both in time and space) and its equivalent continuous counterpart (continuous both in time and space) can be converted in both directions through the bilinear transformation [8] [21].

- discrete to continuous:

$$\bar{A} = H(A - I)(A + I)^{-1} \tag{C.3}$$

$$\begin{bmatrix} \bar{B}_d & \bar{B}_u \end{bmatrix} = \sqrt{2}H(A + I)^{-1} \begin{bmatrix} B_d & B_u \end{bmatrix} \tag{C.4}$$

$$\begin{bmatrix} \bar{C}_z \\ \bar{C}_y \end{bmatrix} = \sqrt{2} \begin{bmatrix} C_z \\ C_y \end{bmatrix} (A + I)^{-1} \tag{C.5}$$

$$\begin{bmatrix} \bar{D}_{zd} & \bar{D}_{zu} \\ \bar{D}_{yd} & \bar{D}_{yu} \end{bmatrix} = \begin{bmatrix} D_{zd} & D_{zu} \\ D_{yd} & D_{yu} \end{bmatrix} - \begin{bmatrix} C_z \\ C_y \end{bmatrix} (A + I)^{-1} \begin{bmatrix} B_d & B_u \end{bmatrix} \tag{C.6}$$

- continuous to discrete:

$$A = (I - H\bar{A})^{-1}(I + H\bar{A}) \tag{C.7}$$

$$\begin{bmatrix} B_d & B_u \end{bmatrix} = \sqrt{2}(I - H\bar{A})^{-1}H \begin{bmatrix} \bar{B}_d & \bar{B}_u \end{bmatrix} \tag{C.8}$$

$$\begin{bmatrix} C_z \\ C_y \end{bmatrix} = \sqrt{2} \begin{bmatrix} \bar{C}_z \\ \bar{C}_y \end{bmatrix} (I - H\bar{A})^{-1} \tag{C.9}$$

$$\begin{bmatrix} D_{zd} & D_{zu} \\ D_{yd} & D_{yu} \end{bmatrix} = \begin{bmatrix} \bar{D}_{zd} & \bar{D}_{zu} \\ \bar{D}_{yd} & \bar{D}_{yu} \end{bmatrix} + \begin{bmatrix} \bar{C}_z \\ \bar{C}_y \end{bmatrix} (I - H\bar{A})^{-1}H \begin{bmatrix} \bar{B}_d & \bar{B}_u \end{bmatrix} \tag{C.10}$$

## C.4 Elimination Lemma

**Lemma C.1 (Elimination Lemma [105])** *Consider a symmetric matrix* $P = \begin{bmatrix} Q & S \\ S^T & R \end{bmatrix}$ *with* $R \geq 0$*, and its inverse* $P^{-1} = \begin{bmatrix} \tilde{Q} & \tilde{S} \\ \tilde{S}^T & \tilde{R} \end{bmatrix}$ *with* $\tilde{Q} \leq 0$*. The quadratic inequality*

$$\begin{bmatrix} I \\ A^T X B + C \end{bmatrix}^T P \begin{bmatrix} I \\ A^T X B + C \end{bmatrix} < 0 \tag{C.11}$$

*has a solution* $X$ *if and only if*

$$B_\perp^T \begin{bmatrix} I \\ C \end{bmatrix}^T P \begin{bmatrix} I \\ C \end{bmatrix} B_\perp < 0 \tag{C.12}$$

$$A_\perp^T \begin{bmatrix} -C^T \\ I \end{bmatrix}^T P^{-1} \begin{bmatrix} -C^T \\ I \end{bmatrix} A_\perp < 0 \tag{C.13}$$

*hold true, where* $A_\perp$ *and* $B_\perp$ *denote arbitrary matrices whose columns form the kernel spaces of* $A$ *and* $B$*, respectively.*

## C.5 KYP Lemma

**Lemma C.2 (KYP Lemma [106])** *Given* $M = M^T \in \mathbb{R}^{(n+m)\times(n+m)}$, $A \in \mathbb{R}^{n\times n}$, $B \in \mathbb{R}^{n\times m}$, *with* $det(j\omega I - A) \neq 0$ *for* $\omega \in \mathbb{R}$ *and* $(A, B)$ *controllable, the following two statements are equivalent:*

- $\forall\omega \in \mathbb{R} \cup \{\infty\}$

$$\begin{bmatrix} (j\omega I - A)^{-1}B \\ I \end{bmatrix}^* M \begin{bmatrix} (j\omega I - A)^{-1}B \\ I \end{bmatrix} \leq 0 \tag{C.14}$$

- *There exists a matrix* $P \in \mathbb{R}^{n\times n}$ *such that* $P = P^T$ *and*

$$M + \begin{bmatrix} A^T P + PA & PB \\ B^T P & 0 \end{bmatrix} \leq 0. \tag{C.15}$$

*The equivalence for strict inequalities holds even if* $(A, B)$ *is not controllable.*

# Bibliography


[1] K. C. Chu, "Decentralized Control of High-Speed Vehicular Strings," *Transport. Sci.*, vol. 8, no. 4, pp. 361–384, 1974.

[2] G. E. Stewart, "Two-Dimensional Loop Shaping Controller Design for Paper Machine Cross-directional Processes," Dissertation, University of British Columbia, Vancouver, Canada, 2000.

[3] S. S. Chughtai and H. Werner, "Modeling and Distributed Control of Transition in Plane Poiseuille Flow," *IEEE Trans. Contr. Syst. Technol.*, vol. 20, no. 3, pp. 755–762, 2012.

[4] M. V. Gandhi and B. S. Thompson, *Smart Materials and Structures*, 1st ed. London and New York: Chapman & Hall, 1992.

[5] R. F. Curtain and H. J. Zwart, *An Introduction to Infinite-Dimensional Linear Systems Theory*, ser. Texts in Applied Mathematics. New York: Springer-Verlag, 1995, vol. 21.

[6] B. Bamieh, F. Paganini, and M. A. Dahleh, "Distributed Control of Spatially Invariant Systems," *IEEE Trans. Automat. Contr.*, vol. 47, no. 7, pp. 1091–1107, 2002.

[7] M. Jovanovic, "Modeling, Analysis, and Control of Spatially Distributed Systems," Dissertation, University of California, Santa Barbara, CA, 2004.

[8] R. D'Andrea and G. E. Dullerud, "Distributed Control Design for Spatially Interconnected Systems," *IEEE Trans. Automat. Contr.*, vol. 48, no. 9, pp. 1478–1495, 2003.

[9] K. Napolitano and M. Schlosser, "Calculation of Rigid Body Mass Properties of Flexible Structures," in *Advanced Aerospace Applications*, ser. Conference Proceedings of the Society for Experimental Mechanics Series, T. Proulx, Ed. Springer, 2011.

[10] J. S. Shamma, "Analysis and Design of Gain Scheduled Control Systems," Dissertation, Massachusetts Institute of Technology, 1988.

[11] P. Apkarian and P. Gahinet, "A Convex Characterization of Gain-Scheduled H$\infty$ Controllers," *IEEE Trans. Automat. Contr.*, vol. 40, no. 5, pp. 853–864, 1995.

[12] P. Apkarian, P. Gahinet, and G. Becker, "Self-Scheduled H$\infty$ Control of Linear Parameter-varying Systems: a Design Example," *Automatica*, vol. 31, no. 9, pp. 1251–1261, 1995.

[13] P. Apkarian and R. J. Adams, "Advanced Gain-Scheduling Techniques for Uncertain Systems," *IEEE Trans. Contr. Syst. Technol.*, vol. 6, no. 1, pp. 21–32, 1998.

[14] F. Wu and K. Dong, "Gain-Scheduling Control of LFT Systems Using Parameter-Dependent Lyapunov Functions," *Automatica*, vol. 42, no. 1, pp. 39–50, 2006.

[15] P. Gahinet, P. Apkarian, and M. Chilali, "Affine Parameter-Dependent Lyapunov Functions and Real Parametric Uncertainty," *IEEE Trans. Automat. Contr.*, vol. 41, no. 3, pp. 436–442, 1996.

[16] J. S. Shamma, "An Overview of LPV Systems," in *Control of Linear Parameter Varying Systems with Applications*, J. Mohammadpour and C. W. Scherer, Eds. Springer US, 2012.

[17] C. Hoffmann and H. Werner, "A Survey of Linear Parameter-Varying Control Applications Validated by Experiments or High-Fidelity Simulations," *IEEE Trans. Contr. Syst. Technol.*, vol. 23, no. 2, pp. 1–18, 2014.

[18] F. Wu, "Control of Linear Parameter Varying Systems," Dissertation, University of Berkeley, Berkeley, CA, 1995.

[19] M. Dettori, "LMI Techniques for Control with Application to a Compact Disc Player Mechanism," Dissertation, Delft University of Technology, Delft, Netherlands, 2001.

[20] A. Helmersson, "Methods for Robust Gain-Scheduling," Dissertation, Linköping University, Sweden, 1995.

[21] F. Wu, "Distributed Control for Interconnected Linear Parameter-Dependent Systems," *IEE Proc., Control Theory Appl.*, vol. 150, no. 5, pp. 518–527, 2003.

[22] K.-J. Bathe, *Finite Element Procedures.* Upper Saddle River, NJ: Prentice Hall, 1996.

[23] R. Holland and E. P. EerNisse, "Variational Evaluation of Admittances of Multielectroded Three-Dimensional Piezoelectric Structures," *IEEE Trans. Son. Ultrason.*, vol. 15, no. 2, pp. 119–131, 1968.

[24] H. Allik and Hughes, Thomas J. R., "Finite Element Method for Piezoelectric Vibration," *Int. J. Numer. Meth. Engng.*, vol. 2, no. 2, pp. 151–157, 1970.

[25] G. L. C. M. d. Abreu, J. F. Ribeiro, and V. Steffen, Jr., "Finite Element Modeling of a Plate with Localized Piezoelectric Sensors and Actuators," *J. Braz. Soc. Mech. Sci. & Eng.*, vol. 26, no. 2, pp. 117–128, 2004.

[26] M. Rios-Gutierrez and G. Silva-Navarro, "Finite Element and Modal Modeling of a Cantilever Beam with Piezoelectric Patch Actuator for Vibration Absorption," in *Proc. 6th IEEE Conf. Elect. Eng., Computing Sci. and Automat. Control*, 2009.

[27] M. Ali, S. S. Chughtai, and H. Werner, "Identification of Spatially Interconnected Systems," in *Proc. 48th IEEE Conf. Decision Control*, 2009.

[28] B. Bamieh and L. Giarré, "Identification of Linear Parameter Varying Models," *Int. J. Robust Nonlinear Contr.*, vol. 12, no. 9, pp. 841–853, 2002.

[29] M. Ali, S. S. Chughtai, and H. Werner, "Identification of LPV Models for Spatially Varying Interconnected Systems," in *Proc. Amer. Control Conf.*, 2010.

[30] J. K. Rice and M. Verhaegen, "Distributed Control: A Sequentially Semi-Separable Approach," in *Proc. 47th IEEE Conf. Decision Control*, 2008.

[31] P. Massioni and M. Verhaegen, "Distributed Control for Identical Dynamically Coupled Systems: A Decomposition Approach," *IEEE Trans. Automat. Contr.*, vol. 54, no. 1, pp. 124–135, 2009.

[32] G. E. Stewart, D. M. Gorinevsky, and G. A. Dumont, "Feedback Controller Design for a Spatially Distributed System: the Paper Machine Problem," *IEEE Trans. Contr. Syst. Technol.*, vol. 11, no. 5, pp. 612–628, 2003.

[33] E. Scholte and R. D'Andrea, "Active Vibro-Acoustic Control of a Flexible Beam Using Distributed Control," in *Proc. Amer. Control Conf.*, 2003.

[34] G. E. Dullerud and R. D'Andrea, "Distributed Control of Heterogeneous Systems," *IEEE Trans. Automat. Contr.*, vol. 49, no. 12, pp. 2113–2128, 2004.

[35] J. Doyle and R. S. Smith, "Control of Plants with Input Saturation Nonlinearities," in *Proc. Amer. Control Conf.* Proc. Amer. Control Conf., 1987.

[36] P. F. Weston and I. Postlethwaite, "Linear Conditioning for Systems Containing Saturating Actuators," *Automatica*, vol. 36, no. 9, pp. 1347–1354, 2000.

[37] G. Grimm, J. Hatfield, I. Postlethwaite, A. R. Teel, M. C. Turner, and L. Zaccarian, "Antiwindup for Stable Linear Systems with Input Saturation: An LMI-based Synthesis," *IEEE Trans. Automat. Contr.*, vol. 48, no. 9, pp. 1509–1525, 2003.

[38] M. C. Turner, G. Herrmann, and I. Postlethwaite, "Incorporating Robustness Requirements Into Antiwindup Design," *IEEE Trans. Automat. Contr.*, vol. 52, no. 10, pp. 1842–1855, 2007.

[39] E. F. Mulder, M. V. Kothare, and M. Morari, "Multivariable Anti-Windup Controller Synthesis Using Linear Matrix Inequalities," *Automatica*, vol. 37, no. 9, pp. 1407–1416, 2001.

[40] M. Kishida and R. D. Braatz, "Robust Anti-Windup Compensation for Normal Systems with Application to the Reaction-Diffusion Equation," in *Proc. 18th IFAC World Congr.*, 2011.

[41] Y. Li and M. Cantoni, "On Distributed Anti-Windup Compensation for Distributed Linear Control Systems," in *Proc. 46th IEEE Conf. Decision Control*, 2007.

[42] A. Megretski and A. Rantzer, "System Analysis Via Integral Quadratic Constraints," *IEEE Trans. Automat. Contr.*, vol. 42, no. 6, pp. 819–830, 1997.

[43] C. W. Scherer, "LPV Control and Full Block Multipliers," *Automatica*, vol. 37, no. 3, pp. 361–375, 2001.

[44] K. Zhou, J. Doyle, and K. Glover, *Robust and Optimal Control.* Upper Saddle River, NJ: Prentice-Hall, 1996.

[45] C. W. Scherer, "Robust Mixed Control and LPV Control with Full Block Scalings." Philadelphia, PA: SIAM.

[46] C. Galassi, *Piezoelectric Materials: Advances in Science, Technology, and Applications*, ser. NATO science series. Series 3, High technology. Dordrecht and Boston: Kluwer Academic Publishers, 2000, vol. 76.

[47] H. Kawai, "The Piezoelectricity of Poly (vinylidene Fluoride)," *Jpn. J. Appl. Phys.*, vol. 8, no. 7, pp. 975–976, 1969.

[48] Y. R. Wang, J. M. Zheng, G. Y. Ren, P. H. Zhang, and C. Xu, "A Flexible Piezoelectric Force Sensor based on PVDF Fabrics," *Smart Mater. Struct.*, vol. 20, no. 4, p. 045009, 2011.

[49] *IEEE Standard on Piezoelectricity.* ANSI/IEEE Std 176-1987, 1988.

[50] PI, "P-876 Datasheet, DuraAct$^{\text{TM}}$ Piezoelectric Patch Transducers."

[51] A. Preumont, *Vibration Control of Active Structures, An Introduction - 2nd Edition*, Dordrecht and Boston, 2002, vol. 96.

[52] W. B. Bickford, *A First Course in the Finite Element Method*, 2nd ed. Burr Ridge, IL: Richard D Irwin, 1994.

[53] H. S. Tzou and C. I. Tseng, "Distributed Piezoelectric Sensor/Actuator Design for Dynamic Measurement/Control of Distributed Parameter Systems: A Piezoelectric Finite Element Approach," *J. Sound Vib.*, vol. 138, no. 1, pp. 17–34, 1990.

[54] V. Piefort, "Finite Element Modelling of Piezoelectric Active Structures," Dissertation, Université libre de Bruxelles, Brussel, Belgien, 2001.

[55] O. A. Bauchau and J. I. Craig, *Structural analysis: With Applications to Aerospace Structures*, ser. Solid Mechanics and its Applications. Dordrecht: Springer, 2009, vol. 163.

[56] J. He and Z.-F. Fu, *Modal Analysis.* Oxford and Boston: Butterworth-Heinemann, 2001.

[57] D. J. Ewins, *Modal Testing: Theory, Practice, and Application*, 2nd ed., ser. Mechanical Engineering Research Studies: Engineering Dynamics Series. Baldock, Hertfordshire, England: Research Studies Press, 2000, vol. 10.

[58] D. W. Marquardt, "An Algorithm for Least-Squares Estimation of Nonlinear Parameters," *SIAM J. Appl. Math.*, vol. 11, no. 2, pp. 431–441, 1963.

[59] D. F. Pilkey, "Computation of a Damping Matrix for Finite Element Model Updating," Dissertation, Virginia Polytechnic Institute and State University, Blacksburg, Virginia, 1998.

[60] Q. Liu, J. Gross, S. Pfeiffer, and H. Werner, "A Local Approach for the LPV Identification of an Actuated Beam Using Piezoelectric Actuators and Sensors," *Mechatronics*, vol. 24, no. 4, pp. 289–297, 2014.

[61] A. A. Khalate, X. Bombois, R. Tóth, and R. Babuška, "Optimal Experimental Design for LPV Identification Using a Local Approach," in *15th IFAC Symp. Syst. Ident.*, 2009.

[62] M. Steinbuch, R. van de Molengraft, and A. van der Voort, "Experimental Modelling and LPV Control of a Motion System," in *Proc. Amer. Control Conf.*, 2003.

[63] R. Tóth, "Modeling and Identification of Linear Parameter-Varying Systems, an Orthonormal Basis Function Approach," Dissertation, Delft University of Technology, Delft, Netherlands, 2008.

[64] H. Benaroya, *Mechanical Vibration: Analysis, Uncertainties, and Control*, 2nd ed., ser. Mechanical Engineering. New York: Marcel Dekker, 2004, vol. 181.

[65] Q. Liu and H. Werner, "Experimental Identification of Spatially-Interconnected Parameter-Invariant and LPV Models for Actuated Beams," in *Proc. 52nd IEEE Conf. Decision Control*, 2013.

[66] Q. Liu, J. Gross, and H. Werner, "Distributed Identification of Spatially-Distributed Systems based on Finite Element Modelling," in *Proc. 54th IEEE Conf. Decision Control*, 2015.

[67] J. Crank and P. Nicolson, "A Practical Method for Numerical Evaluation of Solutions of Partial Differential Equations of the Heat-Conduction Type," *Adv Comput Math*, vol. 6, no. 1, pp. 207–226, 1996.

[68] R. Courant, K. Friedrichs, and H. Lewy, "On the Partial Difference Equations of Mathematical Physics," *IBM J. Res. & Dev.*, vol. 11, no. 2, pp. 215–234, 1967.

[69] J. C. Strikwerda, *Finite Difference Schemes and Partial Differential Equations*, 2nd ed. Philadelphia, PA: SIAM, 2004.

[70] D. E. Dudgeon and R. M. Mersereau, *Multidimensional Digital Signal Processing*. Prentice-Hall Inc. USA, 1984.

[71] M. Ali, "Identification and Control of Spatially Interconnected Systems," Dissertation, Hamburg University of Technology, Hamburg, Germany, 2011.

[72] M. Ali, A. Ali, H. S. Abbas, and H. Werner, "Identification of Box-Jenkins Models for Parameter-Varying Spatially Interconnected Systems," in *Proc. Amer. Control Conf.*, 2011.

[73] M. Ali, H. S. Abbas, S. S. Chughtai, and H. Werner, "Identification of Spatially Interconnected Systems Using Neural Networks," in *Proc. 49th IEEE Conf. Decision Control*, 2010.

[74] R. Tóth, P. Heuberger, and Van den Hof, P., "Asymptotically Optimal Orthonormal Basis Functions for LPV System Identification," *Automatica*, vol. 45, no. 6, pp. 1359–1370, 2009.

[75] L. Herrmann, "Vibration of the Euler-Bernoulli Beam with Allowance for Dampings," in *Proc. World Congr. on Engineering*, vol. 2. Newseood Ltd., International Association of Engineers, 2008.

[76] J. K. Rice and M. Verhaegen, "Distributed Control: A Sequentially Semi-Separable Approach for Spatially Heterogeneous Linear Systems," *IEEE Trans. Automat. Contr.*, vol. 54, no. 6, pp. 1270–1283, 2009.

[77] M. Norgaard, O. Ravn, N. K. Poulsen, and L. K. Hansen, *Neural Networks for Modelling and Control of Dynamic Systems*. London: Springer-Verlag, 2003.

[78] M. Meisami-Azad, J. Mohammadpour Velni, K. Hiramoto, and K. M. Grigoriadis, "Integrated Design of Large-Scale Collocated Structural System and Control Parameters Using a Norm Upper Bound Approach," in *Efficient Modeling and Control of Large-Scale Systems*, J. Mohammadpour and K. M. Grigoriadis, Eds. Springer US, 2010.

[79] Q. Liu, C. Hoffmann, and H. Werner, "Distributed Control of Parameter-Varying Spatially Interconnected Systems Using Parameter-Dependent Lyapunov Functions," in *Proc. Amer. Control Conf.*, 2013.

[80] Q. Liu, A. Mendez Gonzalez, and H. Werner, "Distributed Control of Spatially-Interconnected Parameter-Invariant and LPV Models for Actuated Beams," in *Proc. Amer. Control Conf.*, 2014.

[81] M. Ali, H. S. Abbas, and H. Werner, "MIMO Controller Synthesis for LTI and LPV Systems Using Input-Output Models," in *Proc. 18th IFAC World Congr.*, 2011.

[82] S. Wollnack, H. S. Abbas, R. Toth, and H. Werner, "Fixed-Structure LPV Controller Synthesis Based on Implicit Input-Output Representations," in *Proc. 52nd IEEE Conf. Decision Control*, 2013.

[83] R. Toth, H. S. Abbas, and H. Werner, "On the State-Space Realization of LPV Input-Output Models: Practical Approaches," *IEEE Trans. Contr. Syst. Technol.*, vol. 20, no. 1, pp. 139–153, 2012.

[84] C. W. Scherer, "Theory of Robust Control," Lecture Notes, Delft University of Technology, Delft, Netherlands, 2001.

[85] G. E. Stewart, D. M. Gorinevsky, and G. A. Dumont, "Two-Dimensional Loop Shaping," *Automatica*, vol. 39, no. 5, pp. 779–792, 2003.

[86] R. D'Andrea, "Software for Modeling, Analysis, and Control Design for Multidimensional Systems," in *Proc. IEEE Int. Symposium Comput. Aid. Control Syst. Des.*, 1999.

[87] M. Dettori and C. W. Scherer, "LPV Design for a CD Player: an Experimental Evaluation of Performance," in *Proc. 40th IEEE Conf. Decision Control*, 2001.

[88] S. P. Boyd, L. E. Ghaoui, E. Feron, and V. Balakrishnan, *Linear Matrix Inequalities in System and Control Theory*, ser. SIAM, 1994, vol. 15.

[89] G. Grimm, A. R. Teel, and L. Zaccarian, "Linear LMI-based External Anti-Windup Augmentation for Stable Linear Systems," *Automatica*, vol. 40, no. 11, pp. 1987–1996, 2004.

[90] G. Li, W. P. Heath, and G. Herrmann, "Robust Anti-Windup Compensator Synthesis via Integral Quadratic Constraints," in *Proc. 18th IFAC World Congr.*, vol. 18, 2011.

[91] R. M. Morales, G. Li, and W. P. Health, "Anti-Windup and the Preservation of Robustness against Structured Norm-Bounded Uncertainty," in *Proc. 17th IFAC World Congr.*, vol. 17, 2008.

[92] F. Wu, K. M. Grigoriadis, and A. K. Packard, "Anti-Windup Controller Design Using Linear Parameter-Varying Control Methods," *Int. J. Contr.*, vol. 73, no. 12, pp. 1104–1114, 2000.

[93] Q. Liu and H. Werner, "Distributed Antiwindup Compensation for Spatially-Interconnected Systems," in *Proc. Amer. Control Conf.*, 2015.

[94] M. C. Turner and D. Bates, *Mathematical Methods for Robust and Nonlinear Control: EPSRC Summer School*, ser. Lecture Notes in Control and Information Sciences. Berlin and London: Springer, 2007.

[95] U. Jönssen, "Lecture Notes on Integral Quadratic Constraints," Royal Institute of Technology, Stockholm, Sweden, 2001.

[96] P. J. Seiler, A. Packard, and G. J. Balas, "A Dissipation Inequality Formulation for Stability Analysis with Integral Quadratic Constraints," in *Proc. 49th IEEE Conf. Decision Control*, 2010.

[97] H. Pfifer and P. J. Seiler, "Robust Analysis of Linear Parameter Varying Systems Using Integral Quadratic Constraints," in *Proc. Amer. Control Conf.*, 2014.

[98] M. C. Turner, G. Herrmann, and I. Postlethwaite, "Improving Sector-based Results for Systems with Dead-Zone Nonlinearities and Constrained Control Applications," *Automatica*, vol. 45, no. 1, pp. 155–160, 2009.

[99] C. W. Scherer and I. E. Köse, "Robustness with Dynamic IQCs: An Exact State-Space Characterization of Nominal Stability with Applications to Robust Estimation," *Automatica*, vol. 44, no. 7, pp. 1666–1675, 2008.

[100] C. W. Scherer, "Gain-Scheduled Synthesis with Dynamic Stable Strictly Positive Real Multipliers: A Complete Solution," in *Proc. Europ. Control Conf.*, 2013.

[101] C. L. Beck, J. Doyle, and K. Glover, "Model Reduction of Multidimensional and Uncertain Systems," *IEEE Trans. Automat. Contr.*, vol. 41, no. 10, pp. 1466–1477, 1996.

[102] M. Ali, H. S. Abbas, and H. Werner, "Controller Synthesis for Input-Output LPV Models," in *Proc. Int. Conf. Control Applicat.*, 2010.

[103] S. Wollnack and H. Werner, "Distributed Fixed-Structure Control of Spatially Interconnected Systems," in *Proc. Amer. Control Conf.*, 2015.

[104] M. Vidyasagar, *Nonlinear Systems Analysis*, 2nd ed., ser. Classics in Applied Mathematics. Philadelphia, PA: SIAM, 2002.

[105] C. W. Scherer and S. Weiland, "Linear Matrix Inequalities in Control," Lecture Notes, Delft University of Technology, Delft, Netherlands, 2005.

[106] A. Rantzer, "On the Kalman–Yakubovich–Popov lemma," *Syst. Control Lett.*, vol. 28, no. 1, pp. 7–10, 1996.

# List of Notations, Symbols and Abbreviations

## Notations

| | |
|---|---|
| $\mathbb{R}$ | Field of real numbers |
| $\mathbb{C}$ | Field of complex numbers |
| $\mathbb{R}H_\infty$ | Set of proper, stable and rational functions with real coefficients |
| $l_2$ | Space of sequences square summable over the doubly-infinite time |
| $L_2$ | Space of signals square integrable over the doubly-infinite time |
| $\left[\begin{array}{c:c} A & B \\ \hdashline C & D \end{array}\right]$ | Shorthand for a parameter-invariant state space realization |
| $\left[\begin{array}{c:c} \mathcal{A}(\Theta) & \mathcal{B}(\Theta) \\ \hdashline \mathcal{C}(\Theta) & \mathcal{D}(\Theta) \end{array}\right]$ | Shorthand for a state space realization varying on $\Theta$ |
| $\otimes$ | Kronecker product |
| $\star$ | Star product |
| $*$ | Symmetric terms in LMI |
| $(\cdot)^T$, $(\cdot)^*$ | Transpose/complex conjugate transpose |
| $\ker(\cdot)$ | Null space |
| $\partial_t(\cdot)$, $\partial_s(\cdot)$ | Variation rate with respect to time/space |
| $\mathrm{sat}(\cdot)$ | Saturation function |
| $\mathrm{dz}(\cdot)$ | Deadzone function |
| sym | Symmetric terms in a matrix |
| $\mathcal{O}(\cdot)$ | Truncation error |

## Symbols

| | |
|---|---|
| $a$, $b$ | Coefficients in input/output models |
| $b_p$ | Width of the electrode |
| $d(k,s)$ | Disturbance signal |
| $d$, $d_{31}$, $d_{32}$, $d_{33}$ | Piezoelectric constant |
| $e$ | Error vector |
| $e^T$ | Piezoelectric coupling coefficient under constant stress |
| $e(k)$, $e(k,s)$ | Gaussian white noise signal with zero mean |

| | |
|---|---|
| $f_i$ | $i$-th exogenous force |
| $g_a$, $g_s$ | Actuator/sensor constant |
| $h_p$ | Thickness of the electrode |
| $i_k$, $i_s$ | Temporal/spatial index variable |
| $k_s$ | Spring stiffness |
| $l$ | Length of the structure |
| $l_e$ | Length of an element |
| $l_p$ | Length of the electrode |
| $m_0$ | Size of the temporal state vector |
| $m_+$, $m_-$ | Size of the positive/negative spatial state vectors |
| $n^+(k,s)$, $n^-(k,s)$ | Output noise in positive/negative directions |
| $n_a$, $n_b$ | Size of the denominator/nominator order in input/output form |
| $n_d$ | Size of the disturbance |
| $n_p$ | Number of parameters to be estimated in LTI/LTSI models |
| $n_{\tilde{p}}$ | Number of parameters to be estimated in LTSV models |
| $n_t$, $n_s$ | Number of temporal/spatial scheduling parameters |
| $n_u$ | Size of the external input |
| $n_y$ | Size of the measured output |
| $n_z$ | Size of the fictitious output |
| $n_{\bar{\theta}}$ | Number of operating points |
| $n_{\Theta_t}$, $n_{\Theta_s}$ | Size of the temporal/spatial uncertainty |
| $n_\phi$ | Size of the regressor vector $\phi$ |
| $p$ | Vector of coefficients to be estimated in LTI/LTSI models |
| $\bar{p}$, $\hat{p}$ | True values and approximations of $p$ |
| $\tilde{p}$ | Vector of parameters to be estimated in LTSV models |
| $p^e$ | Vector of elemental-nodal loads |
| $p(\theta_t)$, $p(\theta_s)$ | Vector of coefficients scheduled by tempora/spatial parameters |
| $p^t(k,s)$, $q^t(k,s)$ | Input and output of the temporal uncertainty channel |
| $p^s(k,s)$, $q^s(k,s)$ | Input and output of the spatial uncertainty channel |
| $q$ | Electric charge |
| $q_t$ | Temporal forward shift operator |
| $q_s$, $q_s^{-1}$ | Spatial forward/backward shift operator |
| $r_{\theta_{ti}}$, $r_{\theta_{si}}$ | Multiplicity of temporal/spatial scheduling parameters $\theta_{t_i}$ and $\theta_{s_i}$ |
| $s^E$ | Compliance when the electric field is constant |
| $t$, $k$ | Continuous/discrete temporal variable |
| $u(k)$, $u(k,s)$ | Exogenous plant input |
| $u_0(k)$, $u_0(k,s)$ | Controller output |
| $\tilde{u}(k)$, $\tilde{u}(k,s)$ | Controller output after AW compensation and before saturation |
| $\bar{u}(k)$, $\bar{u}(k,s)$ | Maximum capacity of a physical actuator |
| $\breve{u}(k)$ | Input of a lifted system |
| $u^e$ | Vector of elemental-nodal displacement |
| $v(k)$, $v(k,s)$ | Filtered noise |
| $v_1$, $v_2$ | Outputs of an AW compensator |
| $w$ | Transverse deflection |

| | |
|---|---|
| $x_t(k,s)$ | Temporal state |
| $x_s^+(k,s)$ | Spatial state in the positive direction |
| $x_s^-(k,s)$ | Spatial state in the negative direction |
| $\breve{x}(k)$ | State of a lifted system |
| $x$, $s$ | Continuous/discrete spatial variable |
| $y(k)$, $y(k,s)$ | Measured output (controller input) |
| $y_0(k)$, $y_0(k,s)$ | Plant output |
| $\hat{y}(k)$, $\hat{y}(k,s)$ | Estimated output |
| $\breve{y}(k)$ | Output of a lifted system |
| $z(k,s)$ | Fictitious output |

| | |
|---|---|
| $A_o$ | Cross-section area |
| $A(q_t)$, $A(q_t,q_s)$ | Denominator polynomial of lumped or distributed models |
| $B(q_t)$, $B(q_t,q_s)$ | Nominator polynomial of lumped or distributed models |
| $B_u$ | Derivative of shape function $N_u$ |
| $\mathcal{C}$ | Global damping matrix |
| $C_a$ | Capacitor |
| $C^e$ | Elemental damping matrix |
| $D$ | Electric displacement |
| $E$ | Young's modulus |
| | Electric field |
| $F$ | Vector of exogenous forces |
| $G(q_t)$, $G(q_t,q_s)$ | Input/output representation of a plant model |
| $G(s)$ | Continuous transfer function of a plant model |
| $H(q_t)$, $H(q_t,q_s)$ | Input/output representation of a noise model |
| $I$ | Second moment of area |
| $J$ | Cost function |
| $K(q_t)$ | Discrete transfer function of a controller |
| $K^e_{u\phi}$, $K^e_{\phi u}$ | Mechanical and electrical coupled elemental stiffness matrix |
| $K^e_{uu}$ | Elemental mechanical-stiffness matrix |
| $\mathcal{K}$ | Global stiffness matrix |
| $\mathcal{M}$ | Global mass matrix |
| $M^e$ | Elemental mass matrix |
| $M_i$ | $i$-th Moment |
| $M_p$ | Concentrated moment generated by Piezo actuator |
| $M_u$, $M_y$ | Input/output mask |
| $N_k$, $N_s$ | Size of temporal/spatial measurements |
| $N_u$ | Shape function |
| $N_R$, $N_S$ | Null space |
| $\mathcal{N}_R(\cdot)$, $\mathcal{N}_S(\cdot)$ | Parameter-varying null space |
| $P$ | Global external load |
| $\mathcal{P}$ | Matrix of estimated coefficients $\lambda$ |
| $Q$ | Global electric charge |
| $R_e$ | Resistance |

| | |
|---|---|
| $S$ | Strain |
| $\mathbf{S}$, $\mathbf{S}^{-1}$ | Spatial forward/backward shift operator |
| $T$ | Stress |
| $\mathbf{T}$ | Temporal forward shift operator |
| $U$ | Global mechanical variable |
| $V$ | Volume |
| $W_f$ | Postfilter |
| $W_k$ | Shaping filter of control sensitivity |
| $W_s$ | Shaping filter of sensitivity |
| $X$ | Structured Lyapunov matrix |
| $X_t$, $X_s$ | Temporal/spatial Lyapunov matrix |
| $\boldsymbol{\mathcal{X}}_m$ | Set of structured Lyapunov matrix |
| $\hat{\boldsymbol{\mathcal{X}}}_m$ | Set of structured Lyapunov matrix with only temporal components |
| $Y$ | Output vector |
| $\mathcal{Y}$ | Multiplier set |
| $Z$ | Impedance |

**Greek Letter**

| | |
|---|---|
| $\alpha$, $\beta$ | Parameters to be estimated in LTSV models |
| $\gamma$ | Performance index |
| $\boldsymbol{\Delta}_m$ | Augmented operator |
| $\Delta_{\bar{\theta}}$ | Matrix of exponents of operating points |
| $\Delta T$ | Sampling time |
| $\Delta X$ | Sampling space |
| $\epsilon^T$ | Relative permittivity when the stress is constant |
| $\eta$, $H$ | Regressor vector/matrix in LTSV model identification |
| $\theta_{t_i}$, $\theta_{s_i}$ | Temporal/Spatial scheduling parameter |
| $\theta_t$, $\theta_s$ | Vector of temporal/spatial scheduling parameters |
| $\Theta_t$, $\Theta_s$ | Structured temporal/spatial uncertainty |
| $\boldsymbol{\Theta}_\mathbf{t}$, $\boldsymbol{\Theta}_\mathbf{s}$ | Compact set of structured temporal/spatial uncertainty |
| $\kappa$ | Curvature |
| $\lambda$ | Coefficients of polynomial functions on scheduling parameters |
| $\Lambda$ | Matrix of polynomial coefficients |
| $\xi$ | Dimensionless coordinate |
| $\Xi_t$, $\Xi_s$ | Set of the temporal/spatial variation rate |
| $\Pi$ | Multiplier |
| $\rho$ | Density |
| $\tau$ | Vector of exponents of scheduling parameters |
| $\Upsilon$ | Augmented uncertainty |
| $\hat{\Upsilon}$ | Vertices of augmented uncertainty |
| $\phi$, $\Phi$ | Regressor vector/matrix in LTI or LTSI model identification |
| $\Phi_i$, $\Phi_o$ | Global input/output voltage |
| $\phi_i$, $\phi_o$ | Elemental input/output voltage |

| | |
|---|---|
| $\omega$ | Frequency |
| $\Omega_m$, $\Omega$ | Matrix of mode shapes |

**Superscript**

| | |
|---|---|
| $G$ | Plant model |
| $K$ | Controller |
| $L$ | Closed-loop system |
| $\tilde{L}$ | Permuted closed-loop system $L$ |
| $P$ | Closed-loop system including $G$, $K$, and $\Psi$ |
| $\tilde{P}$ | Permuted closed-loop system $P$ |
| $\Psi$ | AW compensator |

**Abbreviations**

| | |
|---|---|
| ARX | AutoRegressive with eXogeneous |
| AW | AntiWindup |
| BTCS | Backward-Time Central-Space |
| CFL | Courant-Friedrichs-Lewy |
| CLF | Constant Lyapunov Function |
| CTCS | Central-Time Central-Space |
| DOF | Degree of Freedom |
| FBSP | Full Block S-Procedure |
| FD | Finite Difference |
| FE | Finite Element |
| FRF | Frequency Response Function |
| FTFS | Forward-Time Forward-Space |
| IQC | Integral Quadratic Constraint |
| KYP | Kalman-Yakubovic-Popov |
| LFT | Linear Fractional Transformation |
| LMI | Linear Matrix Inequality |
| LPV | Linear Parameter-Varying |
| LTI | Linear Time-Invariant |
| LTSI | Linear Time- and Space-Invariant |
| MEMS | MicroElectroMechanical System |
| MIMO | Multiple-Input Multiple-Output |
| ODE | Ordinary Differential Equation |
| PDE | Partial Differential Equation |
| PDLF | Parameter-Dependent Lyapunov Function |
| PI | Physik Instrumente |
| PVDF | PolyVinylidene DiFluoride |
| PZT | Lead Zicronate Titanate |
| SISO | Single-Input Single-Output |
| SVD | Singular Value Decomposition |

# List of Publications

**Published**

Q. Liu and H. Werner, Distributed Antiwindup Compensator for Spatially-Interconnected Systems, in *IEEE Proc. of American Control Conference*, Chicago, USA, 2015

Q. Liu, A. Mendez, and H. Werner, Distributed Control of Spatially-Interconnected Parameter-Invariant and LPV Models for Actuated Beams, in *IEEE Proc. of American Control Conference*, Portland, USA, 2014

G. Kaiser, M. Korte, Q. Liu, C. Hoffmann, and H. Werner, Torque Vectoring for a Real, Electric Car Implementing an LPV Controller, in *19th IFAC World Congress*, Cape Town, South Africa, 2014

Q. Liu, J. Gross, S. Pfeiffer, and H. Werner, A Local Approach for the LPV Identification of an Actuated Beam Using Piezoelectric Actuators and Sensors, in *Mechatronics*, vol. 24, no. 4, pp. 289-297, Jun. 2014

Q. Liu and H. Werner, Experimental Identification of Spatially-Interconnected Parameter-Invariant and LPV Models for Actuated Beams, in *52nd IEEE Conference on Decision and Control*, Florence, Italy, 2013

Q. Liu, C. Hoffmann, and H. Werner, Distributed Control of Parameter-Varying Spatially Interconnected Systems Using Parameter-Dependent Lyapunov Functions, in *IEEE Proc. of American Control Conference*, Washington D.C., USA, 2013

M. Bartels, Q. Liu, G. Kaiser, and H. Werner, LPV Torque Vectoring for an Electric Vehicle Using Parameter-Dependent Lyapunov Functions, in *IEEE Proc. of American Control Conference*, Washington D.C., USA, 2013

G. Kaiser, Q. Liu, and H. Werner, Torque Vectoring for an Electric Vehicle Using an LPV Drive Controller and a Torque and Slip Limiter, in *51st IEEE Conference on Decision and Control*, Hawaii, USA, 2012

Q. Liu, G. Kaiser, S. Boonto, H. Werner, F. Holzmann, B. Chretien and M. Korte, Two-Degree-of-Freedom LPV Control for a through-the-Road Hybrid Electric Vehicle via Torque Vectoring, in *50th IEEE Conference on Decision and Control*, Orlando, USA, 2011

**Accepted**

Q. Liu, J. Gross and H. Werner, Distributed Identification of Spatially-Distributed Systems Based on Finite Element Modelling, in *54th IEEE Conference on Decision and Control*, Osaka, Japan, 2015

**Submitted**

J. Gross, Q. Liu, M. Gomse and U. Weltin, Eigenpath Tracking in a Two-Dimensional Normal Modes Problem Using the Spectral Element Method and the Modal Assurance Criterion, submitted to *Journal of Sound and Vibration*, 2015